USING SUPER RESOLUTION MICROSCOPY TO INVESTIGATE THE ROLE OF ACTIN IN ADENOSINE RECEPTOR ORGANISATION

UNIVERSITY OF BIRMINGHAM

The University of Nottingham

BY

EVELYN GARLICK

A thesis submitted to the University of Birmingham and the University of Nottingham for the dual degree of

DOCTOR OF PHILOSOPHY

AUGUST 2022

Institute of Cardiovascular Sciences
College of Medical and Dental Sciences
University of Birmingham

Faculty of Medicine and Health Sciences
School of Life Sciences
University of Nottingham

ABSTRACT

Membrane receptors are key to how cells interact with other cells and their environment. G Protein-Coupled Receptors (GPCRs) are a major drug target, with approximately a third of all FDA approved drugs acting on a GPCR [1]. The organisation of GPCRs in the cell membrane can play a key role in determining signalling responses and associated pharmacological parameters. There is significant evidence that the cortical actin skeleton can contribute to this organisation via the picket fence model. The direct contribution of actin architecture and dynamics to organisation of specific receptors requires further study. Therefore, this thesis applies a range of super-resolution microscopy techniques to investigate the role of cortical actin in the organisation of the human adenosine-A_{2A} ($A_{2A}R$) and -A_{2B} receptors ($A_{2B}R$).

Using A549 cells transiently transfected with N-terminally SNAP-tagged receptor constructs, clustering analysis using dSTORM (direct stochastic optical reconstruction microscopy) indicates effects of actin disruption on $A_{2A}R$ clustering but not $A_{2B}R$, while assessment of dynamic behaviour via single particle tracking (SPT) indicates differential effects on the motion patterns of each receptor. This was further supported by 3D-SIM (structured illumination microscopy) imaging of actin and receptors together. Assessment of actin using SRRF (super resolved radial fluctuations) processing showed a change in actin architecture after receptor stimulation. Workflows for imaging and analysing finer actin filaments using 3D-SIM expansion microscopy (ExM) were also developed, with incorporation of the A_2R interacting protein α-actinin-1 serving both as investigation of a potential actin link

and as a demonstration of two colour ExM. Initial experiments using SRRF processing indicated super-resolution imaging of actin was possible on a timescale which allowed concurrent single particle tracking of receptors, opening potential for correlated analysis.

These findings indicate a role for actin in mediating $A_{2A}R$ and $A_{2B}R$ membrane organisation, with potential for different regulatory contributions between receptors and across organisational scales.

ACKNOWLEDGEMENTS

I’m extremely grateful to my two brilliant supervisors, Steve Thomas and Steve Briddon, for their guidance, patience, and for listening to me grumble about the SIM. Thank you, Steves! I could not have done it without you.

Funding from COMPARE made this project possible. Big thanks go to Dee Kavanagh, Amanda Dalby, and Joao Correia for all their help wrangling the microscopes, and to Jeremy Pike for his analysis expertise. Thanks also to Mark Soave and Joelle Goulding for their help with pharmacology and ligand labelling experiments in Nottingham.

Thank you to all the members of Birmingham Platelet group for being such a friendly and supportive group. Special thanks obviously to the wonderful Thomas lab members: Tom - thank you for your company in the imaging suite for those long hours and good anime recs, and Emma, the Expansion Oracle - thank you for our coffee chats and pub visits, and for being an incredible friend.

The patience of my friends is unmatched. Butler Humans, the Litari gang, thank you for listening while I rambled about science! I love you all and am so lucky to have such great people in my life. A million thank yous to my lovely family - Mum, Dad, I’m so so grateful for your support and helping me decide my own path. And Anna - thanks for putting up with a nerdy big sister!

TABLE OF CONTENTS

LIST OF FIGURES

LIST OF TABLES

LIST OF ABBREVIATIONS

Abbreviation	Term
$A_{2A}R$	Adenosine-A_{2A} receptor
$A_{2B}R$	Adenosine-A_{2B} receptor
BAY60, BAY	BAY60-6583
BiFC	Bimolecular fluorescence complementation
cAMP	Cyclic Adenosine Monophosphate
CD	Cytochalasin D
EM	Electron microscopy
EMCCD	Electron Multiplying Charge Coupled Device
ERM	Ezrin-Radixin-Moesin
ExM	Expansion microscopy
Fab	Fragment antigen-binding region
FP	Fluorescent Protein
FRET	Fluorescence resonance energy transfer
GFP	Green fluorescent protein
GPCR	G protein-coupled receptor
LA	LifeAct
mEGFP	Monomeric enhanced green fluorescent protein
Nbs	Nanobodies
NECA	5'-N-Ethylcarboxamidoadenosine
OTF	Optical transfer function
PAINT	Point accumulation in nanoscale topography
PALM	Photo-activated localisation microscopy
PFS	Perfect focus system
PSF	Point spread function
scFv	Single chain variable fragments
sCMOS	Scientific complementary metal oxide semiconductor
SIM	Structured illumination microscopy
SMLM	Single molecule localisation microscopy
SNR	Signal to noise ratio
SPT	Single particle tracking
SRRF	Super resolution radial fluctuations
STED	Stimulated emission depletion
STORM	Stochastic optical reconstruction microscopy
TCR	T cell receptor
TIRF	Total internal reflection microscopy
U-ExM	Ultrastructure ExM

CHAPTER 1 – INTRODUCTION

Sections of this chapter are published as:

Garlick, E., Thomas, S. G., and Owen, D. M. 2021. **'Super-Resolution Imaging Approaches for Quantifying F-Actin in Immune Cells'**. Frontiers in Cell Dev. Bio., 9. https://doi.org/10.3389/fcell.2021.676066

1.1 General Introduction

Understanding of how receptor signalling is regulated has developed rapidly in recent years. Such knowledge is valuable in unpicking complex signalling pathways and potentially developing new methods to modulate receptor behaviour. Membrane organisation of G Protein-Coupled Receptors (GPCRs), for example, plays an important role in determining signalling responses and associated pharmacological parameters, with increasing evidence that this is relevant in disease. The molecular determinants of this organisation, however, are not fully understood. While many models of membrane organisation have been proposed, and indeed demonstrated, relative contribution on the level of individual receptor families remains a somewhat open question.

This thesis therefore aims to describe methods of investigating the contributions of a particular membrane organisation model, the ‘picket fence’, to adenosine receptor organisation and behaviour, using a variety of advanced and super resolution microscopy techniques. Techniques and analysis methods were developed such that receptor behaviour in both fixed and live cell contexts could be investigated relative to actin architecture.

1.2 Membrane Organization

1.2.1 The fluid mosaic model

It is now known that the plasma membrane is comprised of a phospholipid bilayer, traversed by a variety of transmembrane proteins and incorporating further lipid and fatty acid molecules, such as sterols [2]. Early models of the membrane, such as the unit membrane model, suggested a static sandwich running protein-lipid-protein [3]. In 1972, however, Singer and Nicolson proposed the fluid-mosaic model to describe gross membrane organisation [4]. They argued that the 'fluid' lipid bilayer incorporated a 'mosaic' of freely moving membrane proteins. Their core argument was that the standard case for membrane organisation was random protein distribution throughout these fluid lipids, although the original paper did acknowledge potential for 'short range' constraint in the form of protein-protein and protein-lipid interactions [4]. Despite this concession, the authors argued that 'long range' organisation – by their definition, over 'a few tenths of a micrometer' - was unlikely in such a system. More complex organisation in specific circumstances, such as in synapses, was acknowledged, but suggested to be the result of abnormally large 'short range' aggregates or mediated by some factor external to the membrane.

This model also explained the varying ways in which membrane proteins could be embedded in the membrane, suggesting that it was the amphipathic structures of these proteins that allowed intercalation into the hydrophobic lipid tail core of the membrane (Figure 1.1). Previously it had been unclear which component – lipids or

proteins - formed the ‘matrix’ through which the other traversed, or as Singer and Nicolson put it, which was the “bricks”, and which was the “mortar”. This model proposed that a stable matrix of proteins was unlikely, as this would result in a very stable gross membrane protein organisation, which simply was not seen. These hypotheses were supported with the data available at the time. It was known that membrane phospholipids behaved like a fluid at room temperature, and electron microscopy data from early membrane protein labelling experiments were interpreted as supporting the idea of random distribution until an external factor generated larger scale organisation [4].

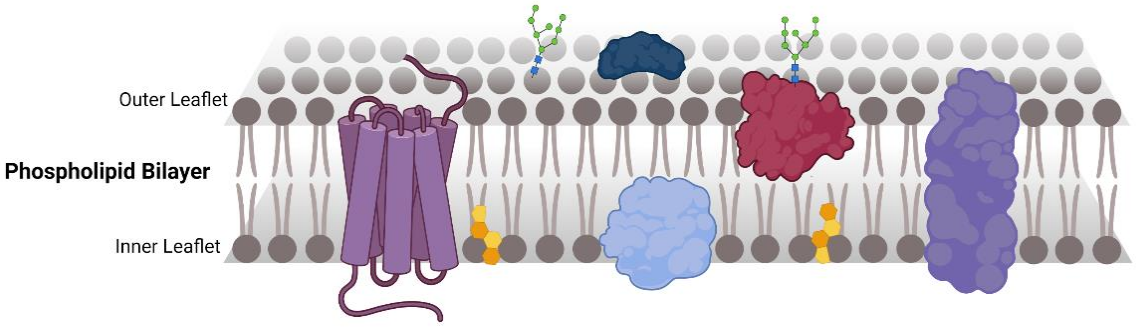

Figure 1.1 – Diagram of basic plasma membrane organisation. *A phospholipid bilayer containing various transmembrane, inner and outer membrane proteins, as well as branching glycoproteins (green) and sterols (yellow).*

1.2.2 Development of understanding and further models

Understanding of plasma membrane organisation has come a long way from the basic principles of Singer - Nicolson's fluid mosaic model. While the fundamental argument that membrane proteins are capable of diffusing through a fluid lipid bilayer stands, as understanding of the physical properties of the membrane advanced it became clear that lipids and proteins were not freely diffusing in a fluid manner - rather, motion was restricted at various scales. In fact, Nicolson himself published a revised version of the fluid mosaic model in the last decade [5], arguing for greater emphasis to be placed on the 'mosaic' portion of the proposal and how this can lead to differential organisation within membrane regions. Understanding how these restrictions are imposed and regulated is vital to understanding the behaviour of membrane proteins. A variety of models have been proposed, supported by significant evidence from a multitude of investigative techniques, including light microscopy, atomic force microscopy, and electron microscopy. Given the wealth of evidence, it is largely accepted that multiple membrane organisations coexist, permitting tuning of organisation and membrane behaviour across the nano, meso, and macro scale. In fact, as Bernardino de la Serna et al. [2] argue in a review of the same name, 'there is no simple model of the plasma membrane organisation'.

A few key organisations are discussed here.

1.2.3 Lipid rafts, protein microdomains, and peripheral organisation

Plasma membranes contain a significant variety of lipids, with a range of properties. More highly ordered domains - lipid rafts (Figure 1.2) - are proposed as a regulator of membrane protein organisation [6]. Evidence suggests these rafts are both small (sub ~ 200 nm) and transient (on the order of tens of milliseconds) under resting conditions [7], resulting in short term enrichment of lipid or protein species. Larger and more stable structures can be found after induction of clustering or signalling processes.

Originally not thought to be directly involved in membrane organisation, membrane peripheral structures including intra- and extracellular matrices can affect membrane organisation through links to lipids and proteins. Examples of these with evidence for organisational function include septins [8] and the glycocalyx [9]. Another important submembrane mesh is the cortical actin network (Figure 1.3). The role that actin and its associated proteins play in membrane organisation forms the basis of this project, and the evidence and origins of the ‘picket fence model’ are therefore explained in greater detail below.

In addition to lipid ordered domains, proteins can also form dynamic microdomains within membranes which regulate organisation and activity. Examples include the tetraspanin family of proteins which form microdomains in membranes and have been shown to regulate protein organisation, trafficking, and cleavage [10, 11].

These models are by no means mutually exclusive. It is heavily indicated that organisation of the membrane is regulated in tandem by combinations of these models. For example, CD44 has been shown to interact both with the actin cytoskeleton and with hyaluronan, a component of the glycocalyx [12]. Disruption of normal interaction with both the actin and hyaluronan meshes resulted in changes in diffusive behaviour, indicating that both interactions are necessary for organisation.

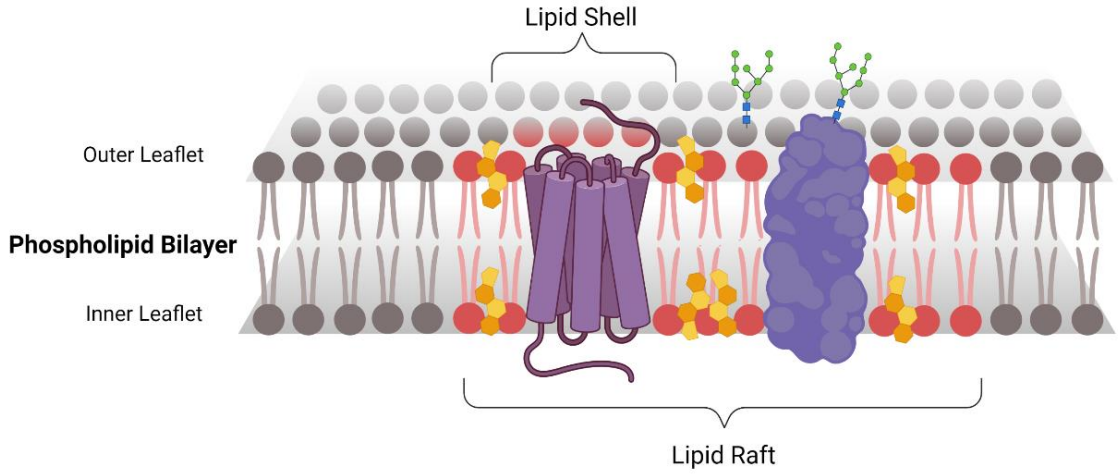

Figure 1.2 – Diagram of lipid-based membrane organisation. *Rafts show altered lipid composition, with cholesterol and sphingolipid enrichment resulting in more ordered domains.*

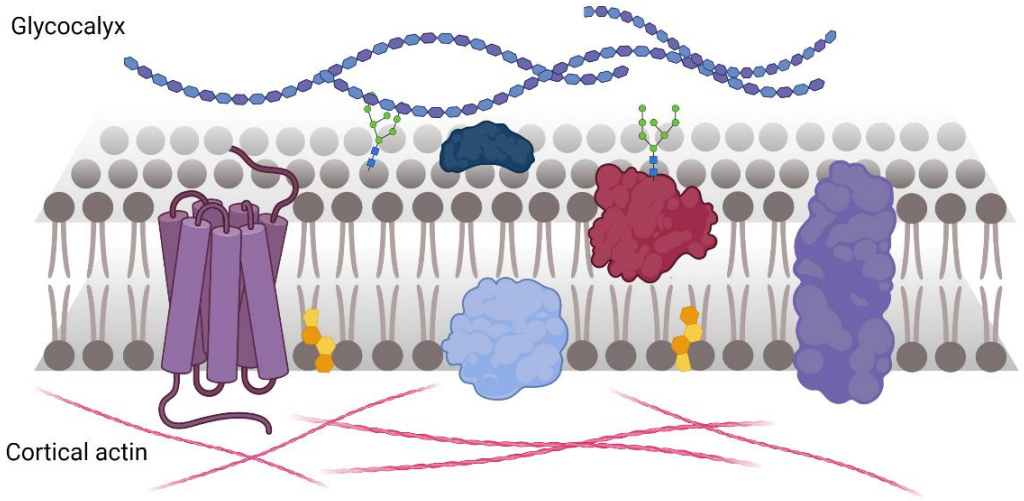

Figure 1.3 – Diagram of membrane peripheral networks implicated in membrane organisation. *There is evidence that both the glycocalyx (pericellular) and cortical actin mesh (intracellular) can contribute to membrane organisation.*

1.3 The Picket Fence Model

1.3.1 Evidence for a ‘picket fence’

Fujiwara et al. [13] proposed the picket-fence model to incorporate previous evidence that immobilised transmembrane proteins can affect phospholipid diffusion coefficients. In particular, this incorporated the finding that actin has influence over transmembrane protein behaviour. The initial model proposed a static arrangement of pickets bound stably to cortical actin fences, creating these small, bounded regions, termed corrals. Confinement radius calculations from imaging data, which accord well with direct measurement of the membrane cytoskeleton using EM techniques, describe cell specific corral sizes. For example, in papers by Morone et al. [14] and Fujiwara et al. [15] using electron tomography, actin corrals in NRK cells were calculated to have a mean length of 200 nm, PtK cells a mean length of 40 nm, and FRSK cells a mean length of 52 nm. Fujiwara et al. [13] showed that within these corrals diffusion was largely unimpeded, but that longer range movement was hindered by the fence – that is, the mobile species had to ‘hop’ between corrals. The rate limiting step in hop diffusion was shown to be the likelihood of the species escaping each corral, calculated as P_{Hop}. While the initial strength of confinement may have been overestimated, subsequent experiments have borne out the fundamental theory. STED-FCS experiments, for example, showed results for lipid diffusion consistent with hop diffusion [16], and also comment on the significant effects localisation error can have on the kind of high speed SPT experiments performed in these early experiments [17].

1.3.2 Importance of actin

The effects of actin on membrane protein behaviour are well described, including findings where disruption with cytochalasin D caused a seven fold increase in the lateral diffusion rate of the membrane protein Na+/K+ - ATPase [18]. Diffusion in blebbed membrane, typically not underlain by actin, has also repeatedly been shown to be faster and less likely to show confinement than in normal membrane [13]. In some cases, truncation of the cytoplasmic domain of a protein (such as class I MHC molecules) can also result in significant increase in lateral diffusion, suggesting direct physical constraint [19]. CD44 has been shown to have direct interaction with the actin cytoskeleton mediated via ERM proteins, again abrogated by C-terminal truncation [12]. LYVE-1 shows increased lateral diffusion and even increased ligand binding after actin disruption, with C-terminal truncation recapitulating the diffusion change, despite showing little direct tethering interaction with actin [20]. A cytoplasmic tail is not needed for all proteins that show cytoskeletal confinement, however; Freeman et al. [12] showed that removal of the C-terminal portion of FcγRIIA receptors had no effect on its dynamics, instead concluding that in this case the pickets played the key confining role.

1.3.3 Role of pickets

The inclusion of picketing proteins in the model helps to explain the confinement of lipid species in corrals. Whilst direct confinement by a proteins' C-terminal hitting the actin fence is not applicable to a lipid, simulations and observations of membrane dynamics have indicated that immobilised membrane proteins can greatly slow local membrane diffusion, either by increased 'packing' around the protein [21], physical steric hindrance [22], or through increased hydrodynamic interactions [23] (Figure 1.4). The identity of specific pickets is still under investigation. CD44 has been shown to act as an anchored picket in macrophages [12], but can also exist in confined and 'free' diffusion states. In a review of membrane organisation, Jacobson et al. [24] discuss the relationship between expression levels of membrane proteins and picketing behaviour, suggesting a rough value of 3×10^6 pickets necessary per 40 μm square "cell". They go on to suggest that with CD44 having an expression level of ~ 1×10^6 copies per cell, it seems unlikely that this protein performs all picketing in this cell type.

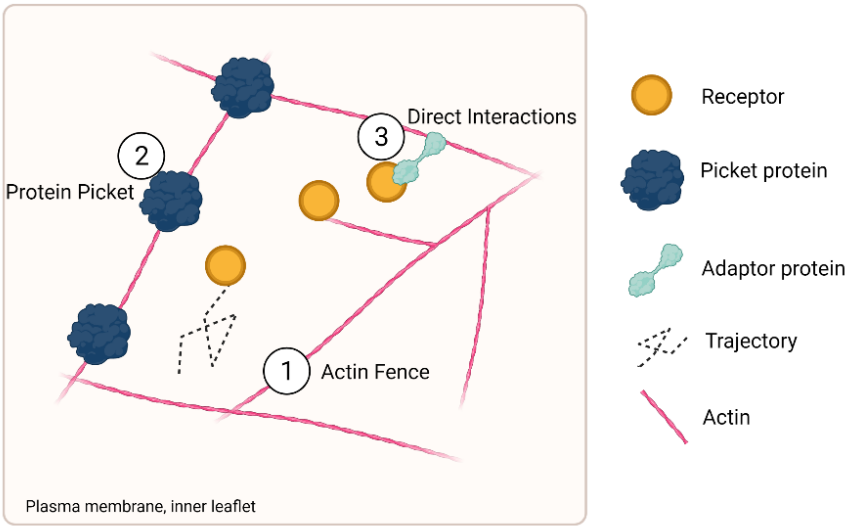

Figure 1.4 - Picket fence model of membrane organisation*. Diagram showing proposed nature of the picket fence model on the inner leaflet of the plasma membrane. Potential methods of receptor confinement include 1) direct physical impediment of receptor movement by the actin filaments, 2) alteration to lipid packing around picketing proteins, and 3) direct interaction with actin filaments, with or without adaptor proteins.*

1.3.4 Examples of evidence of actin involvement in membrane organisation

One of the best described cases of actin structure affecting membrane receptor organisation is in T cells. T cells form an immunological synapse with antigen presenting cells, where signalling takes place in a spatially confined location. Actin remodelling is believed to contribute in three key ways – corralling signalling intermediates, creating a surrounding barrier to vesicle trafficking, and as a regulator of clustering and diffusion [25]. There is also evidence of a direct linking of the actin cytoskeleton and plasma membrane via α-actinin, which is partially responsible for directional plasma membrane flow and associated relocation of receptors and signalling molecules [25]. Recent work suggests a dual role for actin – both as a mechanical support for synapse maintenance, and nanoscale reorganisation of

individual filaments to fine tune signalling responses [26]. Techniques used here to investigate actin/receptor interactions can easily be adapted beyond immune cells – to look, for example, at GPCRs.

1.4 Actin and the Actin Cortex

Actin is one of three cytoskeletal meshworks in the cell, and has the smallest fibres, at approximately 7 nm in diameter. Each filament (F-actin) is made up of globular actin monomers (G-actin), which are polar proteins capable of binding ATP. The basic structure of a G-actin monomer involves two domains, each with two subdomains, arranged around a hinge region. This structure lends itself to the formation of polar antiparallel helical filaments, which can form complex networks. Filaments are nucleated either by formins (largely mDia1 [27]), which form longer, straight filaments, or the Arp2/3 complex, responsible for branched networks [27, 28]. Actin filaments undergo a dynamic process known as treadmilling, where actin associated proteins such as cofilin promote severing and depolymerisation of filaments while nucleators promote growth. This means that the actin cytoskeleton itself is dynamic, capable of reforming and reshaping the cell in response to the cellular environment. Actin is therefore responsible for a host of dynamic processes, such as cell migration and endocytosis as well as maintenance of general cellular shape [29]. Actin forms several distinctive structures within the cell, with key actin macro structures including: filopodia, or bundles of parallel filaments protruding from the cell edge; lamellopodia, or ‘ruffles’ consisting of a branched actin network, usually

at the leading edge of the cell; stress fibres, which are antiparallel contractile bundles; and our major structure of interest, cortical actin.

Cortical actin is a heterogeneous distribution of dense actin filaments of mean thickness 230nm [30] in close proximity to the plasma membrane, which undergoes constant remodelling [31]. The cortex is principally involved in cell morphogenesis, and has been aptly described as a ‘bridge between cell shape and function’ [32]. Contractile stress generated in the actin mesh by myosin motors and the like regulate cytokinesis, migration, and tissue morphogenesis [29]. Disruption of normal actin turnover can show pronounced effects on developmental processes – for example, stabilisation of actin with jasplakinolide significantly delayed the process of spinal neural tube closure in mouse embryos [33].

The close association of cortical actin with the plasma membrane and the proteins found therein underpins the ‘picket fence’ model of membrane organisation. Membrane/actin interaction can be mediated in multiple ways: directly with lipids (e.g. ERM proteins are capable of binding to PIP2 at the N-terminal and F-actin at the C-terminal [34, 35]); through actin binding motifs in membrane proteins (like ERM domains, calponin homology domains [36]); or through protein-protein interactions between membrane proteins and actin interacting proteins (such as ankyrin, filamin, and also ERM proteins [36]).

1.5 Receptor Organisation

1.5.1 G Protein-Coupled Receptors

G Protein-Coupled Receptors (GPCRs) are implicated in an impressive range of cellular processes and are therefore heavily therapeutically targeted – in fact, a third of all drugs target GPCRs [1]. GPCRs are broadly split into six subfamilies, with class A (Rhodopsin-like) receptors making up the largest group. All share a standard structure of 7 transmembrane (TM) domains with varying lengths and compositions of the C- and N- termini and interdomain loops. The ligand binding pocket in class A GPCRs is situated in the extracellular portion of these transmembrane helices. Upon binding, conserved motifs in the TM domains, including DRY, NPxxY, and CWxP [37], act as molecular switches, undergoing conformational changes proposed to contribute to a global switch to an ‘active’ receptor conformation [37].

GPCRs primarily signal via interaction with the heterotrimeric family of guanine nucleotide binding proteins (G proteins). These heterotrimers consist of Gα, Gβ, and Gγ subunits. Specific Gα proteins (G_s, G_q, and G_i, among others) determine the GPCR’s downstream signalling profile (Figure 1.5). The Gα subunit binds to guanosine diphosphate (GDP) when inactive, which is displaced by GPCR stimulation and results in guanosine triphosphate (GTP) binding when Gα is active [38].

GPCRs as a family can range from obligate monomers to constitutive dimers to sizeable clusters, with a spectrum of arrangements and associated signalling effects in between. Strong evidence exists for the existence of GPCR oligomers - for example, FCS data showing diffusion coefficients that are significantly slower than the value to be expected of monomers for A_3R [39], or FRAP data indicating higher order oligomerisation of the β2-adrenergic receptor [40]. There is also evidence that ligand interactions can affect oligomerisation, and vice versa. In β adrenergic receptors, treatment with isoproterenol increased the number of detected dimers, while introduction of the peptide TM VI reduced them, with an accompanying inhibitory effect on adenyl cyclase activation [41].

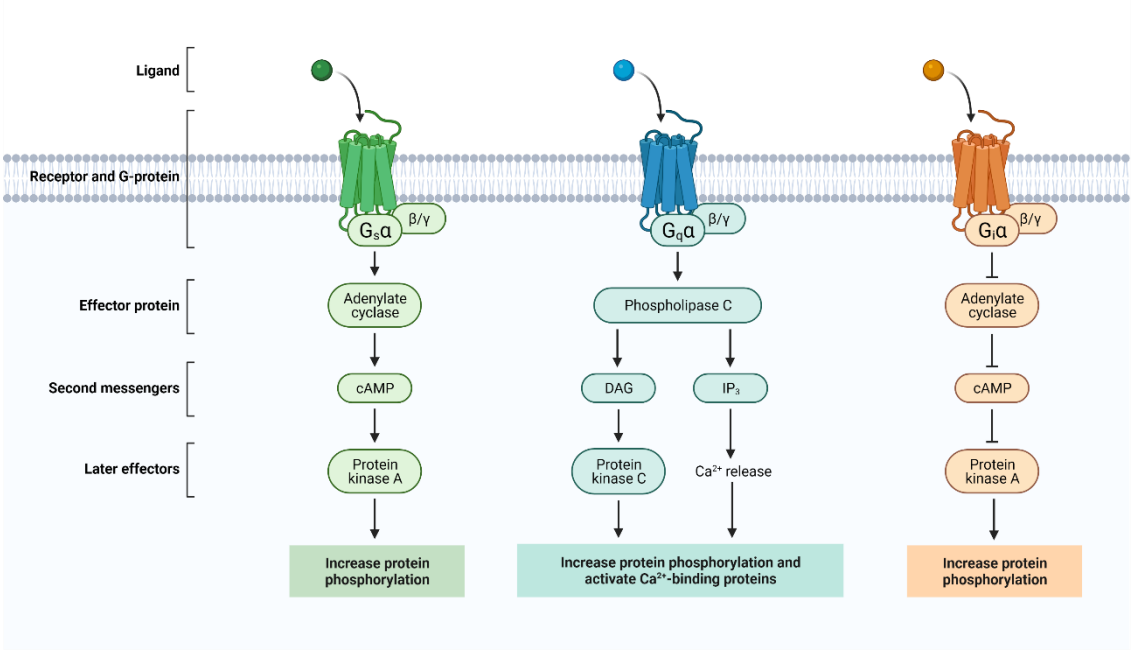

Figure 1.5 – Core GPCR signalling pathways. *The specific G-protein a GPCR couples with affects the downstream outcomes of receptor stimulation. Gs coupled receptors increase cAMP production where Gi coupled receptors decrease it. Gq coupled receptors increase DAG and IP3 levels, allowing calcium modulation. Diagram adapted from "GPCR Effector Pathways" by Biorender.com (2021), retrieved from https://app.biorender.com/biorender-templates.*

1.5.2 GPCR organization and importance

Understanding how GPCRs interact and are arranged within the membrane, as well as how they are trafficked and internalised, is vital to begin to unpick mechanisms by which signalling is regulated. There is evidence to suggest that oligomers can contribute to functional selectivity – that is, signalling by different pathways - and are as such a pertinent drug target [42]. Rational drug design must therefore begin to consider oligomerisation, especially when modelling receptor behaviour computationally. One way in which oligomerisation could be manipulated is through bivalent ligands, artificially forcing dimerisation (for example, [43]). It has also been reported that misregulation of AT1 receptor heterodimerisation is directly linked to preeclampsia [44]. It is therefore necessary to fully understand regulation under normal conditions to be able to start to target disease states.

Dimerisation can be a contentious issue. It is relatively trivial to demonstrate interactions between receptors - through colocalization or coimmunoprecipitation, albeit with the caveats of these methods - but far harder to demonstrate functional effect. A review by Gomes et al. [45] sets out three criteria (specifically for GPCR heteromers, but also applicable more broadly to dimers for the purpose of this introduction): components should colocalise and physically interact; the dimer should have functional properties distinct from the monomers; and there should be evidence that disruption of interaction ablates these distinct properties. As they note, scant few reported GPCR heteromers fulfil all three of these criteria.

In terms of homodimers, as investigative techniques and understanding have developed over time, it has become apparent that behaviour is largely specific to class - and there is further variation within these groupings too. For example, class C GPCRs like $GABA_B$ and metabotropic glutamate receptors must form homodimers in order to function [46]. Particularly for class A, however, the jury is still out - transient interaction appears more common than stable dimerisation, but these more fleeting interactions could still have functional effects. In a more stable but not obligate context, Getter et al. [47] identified small molecules which specifically modulated Rhodopsin dimers, resulting in changes in either photoresponse kinetics or receptor sensitivity depending on the disrupting molecule.

Higher order oligomerisation is also often reported, particularly with tetramers. For example, a combination of FRET saturation studies and ligand treatments demonstrated the ability of β2-adrenoceptors to form tetramers [48]. Interestingly, inverse agonists seem to promote higher-order oligomerisation, which the authors suggest may alter the access of downstream signalling proteins and provide a mechanism for inverse agonist action. Multiples of dimers can also be considered the basis of an oligomeric unit by some [42], blurring the lines somewhat with the definition of a cluster.

Clustering is conceptually more nebulous, and in the literature is sometimes applied as a simile for oligomerisation. However, here it will be used to refer to the gathering of receptors, be that monomers or higher order oligomers. Clusters above a density

threshold can also confer functional effects. The most well-defined example of this is with T Cell Receptors (TCRs). Clustering has also been demonstrated with other receptors, like the β2 adrenergic receptor, though this was also shown to be cell type specific – pre-association in the form of nanoclusters was only seen in cardiac cells [49]. There is evidence that clustering should be considered distinct to dimerisation in terms of its regulatory capacity. Mutation of key residues in the CXCR4 chemokine receptor prevented nanocluster formation, but did not affect dimerisation, allowing it to be shown that clustering is necessary to mediate a full ligand response [50].

1.6 Adenosine Receptors

1.6.1 Adenosine receptor family

The adenosine receptor family in humans is comprised of four members – A_1, A_{2A}, A_{2B}, and A_3. These class A GPCRs are responsible for the mediation of the body's response to adenosine and have diverse signalling pathways and localisations [51]. Family members respond at similar concentrations of adenosine, with the exception of $A_{2B}R$ which has a lower affinity [52]. Adenosine receptors are capable of modulating immune responses, heart rate, and angiogenesis, among other physiological – and pathological - processes (reviewed in [51, 53]). Adenosine levels are significantly higher in pathological states than under normal physiological conditions. Breakdown of the adenine nucleotide ATP is largely responsible for this increase, with release of ATP or adenosine itself from cells enhanced by cell damage or stress [53, 54]. Hypoxia can also enhance adenosine production, as well as

expression of some adenosine receptors [54]. Given this, it is unsurprising that adenosine receptors are linked to some cancers and neurodegenerative conditions [53]. Work in this thesis focuses on the two closely related A_2 receptors, $A_{2A}R$ and $A_{2B}R$.

1.6.2 $A_{2A}R$

The first crystal structure for the A_{2A} receptor ($A_{2A}R$, from the gene ADORA2A) bound to an antagonist was published in 2008 [55], with now over thirty structures resolved, spanning inactive, partially active, and active states [56]. These provide insight into the ligand binding pocket and transmembrane domains, but do not resolve the lengthy and disordered C terminal tail (Figure 1.6a). $A_{2A}R$ is a G_s linked receptor, with a cryo-EM structure of the receptor interacting with the heterotrimeric G-protein reported in 2018 [57].

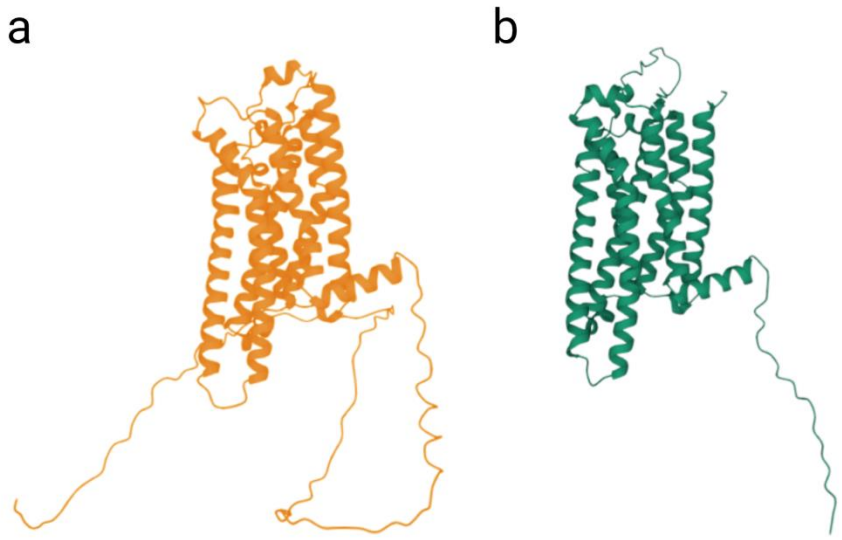

Figure 1.6 – Comparing full predicted structures for $A_{2A}R$ and $A_{2B}R$. *Full structures were generated from AlphaFold for a) $A_{2A}R$ and b) $A_{2B}R$, based on existing structural data for $A_{2A}R$, homology, and sequence data. When shown in the same orientation, the C-terminal tail and some areas of N-terminal loops show the most variation.*

$A_{2A}R$ is widely expressed in the body, but is of particular clinical interest in the brain, where it is implicated or targeted therapeutically in disorders spanning from Parkinson's disease to schizophrenia [58]. Other links to inflammatory processes, vascular regulation [59], immune system modulation, as well as pathologies like cancer, are well established (as reviewed in [60]). $A_{2A}R$ is therefore a very attractive drug target for a host of disorders.

In terms of organisation, it has been shown with fluorescence resonance energy transfer (FRET) and bioluminescence resonance energy transfer (BRET) investigations that homodimers exist and are likely the functional species of the receptor, as opposed to monomers [61]. BiFC (bimolecular fluorescence complementation) FRET experiments have also indicated that higher order structures exist [62]. There is evidence that the disordered C-terminal may be a driving factor in homomer formation [63]. Other identified $A_{2A}R$ partners include the dopamine D2 receptor [64], calmodulin [65], and – of particular interest to this thesis – the actin bundling protein α-actinin-1 [66, 67].

The actin interacting protein α-actinin-1 is a non-sarcomeric isoform of the α-actinins, which is widely expressed and found as antiparallel homodimers (as shown in Figure 1.7). Actinins bundle actin filaments, and in non-muscle cells can be found in adhesion sites as well as along actin filaments and stress fibres [68]. Piirainen et al. [67] recently showed that α-actinin 1 interacts with the C-terminal tail of the A_{2A} receptor in a calcium-dependent manner, with calmodulin competing for the same

binding site. Interaction of $A_{2A}R$ and α-actinin-1 was also shown to have functional effect by way of demonstrating a significant increase in cAMP accumulation when cells were transfected with a modified α-actinin-1 that was unable to bind to actin.

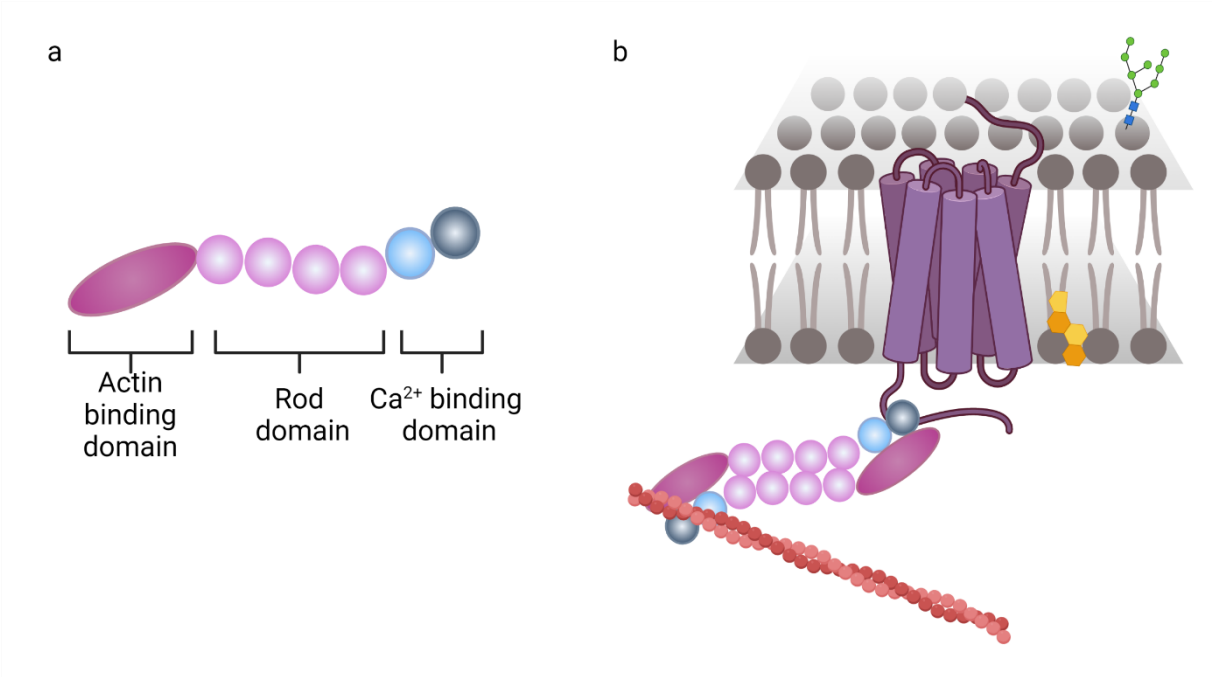

Figure 1.7 – Structure and function of α-actinin-1. *a) Diagram of the core domains of an α-actinin-1 monomer, with a calcium binding domain separated from the actin binding domain by the longer rod domain. b) α-actinin-1 functions as an antiparallel dimer, capable of interacting with both the actin cytoskeleton and adenosine GPCRs.*

1.6.3 $A_{2B}R$

The $A_{2B}R$, from the gene ADORA2B, has the lowest affinity for adenosine in the family [69]. Study of $A_{2B}R$ has traditionally been challenging given the limited number of specific agonists available – particularly complex given the potential for cross stimulation of the other adenosine receptors in the family. The receptor itself is not thought to deviate greatly from the standard GPCR structure. $A_{2A}R$ is the closest

structural relative of $A_{2B}R$ and shares around 60% homology when comparing amino acid sequence using pBLAST. Comparing predicted structures from AlphaFold [70, 71], as shown in Figure 1.6, indicates the lengthy C-terminal tail of $A_{2A}R$ may be a major source of the inter-A_2 receptor variability. It has also been indicated that extracellular loop 2 is the source of differences between $A_{2A}R$ and $A_{2B}R$ adenosine affinity [72].

$A_{2B}R$ is described as a 'promiscuous' receptor, having downstream interaction with G_i, G_s and G_q in differing cell lines and under differing signalling contexts [73, 74], therefore having the ability to regulate both cAMP production and calcium levels. The findings of Gao et al. [73] suggest interaction with different G-proteins can occur within the same cell, either coupling the same downstream signalling event, or a different downstream pathway, dependent on cell type – and potentially explaining previous contradictory findings about $A_{2B}R$ and its pro- and anti-inflammatory effects.

$A_{2B}R$ is widely expressed across organs and cell types (as summarised in [75]), and expression can be regulated by environmental influences, such as hypoxia [76] and inflammation [77]. As adenosine levels also rise under such conditions, this indicates the potential for a protective or regulatory role for $A_{2B}R$ under cell stress conditions. Relatively recently, significant findings with regards to involvement in acute [78] and chronic [79] lung injury, tumour proliferation [80] and progression (reviewed in [81]), and cardiovascular disease (reviewed in [82]), among others, reinvigorated the field and made the $A_{2B}R$ an important drug target.

In terms of interacting proteins, the $A_{2B}R$ has a number of binding partners, including α-actinin 1 [83] which could directly link the receptor to the actin cytoskeleton and help regulate surface expression, and adenosine deaminase [84] which modulates agonist binding and extracellular adenosine levels. There is also evidence of $A_{2A}R$-$A_{2B}R$ heterodimers – for example, FRET and BRET data indicating both an interaction and altered pharmacology for $A_{2A}R$ as part of such a heterodimer [85]. Interestingly, work by Moriyama and Sitkovsky [86] indicates that $A_{2A}R$ could be necessary for $A_{2B}R$ cell surface expression, as alone $A_{2B}R$ is largely degraded and has no dominant forward transport signal to reach the plasma membrane. It is also suggested that the ability of both $A_{2A}R$ and $A_{2B}R$ to interact with α-actinin-1 may provide a mechanism for the formation of such dimers [83].

1.7 Imaging Approaches for Studying Actin and Receptors

Thorough investigation of receptor and actin organisation is best performed using a combination of imaging and pharmacological techniques. While pharmacological experiments can return functional readouts over cell populations, fluorescence microscopy is a specific and sensitive approach that can permit investigation of individual cells and even single receptors. Imaging approaches used in this thesis can be broadly split between diffraction limited and super resolution techniques, but both rely on fluorescence.

1.7.1 Principles of fluorescence microscopy

Fluorescence microscopy relies on the process of fluorescence. Organic fluorophores or fluorescent proteins (FPs) are excited by specific wavelengths of light. Excited molecules return to the ground state, or 'relax', by emitting a photon. This is usually of lower wavelength and less energy than the exciting light, resulting in absorption and emission spectra that are distinct, with the distance between the two termed the Stokes shift. Fluorescent microscopes take advantage of this shift, filtering the excitation light from the emitted with specific optical filters. Transmission of emitted light, either to an eyepiece, a camera, or photomultiplier tube (PMT), allows visualisation of the sample.

1.7.2 Fluorescent proteins

Building on naturally occurring fluorescence, the now ubiquitous green fluorescent protein (GFP) was shown to be usable as a genetic tag in 1994 [87]. As this seminal paper suggested, having a genetically encodable fluorescent reporter allowed investigation of protein expression and localisation in live cells – previously a much more complicated task. Groups quickly began to produce variants that fluoresced across the spectrum and started working with other naturally occurring base FPs (see [88] for a review). Development also focussed on overcoming limitations imposed by FPs propensity for oligomerisation, which could affect protein behaviour. Monomeric variants of GFP, YFP, CFP [89] and RFP [90], among others, quickly followed. Brightness is also a consideration. 'Enhanced' variant eGFP showed 100x improved

fluorescence over standard GFP [91], due both to the shift in absorption spectra and significant improvement in protein folding prompted by the mutation. Further work on FPs provided photoswitchable and photoactivatable variants ideal for some super resolution applications, which are covered in more detail below.

1.7.3 Immunofluorescence

Immunofluorescence as a labelling method is perhaps the most commonly used approach in fixed sample imaging experiments. Primary antibodies against the protein of interest can be directly conjugated with chemical fluorophores, but use of a fluorescent secondary antibody provides more experimental flexibility. The large size of standard antibodies does however lead to 'linkage error' in indirect labelling, by which the fluorophore or other label is located at a distance of ~ 30 nm from the antigen. Variations include the use of smaller fragments of standard antibodies, like fragment antigen-binding region (Fab) fragments and single chain variable fragments (scFv) [92]. These have improved properties over standard antibodies in terms of size and production, as well as potential for in vivo application due to their shorter lifetimes. Even smaller still, and with improved stability and flexibility in application, nanobodies (Nbs) are monomeric camelid heavy-chain variable domains [93]. Nanobodies are an important addition to the light microscopy toolkit, offering improved penetration in fixed cell applications, as well as the potential to express FP conjugated nanobodies – also known as chromobodies - within live cells [94].

1.7.4 Self-labelling approaches

Another strong option for expressed tags, especially useful for live imaging, is the variety of self-labelling systems now available. SNAP [95], HALO [96], and CLIP [97] tags are genetically encoded self-labelling enzymes. These function by undergoing irreversible reactions with labelled substrates. SNAP systems, for example, consist of a modified human DNA repair protein O^6-alkylguanine-DNA alkyltransferase (hAGT) as the enzyme, and the nucleobase O^6-benzylguanine (BG) as the substrate [95]. The covalent interaction between the two allows labelling of whichever protein the enzyme is attached to. Labelling substrates with a wide range of both fluorophores and functional tags (e.g. biotin, NHS) are now commercially available.

1.7.5 Small molecule labels

Another common labelling strategy is the utilisation of small molecules which bind to a protein of interest. Some of the most commonly used are fluorescent phalloidins. Phalloidin is a bicyclic heptapeptide phallotoxin from the mushroom *Amanita phalloides* [98]. Its toxic effects come from the ability to bind and stabilise filamentous actin, and it is this property that allows fluorescent derivatives to act as a high affinity F-actin label in fixed cells. Fluorescent agonists or antagonists are another example and are invaluable for live imaging experiments when receptor stimulation is necessary. In terms of adenosine receptors, fluorescent ligands have been developed for the full family (reviewed in [99] and [100]).

1.8 Diffraction Limited Imaging Approaches

The diffraction limit, first described by Abbe [101] and therefore often referred to as Abbe's Law, is given in x and y dimensions as:

$$Resolution_{x,y} = \frac{\lambda}{2NA}$$

and in the z axis as:

$$Resolution_{z} = \frac{2\lambda}{NA^2}$$

Where λ is the wavelength of incident light and NA refers to the numerical aperture of the objective. Numerical aperture describes the refractive index of the medium between the sample and the objective lens, multiplied by the sine of the aperture angle. This is the angles at which the objective can receive light. Using high NA objectives (~1.4) under ideal conditions can theoretically produce lateral resolutions of between 200 nm and 400 nm axially for commonly used visible light wavelengths.

Diffraction limited techniques encompass the most widely used forms of fluorescence imaging, including widefield epifluorescence, confocal, TIRF, and lightsheet (Figure 1.8). An overview of diffraction limited approaches used in this project is given below.

1.8.1 Epifluorescence

Epifluorescence microscopy, also called widefield microscopy, is the simplest form of fluorescence imaging. The sample is illuminated with a beam of light, either laser or LED illumination, (Figure 1.8) and the emitted fluorescence detected through the same objective lens - hence ‘epi’, from the Greek for ‘same’. Both in- and out- of-focus light alike is collected by a detector or eyepiece, having passed through the relevant wavelength filter for the fluorophore of interest. Although simple, widefield microscopy is widespread and versatile, suitable for both live and fixed sample applications.

1.8.2 TIRF

Total internal reflection fluorescence (TIRF) microscopy is a modification of the widefield approach that results in a reduction in the out of focus light collected. This is achieved by angling the incident light such that it is entirely reflected, rather than refracted. At this so-called critical angle, an evanescent wave of excitation light is generated that decays exponentially with depth, restricting fluorophore excitation to approximately 200 nm from the coverslip and reducing the out-of-focus background. TIRF is therefore often the technique of choice when imaging the basal membrane in adherent cells and flat samples due to increased contrast (the signal to noise ratio, or SNR) and reduced photodamage in other parts of the cell.

1.8.3 Confocal

Confocal microscopy is another workhorse of diffraction-limited imaging. By applying a pinhole in front of the detector at the same focal plane as the sample, out-of-focus light is discarded. Point scanning microscopes must raster scan across the sample, meaning the method is less suited to fast imaging. Laser intensity is often increased too. Spinning disk confocal microscopes can overcome some of the limitations on speed and phototoxicity by inclusion of an array of microlenses, allowing multiple focused beams of light to be swept across the sample to reduce intense laser exposure. Resonant scanning confocal microscopy also improves acquisition speed in single point scanning systems, using a resonant mirror scanner that oscillates at a fixed frequency to improve framerate to video rate (30 fps) and beyond. Confocal microscopes are a solid choice for imaging given their optical sectioning advantages over widefield microscopy and common presence in core facilities.

1.8.4 Lightsheet

Lightsheet microscopy is regarded as one of the gentlest techniques for live-cell imaging. A sheet of light, hundreds of nanometers thick, is generated perpendicular to the imaging objective and moved through the sample. This planar illumination significantly reduces out-of-focus light, improving signal to noise and reducing phototoxicity. This technique also permits rapid capture of 3D data. A variant of this concept, lattice light sheet [102] microscopy, replaces the conventional sheet with an optical lattice, further reducing phototoxicity and improving imaging speed.

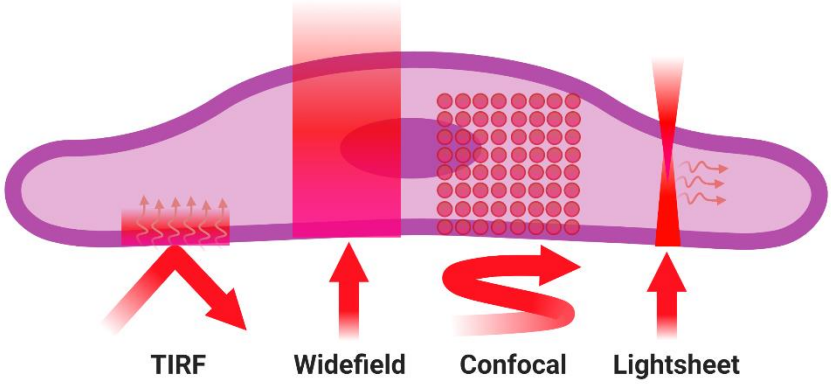

Figure 1.8 – Diffraction limited imaging approaches. *TIRF, showing the incident light and resulting evanescent wave. Widefield epifluorescence, showing illumination of the full volume of the specimen. Confocal, showing the rastering of the scanning focal point. Lightsheet, showing the sheet illumination and resulting detection at an angle to illumination.*

1.9 Super Resolution and Advanced Microscopy

1.9.1 Breaking the diffraction limit

The umbrella of super resolution microscopy encompasses any technique that can improve resolution beyond the ~ 200 nm diffraction limit, significantly enhancing the potential of light microscopy. Where before the only option for resolution in the range of tens of nanometers was electron microscopy, with its associated stringent sample preparation and fixation artefacts, relatively minor changes to standard immunofluorescence labelling protocols can now yield almost comparable resolutions with much greater flexibility in terms of labelling. Great use of these techniques has been made in the fields of cytoskeletal and membrane biology, as discussed below along with the pros and cons in terms of spatial and temporal resolution. For a more

in-depth review of super resolution in imaging the plasma membrane, see Stone et al. [103].

Linking real time dynamics of actin and receptors has only become a possibility with the advent of super resolution microscopy. Confocal laser scanning microscopy, and its resonance scanning and spinning disk derivatives, can result in high quality high framerate imaging of actin dynamics, but given the diffraction limit it cannot resolve fine actin filaments, as these lie far below 200 nm. Bundled actin structures are therefore much more easily studied than single filaments of fine actin, and this may be masking some important dynamics. Even identifying clusters of GPCRs is challenging in diffraction limited systems, so producing a quantitative assessment of oligomer size and mobility has invited many exciting imaging questions.

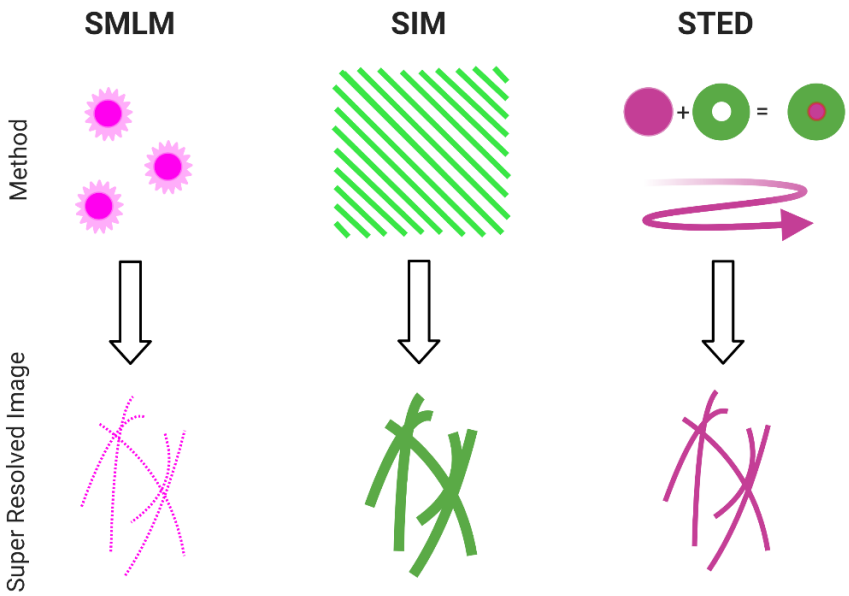

Figure 1.9 – Core concepts in super resolution. *Illustrations of the concepts behind common super-resolution techniques. SMLM requires the stochastic activation and localization of single fluorophores, building up a pointillist image of the structure. SIM involves projection of patterned illumination at multiple angles, using the resulting Moiré fringes to reconstruct a higher frequency information. STED uses a depletion laser that surrounds the point of illumination, reducing the size of the point spread function of the illumination beam.*

1.9.2 Single molecule localisation microscopy techniques

Single molecule localisation microscopy (SMLM) techniques work by stochastic switching of individual fluorophores between ‘on’ and ‘off’ states within a diffraction limited object. Given the point spread function (PSF) of an individual fluorophore approximates to a Gaussian distribution, the distribution of intensity in neighbouring pixels can be used to localise the fluorophore 'centre' with sub pixel resolution. Sparse activation of only a subset of fluorophores permits precise localisation of individual ‘blinks’ to high precisions of <20 nm. The sparsity of emission reduces the chance of two emitting fluorophores being in close proximity in any one frame. Lelek et al. [104] provide a thorough SMLM review. After localisation of points over usually lengthy detection phases (often upwards of 10,000 frames), images can be reconstructed from these identified points, or the point data can be used directly in downstream analysis.

The key behaviour for fluorophores and labels used in SMLM is the capacity to be switched between ‘on’ – emitting photons – and ‘off’ – not emitting or ‘dark’. While this can be a photophysical property, with some fluorophores and fluorescent proteins being capable of photoswitching under specific illumination wavelengths, it can also be a physical property of the experimental design. A key example of this is the SMLM technique point accumulation in nanoscale topography (PAINT), where the on and off states are generated by binding and unbinding of the fluorophore from the target molecule [105].

STORM (stochastic optical reconstruction microscopy) [106] uses photoswitchable organic fluorophores which can blink when in the presence of an appropriate buffer. Fluorophore and buffer combinations are selected for a variety of properties, including the fluorophores' quantum yield (efficiency of photons in to photons out) and therefore photons per on/off cycle, and duty cycle (time spent in the on state). High photon yield is desirable for accurate point fitting, while a low duty cycle reduces the possibility of two PSFs overlapping. Number of cycles before permanent bleaching should also be considered. Dempsey et al. [107] assessed common fluorophores for these properties, among others, and concluded that Alexa 647 (and its close structural homologues) in a GLOX-Thiol buffer performed best for STORM imaging. Alexa 647 has remained a consistently popular choice, but STORM is possible with less efficient fluorophores emitting in green and red wavelengths with appropriate changes in buffer and imaging conditions. This also allows for multi-colour imaging.

PALM, or photoactivatable localisation microscopy [108, 109], relies on photoactivatable or photoswitchable fluorescent proteins rather than organic fluorophores. A commonly used example is the photoswitchable fluorescent protein Eos [110] and its more efficient derivatives like mEos2 [111], which initially emit at ~ 516 nm but can be induced by illumination with 405 nm light to emit at ~ 580 nm – often termed its 'active' state in PALM papers, despite really being a photoswitching event. After a sparse population of fluorescent proteins is activated and photons collected, the sample is bleached, and the cycle repeated until all FPs have been bleached.

The newest entry to the SMLM playing field, PAINT, relies on repeated binding and unbinding of diffusing probes [105]. This has been achieved through transient interaction between complementary DNA oligonucleotides (DNA-PAINT) [112], as well as the repeated binding of the LifeAct peptide in a technique called IRIS [113]. IRIS has also been used with quantitative analysis to dissect the architecture of cortical actin at the T-cell immune synapse [114].

Lengthy detection phases - coupled with the fact that even small levels of drift can have deleterious effects on resolution – makes SMLM live imaging challenging. In addition, the harsh imaging conditions necessary to cause fluorophores to stochastically emit, especially in dSTORM - a redox buffer often including cytotoxic components such as β-mercaptoethanol, very high laser powers in order to push the fluorophore into the dark state, and use of damaging UV light to bring reluctant fluorophores back on, all make localisation microscopy toxic for a living cell. Despite this, several studies have applied SMLM successfully in live cells. Klein et al. [115] initially demonstrated the use of live cell SNAP-label facilitated STORM on histone 2B proteins. SMLM, notably, does provide the greatest resolution increase of all the SR techniques, with individual localisation precisions down to ~ 5 nm and resolving power down to the tens of nanometers. A good recent example of the use of SMLM to investigate receptor behaviour at a nanoscale is the work of Hu et al. [116], showing microcluster formation of TCRs in activated T cells. In the context of this project, SMLM and investigation of fixed cells will be a key approach, as although temporal data is absent, the very high resolutions achieved can be necessary to fully describe systems and correlate with more dynamic techniques.

1.9.3 Structured illumination microscopy

Information in images can be conceptualised in terms of frequency. Nanoscale details are high frequency information, which are not accessible with standard diffraction limited techniques. This can be best described using the concept of Fourier space. Fourier transforms are described by a set of equations proposed by Joseph Fourier in 1822 [117]. In brief, Fourier transformation is the representation of an image (or other patterns) as the sum of its constituent sine waves, taking into account constructive and destructive interference. Grey values in an image are a function of the two axes of the image and the summed sine waves can therefore be plotted against frequencies h and k, corresponding to the x and y axis (this is further explained in the context of SIM in references [118, 119] and a broad description of Fourier transforms is given in reference [120]). Example outputs are shown in Figure 1.10.

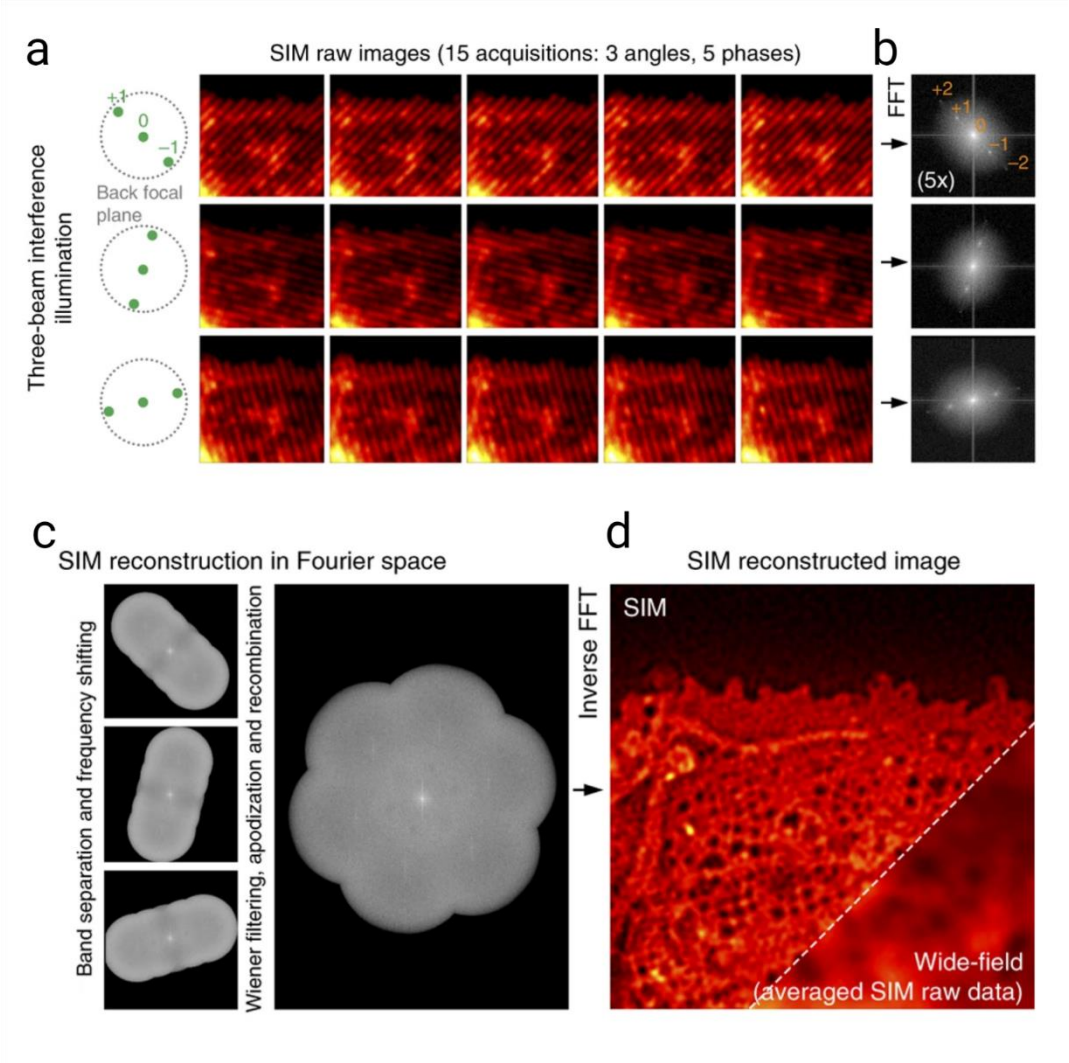

Figure 1.10 – Principles of SIM imaging. *a) A membrane-stained liver endothelial cell is imaged over 3 angles and 5 phases, with the Fourier transform of the data shown in b). c) SIM reconstruction proceeds in Fourier space for each angle before recombination. d) A SIM reconstructed image is generated by a reverse Fourier transform, taking the data back into image space. Fenestrae are clearly visible when compared to widefield data. Figure adapted from a panel in Demmerle et al. [121].*

High frequency information corresponds to the finer details within the sample and is therefore not easily identified during conventional imaging given the diffraction limit. In structured illumination microscopy (SIM), however, illuminating light is patterned to aid in reconstructing this detail. Patterns of light are generated either by physical gratings or specialised illumination modules and projected over the sample at set angles. Interference of the patterns with the sample produces an effect known as a moiré fringe. These interference patterns hold information about the structure of the sample that lies below the resolution limit, simply offset and transposed from high frequency image information to a lower frequency [122]. This data can be used to reconstruct the raw image by way of subtracting the known illumination patterns and reassigning the offset data contained in these moiré fringes [118] using the microscopes' optical transfer function (OTF). With a sufficiently narrow illumination pattern, this technique can improve resolution twofold over standard widefield.

The optical transfer function (OTF) is the Fourier transform of the point spread function and can be calculated for the specific system and objective in use. In commercial software, this is usually done automatically. In SIM reconstruction algorithms, the illumination patterns are a known quantity, meaning it is possible to mathematically calculate the unknown frequencies from the image – the frequencies which correspond to high resolution information. Repeated over multiple angles and phases (3 and 5 for 3D SIM, 3 and 3 for 2D and TIRF SIM), detail that could not be seen in the raw image within a radius of twice the OTF can be calculated and reconstructed [123].

Structured illumination microscopy is favoured by many for live imaging due to its nature as an adapted widefield technique, which can help mitigate some phototoxicity issues. Imaging can be performed in normal media and under cell friendly environmental conditions, with no need for specific buffers or complex set ups. SIM does tend to perform better on objects with distinct – punctate or filamentous – structure, as diffuse molecules or stains suffer more from artefacts introduced by SIM processing. On structures like actin, however, SIM performs particularly well – imaging at high resolutions over relatively large sample areas to demonstrate the intimate interaction of actin and the membrane in liver cell fenestrations [124], for example, or in showing individual F-actin foci within platelet nodules [125].

1.9.4 Stimulated emission depletion microscopy

STED, or Stimulated Emission Depletion microscopy, STED involves the physical reduction of the size of the focal point by a second ‘donut’ shaped laser which depletes emissions in the surrounding region (Figure 1.9). As the size of the excitation point is reduced by the depletion laser, resolutions of 30–80 nm can be achieved. Optical sectioning is also a particular strength, as the technique is point scanning, and diffractive optical elements can be introduced to generate an additional depletion doughnut in z [126]. Intense laser power in the depletion beam is required, making phototoxicity a key consideration. A recent development that uses the fundamental principles of this technique family, MINFLUX [127], reduces the phototoxicity caused by the high laser intensities of STED whilst drastically improving resolution.

STED was used recently to determine the distance between the membrane and underlying cortical actin, showing that proximity is variable around the cell, ranging between less than 10 nm and a maximum of 20 nm distance [30]. This technique has recently been used in live and fixed cells to identify a previously undescribed actin structure in activated T cells, a ‘ramified network’ of fine actin filaments that have likely been obscured by the reliance of other SR techniques on TIRF illumination [26].

1.9.5 Computational super resolution

There are some post-processing methods - such as SRRF [128] and SOFI [129], which require data collection under conditions that are less harmful to the cell than intense SR acquisitions - like widefield or TIRF imaging. These rely on the application of algorithms that use the intensity and radiality, in the case of SRRF, or fluorescence fluctuations from single emitters, for SOFI, of each given pixel to mathematically calculate the central point of the point spread function. As such, these are applicable in live cell contexts, and have resolutions approaching standard SR techniques - even outperforming 3D SIM in some cases [128]. Several studies have used these super resolving algorithms to great effect - SRRF reconstruction, for example, was used to resolve actin in the sperm acrosomal reaction, showing specific dynamic changes in the cortical actin [130]. SOFI has been adapted to investigate protein densities at the cell membrane, clearly showing CD4 clustering changes in mutated proteins [131].

A newer frontier in computational super resolution is the application of deep learning (DL) algorithms. While there is obviously significant nuance to DL application, the theoretical basis holds that by training a neural network with sufficient examples of low resolution and super resolution images, the network would be able to accurately predict a super-resolved image from the low-resolution image alone. Various recent applications are covered in [132]. While impressive results are definitely achievable (see: [133]), it is not yet clear how applicable outputs will be for quantitation purposes. In Qiao et al.'s work [133], for example, inferred images of the actin mesh are shown, clearly missing detail in denser regions that is obvious in the correlated SIM image. Deep learning has also been used to improve speed of SMLM acquisitions, using trained networks to infer SR image outputs from a fraction of the frames usually required by such techniques [134]. While impressive, the outputs are images, not point cloud data, somewhat limiting the normal power of SMLM techniques.

Deconvolution methods can theoretically also improve the resolution of an image as well as improving contrast. In combination with other imaging optimisations, deconvolution can provide a similar resolution to SIM [135]. By combining deconvolution concepts with SIM, however, resolution can be improved still further. SparseSIM is a super resolution deconvolution method which uses modifications to Richardson-Lucy deconvolution, able to reach live cell resolutions of ~ 60 nm at high framerates [136].

1.9.6 Proximity assays

FRET and its sister techniques (TR-FRET, FRET-FLIM, and BRET, among others) are also commonly used in investigation of membrane proteins - for example, identifying higher order oligomerisation of $A_{2A}R$ [62], or assessing interaction of GPCRs with tagged G-proteins [137]. These assays provide evidence of proximity, either through complementation of a split reporter – such as Nano-Luc in BRET – or recording changes to fluorescence wavelength or lifetime upon energy transfer between two fluorophores. While powerful, these approaches are essentially diffraction limited if used to localise interactions. It is also important to note that these techniques are only evidence of close proximity – not necessarily a functional interaction.

1.9.7 Expansion microscopy

Expansion microscopy takes a different approach to breaking the diffraction limit. Instead of modulating fluorophore photophysics or adapting illumination, expansion microscopy increases resolving power by physically moving apart labels (or epitopes, in the case of protein retention variants) anchored into a swellable hydrogel. First developed in the lab of Edward Boyden [138], the technique involves the formation of a dense polyelectrolyte gel throughout the sample of interest, crosslinking labels or biomolecules into this meshwork. After sample homogenisation, the gel can be volumetrically expanded, with between 4 and 5 fold expansion laterally using the

standard protocol [138]. This results in an optically cleared sample, sometimes described as a ‘blueprint’ of the original, ready for imaging in a wide range of modalities.

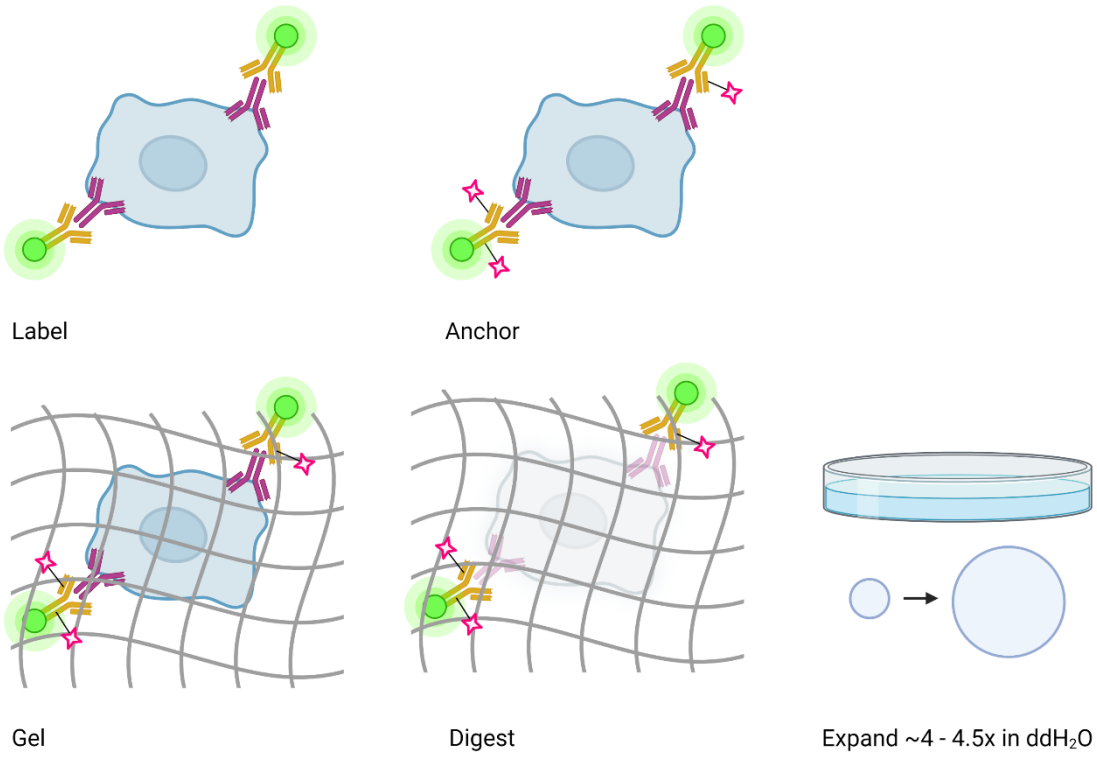

Figure 1.11 – Process of expansion microscopy. *Samples are labelled with standard immunofluorescence protocols and an anchoring chemical applied. The sample is then set in a poly-electrolyte gel, with the labels equipped with anchoring moieties being directly incorporated into the mesh. The sample is then digested to remove any impediment to isotropic expansion. The gel is incubated in ddH2O to a final expansion factor of between 4 and 4.5 times.*

1.9.7.1 Labelling and Anchoring

Incorporation into the gel must be facilitated by anchoring moieties. While the original method accomplished this with custom made trifunctional probes anchored to antibodies via oligonucleotides [138], this was expensive and could have restricted general adoption of the technique. This initial approach – sometimes termed ExM1.0 in the literature – was quickly superseded by ‘proExM’ [139], which permitted anchoring of standard antibody labels and fluorescent proteins. In this thesis, ExM is referring to proExM unless otherwise stated. This method used a commercially available crosslinker, a succinimidyl ester of 6-((acryloyl)amino)hexanoic acid (AcX), capable of functionalising the label with an anchoring moiety. AcX equips the free primary amines of a protein with an acrylamide functional group. These functional groups can anchor to the polymerising gel. Alternate anchoring options such as another amine reactive small molecule methacrylic acid N-hydroxysuccinimidyl ester (NA-MHS) and glutaraldehyde [140] have also proved reliable alternatives to ensure sufficient retention of label in the polyelectrolyte gel. Different anchoring steps may be necessary for modified ExM protocols - for example, an acrylamide/formaldehyde incubation in U-ExM which focusses on preservation of ultrastructures [141] - or for specific biological use cases. If, for example, intra nuclear structures are being investigated, a DNA anchoring step should be considered to ensure fidelity and isotropy [142].

1.9.7.2 Gelation

The hydrogels used for expansion must form a dense mesh throughout the entire sample. These polyelectrolyte gels are ‘tuneable’, with inclusion of lower proportions of bisacrylamide cross-linker in the monomer solution resulting in much larger expansion factors [138]. This, however, comes at the cost of significant gel fragility. 10x expansion is instead performed by modifying the gel composition to use N,N-dimethylacrylamide (DMAA), which functions as both monomer and cross-linker and produces much more robust sample gels [143]. Another gel-based variant that affords improved resolution is iterative ExM (iExM) [144], which involves re-embedding of a ~ 4.5x expanded sample and a further expansion. This ~ 20x expansion process allows resolutions of 25 nm to be reached on conventional microscopes.

Pores in the standard ExM gel mesh are estimated to be 1-2 nm in size unexpanded [138], contributing to the minimal distortion in expanded gels apparent at the nanoscale. Assessment of resolution error introduced by the mesh concluded a potential error of 5-10 nm [144], concordant with the predicted pore sizes. This error should be considered in the context of the ~ 20-30 nm introduced by a standard primary/secondary antibody pairing, commonly accepted – or even overlooked - for traditional SMLM imaging, which does in fact have a resolving power of 30 nm.

1.9.7.3 Digestion/Homogenisation

Post gelation, the sample must be homogenised to reduce any impediment to isotropic expansion. In the standard protocol this is achieved with proteinase K treatment [139], though heat and detergents are also used [141, 145]. Choice of homogenisation protocols should take into account the sample and experimental question itself. If post-gelation labelling is indicated, samples should undergo gentler heat/detergent homogenisation, as in MAP [145] and UltraExM [141], to retain maximal epitopes in the gel. Collagenases should be employed where collagen rich structures are being investigated to prevent impediment to expansion – for example, in kidney sections [146].

1.9.7.4 Distortions

The literature has repeatedly shown that expansion microscopy and its variants permit isotropic expansion with limited local distortion. In fact, a review of the state of ExM techniques from the Boyden group explicitly states that ‘the sample-to-sample reliability for a well-tested protocol is consistent enough that new biological studies are able to use well-tested protocols without further validation, especially for a cell or tissue type that has been previously validated’ [147]. Errors are consistently found to be within 1 and 5% of the measurement length at length scales of hundreds of microns (for example: [138, 139, 144, 146] among others). While the majority of these assessments are made by correlative pre- and post- expansion imaging of

stereotypical structures – microtubules or nuclear pores - attempts have been made to implement distortion assessments that do not require a super resolved ‘pre’ image. One group showed the use of precise photobleaching of nuclei for assessing distortion on both a global and local scale [148], while a preprint demonstrates the potential applications of DNA nanorulers in quantification [149].

1.9.7.5 Expansion and imaging techniques

ExM gels can be imaged using standard confocal or widefield systems – a major benefit to the technique, as many other super resolution approaches require complex and specialised imaging set ups. Imaging of expanded samples is by no means limited to simpler systems, however. The optical clearing inherent in the preparation of the samples makes them amenable to imaging at depth – for example, with lightsheet systems [150].

More traditional super resolution techniques have also been applied to expanded samples to great effect. ExM-SIM (or ExSIM) imaging has been achieved both by direct imaging of entire gels [151] and through a serial cryosectioning approach [152], resulting in lateral resolutions of ~ 30 nm. This is comparable with unexpanded SMLM techniques, iEXM, and 10x ExM approaches, whilst retaining the relative simplicity of the standard proExM protocol. ExSTED can achieve impressive resolutions of sub 10 nm with ~ 4x expansion [141, 153]. ExM SMLM combinations have been technically challenging but have been implemented largely in post-

expansion or specialised labelling contexts for dSTORM [154, 155]. Both note that the resolution increase afforded by SMLM or STED in ExM can be essentially negated by excessive linkage error in labelling.

1.9.7.6 Using ExM for cytoskeletal and receptor imaging

While microtubules are one of the most routinely imaged structures in ExM, actin poses more of a challenge. Anti-actin antibodies are notoriously poor for immunofluorescence applications (as demonstrated in [156]), and fluorescent phalloidin conjugates – the gold standard for fixed actin labelling – lack the needed free primary amine groups for efficient anchoring into the gel mesh. At time of writing, three major methods of labelling actin for ExM have been published. The first involves a phalloidin probe modified with an anchoring moiety in addition to the fluorophore, allowing both for the good labelling of phalloidin and retention post gelation [157]. The second take a more conventional IF approach, labelling as normal with fluorescent phalloidin and using an anti-fluorophore antibody, allowing the protocol to proceed as for standard immunolabelling [156]. The final published example used a SNAP-LifeAct construct labelled with a modified DNA oligostrand, equipped with a benzylguanine group for SNAP interaction alongside an anchoring moiety and fluorophore [158].

In terms of receptor labelling, any receptor with good IF antibody options can easily be incorporated into an ExM workflow. For example, a recent paper shows x10

expansion used on murine platelet receptors, revealing αIIbβ3 receptor clustering under resting and platelet activating conditions [159]. SNAP incorporation has been reported both through using modified trifunctional SNAP ligands which incorporate an anchoring motif and conjugation point for post-expansion dye conjugation [155], and SNAP ligands using a double stranded DNA oligomer directly linked to both an anchoring group and a fluorophore, as for the SNAP-LifeAct labelling above [158].

1.9.8 Single particle tracking

Single particle tracking (SPT) can also be considered a super resolution technique, as the position of each molecule is mathematically localised to a degree of accuracy far greater than the size of the diffraction limited spot it is visualised as. This sub-pixel localising approach is the same as used for SMLM techniques like STORM and PALM. Used predominantly to investigate dynamics, in SPT approaches single particles are labelled and imaged – usually in TIRF or epifluorescence – over time at high frame rates, permitting localisation of the molecule in each frame. These localisations can then be used to generate a track of the single particles' movement and behaviour through time. SPT evidence is core in supporting the picket fence model, with gold nano particle or Cy3 tagged lipids tracked at a temporal resolution of 25 μs [13].

Fluorescent labels for SPT must fulfil several criteria. They must be small enough to not interfere with the normal behaviour of the protein or molecules of interest, non-

toxic to live cells, and be sufficiently bright and photostable for the desired experiment length [160]. Some fluorescent proteins can be used, but organic fluorophores – attached to Fab fragments, DNA oligomers, or self-labelling ligands, for example – provide additional flexibility in experimental design. Another fluorescent option is Quantum Dots (also referred to as QDots or QDs), which are small semiconductor nanocrystals with photostability orders of magnitude greater than traditional organic fluorophores [161]. After imaging and spot detection, the generated trajectories can be assessed for a range of metrics, which are further discussed in Chapter 3.

This generates important information about diffusive behaviour, allowing investigation of speed of motion and switches between movement, confinement, and immobilisation. SPT has been used to great effect in demonstrating GPCR dimerisation [162], and the interaction of GPCRs and G proteins [163].

1.10 Super Resolution Analysis Techniques

1.10.1 Single molecule localisation microscopy analysis

Images are incredibly rich in data, far beyond simple qualitative assessment. An understanding of the properties of images produced by each technique is necessary to choose appropriate parameters for investigation. While some super resolution techniques provide an output image with similar properties to a standard confocal or

epifluorescence image, single molecule and single particle tracking approaches especially can introduce extra considerations for accurate interpretation.

1.10.1.1 Point localisation

Single molecule localisation techniques are all based on the accurate localisation of individual points. A Gaussian distribution is used to fit each point, and the predictable changes in the fluorescence of neighbouring pixels can permit subpixel localisation. The outcome is the recording of both the calculated central coordinate of the point and the precision to which this localisation was possible, among other parameters. One of the most commonly used SMLM software is ThunderSTORM [164], as applied in this thesis, but a range of open source and commercial options are available. A comprehensive assessment and comparison of these software was performed by Sage et al. [165] in their ‘super-resolution fight club’.

Point localisation routines for SMLM are reliant on sufficient sparsity of blinking to accurately localise each point. Excessive blink density can greatly affect localisation precision and introduce reconstruction artefacts, but capturing more data per frame could also reduce often lengthy detection phases. HAWK, or Haar wavelet kernel analysis [166], uses the blinking behaviour of fluorophores to separate overlapping detections before localising, allowing this issue to be overcome.

1.10.1.2 Quantitative SMLM

The first SMLM publication noted the potential issue of overcounting due to reblinking [108]. In both PALM and STORM, fluorophores can blink repeatedly. If these blinks are separated by several frames, it is likely that they will be recorded as separate molecules. This can be particularly detrimental if attempting to perform quantitative analysis. Common correction methods, such as the ThunderSTORM correction used in this thesis [164], rely on merging putative reblinks based on spatial and temporal proximity. Under these conditions, comparison of relative change to control conditions is therefore more robust than attempting to extract absolute numbers from the data.

Improved techniques to correct for reblinking are under development. Existing characterisation of FP behaviours and the reduced likelihood of stochastic blinking means that illumination behaviours can be modelled much more readily than for organic dyes. This allows quantification through mathematical correction of blinking data, taking into account photophysical models of behaviour [167]. However, there have recently been advances made for correction of dSTORM blinking data in the form of a distance distribution correction (DDC) algorithm [168]. This approach does not require specific threshold setting or any calibration experiments, but does require that no stimulating UV light be used during acquisition.

Quantitative PAINT approaches are also an option for a more accurate representation of ground truth counts. The on-off binding kinetics are modellable, allowing calculation of molecule numbers from these blinks [169]. Application of Q-PAINT is not trivial, and many restrictions in terms of labelling density and acquisition time remain, alongside the general quantification issues of stoichiometric labelling.

1.10.1.3 Cluster analysis

Assessment of molecular clustering is vital, especially in cell membrane protein investigations. The point cloud data output by SMLM software can be assessed in a range of clustering approaches, thoroughly reviewed by Khater et al. [170]. Briefly, techniques have been developed to identify clustered point patterns and assign points to specific clusters. The density based DBSCAN [171], topology based ToMATo [172], and Voronoi – Tessellation based SR-Tesseler [173] are all popular choices which allow assignment of individual points to clusters, and accompanying analysis of the size and density of these points. A recent development is the incorporation of machine learning in the space. Williamson et al. [174] demonstrated a supervised machine learning approach which could accurately identify clustering in real data, as well as with the potential to extend the analysis to distinguish clusters from filamentous structures.

A framework for quantitative comparison of cluster algorithm performance is currently under development [175].

1.10.2 SPT analysis

SPT also requires point localisation as the initial analysis step. These points are then linked relative to appropriate parameters. There are many options for track generation, including TrackMate [176], SMTracker [177], Swift [178], TrackIt [179], and U-Track [180], among others. Once parameters have been optimised, these track outputs can be quantitatively assessed. Again, there are a range of options, including inbuilt analysis in many tracking packages, as well as standalone options like Spot-On [181] and SMAUG [182]. Often, diffusion coefficients are calculated from mean squared displacement or moment scaling spectrum analysis. However, membrane proteins often show several modes of motion over the observation period. Transient motion analysis algorithms are therefore important to allow more accurate categorisation of motion behaviour. Techniques underlain by hidden Markov models, which model switching of movement dynamics, can permit better interpretation of changes in receptor dynamics within tracks than fitting of MSD data [183]. Given that they operate on a single step basis, however, these models can still have difficulty differentiating confinement and immobilisation. Advancements on these concepts are plentiful - for example, ‘divide-and conquer moment scaling spectrum’ analysis as developed by Vega et al. [184], which uncouples identification of motion switching from classification. As well as diffusion coefficients, motion classification, and subtrack switching behaviour, confinement radii can be calculated, providing a broad range of information to assess particle behaviour.

1.11 Imaging Approaches for Membranes and Receptors

This project aims to investigate the dynamics of the $A_{2A}R$ and $A_{2B}R$ adenosine receptors in relation to actin. Strides have been made towards understanding receptor dynamics, using techniques such as single particle tracking (for example, [162, 163]) and FCS (as reviewed in [185]). Actin has also been a key challenge for super resolution techniques, as the fine filamentous structure makes it very attractive as an imaging benchmark target. Linking receptor migration and actin dynamics is yet to be directly attempted. Sungkaworn et al. [163] did correlate a static PALM image of LifeAct labelled actin with single particle trajectories for the α2a adrenergic receptor, showing confined diffusion in receptor 'hot spots' and hop escape motions. Importantly, however, the actin image was obtained during an approximately five-minute detection phase post completion of the single particle tracking, and is therefore not directly representative of actin/GPCR interaction at the specific point that the tracking data was obtained. This is especially troublesome when considering the findings of Freeman et al. [12], who described the role of CD44 as a transmembrane picket in macrophages. This work showed a much more dynamic nature of not only the actin network but also its association with the pickets themselves, in contrast to the initial predictions [13] of relatively stable membrane compartments.

1.12 Project Aims

This project aimed to investigate the potential organising effects of cortical actin on adenosine receptors. We hypothesised that adenosine receptors are differentially regulated through interactions with the cortical actin cytoskeleton. Experiments were designed encompassing a range of advanced microscopy techniques to answer several key outstanding questions. As such, the main aims of this project were as follows:

- Investigate the pharmacological response of $A_{2A}R$ and $A_{2B}R$ adenosine receptors to actin disruption.
- Investigate potential clustering behaviour of $A_{2A}R$ and $A_{2B}R$ adenosine receptors in response to activation, as well as actin disruption.
- Investigate the diffusion behaviours of $A_{2A}R$ and $A_{2B}R$ adenosine receptors in response to activation and the potential impact of actin.
- Investigate the structure of cortical actin in relation to receptor activation.
- Develop methods of imaging actin and receptor organisation and dynamics simultaneously.

CHAPTER 2 - MATERIALS AND METHODS

2.1 Reagents and Consumables

2.1.1 Reagents

Table 2.1 – Consumables used in this thesis.

Item	**Supplier**	**Part number/CAS number**
Dulbecco's Modified Eagle's Medium (DMEM)	Sigma-Aldrich	D5796
DMEM, high glucose, no glutamine, no phenol red	Gibco	31053028
Fetal Bovine Serum	Sigma-Aldrich	12103C
Sterile Dimethyl Sulfoxide	Sigma-Aldrich	D2650
Penicillin/ Streptomycin	Sigma-Aldrich	P4333
L-Glutamine	Sigma-Aldrich	G7513
Trypsin	Sigma-Aldrich	T4049
µ-Dish 35 mm, high Glass Bottom (#1.5H)	ibidi	81158
Glass Bottom Dish 35 mm (#1.5)	ibidi	81218
25 mm Ø no. 1.5H coverglass	Marienfeld	0117650
13 mm Ø no. 1.5H coverglass	Marienfeld	0117530
Triton X-100	Sigma-Aldrich	X100
PEI MAX	Polysciences	24765
BamHI-HF restriction enzyme	New England BioLabs	R3136
KpnI-HF restriction enzyme	New England BioLabs	R3142
CutSmart Buffer	New England BioLabs	B7204
α-Select Silver Efficiency Chemically Competent Cells	Bioline	BIO-85026

Lipofectamine 3000	Invitrogen	L3000001
GeneJET gel extraction kit	Thermo Scientific	K0691
NEBuilder HiFi DNA Assembly Master Mix	New England BioLabs	E2621
GenElute Plasmid Maxiprep Kit	Sigma-Aldrich	PLX15
GenElute Plasmid Miniprep Kit	Sigma-Aldrich	PLN70
RED Taq DNA Polymerase	Sigma-Aldrich	D4309
LongAmp Taq DNA Polymerase	New England BioLabs	M0323
1kb Plus DNA Ladder	Invitrogen	10787018
SYBR Green	Sigma-Aldrich	S9430
Hydromount hard set Mounting Medium	Scientific Laboratory Supplies	NAT1324
Vectashield Antifade Mounting Medium	Vector Labs	H-1000-10
Poly-L-lysine	Sigma-Aldrich	P8920
Forskolin	Sigma-Aldrich	93049
IBMX (3-Isobutyl-1-methylxanthine)	Sigma-Aldrich	I7018
NECA	Tocris	1691
CGS 21680	Tocris	1063
BAY60-6583	Tocris	4472
Cytochalasin D	Sigma-Aldrich	C8273
Jasplakinolide	Sigma-Aldrich	420127
LANCE Ultra cAMP kit	Perkin Elmer	TRF0262
OptiPlate-96, white	Perkin Elmer	6005290
Acryloyl-X (AcX)	Invitrogen	A20770
Sodium acrylate, 97%	Sigma-Aldrich	408220
Acrylamide	Sigma-Aldrich	CAS: 79-06-1

N,N'-methylenebisacrylamide	Sigma-Aldrich	CAS: 110-26-9
Ammonium persulfate	Sigma-Aldrich	CAS: 7727-54-0
Tetramethylethylenediamine (TEMED)	Sigma-Aldrich	CAS: 110-18-9
Proteinase K	New England BioLabs	P8107S
Catalase from bovine liver	Sigma-Aldrich	C40
Tris(2-carboxyethyl)phosphine hydrochloride (TCEP)	Sigma-Aldrich	CAS: 51805-45-9
Glucose oxidase from *Aspergillus niger*	Sigma-Aldrich	G2133
2-Mercaptoethanol (MEA)	Sigma-Aldrich	63689

2.1.2 Primary antibodies and direct labels

Table 2.2 – Primary antibodies and direct labels used in this thesis.

	Raised in:	**Working dilution/ concentration**	**Supplier**	**Part number**
Anti-α-Tubulin	Mouse, monoclonal	1:1000	Sigma-Aldrich	T6199
Anti-α -actinin-1	Rabbit, polyclonal	1:100 - 1:500	Sigma-Aldrich	HPA006035
Anti-Alexa 488	Rabbit, polyclonal	1:100 – 1:1000	Invitrogen	A-11094
Phalloidin Alexa 488	N/A	1:1000	Invitrogen	A12379
Phalloidin Alexa 568	N/A	1:1000	Invitrogen	A12380
Actin ExM	N/A	1:40	Chrometra	N/A

SNAP Surface Alexa 488	N/A	1 µM	New England BioLabs	S9129S
SNAP Surface Alexa 647	N/A	1 µM	New England BioLabs	S9136S
SNAP Surface 549	N/A	1 µM	New England BioLabs	S9112S
SNAP Surface Block	N/A	20 µM	New England BioLabs	S9143S
Compound 16 (CY5-$A_{2A}R$ antagonist) [186]	N/A	100 nM	University of Nottingham	N/A

2.1.3 Secondary antibodies

Table 2.3 – Secondary antibodies used in this thesis.

	Raised in:	**Working dilution**	**Supplier**	**Part number**
Anti-rabbit Alexa 568	Goat	1:1000	Invitrogen	A11011
Anti-rabbit Alexa 488	Goat	1:1000	Invitrogen	A11008
Anti-mouse Alexa 488	Goat	1:1000	Invitrogen	A11001
Anti-mouse Alexa 546	Goat	1:1000	Invitrogen	A21123
Anti-mouse Alexa 647	Goat	1:1000	Invitrogen	A21235

2.2 Cell Culture

2.2.1 Routine cell maintenance

A549 cells (ATCC CCL185) and HEK293T cells (ATCC CRL3216) were cultured in complete Dulbecco's Modified Eagle's Medium (DMEM) with 10% Foetal Bovine Serum (FBS) supplemented with 1% Penicillin/ Streptomycin and 2 mM L-Glutamine, at 37^{o}C and 5% CO_2. A549 cells were passaged routinely at 70% confluence by detaching with trypsin and reseeding at a dilution of between 1:10 and 1:2. HEK293T cells were resuspended in DMEM and reseeded at dilutions between 1:50 and 1:10. Cells were discarded after passage 30.

For cryopreservation, cells were resuspended in 1 mL media supplemented with 10% DMSO and frozen gradually, transferring to -80^{o}C freezer, and liquid nitrogen for long term storage. To revive cells, the frozen aliquot was thawed rapidly by agitation at 37^{o}C, then diluted dropwise with 10 mL warmed media to avoid hypertonic shock. After 24 hours, the media was replaced to remove any vestiges of cryoprotectant.

2.2.2 Transfection

For transient transfection, cells were seeded in a 24 or 6 well plate, or 35 mm glass bottomed ibidi dish, at a concentration of $1x10^5$ cells mL^{-1}. After allowing to attach for approximately 18-24 hours, cells were transfected using PEI or Lipofectamine 3000.

Assuming transfection in a 6 well plate, DNA and PEI mixes were made up in 150 µL of OptiMem or serum free media, to a concentration of 2 µg per well of plasmid DNA and a ratio of 1 µg to 4 µL of PEI 12k, or 1:2 for PEI 25k, vortexed gently, and incubated at room temperature for 10 minutes. Lipofectamine mixes were made up and optimised as recommended by the manufacturer. The DNA mix was then added to the cells and swirled gently. Experiments proceeded after an application specific incubation, as detailed in relevant results sections, to ensure appropriate expression levels. Transfection efficiency was assessed using an EVOS widefield fluorescence microscope where appropriate. Original plasmids were generated in the labs of Dr Stephen Briddon (N-terminal SNAP-Human $A_{2A}R$ and N-terminal SNAP-Human $A_{2B}R$, Figure 2.1a,b) and Dr Laura Machesky (Lifeact mEGFP, Figure 2.1d).

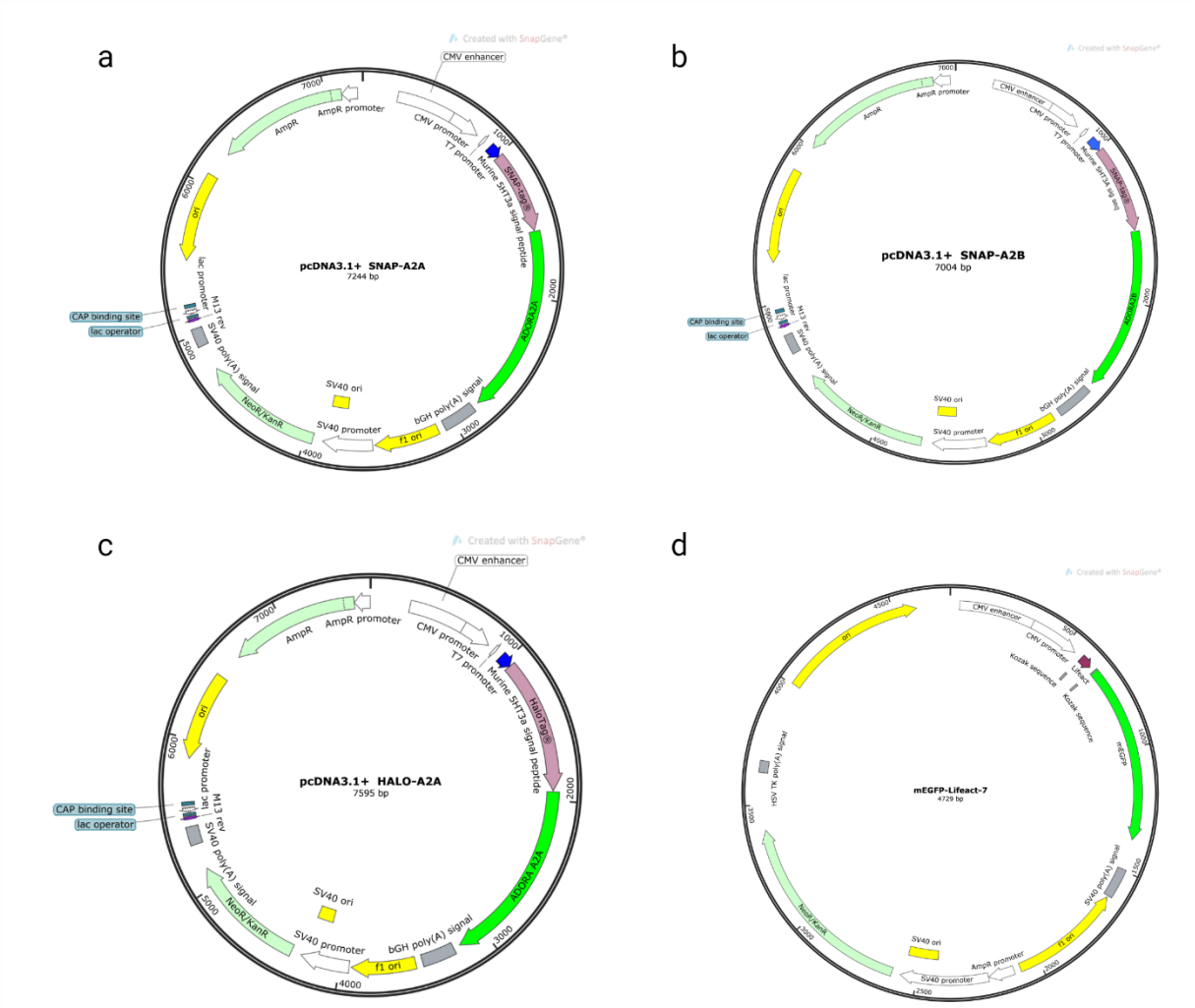

Figure 2.1 – Plasmid maps for constructs used or generated in this work. *a) SNAP-A_{2A} receptor and b) SNAP-A_{2B} receptor plasmids, with c) showing the edited HALO-A_{2A} receptor plasmid generated from a). d) shows the mEGFP-LifeAct plasmid. Plasmid maps generated with Snapgene.*

2.3 Construct Generation and Plasmid Preparation

The HALO-tagged $A_{2A}R$ construct (Figure 2.1c) was modified from the original SNAP-tagged plasmids provided by Dr Briddon. The SNAP-tagged plasmid was digested with KpnI-HF and BamHI-HF in CutSmart buffer (all NEB) for 15 minutes at 37ºC in order to excise the SNAP label sequence. The products were run on a 0.8% agarose gel supplemented with SYBR Green. The plasmid backbone was extracted and purified using a GeneJET gel extraction kit (Thermo Scientific), according to manufacturer's instructions. The construct was then made using the NEBuilder HiFi DNA system, introducing a custom designed gBlock (IDT) containing the HALO tag and linker region to replace the excised SNAP tag. α-select Silver chemically competent bacteria (Bioline) were transformed with constructs by addition of 2 µL of product to one vial of cells. This was incubated on ice for 30 minutes then subjected to a 40 second heat shock at 40°C. Samples were then returned to ice for 2 minutes before suspension of the cells in 950 µL of SOC outgrowth media (NEB). The cells were incubated at 37ºC for 1 hour with shaking.

To prepare all plasmids for use, transformed bacteria either directly from cloning steps as above or from glycerol stocks were spread on agar plates prepared with an appropriate antibiotic (Ampicillin) and incubated overnight at 37ºC. Single colonies were selected to inoculate LB Broth and after overnight culture plasmid preparation proceeded with a Genelute plasmid preparation kit (Sigma Aldrich). Where

necessary, glycerol stocks were also prepared by combining equal parts bacterial culture and 50% glycerol, snap freezing in liquid nitrogen, and storing at - 80ºC.

2.4 PCR and Sequencing

To test plasmid products, PCR reactions were carried out using either Sigma RedTaq or LongAmp Taq (NEB) with reactions being made up to a final volume of 25 µL. Annealing temperatures and extension times were adjusted relative to primer pair and product length, and template DNA concentration adjusted as necessary. Amplification was assessed using agarose gels at percentages relative to product size supplemented with 0.1% ethidium bromide. 5 µL ladder (1 Kb Plus DNA Ladder, Invitrogen) and 5-20 µL PCR product were loaded into the gel and run in TAE buffer at 100V for approximately 40 minutes. Gels were imaged via UV transillumination using the Gene Genius Bioimaging System (Syngene) with GeneSnap software.

Plasmids were directly sequenced to assess insertions by Source BioScience, who performed the clean-up reactions and provided the sequencing primers. Sequence traces were visually assessed using 4Peaks (nucleobytes) and aligned with reference sequences using nBLAST.

2.5 TR-FRET cAMP Assay

To assess cAMP levels in A549 cells, a LANCE Ultra kit (Perkin Elmer) was employed. Experiments proceeded according to the manufacturer's instructions, with cells seeded in a white 96-well OptiPlate (Perkin Elmer) at 10k cells per well. After treatment and addition of the tracer and detection buffers, plates were read on a PHERAstar FSX plate reader (BMG).

2.6 SNAP and Immunofluorescence Staining

Routine SNAP labelling was performed in live cells by incubation with 1 µM SNAP-Surface label in complete DMEM at room temperature for 30 minutes. The mechanism of the self-labelling tag is shown in Figure 2.2. Cells were then washed in prewarmed normal media three times and incubated for 5 minutes at 37^{o}C and 5% CO_2. This wash step was repeated twice more before cells were incubated for a final 30 minutes. Where drug treatment was required, they were added in this final incubation. Any modifications to this procedure are noted in specific technique sections below.

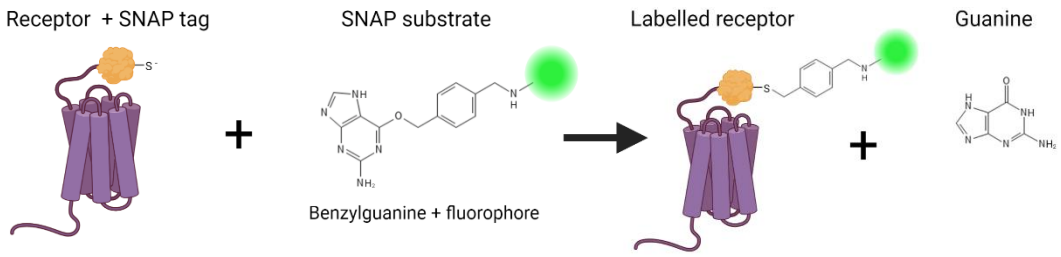

Figure 2.2 – Mechanism of SNAP labelling. The SNAP tag interacts theoretically irreversibly with the benzylguanine substrate, fluorescently tagging the receptor.

For immunofluorescence, samples were fixed in 4% PFA in PBS warmed to 37ºC for 15 minutes. Where actin structure retention was key, PBS was replaced with PEM (0.8 M PIPES (pH 6.95), 4 mM EGTA, 1 mM $MgSO_4$). Fixation was followed by 3 x PBS washes, quenching of free aldehydes with 50 mM $NHCl_4$ for 10 minutes, 3 x PBS washes and, where intracellular staining was necessary, 5-minute extraction with 0.1% Triton X-100.

If antibody labelling was to follow, samples were then blocked with a 0.1% Bovine Serum Albumin (BSA)/ 2% goat serum blocking buffer for 30 minutes. Primary incubations were carried out in the same blocking buffer for either 1 hour at room temperature or overnight at 4ºC. After 3 x PBS washes, samples were incubated for 1 hour with the appropriate secondary antibodies also diluted in blocking buffer. Phalloidin was added at this step if used. Samples were again washed 3 x with PBS and mounted for imaging in an application specific manner.

2.7 Imaging and Microscopy Techniques

2.7.1 Epifluorescence imaging

For epifluorescence imaging, cells were plated on #1.0 13 mm coverslips at a concentration of $1x10^5$ cells mL^{-1} (standard across techniques unless otherwise specified) and allowed to attach for a minimum of 12 hours before immunostaining as above (section 2.6). Slips were mounted onto slides with Hydromount hard set mountant (Scientific Laboratory Supplies). Epifluorescence imaging was performed on a Zeiss Axio Observer 7 inverted epifluorescence microscope with a Hamamatsu Flash 4 V2 scientific CMOS camera and Colibri 7 LED light source. Samples were imaged with a 63 x 1.4 NA oil immersion objective, with acquisition controlled by Zen 2.3 Pro software.

2.7.2 TIRF/SRRF imaging

Cells were seeded in #1.5 high tolerance dishes (Ibidi). For fixed cells, samples were prepared as described above and imaged in PBS. Live imaging of actin required either transfection of cells with LifeAct-mEGFP as above, or labelling with SiR- actin (100 nM, 500 nM, or 1 µM) with 10 µM verapamil. For optimisation see results section 4.3.5. Imaging was performed on a Nikon N-SIM-S system in H-TIRF mode (Ti-2 stand, Hamamatsu Flash 4 scientific CMOS dual cameras with Cairn splitter system, Nikon Perfect Focus system, Nikon laser bed). This system was used with a Nikon 100x 1.49 NA TIRF oil objective with Nikon F2 immersion oil. Critical angle was

determined using the inbuilt alignment capability and manually refined. For SRRF, captured images were then processed using the SRRF plugin as described below (section 2.8.4).

2.7.3 dSTORM

Cells were seeded in #1.5 8 well slides (LabTek). Samples were transfected with SNAP-A_{2A}R or SNAP-A_{2B}R as above, at least 48 hours prior to imaging. Cells were labelled with 1 µM SNAP-Surface Alexa 647 (NEB) in complete media for 30 minutes at room temperature. Cells were then washed in prewarmed normal media three times and incubated for 5 minutes at 37^{o}C and 5% CO_2. This wash step was repeated twice more before cells were incubated for a final 30 minutes. Where drug treatment was required, they were added in this final incubation. Stocks of 50 mM NECA, 2 mM BAY60-6583, and 10 mM Cytochalasin D were prepared in DMSO, and made up in complete media to the appropriate concentration. An equal volume of DMSO was used as a control. After 30 minutes, drug-containing media was removed, and the cells fixed as above (section 2.6). Samples were stored in PBS until imaging.

GLOX STORM buffer composed of 50 µL buffer A (catalase - 20 µg/mL, Tris(2-carboxyethyl)phosphine hydrochloride (TCEP) – 4 mM, KCl – 25 mM, glycerol – 50%, Tris pH 7.5 – 20 mM, glucose oxidase – 1 mg/mL), 400 µL buffer B (glucose – 100 mg/mL, glycerol – 10%), and 100 µL of 1M MEA (Buffer C) was prepared fresh for each experiment, and pH adjusted to 7.4 prior to use. Having introduced the buffer,

wells were sealed via surface tension using a coverslip or slide lid to reduce interference of environmental oxygen.

dSTORM was performed on a Nikon N-STORM system (Andor iXon Ultra DU897U EMCCD, Ti-E stand, Nikon Perfect Focus system, Agilent MLC400 laser bed) with a Nikon 100 x 1.49 NA TIRF oil objective. Samples were illuminated with a 647 nm laser, supplemented with 405 nm illumination as necessary to push fluorophores out of the dark state. 20,000 frames per image were captured, at a rate of 100 fps, with an exposure of '1 frame' or approximately 9.2 ms. The camera data for the Andor EMCCD was as follows:

Table 2.4 – Andor EMCCD camera data and settings

Pixel size (nm)	160
Photoelectrons per A/D count	4.87
Base level offset	100
EM Gain	300

2.7.4 Single particle tracking

Cells were seeded to reach ~90% confluency the morning of the experiment, and transfected as above with SNAP-A_{2A}R or SNAP-A_{2B}R for 5 hours. Cells were then labelled with 1 µM SNAP-549 label for 20 minutes at 37^{o}C and washed stringently in

warmed phenol red free complete DMEM - 3 brief washes followed by a 5 minute incubation, repeated 3 times, and followed by a further 30 minute incubation at 37^{o}C. Drug treatments were applied during this final incubation, with treatments staggered in individual experiments to maintain consistent treatment time. Imaging was performed on the Nikon N-SIM-S system detailed above in H-TIRF mode. Cells were kept in phenol red free DMEM during imaging, and searched for and focussed in TIRF at low laser intensity to avoid bleaching. Laser intensity was then increased to clearly visualise individual fluorophores, and imaging performed at a frame rate of 33 fps.

For dual imaging experiments, two approaches were tested. In the first, cells were transfected with LifeAct-mEGFP, and for some experiments exposure times were dropped to 10 ms (100 fps). Receptor data was later summed in ImageJ to provide the equivalent of a 30 ms exposure, which performed favourably in post processing. The second involved labelling of cells with SiR-actin (as above in 2.7.2).

2.7.5 Structured illumination microscopy

Cells were either seeded on 13 mm coverslips (Marienfeld) or in ibidi dishes, both #1.5 high tolerance. For actin only imaging, samples were prepared as described in section 2.6. Fixed slips were mounted with Vectashield antifade mounting media (Vector Labs) and sealed with nail varnish or, where specified, mounted with Prolong

Glass antifade hardset mountant (Thermofisher). Imaging was performed on the Nikon N-SIM-S system described in section 2.7.2, operating in SIM mode.

2.7.6 Expansion microscopy

proExM

Protein retention expansion microscopy was performed, with slight modification, according to the technique published by Tillberg et al. (2016). Cells were seeded as above and fixed with 4% PFA + 0.1% glutaraldehyde in PEM, prewarmed to 37^{o}C. Immunofluorescence preparation proceeded as normal up to the washes after secondary antibody incubation. After 3 x PBS washes, slips were anchored with 0.1 mg/mL Acryloyl-X, SE (6-((acryloyl)amino)hexanoic acid, succinimidyl ester (abbreviated as AcX) overnight. Slips were washed once in PBS and labelled (if appropriate) with Actin ExM (Chrometra) at 1 unit/coverslip for 1 hour. Gelation proceeded immediately after 3 brief PBS washes.

To make the gel, monomer solution (1x PBS, 2M NaCl, 8.625% (w/w) sodium acrylate (SA), 2.5% (w/w) acrylamide (AA), 0.15% (w/w) N,N'-methylenebisacrylamide (BIS)) was made up and aliquoted, storing at -20^{o}C until use. During gel preparations, all solutions were kept on ice to slow initial gelation. Concentrated stocks (10% w/w) of ammonium persulfate (APS) initiator and tetramethylethylenediamine (TEMED) accelerator were added to the monomer solution up to 0.2% (w/w) each. After thorough vortexing of the gel mixture, 80 µL

droplets were pipetted onto parafilm covered glass slides that were placed in a humid chamber. Coverslips were quickly inverted onto the droplets and gelation was allowed to proceed at room temperature for approximately one minute, before moving to incubate at 37°C in the dark for 2 hours. It is essential that the humid chamber remains moist during gelation in order to reduce the risk of the gel ripping from the coverslip prematurely in later manipulations.

Once gelation was complete, gelled coverslips were carefully removed from the parafilm with flat tweezers and placed in a 6 well plate. Digestion buffer (50 mM Tris (pH 8), 1 mM EDTA, 0.5% Triton X-100, 0.8 M guanidine HCl) was supplemented with Proteinase K (New England Biolabs), diluted 1:100 to 8 units/mL. Gelled coverslips were submerged in this digestion buffer overnight at room temperature.

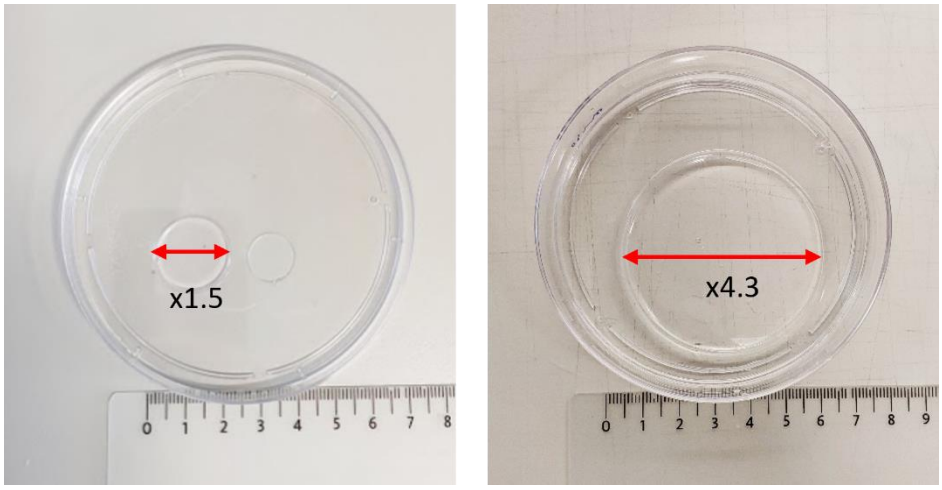

Figure 2.3 – Examples of expansion gels. *An expansion gel post digestion is shown next to the coverslip it was attached to, which measures 13 mm. The gel post incubation in diH_2O shows an expansion factor of ~ 4.3x.*

Gels - expanded 1.5x post digestion - were then transferred to excess deionised water and incubated. Water was replaced 2 - 5 times until expansion plateaued (an approximate diameter of 5.2 cm for the full gel).

Ultrastructure ExM

U-ExM was performed, with slight modification, as published by Gambarotto et al. [141]. Briefly, samples were fixed as usual, but PFA/GA incubation was followed by incubation in a solution of 0.7% formaldehyde and 1% Acrylamide in PBS for 5 hours at 37^{o}C. Actin labelling was carried out after this stage as above. Samples were then gelled, also as above, but with a modified monomer solution (19% (wt/wt) SA, 10% (wt/wt) AA, 0.1% (wt/wt) BIS in 1× PBS supplemented with 0.5% APS and 0.5% TEMED). Gelation was carried out in the dark at 37^{o}C for 1 hour before careful removal of the gelled slip and denaturation for 15 minutes at room temperature in denaturation buffer (200 mM SDS, 200 mM NaCl, and 50 mM Tris in ultrapure water, pH 9). After this, gels were carefully removed from the coverslips and placed in a 1.5 mL Eppendorf with fresh denaturation buffer followed by incubation at 95^{o}C for 1.5 hours. Gels were then fully expanded in diH2O.

For post gel labelling with antibodies, the gels were collapsed by incubation in 1x PBS. A section was then incubated for 3 hours with gentle shaking in primary antibody made up in standard 0.1% BSA/ 2% GS blocking buffer. 3 wash steps in PBS + 0.1% Tween 20 (PBST) followed, each incubating for 10 minutes with gentle

shaking. Secondary antibody incubation and final washes proceeded in the same fashion. Gels were then re-expanded by repeated incubation in diH2O, making sure to protect from light to minimise bleaching.

Mounting and imaging

For SIM and widefield imaging, #1.5 high precision Ibidi dishes were coated with poly-L-lysine (Sigma) and dried on a hotplate at 95^{o}C. Once fully expanded, a portion of gel was cut with a rectangular coverglass to fit the dish. Excess water was wicked from the gel with tissue to ensure solid adherence to the coverslip and reduce movement of the gel. The gel was gently pressed once placed on the coverslip to remove bubbles and increase attachment. A drop of water was then added to the top of the gel to minimise shrinkage over the course of the imaging session. Samples were imaged using the Nikon N-SIM-S system (detailed in 2.7.2, operating in SIM mode) and a Nikon 100x 1.35 NA silicone oil objective with Nikon silicone immersion oil.

Correlative Expansion Microscopy

For correlative experiments, cells were seeded and fixed on 25 mm high tolerance coverslips (Marienfeld). Labelling and gelation proceeded as normal, but prior to digestion a small region of gel was sliced in situ with a scalpel, resulting in cuts visible when imaging the gel. SIM images were then acquired of the gelled, but

unexpanded, sample. Following the standard expansion protocol, the same region of gel was reimaged post expansion.

2.8 Image Analysis

2.8.1 dSTORM reconstruction

Raw data was analysed using ThunderSTORM [164]. Settings were as follows:

Wavelet filter, B spline order 3 and B spline scale 2.
Local max set to std(wave.F1), 8 neighborhood.
PSF: Integrated Gaussian, 3.
Weighted least squares: 1.6 sigma.

Duplicates were merged at 80nm over 5 frames, and then filtered based on values as follows:

Table 2.5 – Filter values for dSTORM reconstructions

Point intensity	500 < x < 10,000
Uncertainty	x < 40
Sigma	x < 250

Reconstruction quality was assessed using NanoJ SQUIRREL (Culley et al., 2018).

2.8.2 dSTORM cluster analysis

Further quantification of randomly selected 5 µm x 5 µm regions of interest within each cell was undertaken using the R package RSMLM to apply a persistence-based clustering method called ToMATo [172]. Parameter selection was assessed via ToMATo persistence graphs and by plotting cluster maps with custom MATLAB script (courtesy of Jeremy Pike). Parameters were set at a search radius of 18 nm and persistence threshold of 12. Clusters with less than 10 detections were removed from the analysis. Cluster statistics, including area, number, and density, were then collected.

2.8.3 SRRF reconstruction

For SRRF imaging, data was processed using the NanoJ SRRF plugin for FIJI [128] using default settings and a PSF of 1.3. For FRC analysis (also using the NanoJ SRRF plugin), raw stacks were split into odd and even frames and then processed as above to permit comparison and calculation of resolution. Full width half maximum calculations were performed in FIJI using a plugin written by John Lim (2011), previously available online.

2.8.4 SRRF actin analysis

For corral analysis, SRRF images were cropped to an ROI of 10 μm^2, as centrally in the cell of interest as possible. The image was then manually thresholded using Otsu's method [187] in FIJI. The threshold was applied and the binary image inverted, eroded using FIJI's 'Erode' function, and inverted again. A classic watershed segmentation was then applied, and the resulting regions analysed for a range of descriptors.

For simulation of meshworks to test the analysis, all image simulation was performed in MATLAB 2019b. Filaments were simulated through random generation of start and end points. Each individual filament was given a daughter filament, branching at a 70-degree angle. Lines were dilated to more closely resemble the 7 nm nature of individual actin filaments. Pixels were binned to sizes appropriate for our system and cameras, and a Gaussian convolution based on the PSF estimated from our optics applied. Poisson and Gaussian noise were also applied to give a general approximation of read and shot noise. Analysis then proceeded as for real images. The code used is commented in appendix 1.

2.8.5 Single particle tracking

Raw movies were cropped to 256 x 256 pixels (16.55 µm x 16.55 µm) and any non-cell areas masked out. Movies were then analysed using the MATLAB software u-

track [180] using the single particles (2D) tracking setting. Detection method was set to point source detection, with the PSF calculated based on pixel size and channel wavelength provided. For tracking, max gap closing was set to 4 frames, with both frame-frame linking and gap closing/merging/splitting set to Brownian and directed motion models as their cost functions, with settings as default. Kalman filter functions were also set to Brownian and directed motion models. Segment merging and splitting were turned off. The alpha value for moment scaling spectrum analysis was set to 0.05. The method for confinement radius calculation was set to mean positional standard deviation.

Tracks were filtered, using a script adapted from a process embedded in plotTracks2D, included with the u-track package. DC-MSS analysis [184] was then performed on filtered tracks, with settings as described in their paper. Results were extracted and analysed with custom scripts.

When using TrackMate [176] for figure generation, particles were identified using the DoG detector with sub-pixel localization applied. Tracks were assigned using the simple LAP tracker with frame to frame linking of 0.5 µm and gap closing of 0.2 µm over 2 frames.

2.8.6 SIM reconstruction

SIM data was reconstructed using NIS-Elements (v. 5) slice reconstruction, or, where specified, stack reconstruction. Reconstructions reporting a score of 8 in the software were saved for further analysis, as this indicated good signal in all illumination phases and rotations. Representative reconstructed SIM data was assessed by way of the SIMCheck FIJI plugin [188]. Widefield images were generated from raw SIM acquisitions using NIS-Elements.

2.8.7 SIM analysis

For A_2 receptor - actin analysis, point detection in the TrackMate plugin in FIJI was applied to the receptor channel, with centroid coordinates of detected points then exported. The actin channel was thresholded using Otsu's method and the binary image saved. Using a custom written MATLAB script, point coordinates were then categorised as either on, off, or adjacent (defined by a radius of 2 pixels) to the binarized actin. The script is commented in appendix 1.

An adaptation to this script was used for α-actinin-1 - A_2 receptor – actin analysis, additionally calculating the nearest neighbour to each α-actinin-1 point in the A_2R channel.

2.8.8 Expansion microscopy

For filament density approximation, a script was written in MATLAB 2019b to assess fluorescence intensity across ROIs (40 μm^2) cropped from 3D SIM ExM images (see appendix 1). ROIs were selected to ensure blank extracellular regions were not included. Randomly oriented lines across the full image were used to plot fluorescence intensity graphs. These values were normalised and local maxima identified, with a threshold to eliminate background but no threshold on peak prominence to allow resolution of closely adjacent yet still separate filaments. Where peaks were not clearly delineated, a straight line was drawn to separate each peak, and width at half prominence calculated from these. This operation was repeated 100 times over each ROI, recording the number of peaks and mean distance between peaks. The script is commented in appendix 1.

2.9 Statistical Analysis and Data Presentation

Statistical analysis was performed in GraphPad Prism 8 and 9. Differences between two groups were assessed using unpaired Student's t-test, with multiple groups compared by one way ANOVA with Tukey's multiple comparisons, as relevant. Graphs were generated in GraphPad. Final figures and illustrations were assembled in Biorender.com.

2.10 Work Performed by Others

2.10.1 $A_{2A}R$ fluorescent ligand labelling

Performed by Dr. Joelle Goulding at the University of Nottingham, as follows:

A549 cells seeded into 8-well Nunc LabTek chambered coverglasses (No. 1.0 borosilicate glass bottom) were transfected with SNAP-$A_{2A}R$ as described previously and imaged 48hrs later on a Zeiss LSM 880 on a Zeis Axio Observer Z1 stand (Carl Zeiss) with a 40x C-apochromat water immersion objective (NA 1.2). Prior to imaging cells were labelled with 1 μM SNAP-Alexafluor-488 for 30 min at 37°C in full media and then incubated in the presence or absence of 1 μM SCH586241 for 30 min at 37°C in HEPES buffered saline solution (HBSS) containing 10 mM Glucose. Compound 16 (100 nM; selective $A_{2A}R$ antagonist with a CY5 fluorophore) was then added to each well and incubated for 30 min at 37°C before being left to cool to room temperature and then imaged. SNAP-Alexa fluor-488 was visualised using an Argon 488 nm laser with 493-628 nm emission band pass and compound 16 was visualised using a HeliumNeon 633 nm laser with 638-759 emission band pass. Cells were imaged with 1 airy unit pinhole (40 μm) for the longer wavelength and a 488/561/633 multi beam splitter. Laser power, gain and offset were kept consistent across images within an individual repeat.

2.10.2 CRE-SPAP assay

Assessment of $A_{2A}R$ function in Chinese Hamster Ovary cells was performed by Dr. Mark Soave at the University of Nottingham, using a cyclase response element (CRE) secreted alkaline phosphatase (SPAP) reporter gene assays as described in [189]. CD treatment proceeded for 30 minutes at 37^{o}C prior to the 5 hour agonist incubation.

2.10.3 SPIM ExM imaging and processing

Performed by Dr. Emma Faulkner at the University of Birmingham, as follows:

Sample preparation

For SPIM imaging, gels were cut to fit the SPIM holder and placed cell-side up in the SPIM holder. 2% agarose was pipetted into the holder until the bottom of the holder was covered, taking care not to get agarose in the interface between the top of the ExM gel and the objective lens. Deionised water was then added to the SPIM holder containing the gel to fully immerse the gel for imaging. Gels were left for at least an hour prior to imaging to aid stability of the specimens during image acquisition.

ASI iSPIM microscopy

SPIM imaging was performed on an ASI RAMM microscope with SPIM-MOUNT, equipped with Nikon 40x objectives attached to Piezo object movers to scan the sample. Illumination was from 100mW OBIS CW lasers. The system is equipped with a Hamamatsu Flash 4 scientific CMOS camera. Micromanager was used to control the system and scan the sample.

CHAPTER 3 - INVESTIGATING ADENOSINE RECEPTORS

3.1 Chapter Overview

In general, behaviour of specific receptors in interaction with actin are relatively sparsely researched. There is evidence for a functional relationship between the serotonin receptor 1A and actin structure [190, 191], as well as evidence of an undisrupted cortex being essential for CD36 signalling post activation [192]. Most papers, however, show only a dynamic or an organisational link. It is therefore unsurprising that a solid functional link between adenosine receptor organisation and cortical actin is yet to be described in the literature.

Despite their important regulatory roles and implication in numerous pathologies, investigations into the membrane organisation of adenosine receptors $A_{2A}R$ and $A_{2B}R$ have many outstanding questions. In terms of known interactions, inter-adenosine receptor family heteromers have been demonstrated with proximity based techniques like BRET and FRET, including A_{2A}-A_1 [193], A_{2A}-A_3 [194], and A_{2A}-A_{2B} receptor heteromers [85]. Higher order clustering, or regulation thereof, is yet to be studied. Evidence is also limited in the context of clustering and internalisation of receptors in the family. $A_{2A}R$ dynamics in the presence of Latrunculin A (Lat A) have been investigated with the bulk motion analysis technique FRAP (fluorescence recovery after photobleaching), indicating no change to the mobile fraction of receptor [195], but more granular and high resolution investigation is possible.

This chapter will use super resolution techniques to assess functional, static, and dynamic behaviours of A_{2A} and A_{2B} receptors. Pharmacological investigations were conducted with the intent of identifying any effects on signalling that may be apparent after disruption of normal actin organisation. Single molecule localisation microscopy has been applied in multiple receptor imaging contexts and was used here to assess receptor clustering at the nanoscale. As covered in introduction section 1.10.2, SPT analysis was instrumental in demonstration of the picket fence model, being used to show that membrane protein and lipid confinement radii correlated well with sizes of actin fenced regions identified in EM experiments [14, 15]. Here it was used to investigate the dynamic behaviour of each receptor at high framerates on a sub-track basis.

So, this chapter aims to investigate the potential organising effects of cortical actin on the A_{2A} and A_{2B} adenosine receptors. Imaging experiments to investigate the organisation, behaviour, and dynamics of the receptors are coupled with pharmacological investigations, recording response to receptor stimulation and actin disruption. These experiments provide insight into a differential behaviour in the two receptors, as well as a quantifiable effect of cortical actin disruption on the A_{2A} receptor in multiple contexts.

Core Aims:

- Assess signalling behaviour of A_2 receptors under actin disrupting conditions.
- Identify and quantify any changes in A_2 receptor clustering under stimulating and actin disrupting conditions.
- Identify and quantify any changes in A_2 receptor dynamics under stimulating and actin disrupting conditions.

3.2 Expression and Labelling of SNAP-A_{2A} and – A_{2B} Receptors

3.2.1 Transient transfection of SNAP tagged A_{2A} and A_{2B} receptors

In order to visualise the receptors, A549 cells were transiently transfected with N-terminally SNAP tagged A_2R constructs. These variants of the human A_{2A} and A_{2B} receptors were based on plasmids used previously in the lab of Dr Briddon, with a similarly sized NLuc tag showing no impediment to receptor function.

Incubating with cell impermeable SNAP-Surface ligands as according to the manufacturer's instructions resulted in clear labelling of receptor in the membrane, with some internalised label (Figure 3.1), but also significant background on the coverslip. As such, a more stringent wash routine (methods section 2.6) was used in all experiments when using SNAP label. Cells were labelled live for all experiments. Labelling of untransfected cells, both as separate controls and observing non-expressing cells within transfected samples, showed no membrane labelling and minimal uptake of label into the cell. Transfected cells were therefore easily distinguishable (Figure 3.1). Formal assessment of cell viability was not carried out following transfection or SNAP labelling.

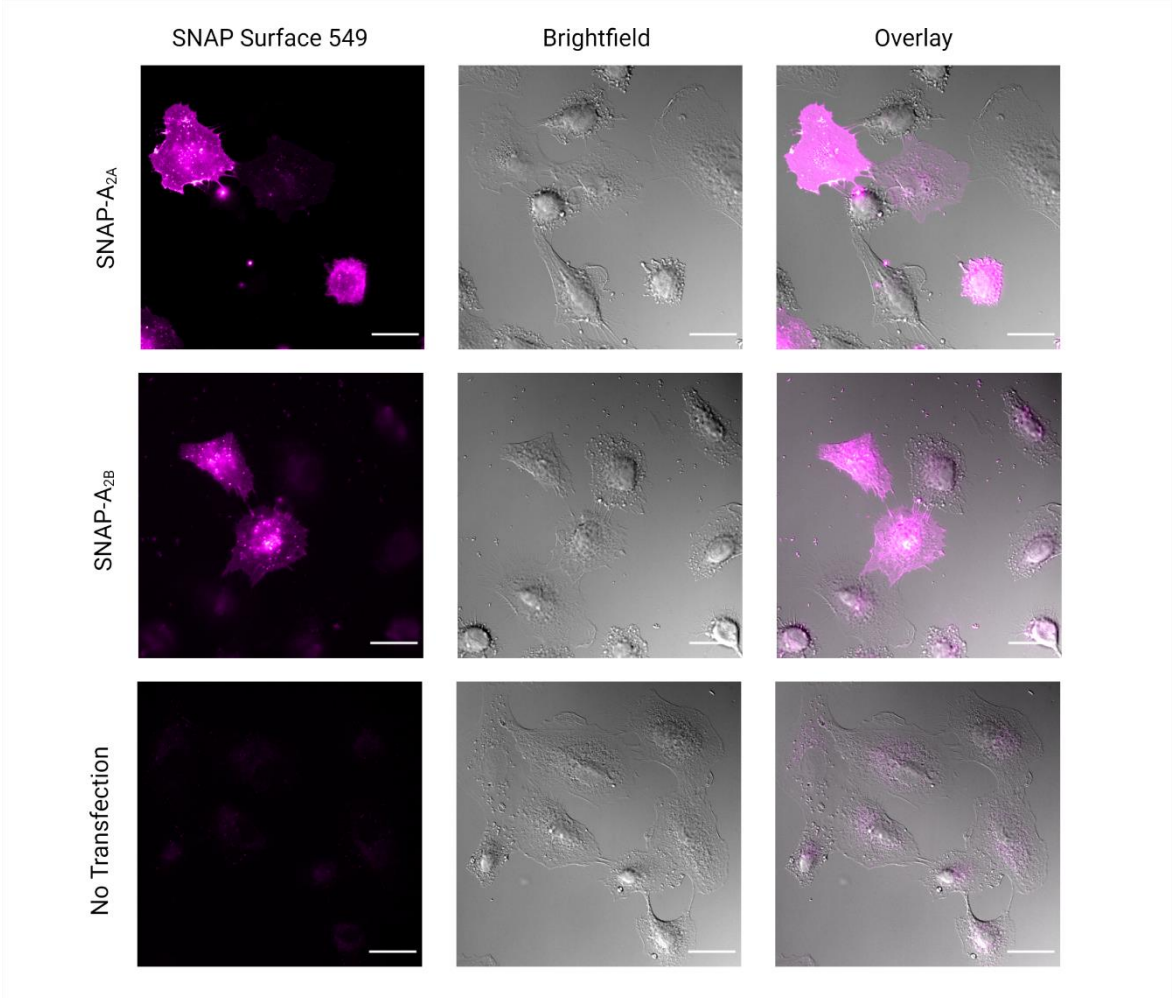

Figure 3.1 – SNAP-A_{2A}R and SNAP-A_{2B}R constructs allow specific labelling of receptors. *SNAP Surface 549 shows membranous labelling on SNAP-construct expressing A549 cells, with no labelling on untransfected cells both within transfected samples and in control experiments. Scale bars = 20 µm.*

3.2.2 Fluorescent A_{2A}R ligand labelling suggests no endogenous expression

As noted in the introduction, endogenous transcription levels for the A_{2A}R in A549 cells appear to be below the threshold expected for expression [196]. To confirm this in our A549 cells, the A_{2A}R selective fluorescent antagonist ‘compound 16’ [186] was used to image potential endogenous receptors.

Having labelled SNAP-A_{2A}R expressing cells with SNAP Alexa 488, samples were then incubated with compound 16 to assess endogenous expression in non-transfected cells. As shown in Figure 3.2, the ligand shows clear labelling of the SNAP-A_{2A}R expressing cells, with no labelling of neighbouring cells, indicating no endogenous expression of A_{2A}R in these cells. Treatment with the non-fluorescent antagonist SCH586241 prior to compound 16 labelling almost completely prevented binding by the fluorescent antagonist, confirming the interaction to be receptor

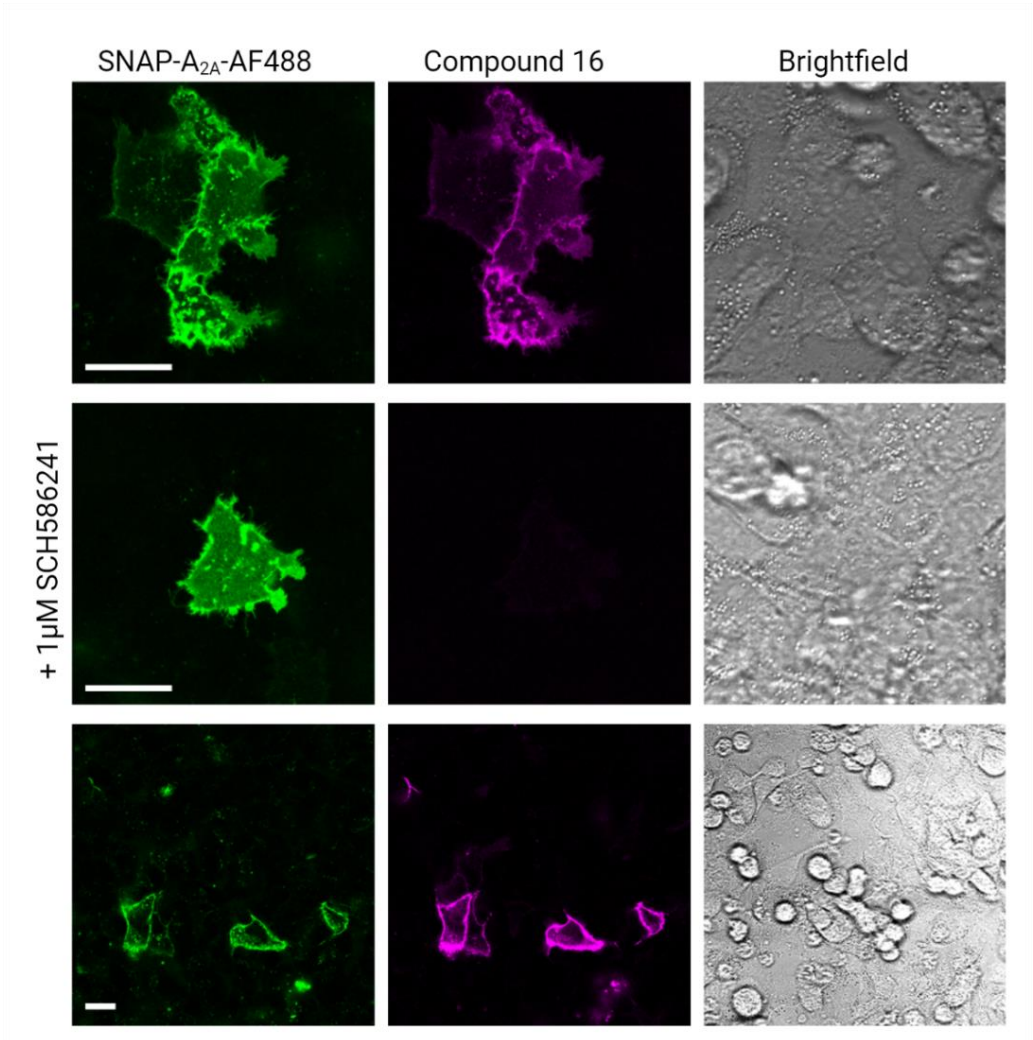

Figure 3.2 – Fluorescent antagonist Compound 16 labels SNAP-A_{2A}R but suggests no endogenous A_{2A}R expression in A549 cells. *SNAP Surface Alexa 488 labelled SNAP-A_{2A}R expressing A549 cells show label after incubation with 100 nM compound 16. Labelling inhibition is evident when cells are pre-treated with unlabelled antagonist. Scale bar 20 µm. Images courtesy of Dr Joelle Goulding.*

binding and not some kind of interference by the SNAP tag. These experiments and imaging were performed by Dr Joelle Goulding at the University of Nottingham.

As indicated in Figure 3.3, SNAP-Surface Alexa 488, SNAP-Surface Alexa 647, and SNAP-Surface 549 substrates were largely consistent in terms of specificity and background and were therefore used as required for subsequent imaging experiments.

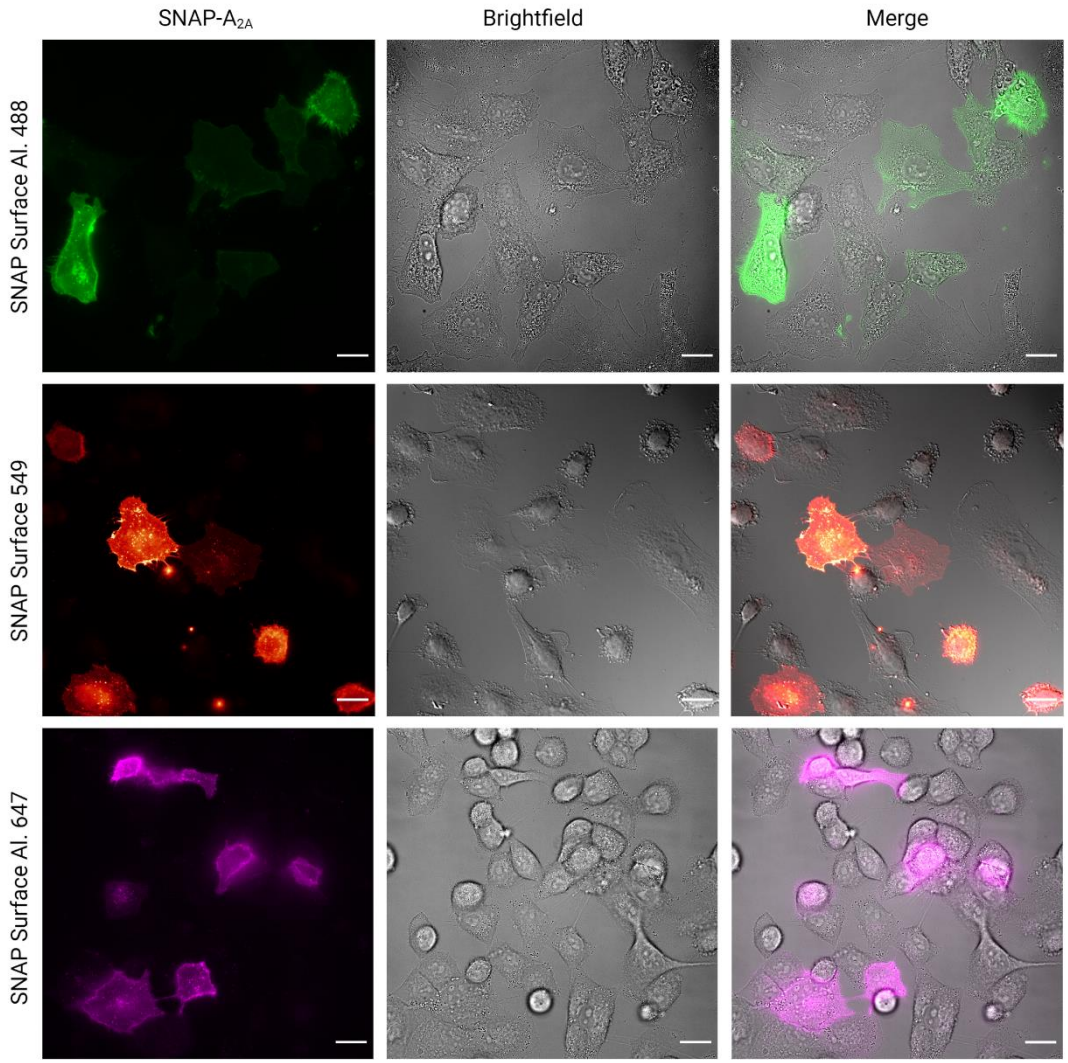

Figure 3.3 – SNAP surface ligands AlexaFluor 488, 549, and AlexaFluor 647 show consistent performance. *A549 cells expressing SNAP-A_{2A}R were labelled with 1 µM of various SNAP ligands for 30 minutes at 37°C. Scale bars = 20 µm.*

3.3 Pharmacological Characterisation of SNAP-A_{2A} Receptor Signalling

3.3.1 Characterisation of SNAP-A_{2A} and -A_{2B} receptor signalling

To assess the response of the SNAP tagged receptors, both with standard stimulation and with additional actin disruption, stable CHO cell lines were generated. CHO cells do not endogenously express any of the adenosine receptor family, meaning that any response to adenosine agonists should be solely a result of the transfected SNAP construct. The cell line used also contains a reporter gene system, using a cAMP-responsive cyclase response element (CRE) promoter to control expression of the reporter, secreted placental alkaline phosphatase (SPAP). SPAP levels can be determined by colorimetric assessment of the sample after hydrolysis of *p*-nitrophenol phosphate [197]. The CRE-SPAP reporter gene assay is a robust method for assessing both G_s and G_i coupled GPCRs, and has previously been used for all four members of the adenosine receptor family (examples of studies include: A_1R [198], $A_{2A}R$ and $A_{2B}R$ [199], and A_3R [200]). The mechanism of the system is given in Figure 3.4.

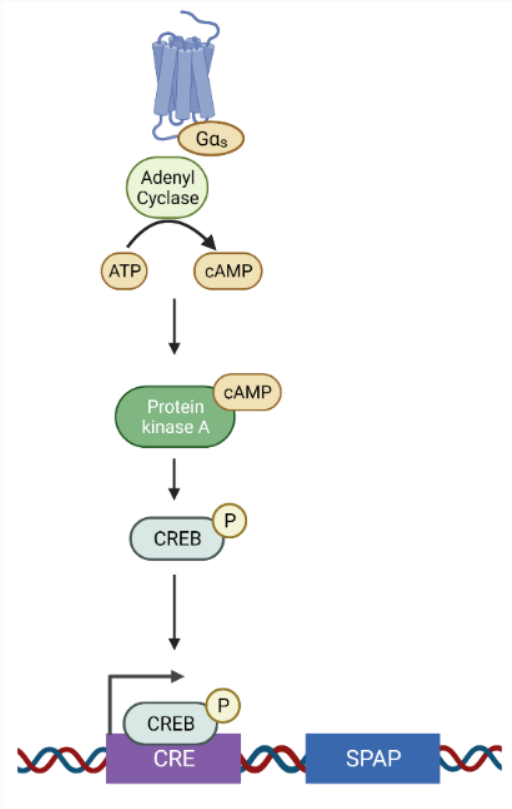

Figure 3.4 – Mechanism of CRE-SPAP reporter gene system. *cAMP increases result in phosphorylation of CREB, which binds to the CRE promoter and results in expression of Secreted Placental Alkaline Phosphatase (SPAP).*

Both transiently (Figure 3.5a) and stably (Figure 3.5b) SNAP-$A_{2A}R$ expressing CHO cells were used in initial optimisation. Responses to the agonists NECA and CGS21680, in the presence and absence of the $A_{2A}R$ selective antagonist ZM241385, were determined. NECA, which is a non-selective adenosine receptor agonist, showed a concentration-dependent increase in SPAP production with a $logEC_{50}$ of -7.25 ± 0.20 (mean ± S.E. mean; n = 3) for the transiently expressing population, and -6.88 ± 0.23 (n = 6) for the stably expressing cell line. The $A_{2A}R$ selective agonist CGS21680 showed a similar response, with a $logEC_{50}$ of -7.07 ± 0.32 for the transient line and -7.81 ± 0.29 for the stable expressors. Both responses

were significantly inhibited by treatment with 1 µM ZM241385 (Figure 3.5) indicating the responses were mediated through stimulation of the $A_{2A}R$. All E_{max} and $logEC_{50}$ values are shown in Table 3.1 and Table 3.2. The stably expressing clone was chosen for further experiments as responses were more consistent.

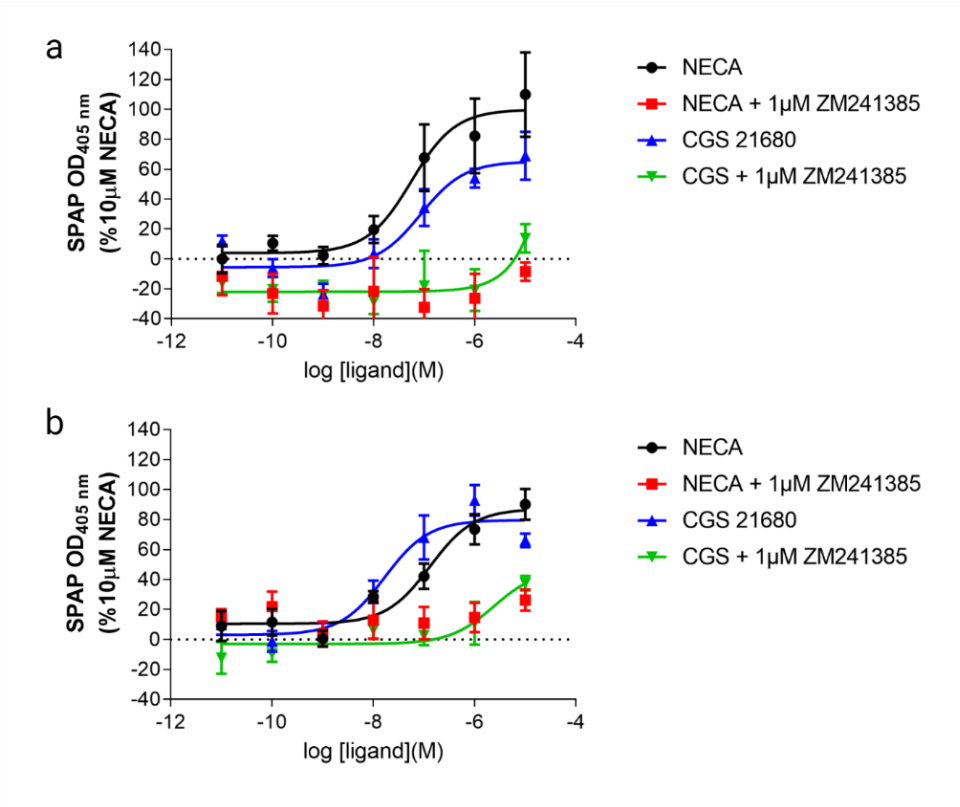

Figure 3.5 – SNAP-$A_{2A}R$ expressing CHO cells respond to NECA and CGS21680. *CHO cells either a) Transiently transfected or b) stably expressing SNAP-$A_{2A}R$ showed a dose dependent response to $A_{2A}R$ agonists which was abrogated in the presence of antagonist ZM241385. Transiently transfected cells displayed more variability in response when compared to the stably expressing line. Antagonist pre-incubation proceeded for 30 minutes before addition of the agonist for a 5 hour incubation at 37°C. Mean ± SEM of indicated number of independent experiments. For a: n = 3, for b: n = 6.*

Having confirmed function of the SNAP-A_{2A} receptor, increasing concentrations of cytochalasin D (CD) were added during stimulation to investigate the effect of disrupting normal actin structure on receptor response. This resulted in decreases in

the calculated log EC_{50} when compared to NECA alone for the two higher CD concentrations (Table 3.3). Addition of 3 µM CD produced the largest shift (log EC_{50} = -7.30 ± 0.30), but neither shift was statistically significant (NECA vs. +3 µM CD: p = 0.65, NECA vs. +10 µM CD: p = 0.98). Maximal responses were elevated by addition of CD, with 3 µM and 10 µM of CD showing a significant increase relative to NECA alone (NECA vs. +3 µM CD: p = 0.0035, NECA vs. +10 µM CD: p = 0.0021). Basal responses also showed an upward trend, but were not significantly affected by addition of CD. Only the addition of 10 µM CD showed a statistically significant increase in response span over NECA alone (NECA vs. +10 µM CD: p = 0.0417) (Figure 3.6, Table 3.3).

Unfortunately, data for $A_{2B}R$ was not gathered. Attempts to produce stable cell lines expressing both the receptor and reporter constructs at sufficient levels for the assay were unsuccessful. Additionally, transient expression of the constructs proved too variable to provide robust data, and so it was not possible to generate curves for $A_{2B}R$.

This work was performed by Dr Mark Soave at the University of Nottingham.

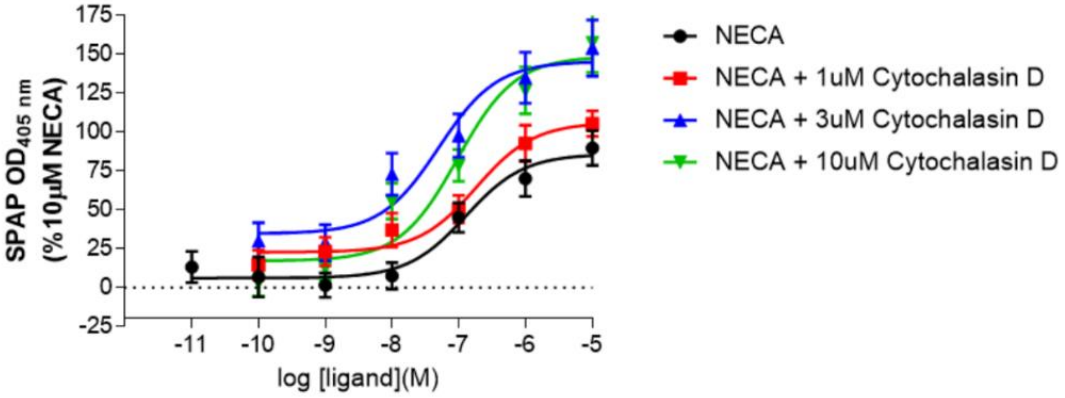

Figure 3.6 – Actin disruption shows an increased cAMP response over NECA treatment alone. *Clonally selected stably SNAP-A_{2A}R expressing CHO cells showed a dose dependent response to NECA, somewhat enhanced by incubation with increasing concentrations of CD. CD incubation proceeded for 30 mins before addition of the agonist for a 5 hour incubation, both at 37°C. Mean ± SEM. n = 6, for NECA only n = 7.*

Table 3.1 – CHO SNAP-A_{2A}R mixed population responses. *CHO cells transiently transfected with SNAP-A_{2A}R showed a dose-dependent response to A_{2A}R agonists which was abrogated in the presence of antagonist ZM241385. Antagonist pre-incubation proceeded for 30 minutes before addition of the agonist for a 5 hour incubation at 37°C. Mean ± SEM. * Curve not fit, data given is the response at 10^{-5} M NECA.*

Ligand	**Log EC50 (mean ± SEM)**	**Emax (% 10µM NECA)**	**n**
NECA	-7.25 ± 0.20	99.9 ± 7.2	3
NECA + 1 µM ZM241385	ND	-8.4 ± 6.2 *	3
CGS 21680	-7.07 ± 0.32	65.2 ± 11.0	3
CGS 21680 + 1 µM ZM241385	ND	13.8 ± 9.5 *	3

Table 3.2 – CHO SNAP-A_{2A}R Clone 4 responses. *Clonally selected stably SNAP-A_{2A}R expressing CHO cells showed a dose-dependent response to A_{2A}R agonists which was abrogated in the presence of antagonist ZM241385. Antagonist pre-incubation proceeded for 30 minutes before addition of the agonist for a 5 hour incubation at 37°C. Mean ± SEM.*
** Curve not fit, data given is the response at 10^{-5} M NECA.*

Ligand	**Log EC50 (mean ± SEM)**	**Emax (% 10µM NECA)**	**n**
NECA	-6.88 ± 0.23	92.0 ± 4.7	6
NECA + 1 µM ZM241385	ND	28.3± 8.0 *	6
CGS 21680	-7.81 ± 0.29	82.6 ± 7.7	6
CGS 21680 + 1 µM ZM241385	ND	37.7 ± 5.6 *	6

Table 3.3 – CHO SNAP-A_{2A}R responses to CD treatment. *Clonally selected stably SNAP-A_{2A}R expressing CHO cells showed a dose-dependent response to NECA, somewhat enhanced by incubation with increasing concentrations of CD. CD incubation proceeded for 30 mins before addition of the agonist for a 5 hour incubation, both at 37°C. Mean ± SEM.*

Ligand	**Log EC50**	**Basal (% 10 µM NECA)**	**Max (% 10 µM NECA)**	**Emax (% 10 µM NECA)**	**n**
NECA	-6.89 ± 0.17	6.2 ± 3.6	85.9 ± 5.9	79.8 ± 6.6	7
NECA + 1 µM Cytochalasin D	-6.78 ± 0.20	22.8 ± 4.7	106.2 ± 7.0	83.4 ± 8.0	6
NECA + 3 µM Cytochalasin D	-7.30 ± 0.30	34.7 ± 10.5	145.4 ± 11.8	110.7 ± 14.9	6
NECA + 10 µM Cytochalasin D	-7.02 ± 0.31	17.2 ± 12.7	148.7 ± 16.3	131.5 ± 19.6	6

3.3.2 Characterisation of SNAP adenosine receptor in A549 cells

Assessment of SNAP-$A_{2A}R$ function was also carried out in A549 cells, as these were the cells used in subsequent imaging studies. Pharmacology of this cell line was assessed by measuring cAMP levels via a competition TR-FRET assay. Using a commercial kit (LANCE ultra, Perkin Elmer), response to both NECA alone and with CD treatment were assessed by measuring a reduction in FRET between the Europium tagged cAMP tracer and fluorescently labelled cAMP antibody (see Figure 3.7). Increased endogenous cAMP outcompetes interactions between the two labelled components, allowing calculation of cAMP concentration in the cellular samples.

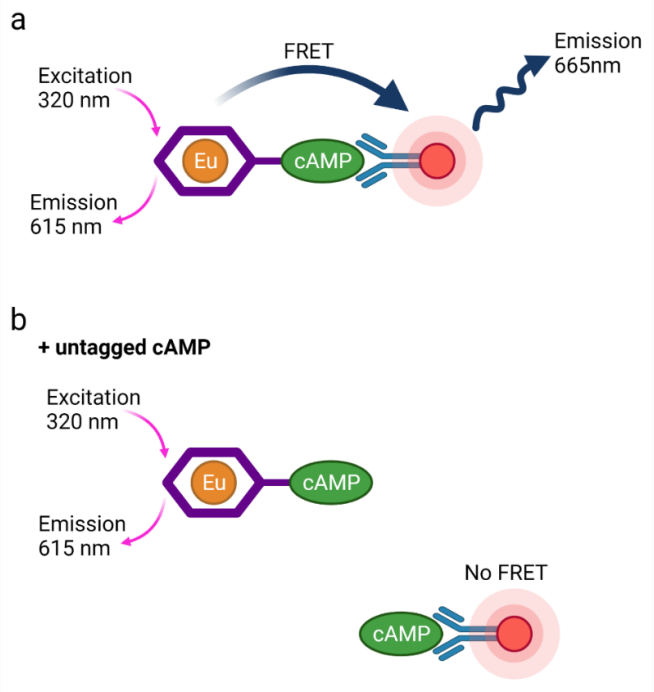

Figure 3.7 – Mechanism of TR-FRET cAMP detection. *a) When endogenous (untagged) cAMP levels are low, Eu-tagged cAMP and the anti-cAMP antibody will interact, resulting in FRET. b) When endogenous cAMP levels are high, the likelihood of tagged cAMP interacting with the antibody is reduced, also reducing the FRET specific emissions.*

A cAMP calibration curve was performed with serial dilutions of a cAMP standard (Figure 3.8). The calibration curve also represents the dynamic range of the assay. Standards were included on each plate going forward. The system was then tested by treating $A_{2A}R$ expressing A549 cells with 1 µM forskolin, an adenylyl cyclase activator, as a positive control. Forskolin stimulation resulted in clear cAMP increase, with an estimated cAMP concentration of ~ 4.2 nM.

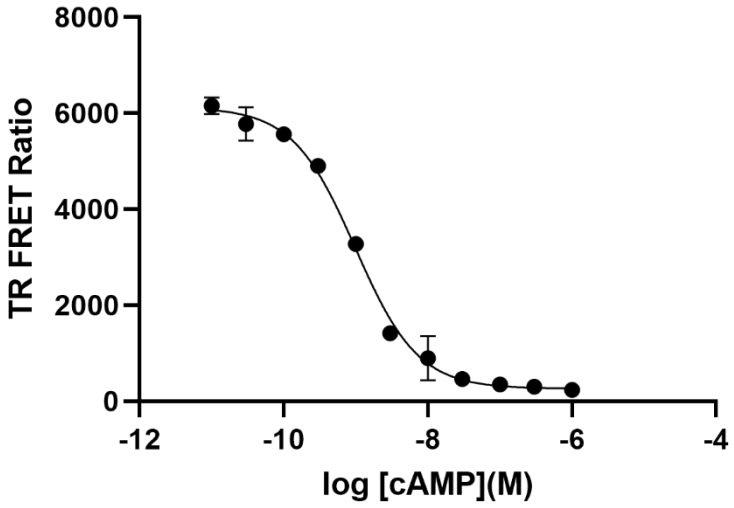

Figure 3.8 – cAMP standard curve for LANCE TR-FRET kit. *Serial dilutions of a cAMP standard assessed with LANCE TR-FRET reagents to generate a standard curve.*

$A_{2A}R$ expressing A549 cells were then exposed to a range of concentrations of NECA from 10^{-9} – 10^{-5} M. Cells showed a concentration-dependent increase in cAMP with a log EC_{50} value of -6.20 ± 0.35 (Mean ± S.E. mean, n = 3) and a maximal response seen at 10 µM NECA of 1472.10 ± 436.6, but this was unlikely to be the maximal response the system was capable of. To assess actin disruption in these cells, treatment with NECA was repeated alongside 100 nM, 1 µM, or 10 µM cytochalasin D. The potency of NECA was decreased at 1 µM and 10 µM CD treatment, with a significant increase in basal response seen at all concentrations of CD (NECA vs. +100 nM CD: p = 0.023, NECA vs. +1 µM CD: p = 0.039, NECA vs. +10 µM CD: p = 0.028). A decrease in the NECA E_{max} was seen for all CD concentrations, although this was driven predominantly by an increase in basal cAMP values, with little change in the maximum response. Data are shown in Figure 3.9 as raw (a), normalised (b), and interpolated mean cAMP values (c). Raw TR-FRET ratios are reported in Table 3.4.

As negative controls, alongside unseeded wells, experiments were performed with DMSO vehicle or CD treatment alone, indicating there may be some basal effect of DMSO treatment on cAMP production (Figure 3.10). DMSO at all points was < 0.18% of reaction volume.

$A_{2B}R$ expressing A549 cells were also tested, but showed limited response. A NECA response curve comparison of $A_{2A}R$ and $A_{2B}R$ response is shown in Figure 3.11a, where even 10 µM NECA treatment shows only minor reductions in TR-FRET ratio

for the $A_{2B}R$ expressing cells. Attempts to characterise with the $A_{2B}R$ specific partial agonist BAY 60-6583 were also met with limited success, again showing minimal response at 100 µM of agonist (Figure 3.11b).

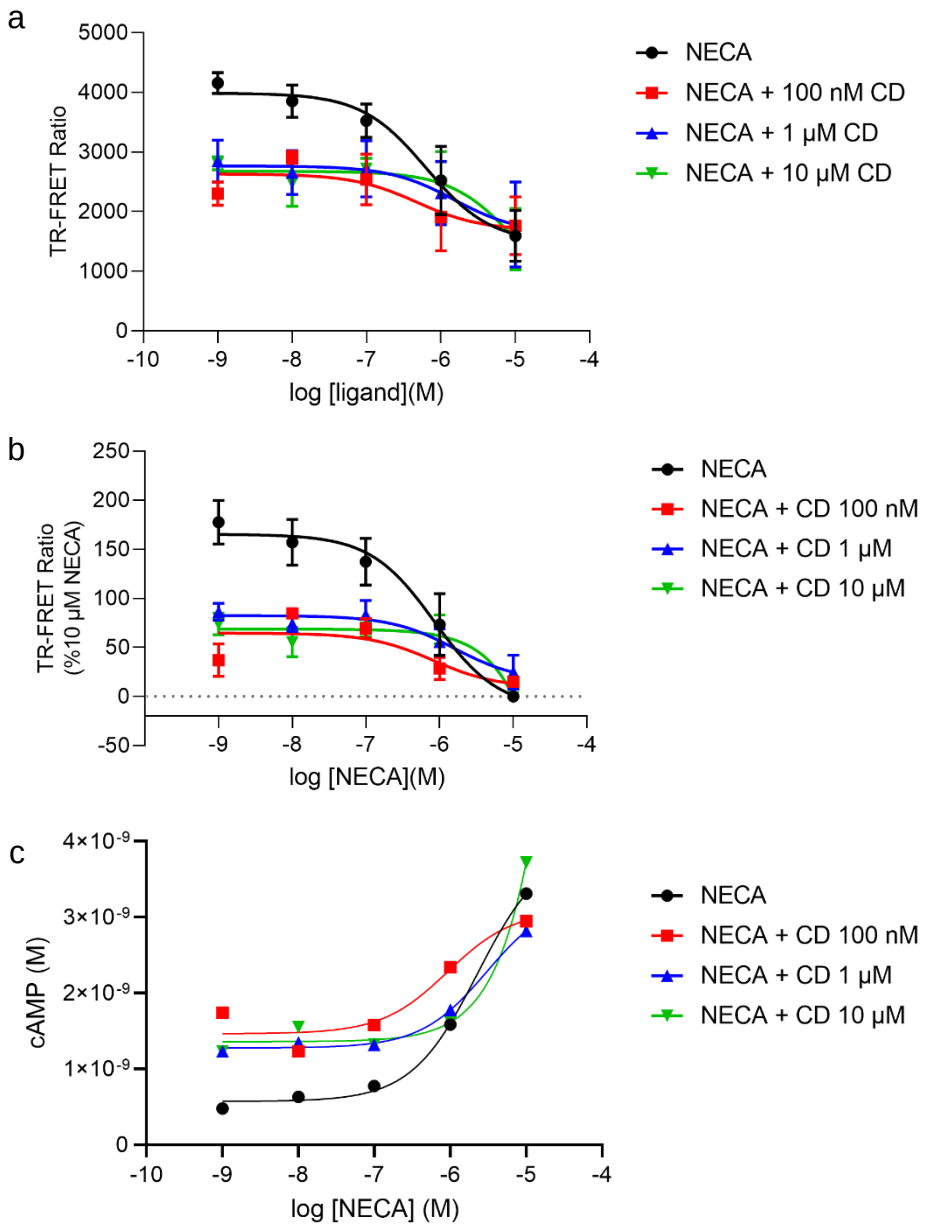

Figure 3.9 – cAMP response to NECA and CD treatment in $A_{2A}R$ expressing A549 cells. *A549 cells transiently expressing SNAP-$A_{2A}R$ were treated with increasing concentrations of CD (100 nM, 1 µM, and 10 µM) alongside NECA for 30 minutes at room temperature. a) Raw TR-FRET ratio data and b) data normalised to the response of 10 µM NECA. c) Mean TR-FRET ratio responses were interpolated using a cAMP standard curve to provide estimates of cAMP concentrations for each treatment. For a and b, data is represented as mean ± SEM.*

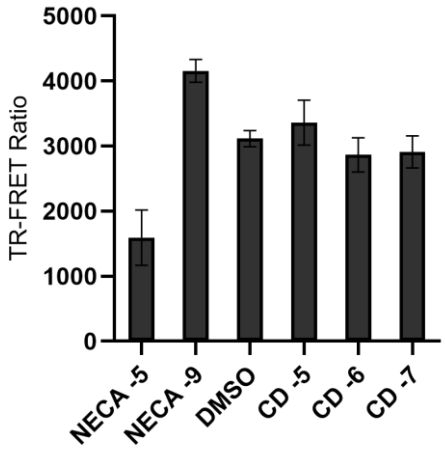

Figure 3.10 – Comparing CD and DMSO basal responses to NECA outcomes. *Minimal (logM-9) and maximal (logM- 5) NECA responses are provided as comparison for DMSO and CD control experiments, where all drug treatments were carried out at room temperature for 30 minutes. n = 3. Mean ± SEM.*

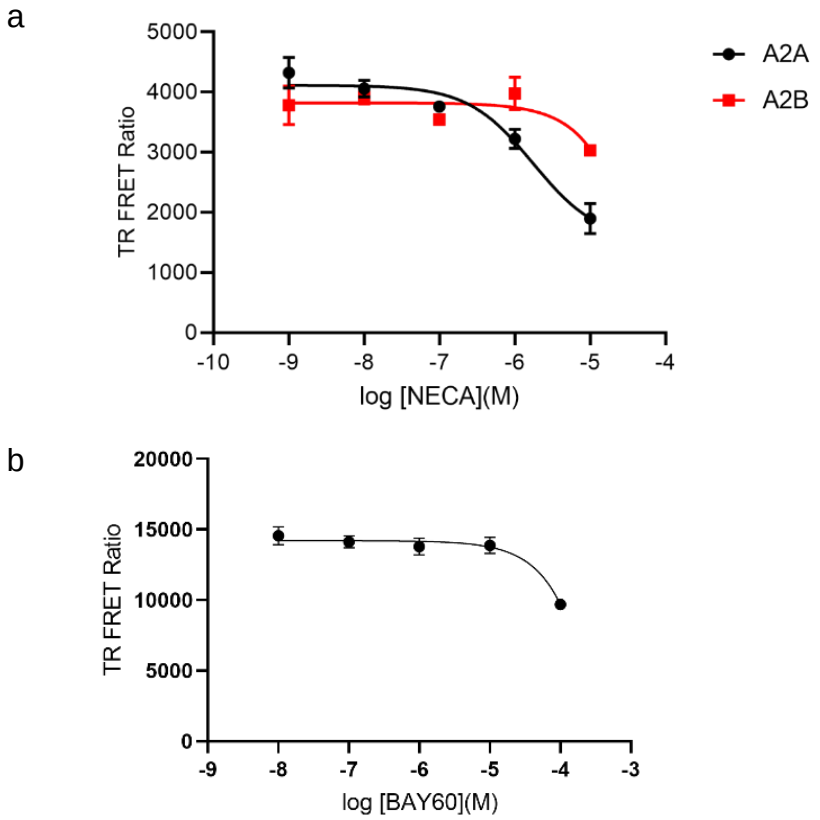

Figure 3.11 – A_{2B}R responses to agonists were limited. *Transiently transfected A549 cells expressing SNAP-A2BR showed limited cAMP response after a 30-minute room temperature incubation with a) NECA and b) BAY60-6583. The A2AR response to NECA treatment is included in a) as a reference. Data displayed as mean ± SEM.*

Table 3.4 – A549 expressing SNAP-A_{2A}R responses to NECA and CD treatment. *Transiently transfected SNAP-A_{2A}R expressing A549 cells showed a dose-dependent response to NECA and increasing concentrations of CD. Drug incubation proceeded for 30 minutes at room temperature. Mean ± SEM. * Bottom of curve not fit; values given based on mean response at 10^{-5} M NECA.*

Ligand	Log EC50	Basal (TR-FRET ratio)	Max (TR-FRET ratio)	Span (TR-FRET ratio)	n
NECA	-6.20 ± 0.4	3986.54 ± 235.3	1472.10 ± 436.6	2514.44 ± 461.6	3
NECA + 100 nM Cytochalasin D	-6.32 ± 1.0	2631.75 ± 270.5	1686.22 ± 453.4	945.53 ± 485.5	3
NECA + 1 µM Cytochalasin D	-5.82 ± 1.1	2765.88 ± 291.5	1636.35 ± 752.9	1129.54 ± 758.8	3
NECA + 10 µM Cytochalasin D	-4.98 ± 2.2	2677.15 ± 218.8	1541.08 ± 513.19 *	1130.07 ± ND*	3

Taken together, initial pharmacological data indicates that actin disruption may affect basal A_{2A}R signalling outcomes, a conclusion which could be strengthened with further experimentation. Assessing receptor organisation with imaging techniques was a logical next step in developing a functional model for actin/receptor interaction.

3.4 dSTORM

3.4.1 dSTORM imaging of $A_{2A}R$ and $A_{2B}R$

In order to assess receptor clustering at the nanoscale, the SMLM technique dSTORM was used. SNAP tagged A_{2A} and A_{2B} receptors were transiently transfected into A549 cells and optimal expression for dSTORM imaging was determined to be at 48 hours post transfection. As dSTORM relies on the photophysics of the labelling fluorophore to generate the necessary stochastic blinking, cells were labelled with a SNAP-Surface substrate conjugated to Alexa 647, a fluorophore that, according to Dempsey et al. [107] performs the most robustly for dSTORM imaging. After sample preparation as described in methods section 2.7.3, good SNR was achieved when imaging the samples in widefield (see Figure 3.1 in section 3.2.1) and TIRF (Figure 3.12), with expected heterogenous membrane distribution of both receptors.

Fixed SNAP-labelled cells were then imaged in TIRF at a framerate of 100fps for 20,000 frames. Blinking was facilitated using a GLOX-thiol buffer, with the introduction of 405 nm laser to maintain consistent blinking. A description of the workflow is shown in Figure 3.12.

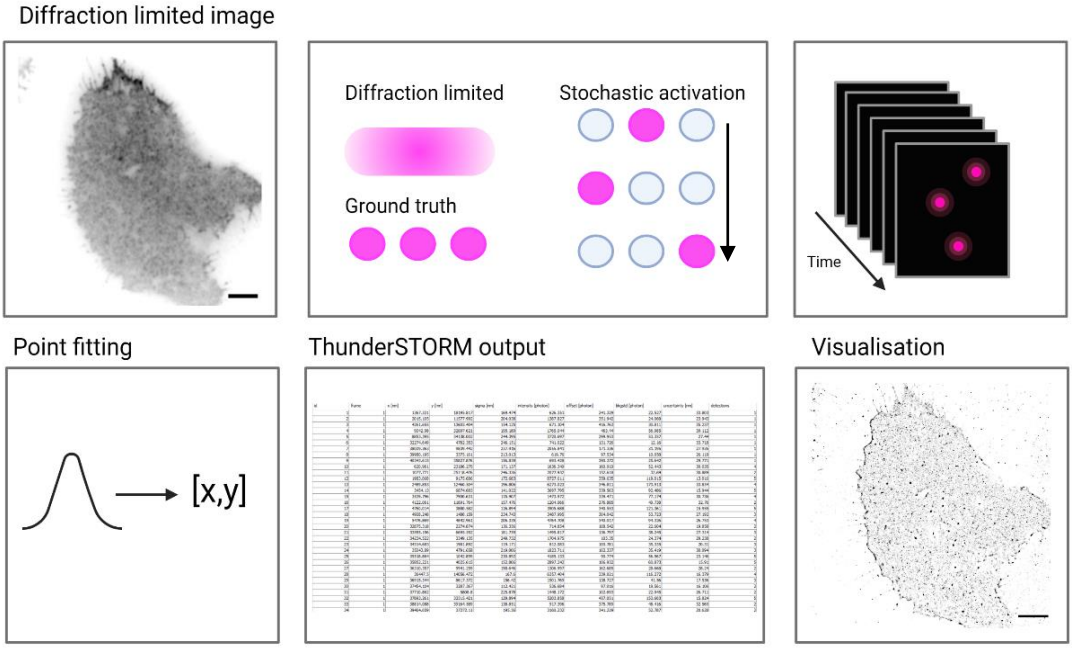

Figure 3.12 – dSTORM workflow. *Blinks are imaged over time then a point fitting routine is applied to localise each detection. Thousands of points are fitted, with metadata including intensity and precision of localisation. Super resolved images can then be visualised by fitting of Gaussian convolution.*

3.4.2 Image reconstruction

After image acquisition, parameters for point localisation using the FIJI plugin ThunderSTORM [164] were optimised. As standard for SMLM analysis with this plugin, data was drift corrected, here using 5 bin cross correlation. Merging of repeat blinks or exceedingly long emissions was set to repeat detections within 80 nm, determined through assessment of data performance over multiple merge distances (Figure 3.14), and over a maximum of 5 frames, as indicated by Jimenez et al. [201]. Filters on point intensity were applied to exclude those with an intensity value of less than 500 e^- and more than 10,000 e^-. Detections with an uncertainty of more than 40 nm were also excluded. These values were chosen based on the histograms of data

distribution (Figure 3.13). Sigma values (the standard deviation of the Gaussian fitted to the point peak) were also used to exclude detections likely to be out of focus (based on ideas discussed in [202] and personal communications (Susan Cox, ESRIC 2019)).

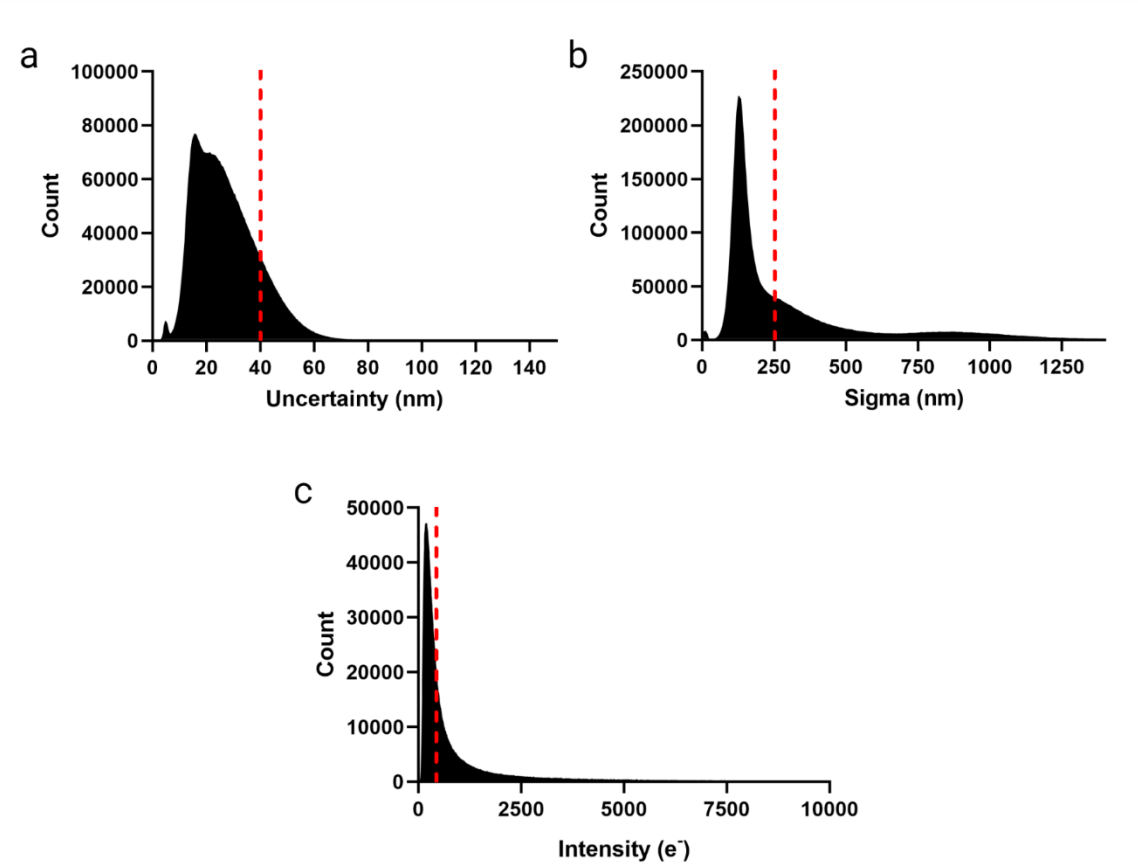

Figure 3.13 – Example histograms for ThunderSTORM outputs. *a) Uncertainty or localisation precision, b) sigma or standard deviation of the Gaussian fit, and c) intensity reported for all detections in an image. Dotted lines represent filtering values discussed above.*

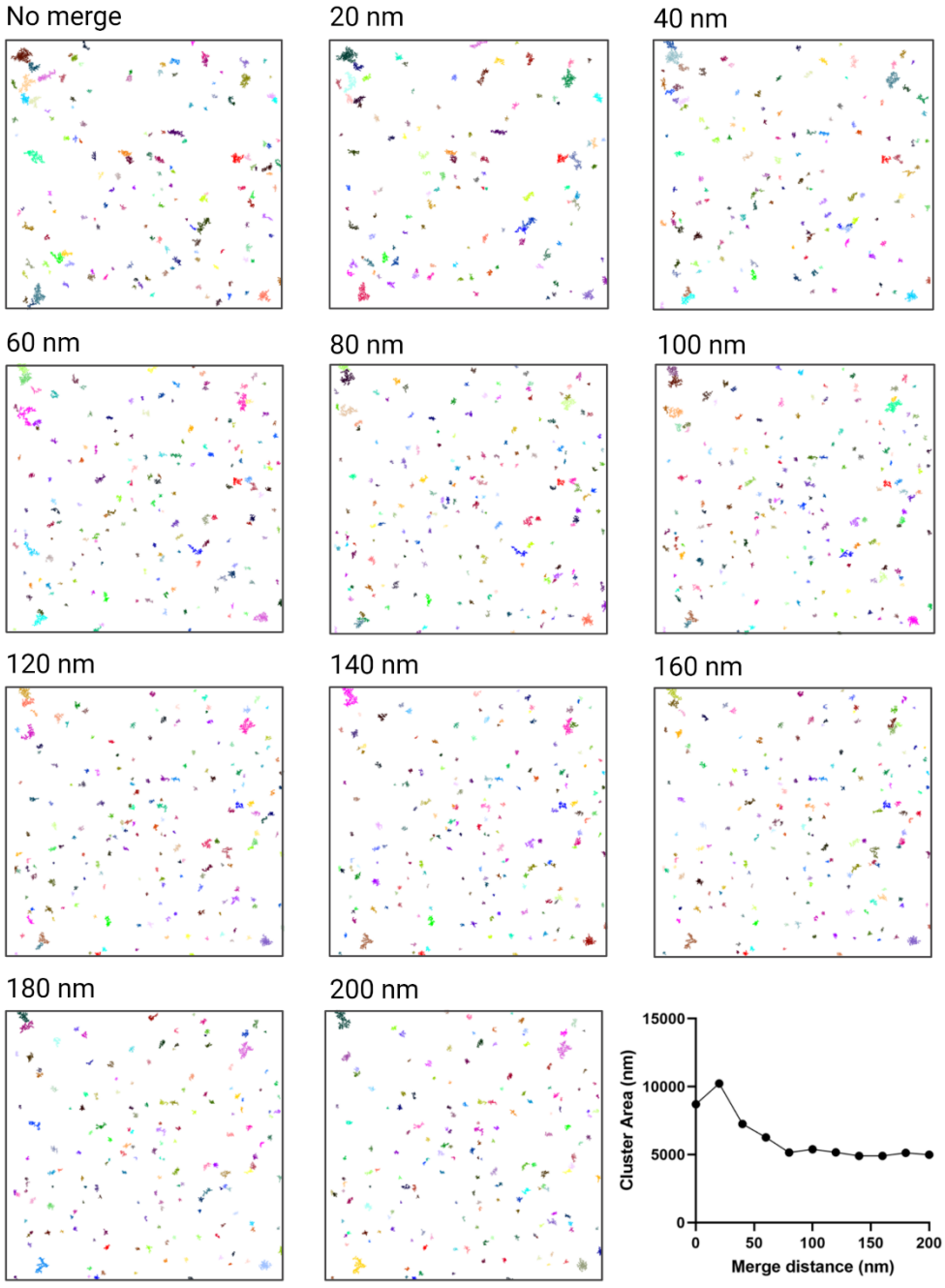

Figure 3.14 – Performance of ToMATo cluster analysis is dependent on merge distance. *Examples are given for no merging of reblinking, then every 20 nm to 200 nm. Area of clusters is plotted. Filtered data is a region of interest from a SNAP $A_{2A}R$ expressing A549 cell imaged using dSTORM.*

In order to visually assess results, point cloud data was reconstructed using a Gaussian convolution (ThunderSTORM normalised Gaussian render at magnification 10 with a lateral uncertainty of 20 nm) to give a more intuitive representation of the high-resolution point data.

When visually assessing the reconstructed images, receptor localisation was generally consistent with expected distribution when comparing with TIRF images of the basal membrane, though ‘edge’ artifacts - likely artificial sharpening due to high blink density in these regions, or the incident light beam illuminating a small part of the apical membrane during imaging - did appear often when sigma filtering was insufficient (Figure 3.15). The edge of cells was excluded in downstream quantitative assessments, but this issue was also largely resolved by improving point filtering. Filtering also largely removed background detections.

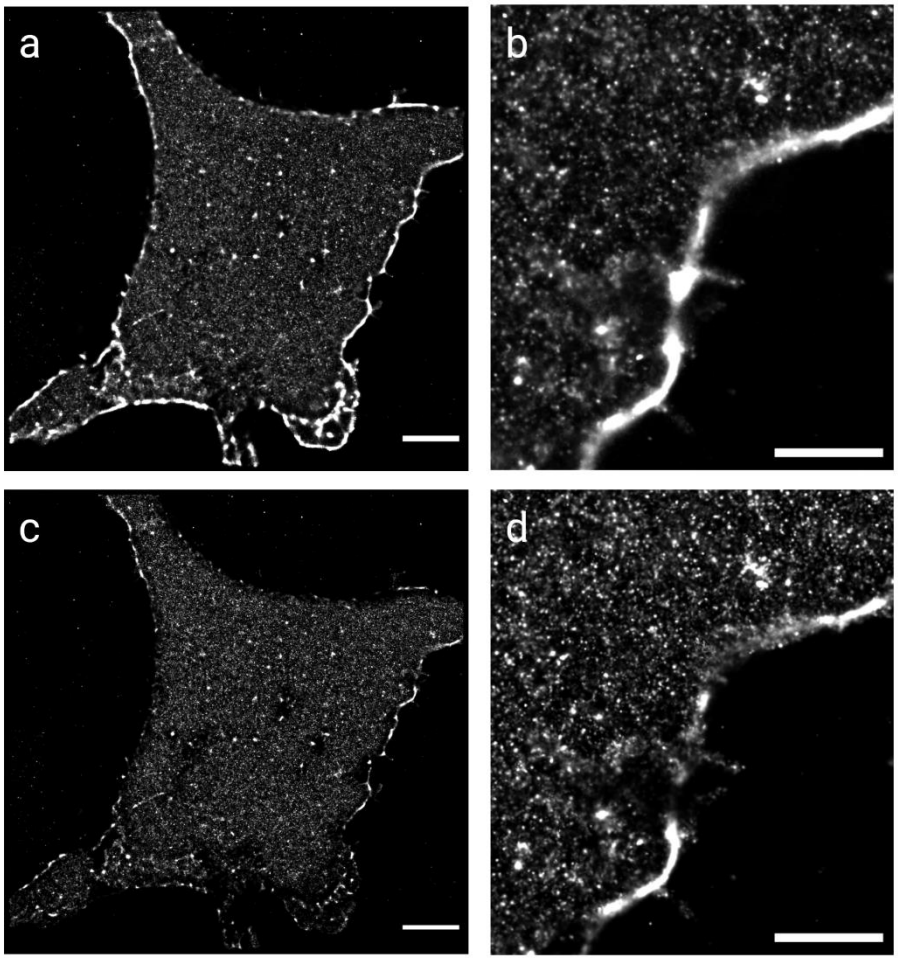

Figure 3.15 – Appropriate filtering removes some artefacts in dSTORM reconstruction. *Reconstructions of a SNAP-647 labelled $A_{2A}R$ expressing A549 cell. a) An unfiltered example, with clear edge artefacts, with a zoom shown in b). c) The same dataset represented in a) with the filters described in text above applied, reducing the appearance of these dense faux sharp regions. A zoom is shown in d). Scale bars for a and c = 10 µm, for b and c = 2 µm.*

In order to assess quality and accuracy of reconstruction, images were assessed using NanoJ-SQUIRREL, a super resolution image quality checking plugin for ImageJ [203]. The technique compares the reconstructed image, a widefield reference image, and a convolved estimate to identify artefacts in reconstruction. Resolution scaled Pearson values are comparable across images and techniques, with 1 being perfect correlation and -1 perfect anti-correlation. Assessment of control samples across all $A_{2A}R$ expressing repeats reported an average RSP value of 0.908 (Figure 3.16c). An internally consistent error map was also generated, highlighting areas of potential inconsistency. Representative examples are given in Figure 3.16. During optimisation, images with major artifacts highlighted in this error map (for example, Figure 3.16b) were discarded from downstream processing.

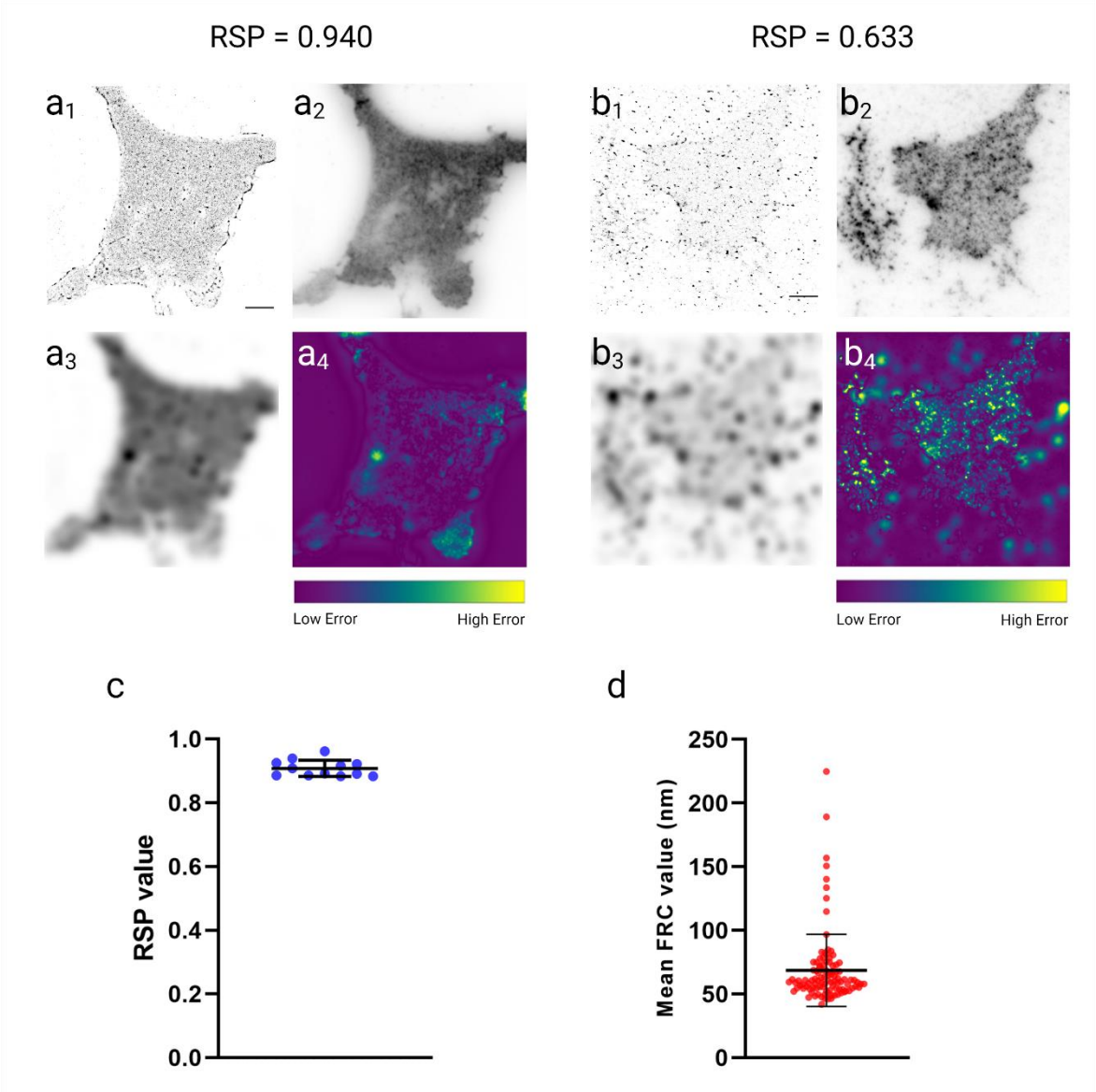

Figure 3.16 – dSTORM data quality was assessed using NanoJ SQUIRREL. *Examples of good quality (a) and poor quality (b) data with accompanying SQUIRREL workflow. In both cases, 1 shows the reconstructed data, 2 shows a TIRF image of the cell, 3 shows RSF convolved 1, and 4 shows the error map derived from comparison of 2 and 3. Resolution scaled Pearson's (RSP) values for each example are given at the top of the figure. Scale bars = 5 µm. c) shows average RSP values calculated over 12 samples. d) shows average FRC value calculated over all 105 analysed cells.*

Resolution was also calculated using the Fourier Ring Correlation (FRC) map portion of this plugin, resulting in an average value across all analysed samples of 68.65 nm ± 28.39 SD (Figure 3.16d). This FRC resolution output is comparable with previously published dSTORM data from the lab [204, 205], and accords well with estimated maximal resolution of the system when considering the localisation precision and pixel size of the system.

3.4.3 Cluster analysis

In order to quantitatively compare between drug treatments and assess the effects of actin disruption and receptor stimulation, a method of cluster analysis was required. As point localisations are the main data output of single molecule techniques, these should form the basis of most all analysis of SMLM data. By reintroducing a convolution for image-based analysis, information in the data can be lost. With this in mind, topography-based point cluster analysis method ToMATo was trialled for the data.

After initial filtering and processing of the data as in 3.4.2, 5μm^2 regions, randomly selected from within central regions of the cells' basal membrane, were cropped, taking care to avoid cell edges. As described above, edge artefacts were largely combatted by sufficient sigma filtering, but these regions were still avoided to ensure consistency.

Clustering of points was assessed using the methods incorporated into the R package RSMLM [172]. The main method tested was a persistence-based technique called ToMATo. Parameters were set by visual assessment of the cluster maps produced with a custom written MATLAB script (courtesy of Jeremy Pike) (Figure 3.17). Clusters were assessed for area, density and number of detections assigned to each cluster.

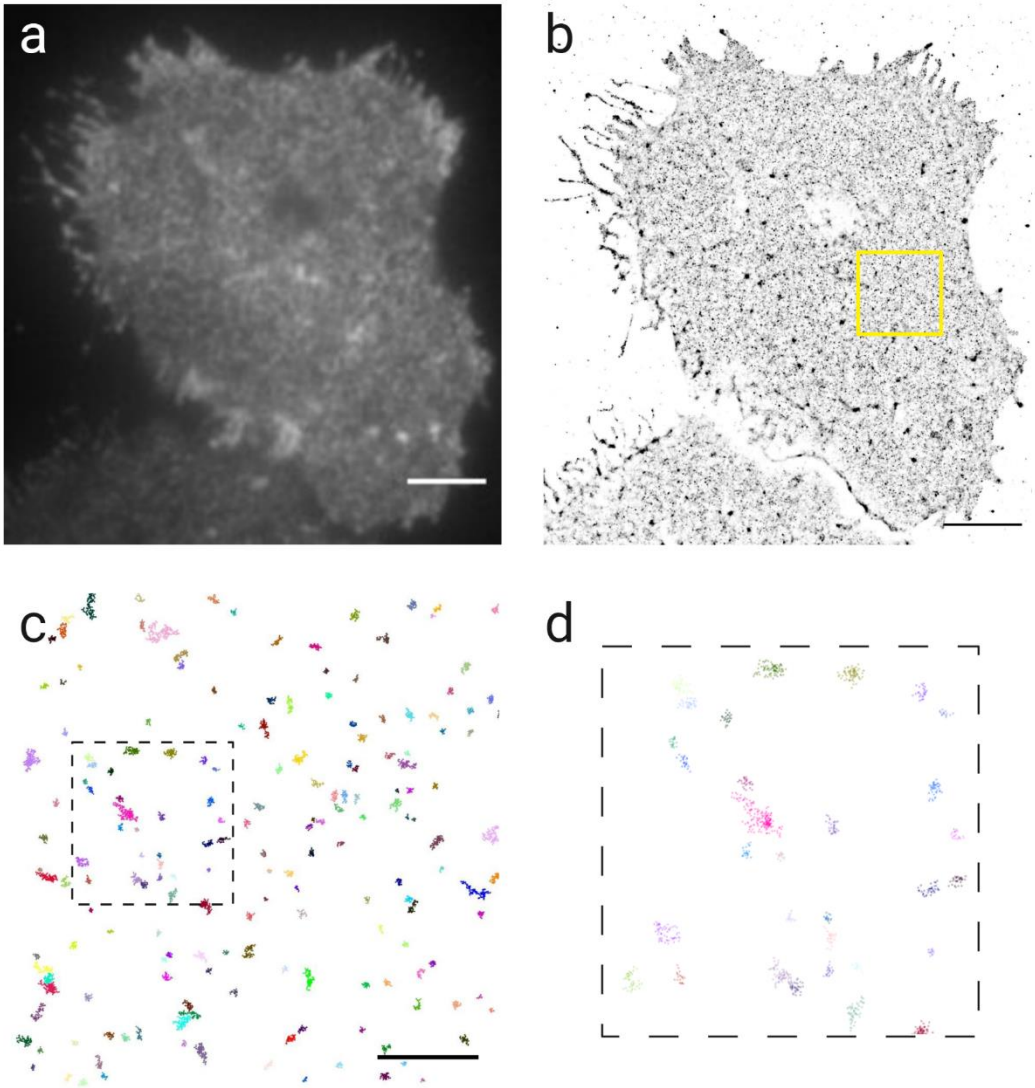

Figure 3.17 – Example of ToMATo cluster analysis output*. a) TIRF image of example cell, with b) showing the superresolved reconstruction from dSTORM imaging. c) shows identified clusters in the ROI marked in yellow in b). d) shows a magnification of the area marked with a dotted square in c), clearly showing individual points in each cluster. Scale bars a - b = 5 µm, c = 1 µm.*

3.4.4 Effect of agonists and actin disruption on A_{2A} and A_{2B} receptor distribution and clustering

Using the workflows described above, dSTORM imaging was used to investigate the response of the A_{2A} and A_{2B} receptors to the non-selective adenosine receptor agonist NECA, their behaviour when the actin cytoskeleton was disrupted by Cytochalasin D, and the effects of simultaneous stimulation and actin disruption.

Upon analysing ROIs selected from central regions on the basal cell membrane, SNAP-A_{2B}R showed no major response to either receptor stimulation or actin disruption after cluster quantification (Figure 3.18). Example ROIs for each drug treatment are shown in Figure 3.19. No significant changes in means from basal were observed across treatments and repeats for all parameters, though variations between repeats were somewhat sizeable, as demonstrated by the error bars plotted in Figure 3.18. When looking at the histogram of all clusters in each ROI, as opposed to the averages over each ROI and again for each repeat, no major shifts in behaviour are discernible. Data is given in Table 3.6.

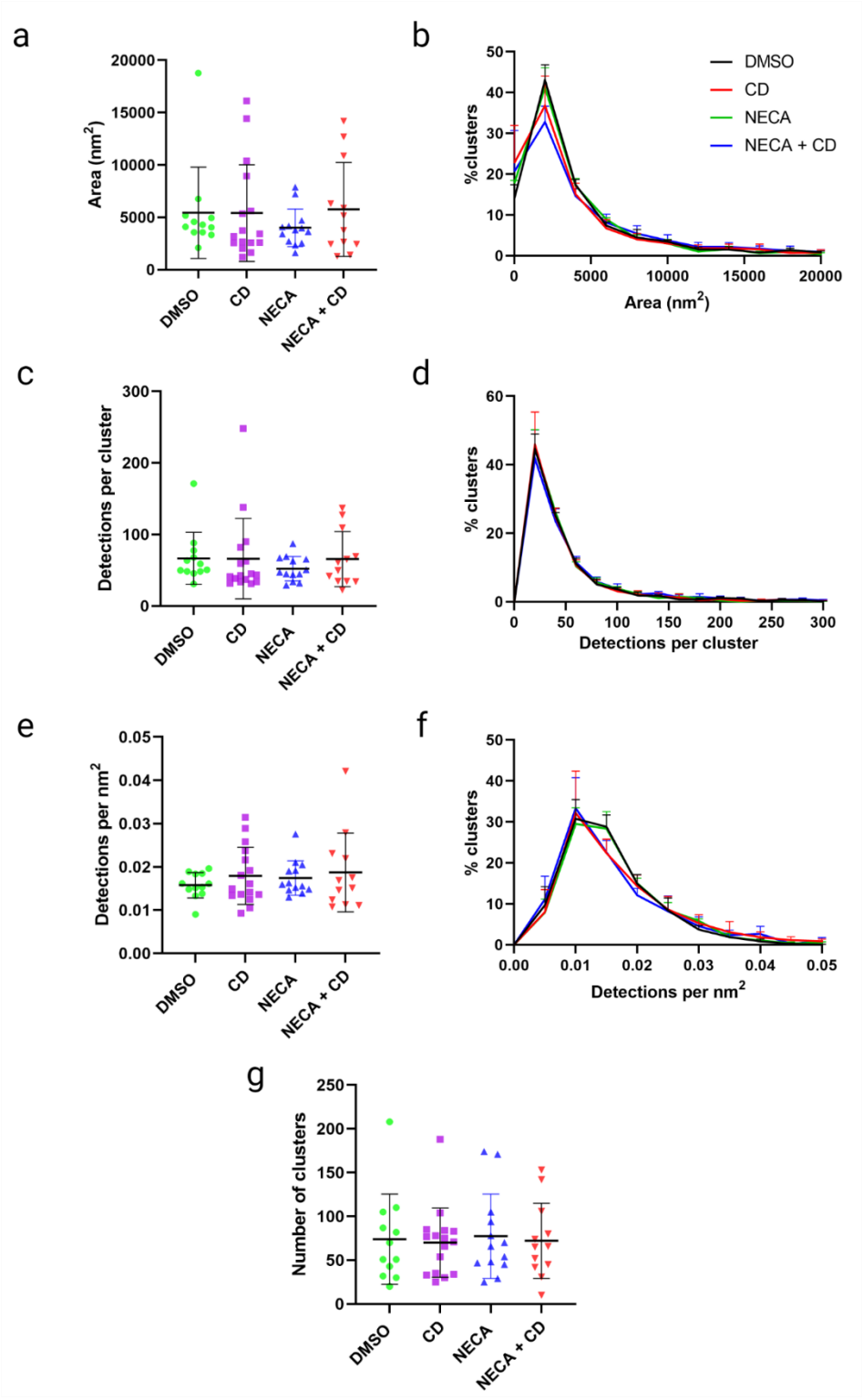

Figure 3.18 – Neither drug treatment nor actin disruption induce significant differences in $A_{2B}R$ clustering. *Transiently A2BR expressing A549 cells were imaged using dSTORM microscopy after actin disruption (1 µM CD), receptor stimulation (10 µM NECA), or both. Areas (a, b), detections in each cluster (c, d), density of detections in each cluster (e, f) and the number of clusters identified in each ROI show no significant differences. Data is represented, where appropriate, as both means for each ROI ± SD (a, c, e, g) and as histograms of all cluster data – error bars = ± SEM (b, d, f). n = 3 independent experiments. ROIs analysed per treatment: DMSO = 12, CD = 16, NECA = 13, CD + NECA = 12. All drug incubations proceeded for 30 mins at 37°C.*

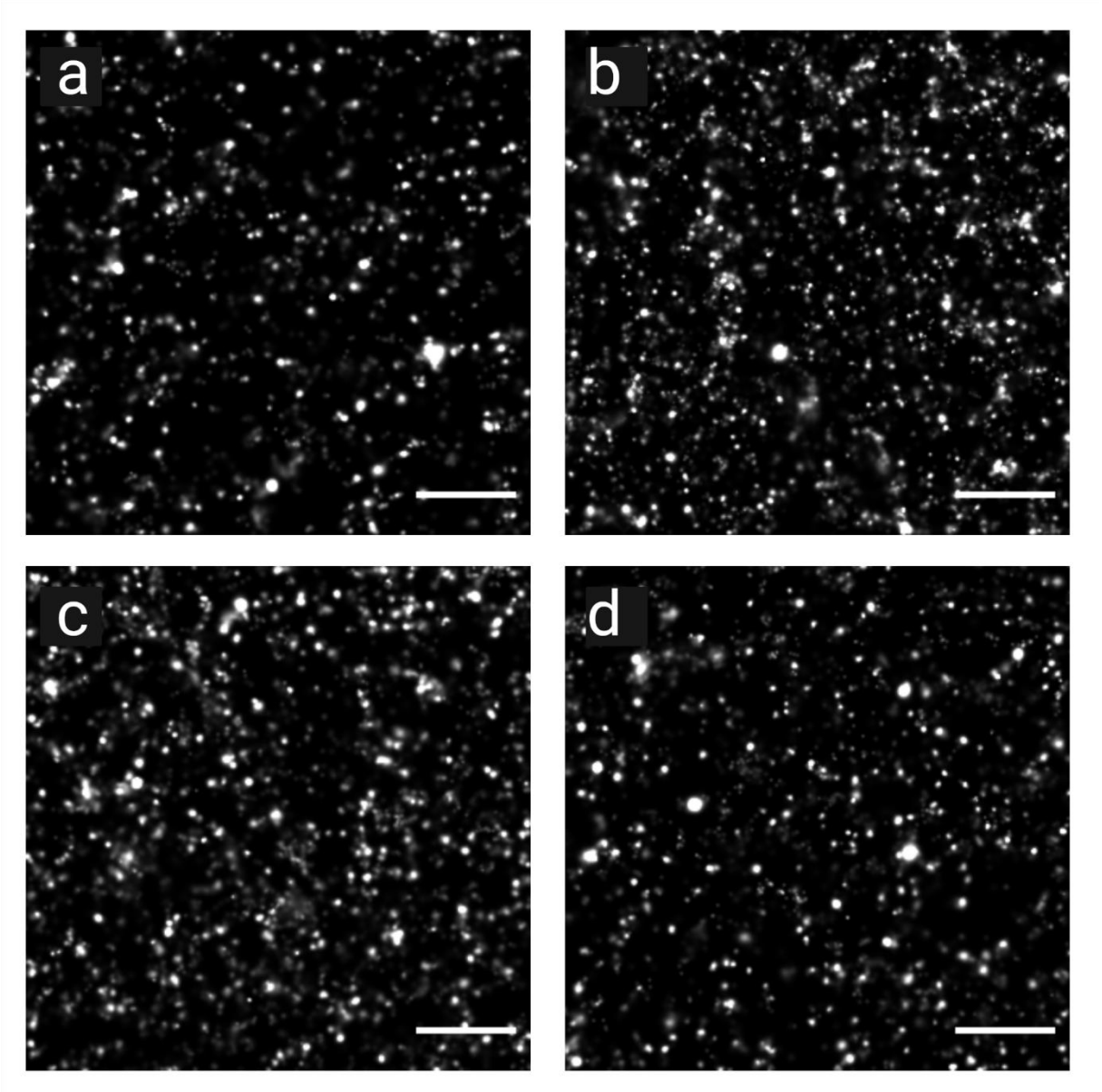

Figure 3.19 – Example regions of interest from drug treated SNAP-A_{2B}R expressing cells. *After dSTORM acquisition and postprocessing, a 5 µm^2 ROI in the central portion of the cell was selected, ensuring cell edges were excluded. These example ROIs were visualised using ThunderSTORM's Normalized Gaussian method with a lateral uncertainty of 20 nm and magnification of 5. Cells treated with either a) DMSO, b) 1 µM CD, c) 10 µM NECA, or d) 1 µM CD + 10 µM NECA. Scale bar for all images = 1 µm.*

SNAP-$A_{2A}R$, however, did show some significant changes post treatment. Example ROIs for each drug treatment are shown in Figure 3.21. $A_{2A}R$ clusters in cells treated with CD were significantly smaller than NECA treated cells. Actin disruption also showed significantly fewer detections in clusters than those in control cells, or those treated with NECA. Interestingly, treating actin disrupted cells with NECA concurrently showed an abrogation of the CD effect, with CD + NECA clusters not being significantly different to control cells. Density of clusters was largely consistent across treatments. Data is given in Table 3.5. When plotting data as histograms for SNAP- $A_{2A}R$ data, relative increases in smaller cluster area proportions are seen in both CD and CD + NECA treated samples. Major shifts, as with $A_{2B}R$ data above, are hard to discern.

Table 3.5 – $A_{2A}R$ clustering data. *Transiently transfected $A_{2A}R$ expressing A549 cells were treated with CD, NECA, AND CD + NECA for 30 minutes prior to fixation and dSTORM imaging with ToMATo cluster analysis. n = 3 independent experiments. ROIs analysed per treatment: DMSO = 13, CD = 14, NECA = 12 , CD + NECA = 13.*

Treatment	Cluster density (detections/nm^2)	Cluster area (nm^2)	Detections per cluster	Number of clusters/ 5 µm^2 ROI
A_{2A} SNAP + DMSO	0.015 ± 0.00082	6295 ± 2328	80.90 ± 26.60	39.17 ± 6.75
A_{2A} SNAP + 1 µM CD	0.016 ± 0.00090	3496 ± 760	48.12 ± 13.44	42.89 ± 13.09
A_{2A} SNAP + 10 µM NECA	0.016 ± 0.0016	5747 ± 371	84.05 ± 19.41	34.74 ± 4.52
A_{2A} SNAP + 1 µM CD + 10 µM NECA	0.015 ± 0.0013	5065 ± 493	69.10 ± 4.77	49.50 ± 9.34

Table 3.6 – $A_{2B}R$ clustering data. *Transiently transfected $A_{2B}R$ expressing A549 cells were treated with CD, NECA, AND CD + NECA for 30 minutes prior to fixation and dSTORM imaging with ToMATo cluster analysis. n = 3 independent experiments. ROIs analysed per treatment: DMSO = 12, CD = 16, NECA = 13, CD + NECA = 12.*

Treatment	Cluster density (detections/nm^2)	Cluster area (nm^2)	Detections per cluster	Number of clusters/ 5 µm^2 ROI
A_{2B} SNAP + DMSO	0.016 ± 0.0013	5044 ± 2464	62.57 ± 26.52	73.89 ± 33.67
A_{2B} SNAP + 1 µM CD	0.018 ± 0.0067	5163 ± 4347	63.28 ± 43.38	73.97 ± 26.74
A_{2B} SNAP + 10 µM NECA	0.017 ± 0.0029	4067 ± 1437	52.17 ± 8.30	73.87 ± 39.83
A_{2B} SNAP + 1 µM CD + 10 µM NECA	0.019 ± 0.0086	5393 ± 3740	62.24 ± 33.34	76.85 ± 38.33

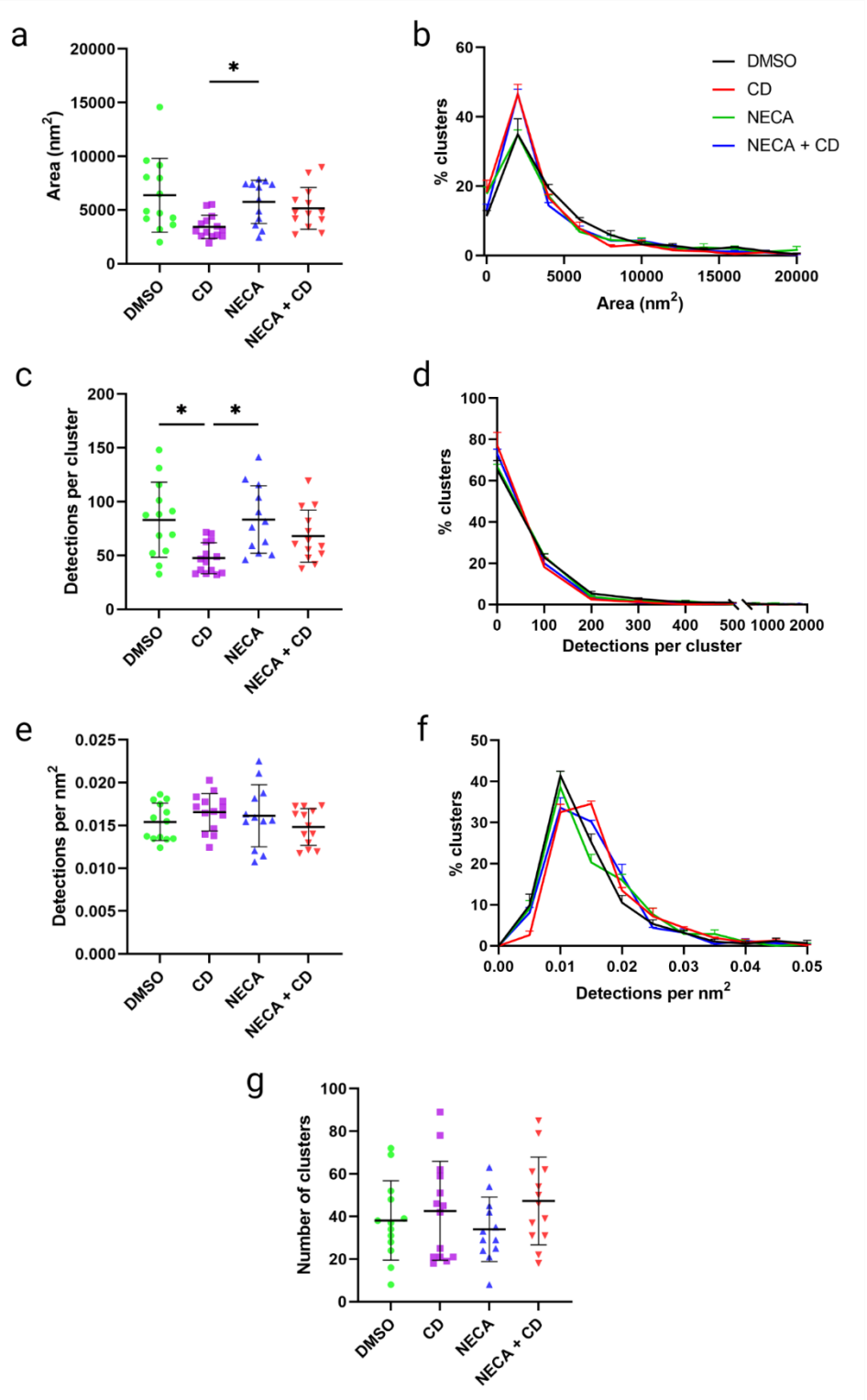

Figure 3.20 – Actin disruption significantly affects $A_{2A}R$ clusters. *Mean cluster area in 1 µM CD treated transiently $A_{2A}R$ expressing A549 cells is significantly smaller than cluster area in 10 µM NECA treated cells (a, b). Actin disruption also results in clusters with fewer detections than both DMSO and 10 µM NECA treated samples (c, d). Density of detections in each cluster (e, f) and the number of clusters identified in each ROI show no significant differences. Data are represented, where appropriate, as both means for each ROI ± SD (a, c, e, g), * = $p \leq 0.05$, and as histograms of all cluster data – error bars = ± SEM (b, d, f). n = 3 independent experiments. ROIs analysed per treatment: DMSO = 13, CD = 14, NECA = 12, CD + NECA = 13. All drug incubations proceeded for 30 mins at 37°C.*

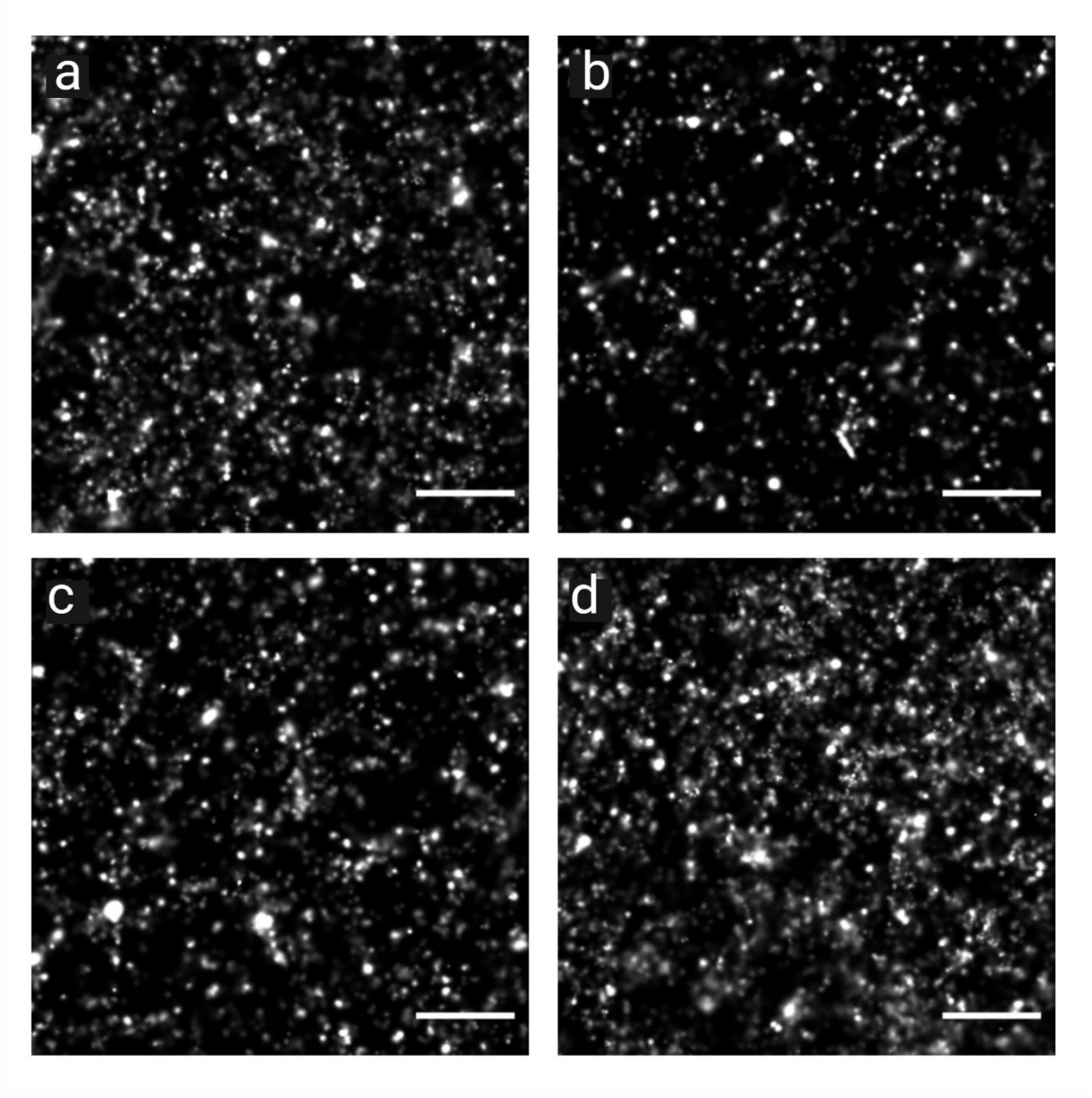

Figure 3.21 - Example regions of interest from drug treated SNAP-A_{2A}R expressing cells. *After dSTORM acquisition and postprocessing, a 5 µm^2 ROI in the central portion of the cell was selected, ensuring cell edges were excluded. These example ROIs were visualised using ThunderSTORM's Normalized Gaussian method with a lateral uncertainty of 20 nm and magnification of 5. Cells were treated with either a) DMSO, b) 1 µM CD, c) 10 µM NECA, or d) 1 µM CD + 10 µM NECA. Scale bar for all images = 1 µm.*

So, these experiments show an effect of CD treatment on $A_{2A}R$ clusters but not $A_{2B}R$, with NECA treatment acting to partially rescue from this effect. Building on this data, the next step was to investigate the dynamic behaviours of the two A_2 receptors. This was achieved by moving to live cell imaging and using the single particle tracking technique.

3.5 Single Particle Tracking

3.5.1 Receptor expression and labelling for single particle tracking

Single particle tracking (SPT) here refers to the tracking of individual fluorescently SNAP labelled receptors in the basal plasma membrane over time. Metrics extracted from these tracks can then be used to quantify diffusion behaviours. Receptor expression was reoptimized for SPT to limit receptor density and permit accurate point localisation. It was determined that labelling cells 4 hours post transfection resulted in sufficient expression in a significant proportion of transfected cells to resolve single receptors (Figure 3.22).

SNAP-Surface 549 was chosen as the label for these experiments given relative stability and good SNR at short illumination times. Wash steps as described in methods section 2.7.4 were also applied to minimise non-specific labelling. Insufficient washes resulted in apparent trapping of excess SNAP ligand between the

cell basal membrane and the coverslip, which can display Brownian motion (Figure 3.22e).

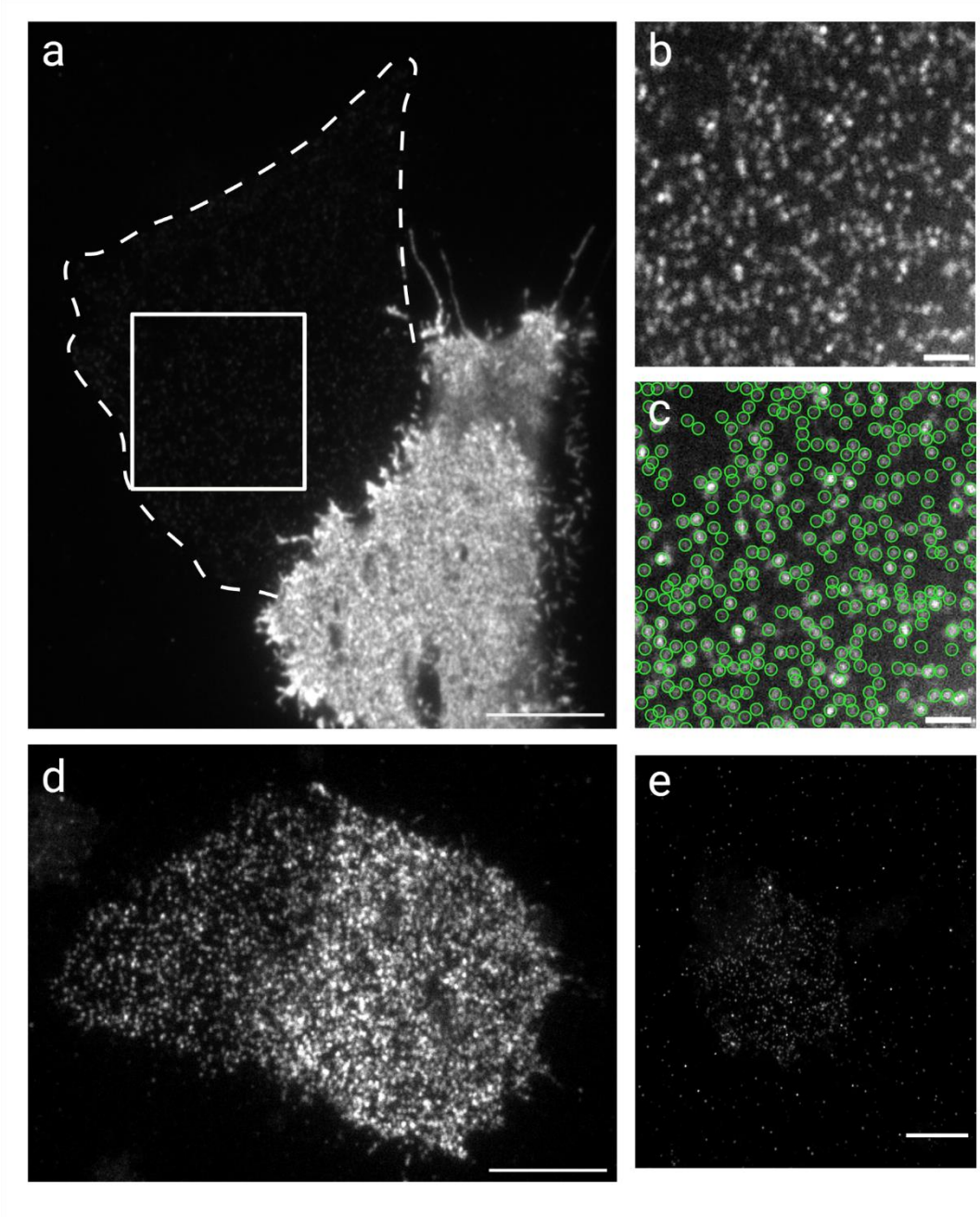

Figure 3.22 – Expression levels 4 hours post transfection. *a) TIRF image of two SNAP-549 labelled A2A expressing cells, showing one cell (outlined) at an appropriate expression level for SPT analysis. The boxed area is shown enlarged and at higher contrast in b), with c) showing point identification in this frame. d) shows a further example of the variable expression levels seen in each sample. e) Example of insufficient wash steps, resulting in retention of unbound SNAP label under an untransfected cell. Scale bars: a, d & e = 10 µm. b & c = 2 µm.*

3.5.2 Track generation

Analysis requires detected single points to be linked in both time and space between frames. The MATLAB software U-Track [180] was chosen for this purpose. The software performs spot detection and frame by frame linking in dense particle fields, with capacity to bridge gaps in tracks subject to parameter setting. General parameters were set relative to our imaging system specifications (see methods section 2.8.5) and gap closing especially was visually assessed for accuracy of performance. Suboptimal settings showed either short, disjointed tracks, or erroneous connections between unrelated points (Figure 3.23).

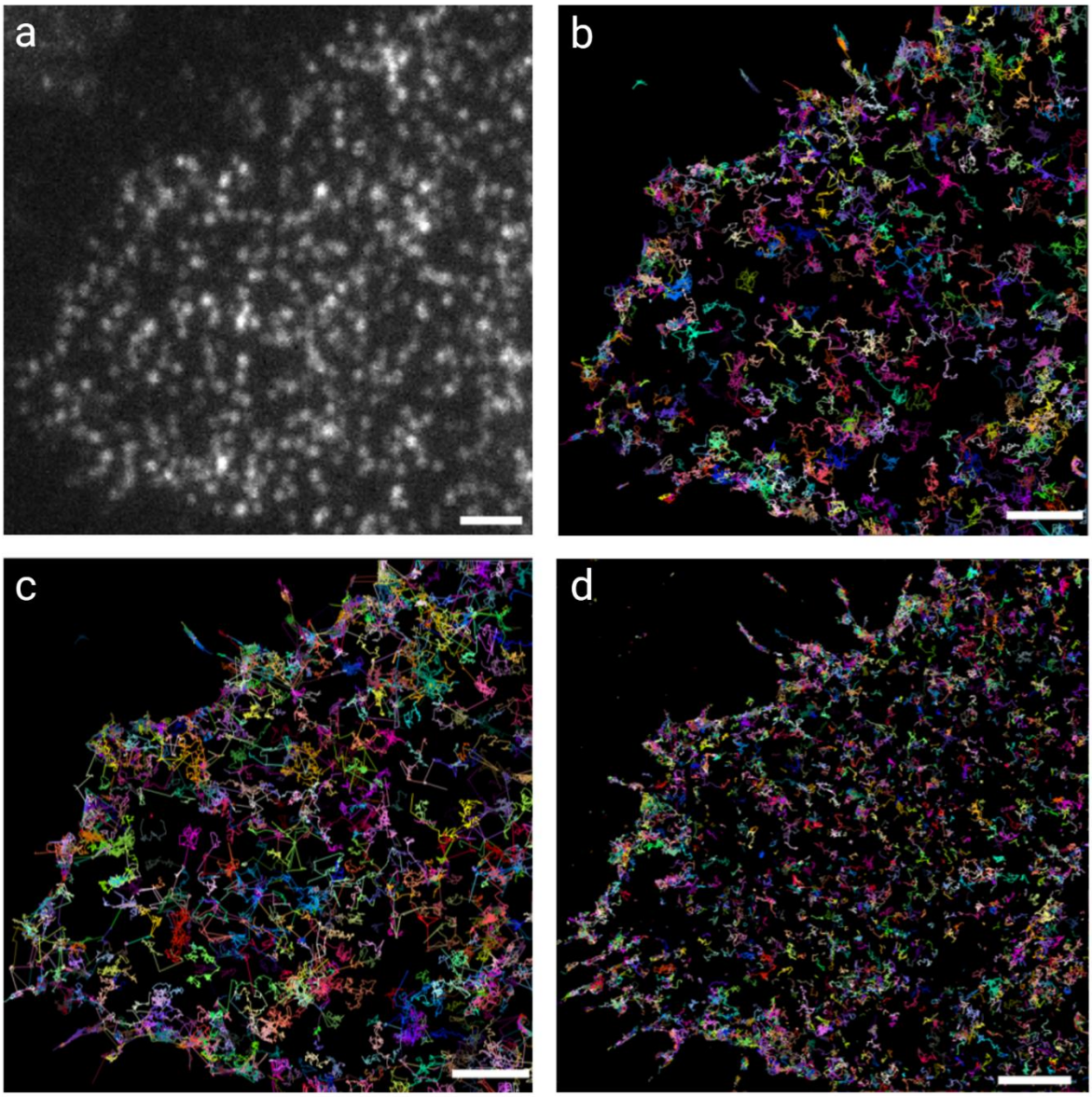

***Figure 3.23 – Frame to frame linkage requires careful optimisation**. a) Representative frame from a 30 s 1000 frame video of SNAP-549 labelled $A_{2A}R$ expressing A549 cell. b) Tracks resulting from LAP tracking with 0.5 µm frame to frame linkage, 0.2 µm over 2 frames for gap closing. c) Tracks resulting from 1 µm frame to frame linkage, 0.2 µm over 2 frames for gap closing. Large inappropriate jumps are seen. d) Tracks resulting from 0.1 µm frame to frame linkage, 0.2 µm over 2 frames for gap closing. Tracks are very short and discontinuous. Scale bars = 2 µm.*

3.5.3 Identifying changes in track motion

Numerous analytical techniques are available for trajectory data, again with many software solutions, as covered in section 1.10.2. A common issue in many approaches is the ensemble nature of data, where diffusion coefficients or particle displacement is calculated over a full track. Especially at longer time frames, particles can undergo multiple behavioural switches, passing between categories of motion. Averaging calculations over a full track can mask these transient changes.

In this work, an approach which accounts for these subtrack behaviours was applied. DC-MSS, or 'divide-and-conquer moment scaling spectrum', is a mobility analysis framework capable of identifying motion changes within tracks as well as reporting switches between these [184]. As described in the publication, tracks undergo initial segmentation which is then refined in the context of MSS classifications. Motion is categorised as either immobile, confined, free, or directed (Figure 3.25a), with switches between these states also recorded. Multiple papers have been published using this method of analysis (for example, [206-208]).

3.5.4 Response to agonists and actin disruption

Cells expressing $A_{2A}R$ or $A_{2B}R$ were labelled as described and treated for 15 minutes at 37^{o}C with one of four conditions during the final post label wash step - DMSO vehicle control, 10 µM NECA, 1 µM CD, or 10 µM NECA + 1 µM CD. Samples were

all imaged within 15 minutes of application of the drug treatment to minimise variability in incubation times. After U-Track trajectory generation and using DC-MSS analysis, several parameters were assessed for each treatment. The numbers of tracks analysed for each treatment and receptor are shown in Table 3.7.

Table 3.7 – Number of tracks analysed per treatment condition. *Tracks were accumulated over 3 independent repeats. For SNAP-A_{2A}R expressing cells*: *DMSO: n = 25 cells, CD: n = 27, NECA: n = 29, CD NECA: n = 28, collected over 3 independent experiments. For SNAP-A_{2B}R expressing cells, DMSO: n = 19 cells, CD: n = 18, NECA: n = 20, CD NECA: n = 16, collected over 3 independent experiments.*

Receptor	**DMSO**	**1 µM CD**	**10 µM NECA**	**1 µM CD + 10 µM NECA**	**Total**
SNAP-A_{2A}R	28661	29575	35776	25727	119739
SNAP-A_{2B}R	22061	19056	20810	17383	79310

3.5.4.1 Diffusion coefficients of subclasses are mostly unaffected by drug treatment

DC-MSS analysis allowed categorisation of each subtrack segment (Figure 3.25a). Mean squared displacement (MSD) values could then be calculated for each category, allowing estimations of diffusion coefficient for each motion type (Figure 3.24a,b). Mean diffusion coefficients are slowest in immobile subtracks – given the non-zero localisation precision – and fastest in directed motion. Directed motion is, however, significantly slower in CD + NECA treated A_{2B}R expressing cells than in the DMSO treated control. All means are reported in Table 3.8 & Table 3.9. When plotting all diffusion coefficients calculated across treatments and repeats as a histogram (Figure 3.24c,d), the lack of major shifts is more readily apparent.

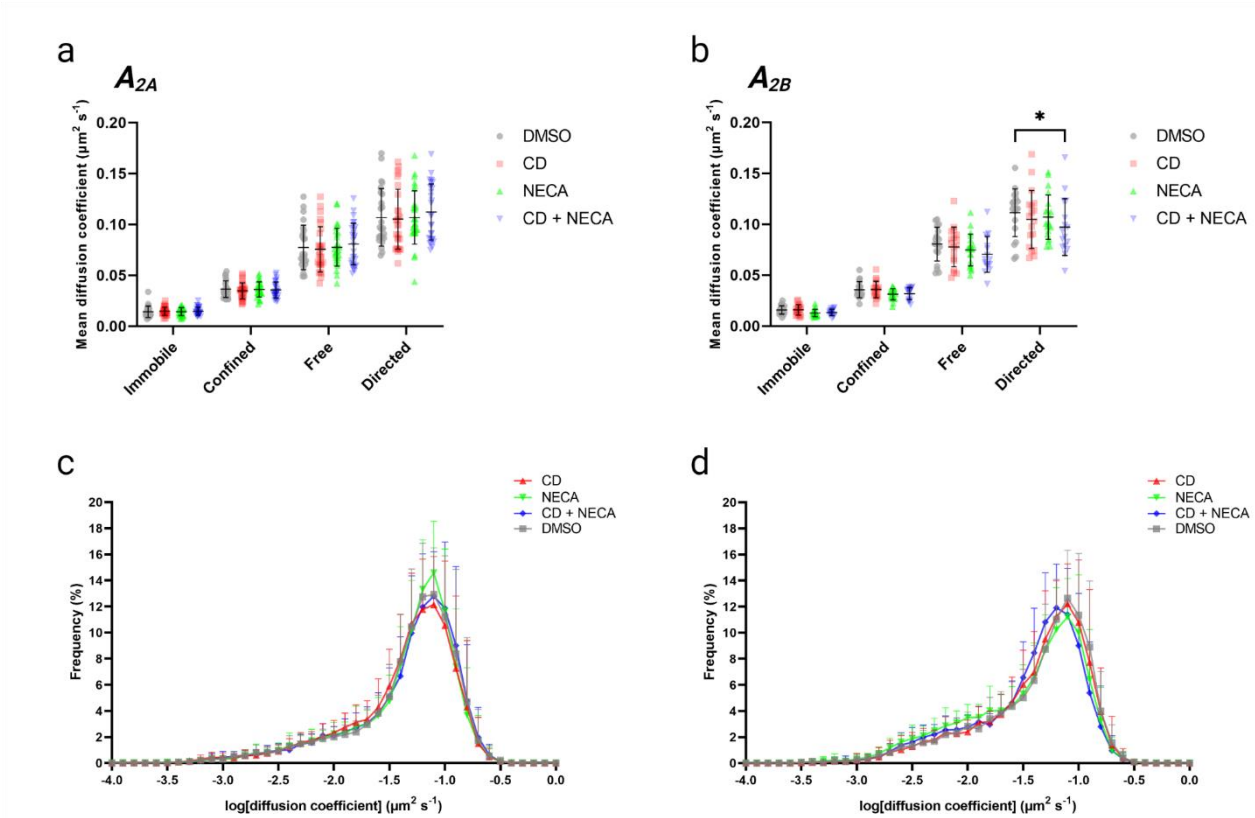

Figure 3.24 – Diffusion coefficients are not significantly affected by treatment. *A549 cells were transiently transfected with either $A_{2A}R$ or $A_{2B}R$ and SNAP-labelled receptors imaged over time. a) $A_{2A}R$ and b) $A_{2B}R$ mean diffusion coefficients for each motion type. Mean ± standard deviation. * = p ≤ 0.05. c) Histograms of $A_{2A}R$ and d) $A_{2B}R$ diffusion coefficients on a log scale. Mean + standard deviation.*

***Table 3.8 – $A_{2A}R$ diffusion coefficients**. Mean diffusion coefficients ($\mu m^2 s^{-1}$) for each condition for transiently $A_{2A}R$ expressing A549 cells, ± standard deviation. For DMSO: n = 25 cells, CD: n = 27, NECA: n = 29, CD NECA: n = 28, collected over 3 independent experiments.*

	DMSO	**1 µM CD**	**10 µM NECA**	**1 µM CD + 10 µM NECA**
Immobile	0.0142 ± 0.0055	0.0147 ± 0.0041	0.0143 ± 0.0039	0.0147 ± 0.0039
Confined	0.0364 ± 0.0081	0.0347 ± 0.0079	0.0361 ± 0.0075	0.0356 ± 0.0078
Free	0.0773 ± 0.0219	0.0755 ± 0.0223	0.0775 ± 0.0187	0.0808 ± 0.0205
Directed	0.1070 ± 0.0283	0.1052 ± 0.0295	0.1069 ± 0.0262	0.1123 ± 0.0275

***Table 3.9 – $A_{2B}R$ diffusion coefficients**. Mean diffusion coefficients ($\mu m^2 s^{-1}$) for each condition for transiently $A_{2B}R$ expressing A549 cells, ± standard deviation. For DMSO: n = 19 cells, CD: n = 18, NECA: n = 20, CD NECA: n = 16, collected over 3 independent experiments.*

	DMSO	**1 µM CD**	**10 µM NECA**	**1 µM CD + 10 µM NECA**
Immobile	0.0158 ± 0.0041	0.0160 ± 0.0051	0.0128 ± 0.0036	0.0133 ± 0.0031
Confined	0.0356 ± 0.0079	0.0359 ± 0.0081	0.0312 ± 0.0054	0.0318 ± 0.0059
Free	0.0805 ± 0.0166	0.0778 ± 0.0194	0.0748 ± 0.0157	0.0705 ± 0.0177
Directed	0.1114 ± 0.0234	0.1048 ± 0.0284	0.1071 ± 0.0218	0.0972 ± 0.0280

3.5.4.2 Treatments affect relative time spent in each behaviour state

Subtrack data was then used to calculate relative time spent in each motion state for each drug treatment. A_{2A} receptors showed a significant increase in the time spent moving freely when treated with NECA compared to CD and CD + NECA treated samples, but not the DMSO control (Figure 3.25b). An accompanying drop in time spent in confined motion is seen for NECA treatment, but in this case only when compared to CD treated cells, indicating perhaps more contribution of immobile receptors in the CD + NECA treatment.

Time spent in free motion is also significantly different for NECA treated samples in $A_{2B}R$ expressing cells, showing a significant drop when compared with control and CD only treatment. No significant differences are apparent in other motion categories, suggesting a balanced increase in time spent both confined and immobile to compensate.

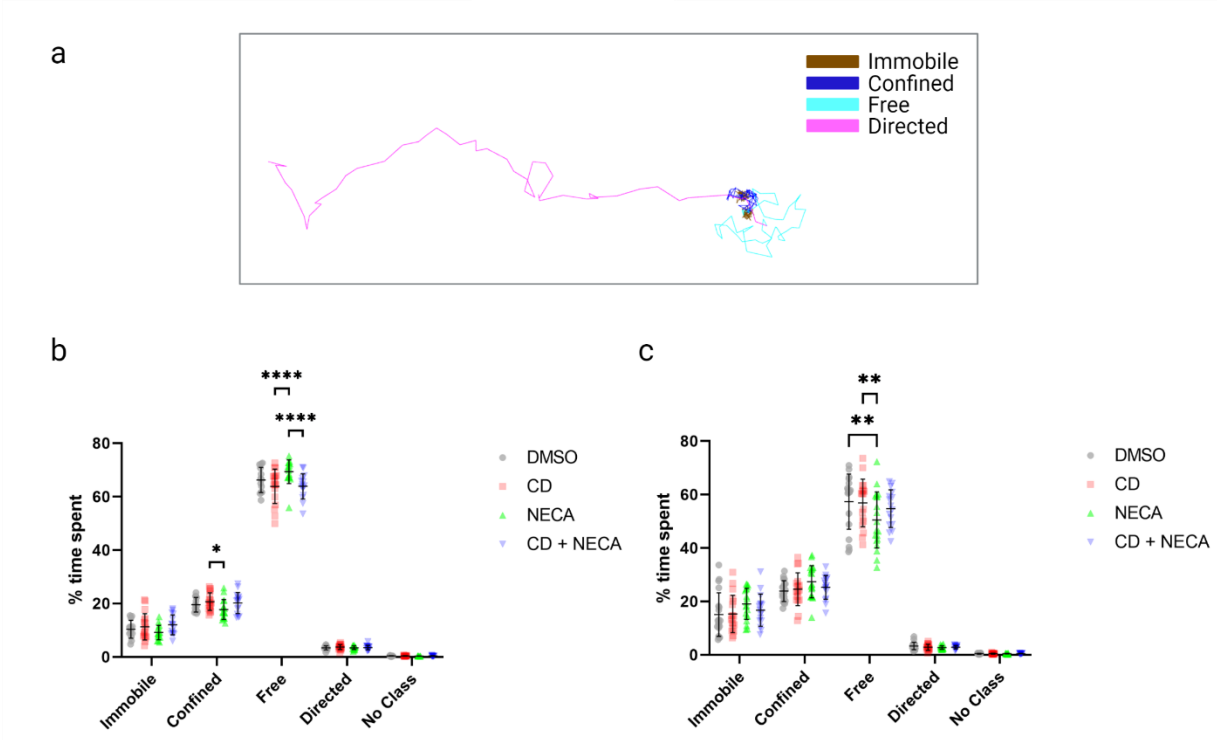

Figure 3.25 – Drug treatment affects time spent in each motion state. *a) Example track to demonstrate each motion type. b) Percent of all track time spent in each motion state for $A_{2A}R$ transiently expressing cells. c) Percent of all track time spent in each motion state for $A_{2B}R$ transiently expressing cells. Mean ± standard deviation. * = p ≤ 0.05, ** = p ≤ 0.01, **** = p ≤ 0.0001.*

3.5.4.3 NECA treatment reduces confinement radii of A_{2B} receptors

For subtracks undergoing sub-diffusive movement, the confinement radius from the area explorable by the receptor during the subtrack were calculated for the immobile and confined subtracks (means presented in Table 3.10 & Table 3.11, means for each cell analysed plotted in Figure 3.26). These radii could represent the size of constraining membrane regions. $A_{2A}R$ expressing cells showed largely consistent immobilisation and confinement areas between treatments, but $A_{2B}R$ expressing cells showed more pronounced confinement when treated with NECA alone compared with DMSO control and CD only treatments. CD + NECA in combination did not replicate this significant decrease.

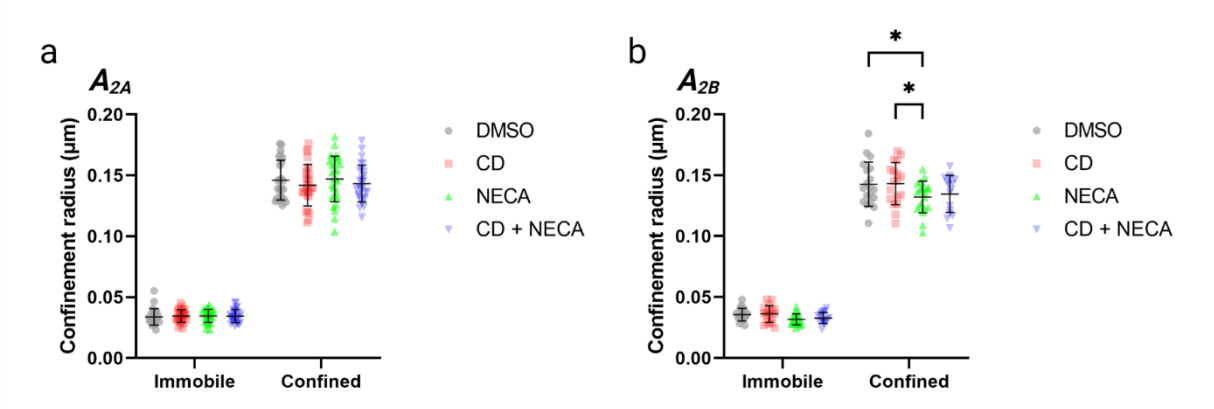

Figure 3.26 – NECA treatment significantly reduces confinement radius of A_{2B} receptors. *a) $A_{2A}R$ and b) $A_{2B}R$ confinement radii. Mean ± standard deviation. * = p ≤ 0.05.*

Table 3.10 – Confinement radii for $A_{2A}R$ expressing cells. *Radii given in µm, ± standard deviation.*

	DMSO	**1 µM CD**	**10 µM NECA**	**1 µM CD + 10 µM NECA**
Immobile	0.034 ± 0.007	0.035 ± 0.005	0.035 ± 0.005	0.034 ± 0.005
Confined	0.146 ± 0.016	0.142 ± 0.017	0.147 ± 0.019	0.143 ± 0.015

Table 3.11 – Confinement radii for $A_{2B}R$ expressing cells. *Radii given in µm, ± standard deviation.*

	DMSO	**1 µM CD**	**10 µM NECA**	**1 µM CD + 10 µM NECA**
Immobile	0.036 ± 0.005	0.036 ± 0.007	0.032 ± 0.004	0.033 ± 0.005
Confined	0.143 ± 0.018	0.143 ± 0.017	0.132 ± 0.013	0.135 ± 0.015

3.5.4.4 Switching behaviour is significantly affected by treatment

DC-MSS analysis also permits recording of switches between motion states. For $A_{2A}R$ and $A_{2B}R$ the number of switches per track (calculated by dividing total switches by total tracks – not segments – for each cell) remained consistent between treatments (Figure 3.27a, Figure 3.28a). Switches between immobile and free states – in either direction – are the least prevalent for both receptors, with confined/free switches being the most common across treatments for $A_{2A}R$ (Figure 3.27c,d). A_{2B} receptors, however, show a similar amount of immobile/confined switches as confined/free (Figure 3.28c,d).

For $A_{2A}R$ expressing cells, when comparing the mean switches per track (Figure 3.27c), CD treatment causes a significant reduction in the number of free-to-confined switches, but no other significant changes are apparent. When comparing relative to the proportion of switches (Figure 3.27d), both CD and CD + NECA treatment show an increase in immobile-to-confined switches.

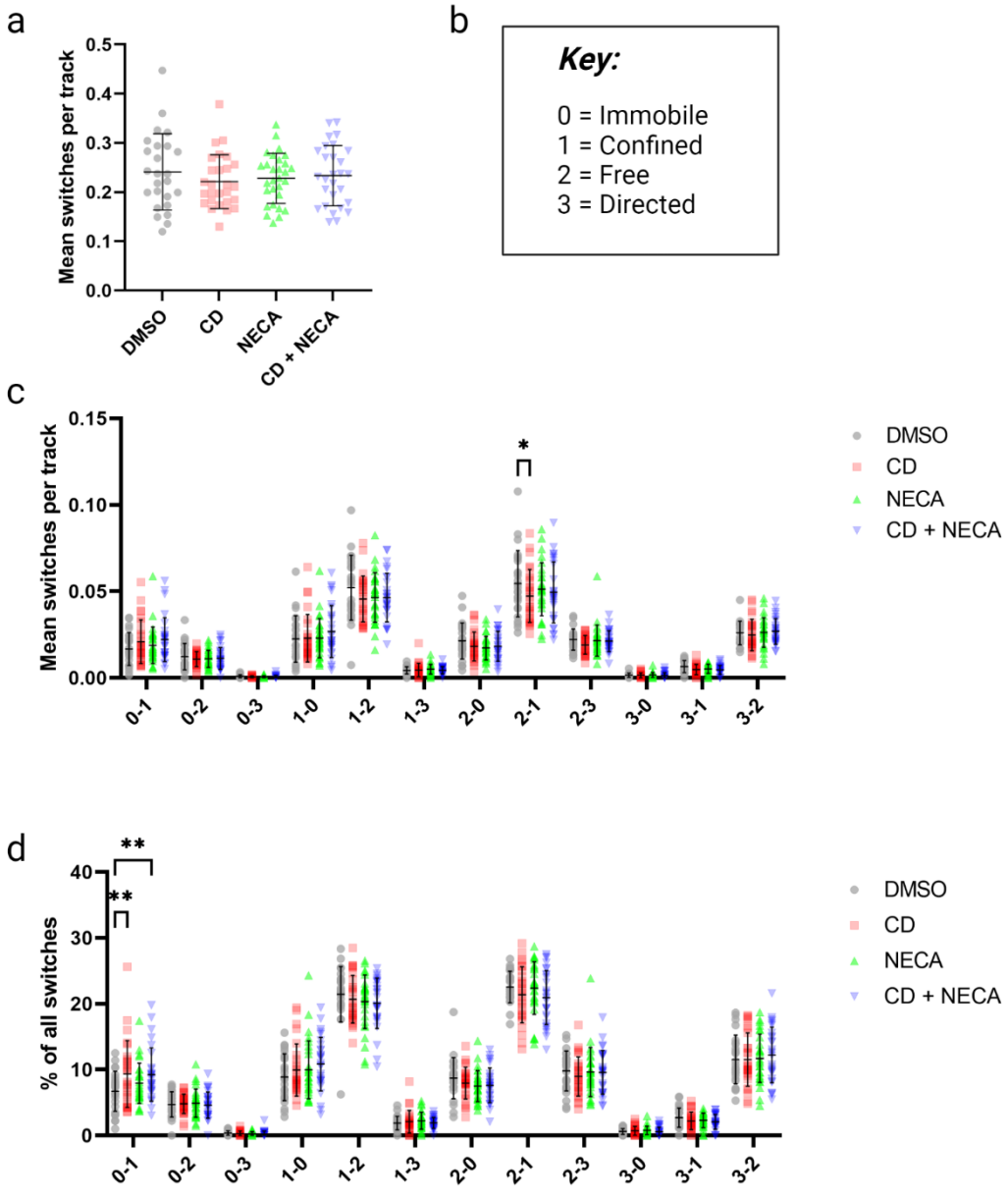

Figure 3.27 – Switching behaviour for A_{2A} receptors*. a) Mean total switches per track for all treatments. b) Key for c) mean switches per track and d) percent of all switches. Mean ± standard deviation. * = p ≤ 0.05, ** = p ≤ 0.01.*

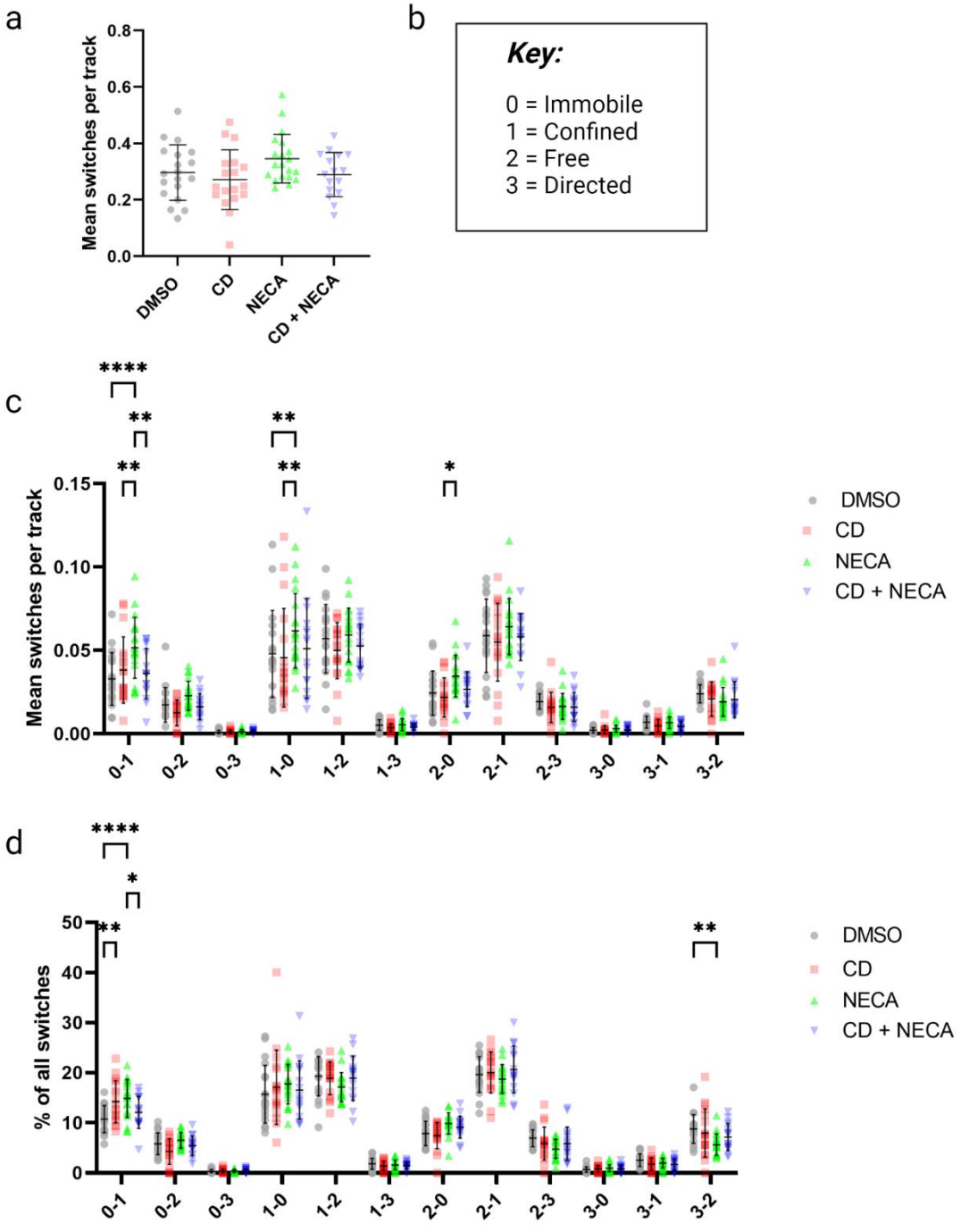

***Figure 3.28 - Switching behaviour for A_{2B} receptors**. a) Mean total switches per track for all treatments. b) Key for c) mean switches per track and d) percent of all switches. Mean ± standard deviation. * = p ≤ 0.05, ** = p ≤ 0.01.*

For $A_{2B}R$ expressing cells, treatment results in more significant changes to switching behaviour. Represented as mean switches per track (Figure 3.28c), NECA treatment greatly increased immobile-confined switching in both directions over DMSO and CD treated samples. Switches from free to immobile are also significantly greater than in CD treated samples, but the inverse is not true. As a proportion of all switches (Figure 3.28d), both CD and NECA treated cells show increased immobile to confined switching when compared to DMSO only. There is no accompanying significant difference for confined to immobile switches. NECA treated cells also showed a smaller proportion of directed to free switches.

3.6 Discussion

This chapter aimed to investigate the signalling response to actin disruption, and how this relates to the clustering and dynamic behaviours of the A_2 receptors.

3.6.1 Receptor labelling for fluorescence microscopy

Throughout this thesis, N-terminally SNAP-tagged A_2 receptors were used to permit fluorescent labelling of both live and fixed receptors. N-terminal tagging was preferable for these experiments, as it had previously been reported with N-Luc tagging that this did not affect the pharmacology of the receptor [209]. The C-terminal, however, is the region of the receptor which interacts with G-proteins and other relevant regulators, such as α-actinin-1. Attachment of a tag on this terminus, then, may have resulted in reduced signalling capacity. An additional benefit of an N-terminal tag is the ability to use SNAP-Surface ligands, which are cell impermeable. This greatly reduced the potential background as internal receptors – barring those which had been present on the membrane and internalised – were not labelled.

The tag itself should also be considered. A comparative study of SNAP and HALO constructs by Erdmann et al. [210] showed that for internal labelling – and especially in STED with far red labels – HALO labelling was ~ 4x brighter. Quantification of performance of the two tags for surface labelling would be of interest before implementing any kind of dual receptor expression, or before generation of a stable

line for imaging. In chapter 6, the generation of a HALO-tagged $A_{2A}R$ construct and how this may aid understanding is explored in more detail.

Fluorescent ligands hold potential for future investigations. Used here to investigate the potential for endogenous $A_{2A}R$ expression, fluorescent ligands could also be used to great effect in endogenously expressing cells for single particle tracking experiments looking at dynamic behaviour coupled with an antagonist – or agonist - at an untagged, endogenous level. An $A_{2B}R$ fluorescent antagonist has also been reported [211], as have ligands for the rest of the adenosine receptor family (as reviewed in [99]).

3.6.2 Pharmacology of adenosine receptors

Linking signalling behaviour to effects on receptor organisation and dynamics is necessary to argue for a functional link between actin-based membrane organisation and the A_2 receptors.

3.6.2.1 Technique considerations

Two different techniques (CRE-SPAP and TR-FRET) were used here measure to cAMP levels, the second messenger in G_s coupled A_2 receptor signalling. The CRE-SPAP assay requires a lengthy incubation (5 hours, as the system is based on gene transcription) while cells in the TR-FRET set up are lysed after only a 30-minute incubation, giving data on both long- and short-term responses. It must be

considered that cAMP is not solely linked to adenosine receptor responses, and CD will also affect the actin cytoskeleton in a more general way. To mitigate this as best possible, CD concentrations were kept low enough to trigger visible structural alterations but not so high as to induce major morphological change. Regardless, any other membrane proteins that are organised by CD will also be affected by this treatment and could impact cAMP levels. This could explain the increase in basal response seen with CD addition in the A549 experiments above, but DMSO - added at the maximal concentration that would be apparent in the drug dilutions - also showed an increase over the lowest concentrations of NECA. DMSO may therefore be the issue here, and repeats with increasing DMSO volumes in both the CRE-SPAP CHO cell model and transfected A549 cells would be necessary to fully elucidate this.

3.6.2.2 A_2 receptor signalling and links to actin

In both of these assays, the $A_{2B}R$ response was unreliable. Generation of a stable line would be a priority for future experiments, as the relative insensitivity of $A_{2B}R$ to NECA (when compared to the rest of the family, e.g. [212]) coupled with variable expression from transient transfection may be the cause of the issues seen here. It should be considered that $A_{2B}R$ is also capable of signalling via mechanisms other than cAMP, having been shown to function via both ERK and calcium modulation in a cell line specific manner [73]. It has not been shown in the literature which pathways $A_{2B}R$ signals via in A549 cells, so it could be that responses are occurring via other pathways.

$A_{2A}R$ responses to actin disruption, however, support previous findings in the literature. There is evidence for the existence of GPCR signalling ‘hotspots’, or nanodomains within the membrane where G-proteins, adenylyl cyclases, and GPCRs are enriched [213]. These regions are at least in part regulated by the actin cytoskeleton [163].

One argument for the increase in cAMP production could be that removing actin allows more free motion of the receptor, and therefore enhances the likelihood of interaction with key regulators or other receptors. In their paper investigating the serotonin 1A receptor and its response to actin disruption, Ganguly et al. [190] showed that actin disruption led to increased receptor mobility, in turn correlating directly with improved signalling efficiency. They argue that this mobility increases the ‘sampling space’ of the receptor, making interaction with the relatively static G proteins more likely.

Combining the idea of signalling ‘hotspots’ and an increase in free motion would certainly argue for the co-existence of multiple modes of membrane organisation, as the other components of the signalling cascade would have to remain at least somewhat restricted under actin disrupting conditions to maintain the heterologous arrangement.

So, these findings provide some evidence for a role for actin in A_{2A} receptor function, giving a basis on which to investigate potential changes in organisation and dynamics that may correlate with this data.

3.6.3 dSTORM assessment of receptor clustering

With pharmacological data indicating that – at least for $A_{2A}R$ – there is a functional link between actin disruption and receptor function, the next steps were to visualise the receptor under such conditions.

When interpreting clustering responses, behaviour must be considered in the context of the receptor overexpression that was necessary to perform these experiments. Expression levels were inherently variable across the cell population, which could affect how cells respond to stimuli. This was accounted for partially by selection of cells showing similar receptor densities or intensities. Overexpression can mask genuine organisational changes – for example, Khan et al. [214] showed that ligand induced clustering of the GPCR CXCR4 was only identifiable in endogenously tagged CRISPR lines, as opposed to transient overexpressors. It could also give evidence for a supra-physiological response. An example of this was demonstrated in work by Hinz et al. [215], who demonstrated that BAY60-6583, a partial agonist specific for $A_{2B}R$, had limited effect on cAMP levels or calcium mobilisation in HEK293 cells that expressed only endogenous levels of $A_{2B}R$. Stably transfected overexpressors, however, displayed a more significant response to BAY60-6583 treatment. In addition, regulatory systems have been proposed for $A_{2B}R$ surface

expression via $A_{2A}R$ heterodimerisation [86]. Dysregulation through overexpression could therefore impact the amount and speed of receptors reaching the membrane, and therefore downstream behaviour.

The $A_{2B}R$ results showed no clustering changes. Even taking the above into account, there is currently no direct evidence that $A_{2B}R$ does cluster, when bound by its ligand or otherwise. It is perfectly possible that no regulated clustering response exists for this receptor in this cell type, with the observed clusters being as a result of random distribution, but robust positive controls would be necessary in order to demonstrate this satisfactorily.

The A_{2A} receptor also did not show significant changes to clusters when treated with NECA alone, but had significantly smaller clusters after actin disruption. This effect was only seen in the absence of NECA, which would suggest that actin may play a role in basal organisation of the receptor, rather than regulating response to stimulation.

Taken together, this data indicates differential regulation of $A_{2B}R$ and $A_{2A}R$. When taken with the idea that actin regulates basal rather than stimulated $A_{2A}R$ clustering, this would also suggest that basal $A_{2B}R$ organisation may be independent of actin. A potential explanation could lie in the difference in C-terminal tails. The long, disordered $A_{2A}R$ C-terminal tail could increase the likelihood of steric interaction with the cortical actin, while the comparatively short tail of the A_{2B} receptor has a reduced

likelihood of hitting the mesh. There is also evidence that the binding of α-actinin-1 to the $A_{2A}R$ C-terminal can be displaced by calmodulin binding, in a Ca^{2+} dependent fashion [67]. This may also contribute to differences in the way $A_{2A}R$ and $A_{2B}R$ are organised by actin.

As covered in detail in section 1.10.1, dSTORM alone is not a quantitative technique. Reblinking of fluorophores can lead to significant overcounting, while the potential for non-stoichiometric labelling of the SNAP-tagged sample and the presence of endogenous untagged receptor can result in under-estimates. Work from the Herten lab indicates only about a 70% labelling efficiency with a SNAP-labelling system (personal correspondence). Taking this into account, in these kinds of experiments where only semi-quantitation is possible, it is important to frame results as only internally relative – that is, comparing treatments to the internal control – to avoid over interpretation.

3.6.4 SPT analysis of receptor dynamics

SPT experiments made it possible to assess the potential effects of actin disruption on receptor dynamics. Cells were chosen at appropriate minimal expression levels, allowing accurate single particle identification. Label titration would be a second option for controlling point density in the image, but this would result in more 'invisible' – unlabelled – yet functional receptors that may affect behaviours.

Having optimised expression time and labelling, data required analysis. While there are many freeware options to perform SPT track generation (TrackMate [176], SMTracker [177], Swift [178], TrackIt [179], among others), UTrack [180] was chosen here given its robust performance on data of this type and its direct integration with DC-MSS subtrack analysis [184]. It is important to note that, even with subtrack motion sensitive analysis, the frame rate of SPT data capture and the length of observation will directly affect the types of motion detectable. A good example of this is shown by Murase et al. [216] (Figure 3.29).

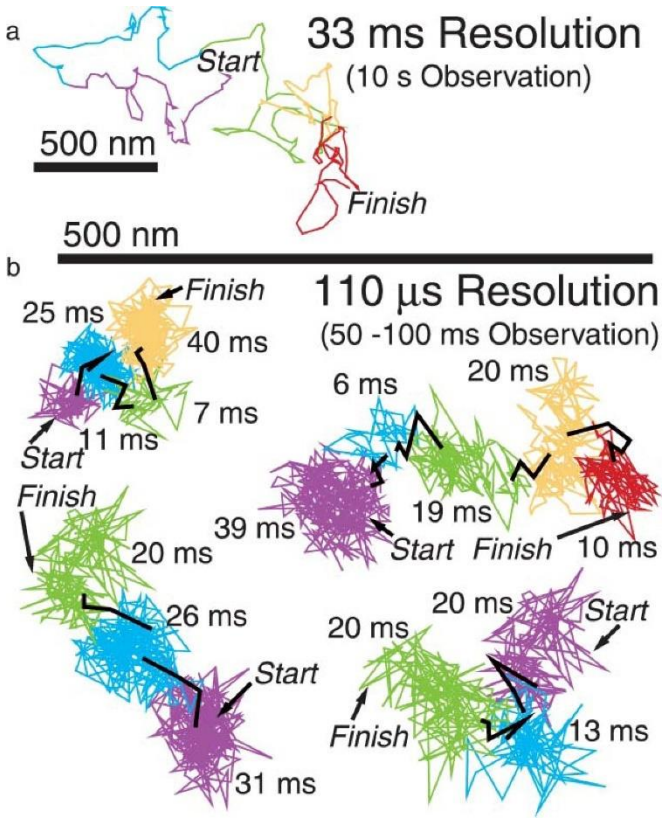

Figure 3.29 – Framerate can affect identifiable diffusion behaviours. *Gold tagged DOPE, an unsaturated phospholipid, was imaged at different framerates and the outcomes compared. a) A 'video rate' example of DOPE diffusion over a 10 second timeframe. b) DOPE imaged at a much higher framerate, with proposed corral confinement depicted by different colours and potential 'hop' events coloured in black. Figure from Murase et al. [216].*

Longer, ‘slower’ observations, as in Figure 3.29a and the work in this chapter, do not show the characteristic trap and hop behaviour visible at shorter time frames (Figure 3.29b) thought to be a result of the actin mesh confinement. This behaviour can instead be surmised from the impediment to diffusion speed when comparing to theoretical Brownian free motion. So, what is described here as confinement and free motion is not likely to directly represent corralling and hop diffusion. The data collected could still show changes to these motion forms, and other interactions with the actin cytoskeleton – direct tethering, for example – may contribute to the ‘confined’ motion type classification in this work.

The SPT data presented in this chapter supports a differential regulation between the two receptors, as also proposed by the STORM data. The findings also indicate, however, that the dynamics and clustering behaviour may not be regulated in the same manner (see Figure 3.30 for direct comparison of findings).

$A_{2A}R$ shows actin mediated clustering responses in the above STORM data. When investigating dynamics, there was no significant change in diffusion coefficient observable with drug treatment. In terms of time spent in each movement type, there were only significant changes between the drug treated samples – that is, motion classification was not calculated to be significantly different to the DMSO controls. Relative to CD treated samples, however, NECA treated A_{2A} receptors showed significantly more free motion and significantly less confined motion. This could be indicative of NECA acting to enhance mobility in a relatively subtle way, so as to explain the lack of significance when compared with the control.

While $A_{2B}R$ clustering was not affected by stimulation or actin disruption, its dynamics were. NECA treatment reduced the proportion of time tracks spent freely moving compared to DMSO and CD. $A_{2B}R$ has previously been shown to undergo agonist induced desensitization and internalisation [217, 218] (although both of these studies used the rat $A_{2B}R$), which could explain this reduction in free motion. The confinement radius for tracks classified as confined (as opposed to immobile) was also decreased significantly upon addition of NECA when compared to DMSO and CD alone. This could suggest an activation-specific confinement, in line with agonist induced internalisation. Interestingly, both the reduction in free motion and in confinement radii were abrogated by addition of NECA and CD treatment together. Actin disruption could be affecting this confinement either by affecting resting organisation or by directly removing confining structures.

For both receptors, significant changes also occurred within switching behaviour. In general terms, this is important to consider as while overall diffusion coefficients or proportions of time spent in a particular motion type could remain consistent, switches between motion types could be altered. For $A_{2B}R$, the increase in immobile to confined and confined to immobile switching with NECA treatment could be related to receptor desensitisation and internalisation processes. $A_{2A}R$'s reduced free-to-confined switches with CD treatment may indicate actin is necessary to mediate switching of receptors to a particular kind of constraint.

An existing paper investigating $A_{2A}R$ dynamics showed that lateral mobility of $A_{2A}R$ was unaffected at the level of fluorescence recovery after photobleaching (FRAP)

experiments by CGS 21680 stimulation, or by Latrunculin A actin disruption [195]. This agrees with our SPT findings somewhat – CD actin disruption in our hands had no significant effect on receptor diffusion coefficient relative to the control. NECA treatment, however, did show some increase in free motion, though only compared to CD treated samples. This could be as a result of the increased sensitivity of SPT as a technique over FRAP, as FRAP is both diffraction limited and a bulk assessment of membrane receptor population, as opposed to assessment of individual receptors at a sub-diffraction limited resolution. Charalambous et al. argue for a cholesterol-based mobility restriction for $A_{2A}R$ rather than actin related, as in their experiments depletion of cholesterol impaired $A_{2A}R$-Gs coupling [195].

The method of actin disruption could also play a role in how or if membrane proteins are affected. Murase et al. found that treatment with CD could modulate DOPE diffusion in FRSK cells [216], which was built on by Fujiwara et al. [15] who demonstrated that CD but not Lat A significantly increased the size of actin corrals using electron microscopy.

3.7 Chapter conclusions

In this chapter, the use of SNAP-tagged receptors in a range of imaging techniques allows us to demonstrate that A_{2A} and A_{2B} receptors respond differently under actin disrupting and receptor stimulating conditions. Changes in clustering behaviour with actin disruption are only identifiable for $A_{2A}R$ expressing cells in this experimental set up. Both receptors, however, show various changes in dynamic behaviour with

treatments. Pharmacological data for the A_{2A} receptor support a change in signalling behaviour with actin disruption, showing enhanced cAMP levels with CD treatment.

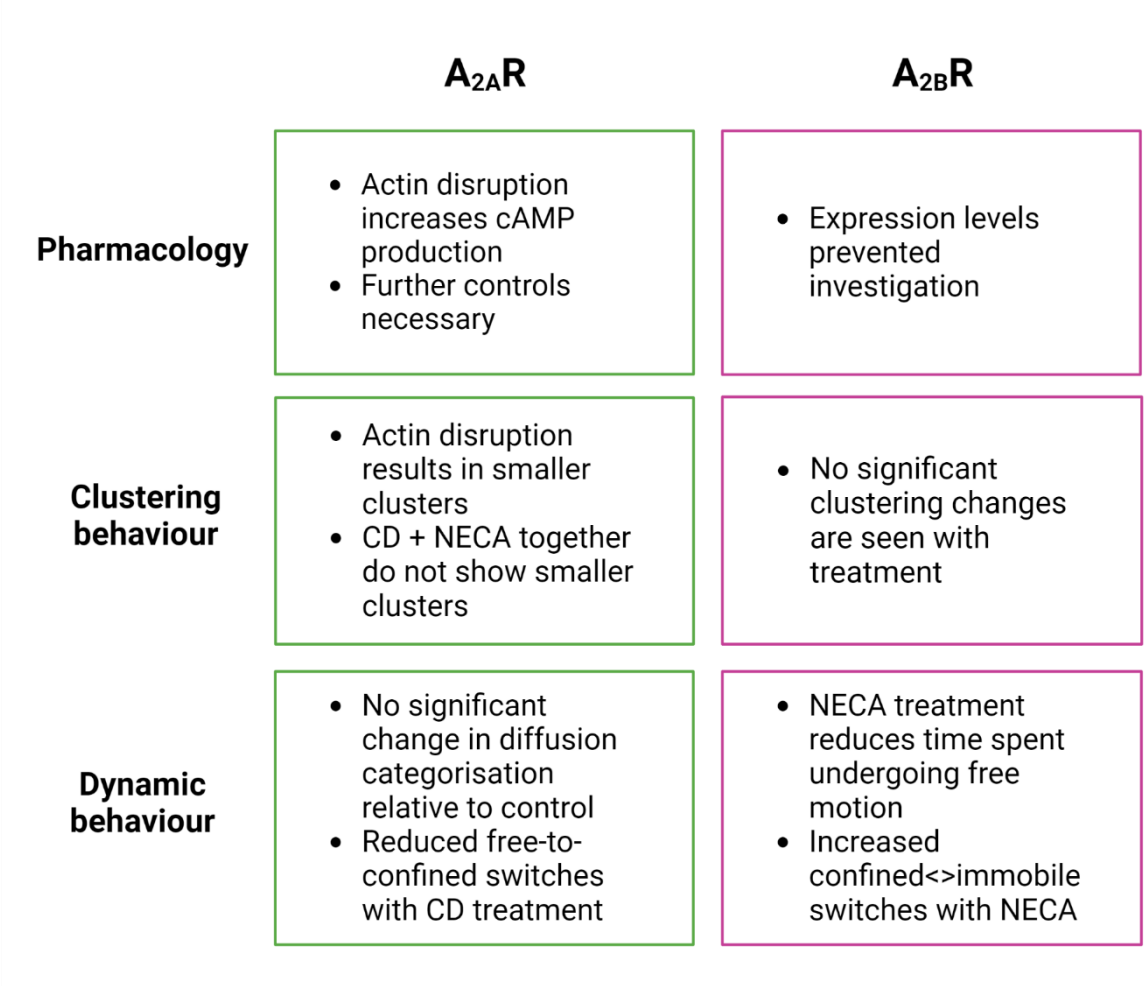

Figure 3.30 – Summary of results presented in Chapter 3. *Key findings for each receptor and technique used in this chapter are listed.*

As listed in Figure 3.30, the $A_{2A}R$ data from these SPT experiments, from the STORM experiments, and accompanying pharmacological data are not inherently contradictory, but may not be initially intuitive. A lack of significant effect of NECA on $A_{2A}R$ clustering is in accordance with a potential increase in free motion – the heterologous distribution of receptors within the membrane would show a basal level

of ‘clustering’ when fixed. This again can be linked with the pharmacological investigations, as there is a growing consensus that $A_{2A}R$ does not show internalisation upon activation (Kilpatrick, personal communication). An increase in free motion may also enhance the ability of the receptor to interact with signalling partners, thereby explaining the increase in cAMP production. For $A_{2B}R$, the lack of NECA induced clustering response is not contradicted by the apparent NECA induced immobilisation evident in SPT data, especially given the caveats to the clustering interpretation discussed above.

CHAPTER 4 – INVESTIGATING ACTIN BEHAVIOUR

Data from this chapter are published as:

Garlick, E., Faulkner, E.L., Briddon, S.J., and Thomas, S. G. 2022. **'Simple methods for quantifying super-resolved cortical actin'**. *Sci Reps*, 12, 2715. https://doi.org/10.1038/s41598-022-06702-w

4.1 Chapter Overview

The major functions ascribed to the actin cortex are largely morphological – maintaining cellular shape and contributing to motility and division [219]. The picket fence model of membrane organisation posits that this actin structure also serves to compartmentalise membrane proteins. Imaging the fine actin mesh proximal to plasma membrane was, until the advent of super-resolution techniques, only accessible by electron microscopy (EM) techniques [14, 15]. One core study incorporating EM and SPT analysis of membrane species showed cell-type specific actin mesh corrals, which closely correlated with the compartment sizes calculated from SPT data [15]. It has been proposed, however, that this actin is more dynamic than initially assumed – and that this property may also contribute to membrane organisation [220]. This chapter therefore will work on incorporating live SR actin imaging, as well as exploiting benefits of fixed super-resolved methods over traditional EM.

Advancement of super resolution microscopy techniques has been of particular importance to the investigation of the actin cytoskeleton. As described in chapter 1, actin filaments are the smallest of the three major cytoskeletal fibres - ~ 6-7 nm diameter, in comparison to intermediate filaments at ~ 10 nm and microtubules at ~ 25 nm [221]. While clearly all cytoskeletal filaments fall well under the diffraction limit, some SR techniques are capable of resolving microtubules to the point that even labelling error is appreciable (for example, post-expansion labelling coupled

with dSTORM can reduce linkage error by a factor of 10 [154]). An example of the importance of investigating actin with super resolution techniques is the identification of actin rings in axons [222]. Without the additional resolution afforded by breaking the resolution limit, these regularly spaced rings with an interval of ~180 nm would have been impossible to resolve.

A key consideration in the SR imaging of actin, especially in live cell contexts, is labelling. Actin antibodies perform consistently poorly in immunofluorescence application (for example, see [156]), and direct tagging of actin monomers with fluorescent proteins can have major effects on actin dynamics [223-225]. For fixed samples, fluorophore conjugated phalloidin is the gold standard when visualising actin, though variation is seen in performance between specific fluorophores. Phalloidin-AlexaFluor 488, for example, has been shown to provide superior detail and longevity of stain over derivatives like AlexaFluor 405 [226]. Fluorophore choice will obviously also depend on the application - dSTORM is performed with Alexa-647 Phalloidin labelled samples [201], given its key blinking properties. This conjugate does have limitations, being notably more labile than other Phalloidin labels, requiring longer incubations and higher concentrations to minimise dissociation [201, 227]. Adequate labelling density is vital to improve fidelity of actin imaging, and is a core concern addressed in the development of IRIS [113] (further discussed in section 1.9.2), as well as reduction of appreciable linkage error.

The properties of the plasma membrane proximal actin meshwork have been investigated using SMLM (dSTORM [228], PALM [163]), AFM [229], and STED [30], amongst others. While all can give high resolution structural information (and mechanical, in the case of AFM), adaptation to live multicolour imaging can be challenging.

In this chapter, imaging techniques were assessed for application in both fixed and live contexts in order to image fine cortical actin meshworks in detail. Effects of actin disruption and receptor activation on cortical actin structure were also tested. Techniques were trialled and optimised with a view to future multiplexing with receptor imaging, a goal which informed many of the decisions made during the following experiments.

Core chapter aims:

- Test, optimise, and develop analysis for SRRF imaging for fixed and live actin imaging
- Test, optimise, and develop analysis for ExM and 3D SIM ExM for fixed actin imaging
- Assess cortical actin structure changes under receptor stimulating and actin disrupting conditions
- Create workflows amenable to later multiplexing of actin and receptor imaging.

4.2 Fixed Actin Imaging Reveals Fine Details of The Actin Cortical Mesh

4.2.1 Sample preparation and imaging approaches for fixed cells

Optimal fixation techniques can vary depending on the imaging target. Methanol fixation, for example, can produce impressive results when imaging tubulin, but causes significant disruption to the actin cytoskeleton. Although PBS is commonly used as a buffer for fixatives, cytoskeleton stabilising buffers can ensure better retention of structure. As such, 4% PFA fixation buffers were made up in PEM (unless otherwise stated) to ensure optimal and robust actin preservation. Fixatives were also warmed to 37^{o}C before addition directly to samples after removal of media. For general applications, cells were labelled with AlexaFluor 488 conjugated phalloidin, the gold standard for imaging of fixed filamentous actin. This resulted in consistent and stable labelling in all fixed cell techniques trialled, as shown throughout this chapter. Cells imaged were generally touching neighbouring cells, but overconfluent regions were avoided. Widefield epifluorescence examples are shown in Figure 4.1.

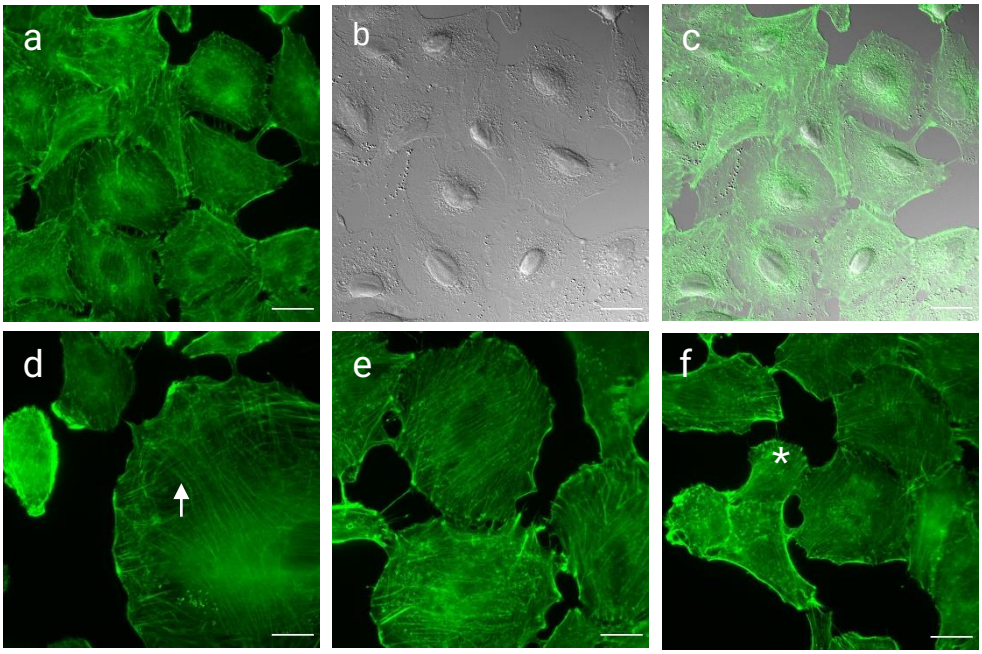

Figure 4.1 – Fixation and labelling regime allows imaging of actin structures*. a) Widefield epifluorescence image of phalloidin-Al.488 labelled A549 cells, with b) showing the brightfield image of these cells. c) Merge of a and b. d,e,f) Further examples of widefield actin images, especially showing clear stress fibres (arrows) and lamellipodia (asterix). All scale bars = 20 µm.*

The actin cortex relevant to membrane protein organisation is directly adjacent to the plasma membrane. In spread adherent A549 cells, the basal membrane is an attractive imaging target due to its proximity to the coverslip. Actin structures that affect receptor organization are on a nanoscale, meaning the diffraction limit of standard light microscopy significantly limits what of interest is resolvable. Having optimised basic fixation and phalloidin labelling using widefield, better signal to noise and improved resolution was key.

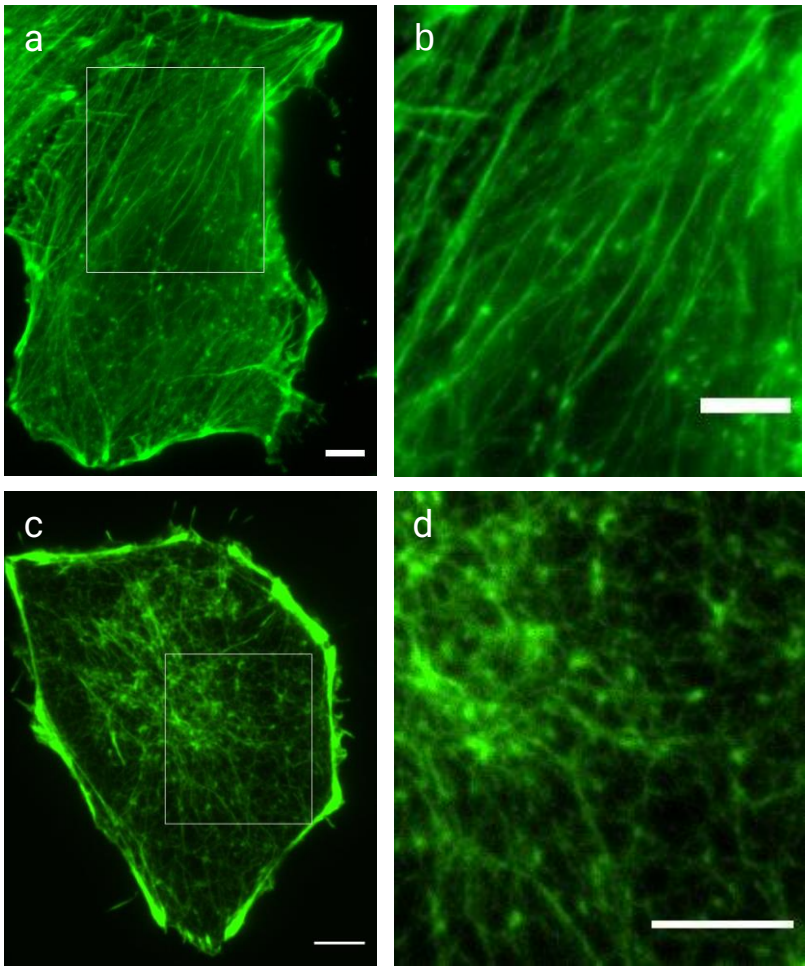

Figure 4.2 – TIRF vs. widefield imaging of basal cortical actin. *a) Widefield image of cortical actin, with zoom in panel b) showing stress fibres as well as the out of focus (OOF) light inherent to the technique. c) TIRF image of cortical actin, with zoom in panel d) demonstrating the minimisation of OOF light possible with the technique. All scale bars = 5 µm.*

Several imaging techniques were used in this thesis, with future application to live imaging a key determinant for further development. While not capable of breaking the diffraction limit itself, TIRF imaging captured basal cortical actin with a good signal to noise ratio (Figure 4.2), making it possible to clearly image structures like stress fibres as well as regions of finer cortical mesh (Figure 4.2c & d). Full width half maximum (FWHM) calculations based on 60 intensity profiles (from 20 cells) of individual, well defined filaments indicated a mean resolution of 256.80 nm ± 60.35 s.d.. Given the fine nature of the actin mesh and the known sub-resolution length scales of the actin corrals of interest, super resolution imaging was required to further unpick nanoscale structures.

Initial imaging was performed using 3D and TIRF SIM, as well as the computational super resolution technique SRRF. To illustrate the differences in resolving power and image output, the three techniques are compared in Figure 4.4 below.

SIM acquisition and reconstruction was first optimised, with representative data assessed via the SIMCheck FIJI plugin [188] to ensure good quality outputs. For example, the reconstructed example in Figure 4.3b shows good contrast and no major artefacts in the reconstruction, as well as a gradual decrease in signal at higher frequencies and lack of repetitive patterning in the Fourier transform (Figure 4.3e,f). Poorer raw data report much sharper edges in Fourier transforms, which can indicate artefactual data at the highest frequencies. Repeated patterns visible within the FT are also indicative of major artefacts. During the reconstruction process, raw data with clear issues in one or more rotations were identified by the Nikon Elements

software and immediately discarded from further analysis. Other artefacts, such as honeycombing, hatching, or shadowing, for example, had to be assessed visually and were discarded from subsequent analysis as necessary. The 3D SIM image in Figure 4.4a reported a FWHM of 130.10 nm +/- 25.33 s.d., which correlates with expected performance of the technique. TIRF SIM imaging was also trialled on these samples, showing the improved optical sectioning expected of the technique (Figure 4.4b), as well as improved FWHM measurements of 87.21 nm +/- 11.23 s.d.. Unfortunately, TIRF SIM could not be carried forward in the project due to technical issues with TIRF SIM mode on our microscope compounded by coronavirus restrictions.

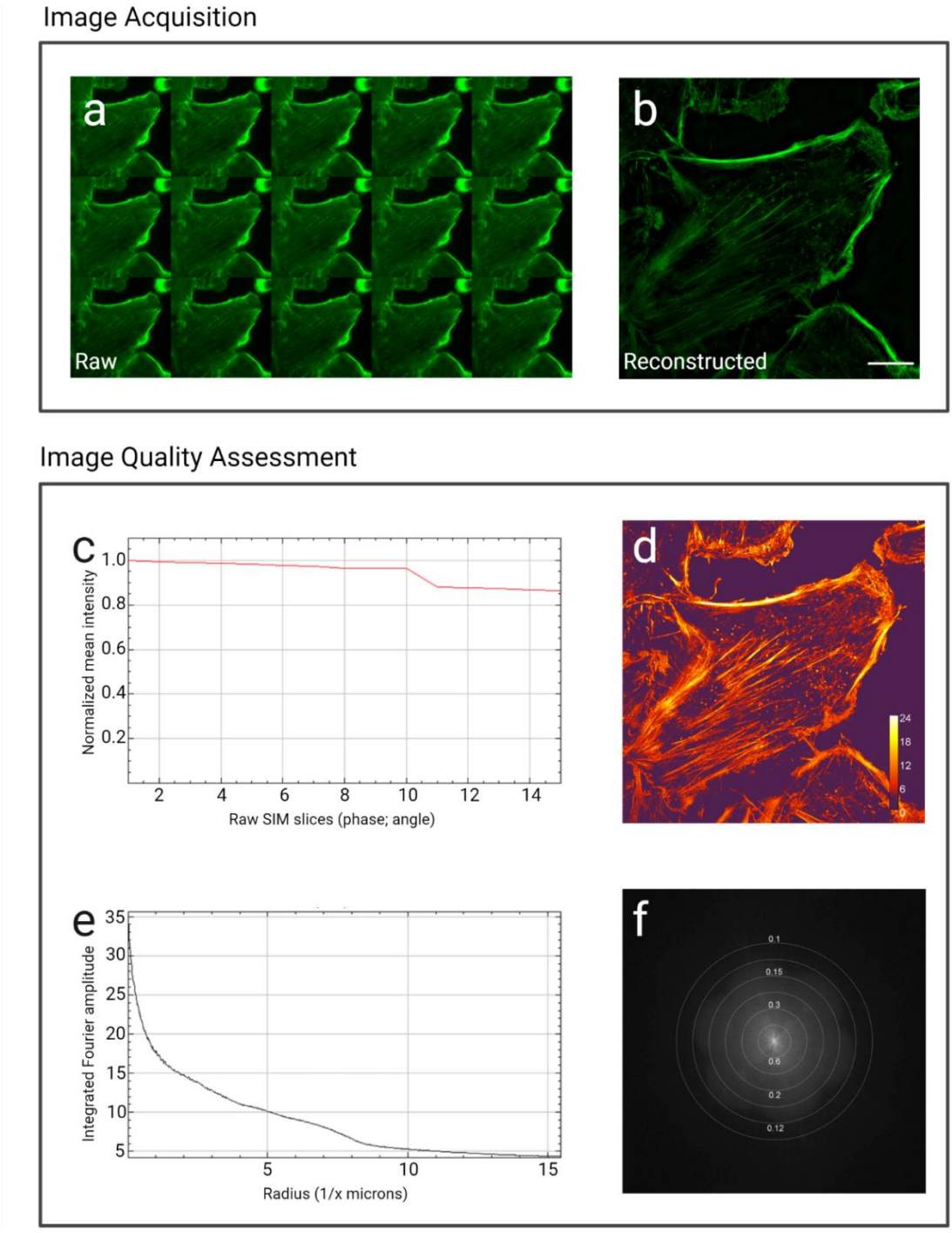

Figure 4.3 – SIMCheck indicates good performance of 3D SIM*. a) Raw and b) reconstructed example outputs from Nikon Elements software, assessed for c) fluorescence intensity and d) modulation contrast to noise. Average feature MCNR is 8.83 for this example. e) Fourier frequency plot showing expected gradual decrease and f) typical flower shaped Fourier transform, showing soft edges at the highest frequencies.*

When comparing images of the same cells across all three techniques, benefits and pitfalls of each are more readily apparent. All of the super resolution techniques show clear imaging of larger structures as readily described by TIRF imaging but also show detail obscured by the resolution limit, like branching of filaments (Figure 4.4). FWHM calculations for the SRRF example illustrated here indicate resolution of 112.90 nm +/- 12.11 s.d.. Detail identified in SRRF images is well correlated to both the SIM and TIRF images (Figure 4.4) but does show false sharpening and object collapsing that can be characteristic of this kind of image processing - for example, as shown by Marsh et al. and their comparisons of super resolution reconstruction techniques [166].

As images of the same regions and cells taken with both SIM and SRRF correlated well in terms of structure, it was decided that analysis of SRRF images should be focussed on for further development. Given that SRRF images are generated from stacks of standard widefield or TIRF images, the speed of acquisition can be significantly faster than standard 3D SIM. SRRF was further deemed a better choice for live imaging due to ease of multiplexing with planned single particle tracking experiments. Although SIM is a solid contender for use in live imaging due to its relatively low phototoxicity (that is, compared to other SR techniques), further modifications to the technique are necessary to improve framerate for suboptimal signal to noise situations.

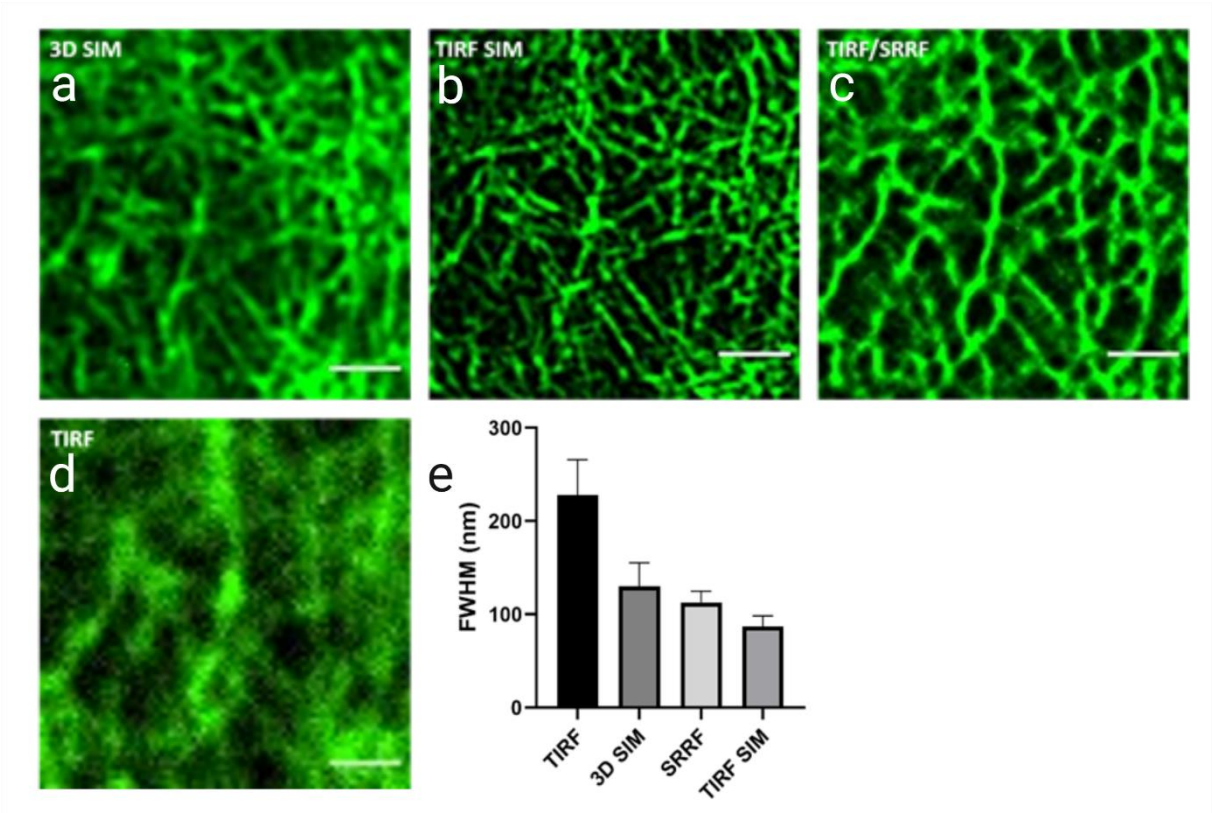

Figure 4.4 - 3D SIM, TIRF SIM, and SRRF super resolved images of phalloidin-488 labelled actin. *N.B SRRF intensity does not correlate to fluorescence intensity, rather how well the algorithm could fit each feature. Image d) shows a raw TIRF image corresponding to this ROI. e) FWHM calculations show expected trends, with TIRF SIM providing the greatest increase in resolving power. Scale bars = 1 µm.*

4.3 SRRF Imaging Permits Rapid and Simple Super Resolution Actin Acquisitions

4.3.1 SRRF imaging optimisation and fidelity testing

Having determined SRRF was the best technique for dual live imaging, Fourier Ring Correlation (FRC) measurements were performed in addition to FWHM calculations, and showed a significant increase in resolution over standard TIRF images (Figure 4.5a-c). Use of NanoJ-SQUIRREL [203] to assess SRRF images indicated robust and accurate reconstruction, routinely reporting Resolution Scaled Pearson's (RSP) correlation coefficient values of >0.95 (Figure 4.5d), indicating good reconstruction of SRRF images. Visualisation of error as a heat map indicated that where issues did exist, they were largely around the thicker filaments (Figure 4.5f). When overlaying SRRF reconstructions on top of the raw TIRF data, good agreement was observed between the two - even with smaller filaments and less intense regions of signal (Figure 4.6). This approach does not, however, provide sufficient resolution to image single or very fine bundles of actin filaments, which are only accessible with EM or some single molecule techniques.

When comparing this resolution to FWHM calculations across TIRF, SRRF, and SIM techniques, we see good performance for SRRF borne out across both measures (Figure 4.4e, Figure 4.5c).

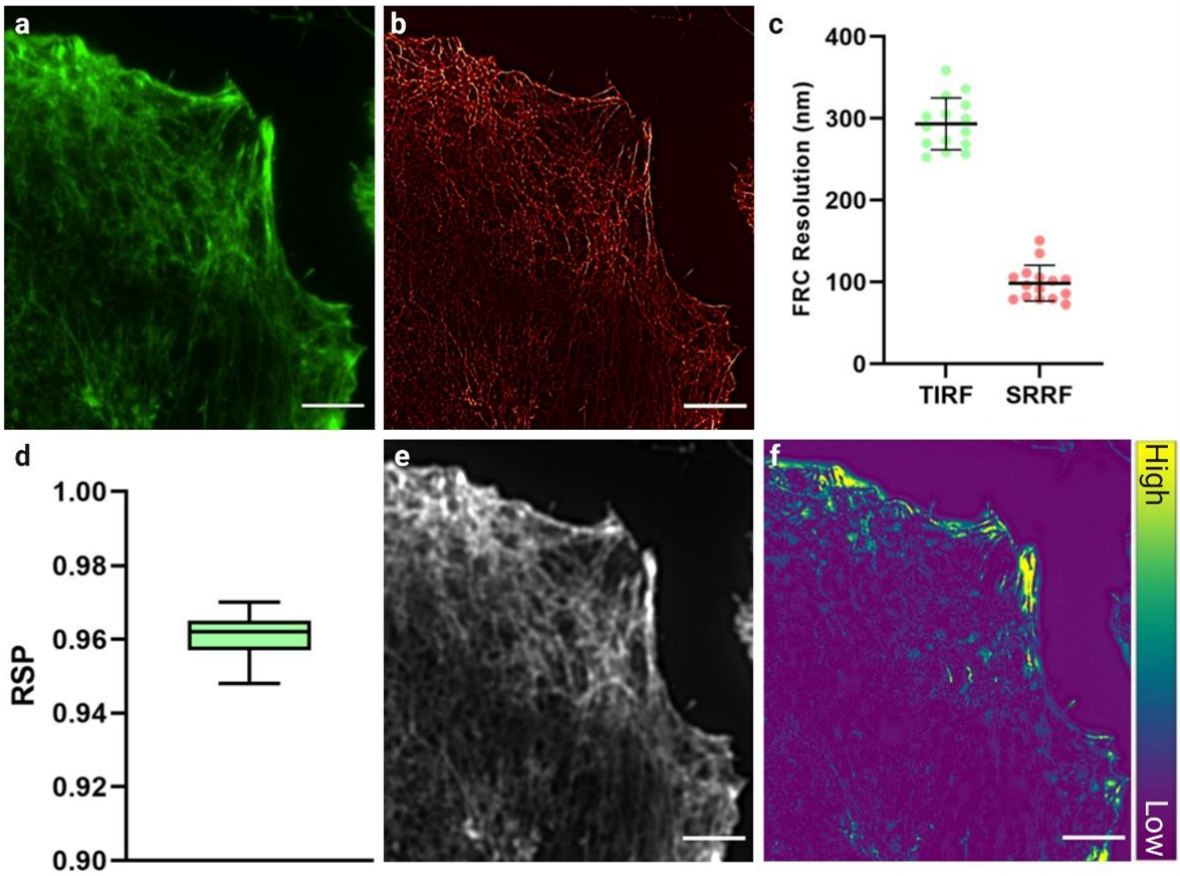

Figure 4.5 - SRRF reconstructions show minimal error compared to TIRF images. *a) Representative TIRF image of actin in A549 cells labelled with phalloidin Alexa 488. b) SRRF reconstruction from 100 frames of TIRF data represented in a). c) Mean Fourier ring correlation (FRC) resolution ± standard deviation for the TIRF and SRRF images (n = 15 images from 3 independent experiments). d) Plot showing mean resolution scaled Pearson's correlation coefficient ± standard deviation for 15 images over 3 independent experiments, as calculated with NanoJ-SQUIRREL. 1 is total correlation and -1 is total anticorrelation. e) Convolved image from b) generated by Nano-J SQUIRREL to calculate error. f) Error map, assessing e) vs a), indicating artefacts in reconstruction occur in areas of thicker and more dense filaments.*

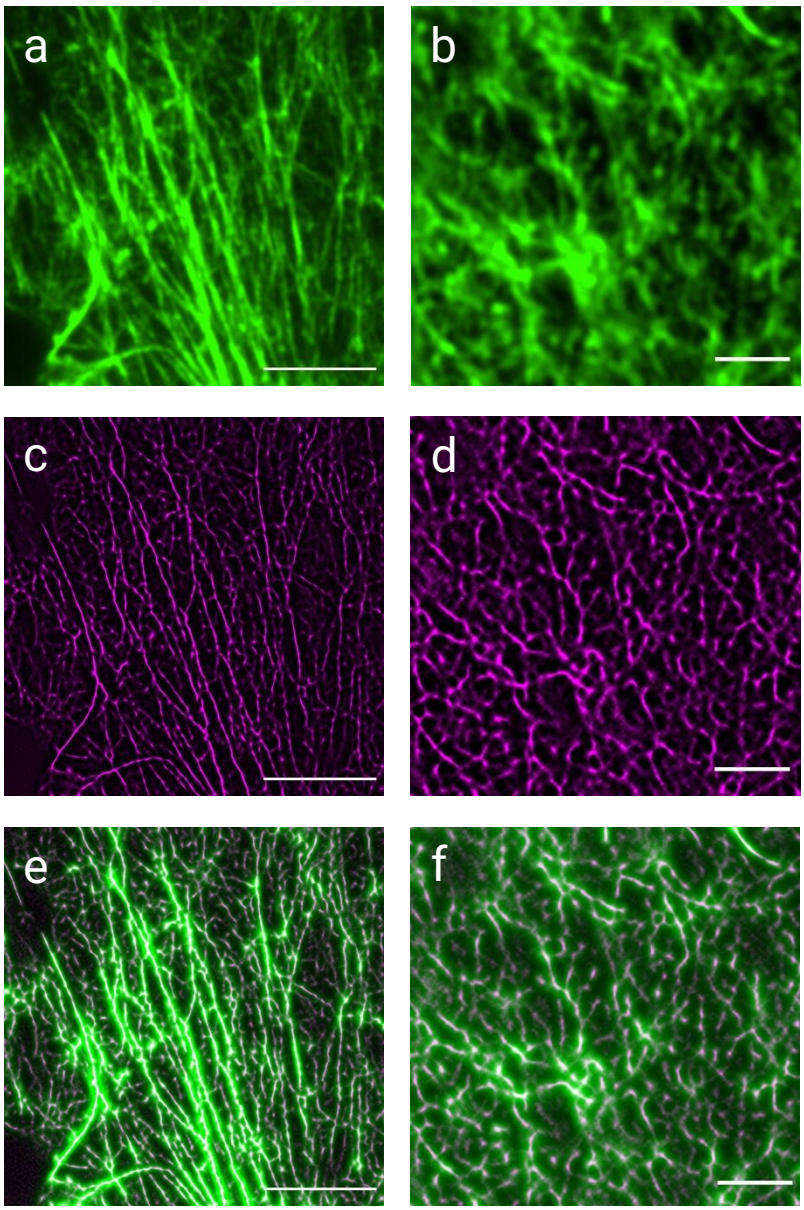

Figure 4.6 – Fine detail in SRRF images is supported by raw TIRF data. *a) and b) show Phalloidin 488 labelled actin imaged in TIRF. c) and d) show corresponding SRRF outputs, with e) and f) showing the two overlaid. Scale bars for a, c, and e = 5 µm. b, d, and f = 2 µm.*

4.3.2 Development of SRRF image analysis

With robust and reliable SRRF imaging of the actin possible, quantification was required in order to compare actin structure between drug treatments. Various approaches were trialled, including skeletonization and fibre tracing, with limited success and so development was focused on methods using thresholding.

Taking into account the particularities of SRRF images, especially the non-linear connection between reconstruction intensity and raw fluorescence intensity, as well as other published actin or meshwork analysis methods (e.g. [228, 230]), I created a simple workflow to quantify the actin meshwork (Figure 4.7a). In FIJI, SRRF images were cropped to an ROI of 10 μm^2, as centrally in the cell of interest as possible (Figure 4.7b). The image was then manually thresholded using Otsu's method. The threshold was used to generate a binary mask of the network, which was followed by erosion (Figure 4.7c, d). A classic watershed segmentation was applied (Figure 4.7e), and the resulting regions ('particles', or 'corrals') analysed for a range of descriptors, including area and perimeter. The term corral is used here to refer to a gap or hole in the actin mesh that is bounded on all sides by actin filaments. Although the terminology has been borrowed from descriptions of similar holes identified with electron microscopy in key works underpinning the picket fence model (e.g. [15]), the 'corrals' referred to in this work are much larger, given the relative resolving power of SRRF.

To validate the analysis, corrals in the original image were measured manually and compared to the thresholded image. This revealed good correlation in terms of the location of corrals identified (Figure 4.7f-j), while providing a more consistent assessment of filament delineation. This results in larger estimates of corral area (Figure 4.7j). This thresholding approach enables greater degree of consistency between images, and a much higher throughput than via manual assessment.

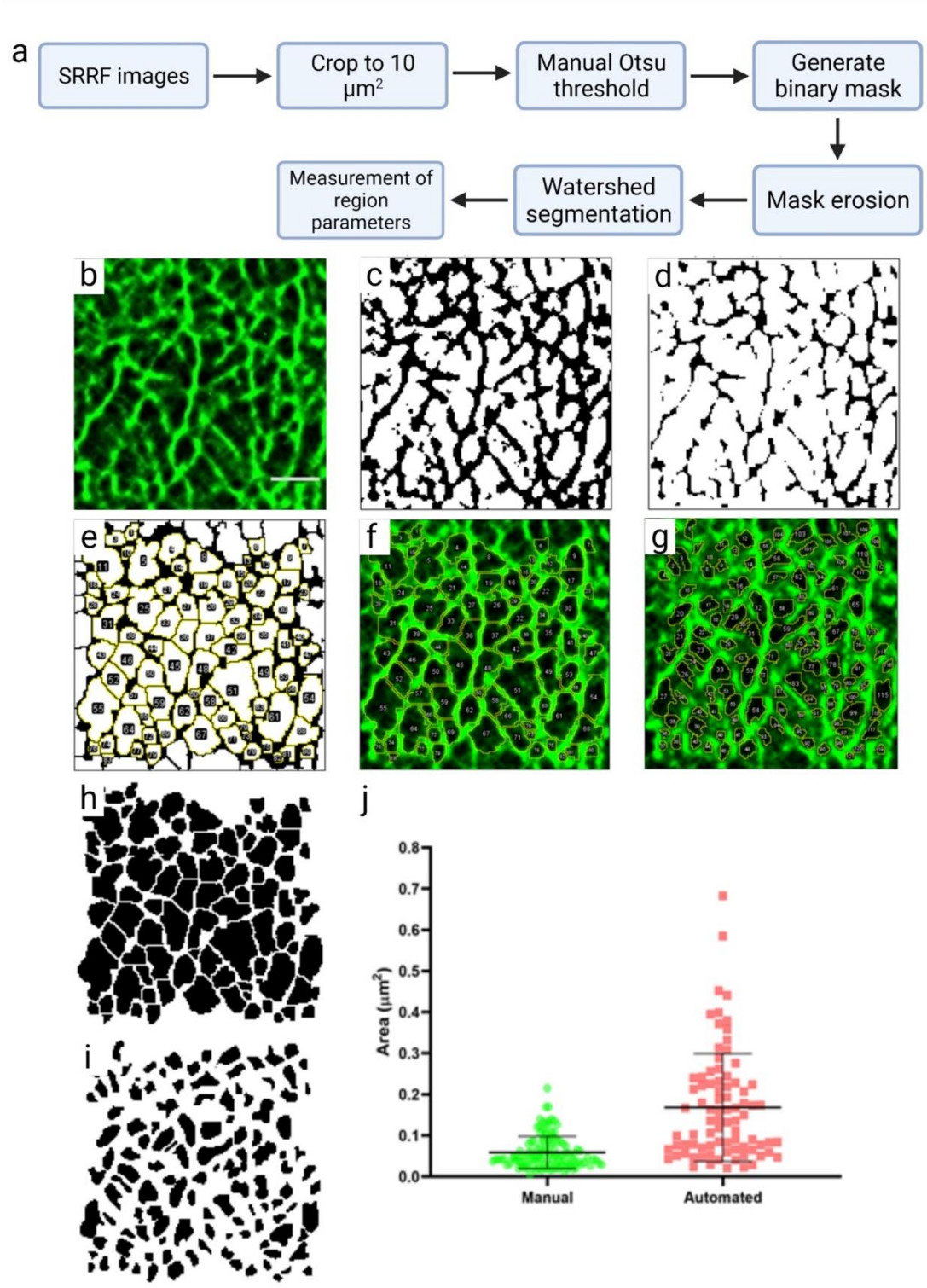

Figure 4.7 – Comparison of manual and automated analysis outcomes. *a) Analysis workflow. b) Raw SRRF image (scalebar = 1 µm, scale consistent across images). c) Otsu thresholding and binarization of image b, followed by d) erosion e) watershed segmentation, and corral identification. f) Overlay of corrals detected via automated analysis on image a, with manually drawn corrals shown in g). h) Corrals from f). i) Corrals from g). j) Comparison of manual and automated corral area estimation.*

In order to further validate this analysis, simulated meshworks with a known ground truth were generated, and the analysis applied to both for direct comparison. These simple actin meshworks were simulated as straight lines using a custom written MATLAB script (see appendix 1). These ground truth images were then processed to resemble imaging outputs obtained from our system in terms of pixel size, PSF, and noise. Filaments were simulated through random generation of start and end points, with each individual filament being given a daughter filament, branching from the original at a 70-degree angle, to mimic Arp2/3 nucleated daughter filaments common in cortical actin networks [231] (Figure 4.8a). Filament number is settable in this script, but for this experiment it was kept at 25 filaments per image, with one daughter filament each. Lines were dilated to more closely resemble the ~7 nm nature of individual actin filaments, and pixels were binned to sizes appropriate for our system and cameras (Figure 4.8b). A Gaussian convolution, based on the PSF estimated from our optics, was applied (Figure 4.8c). Poisson and Gaussian noise were also applied to give a general approximation of read and shot noise and the image smoothed (Figure 4.8d, e). This produced a good representation of our TIRF images of cortical actin networks (Figure 4.8f), displaying a similar range of corral sizes within the ground truth data set.

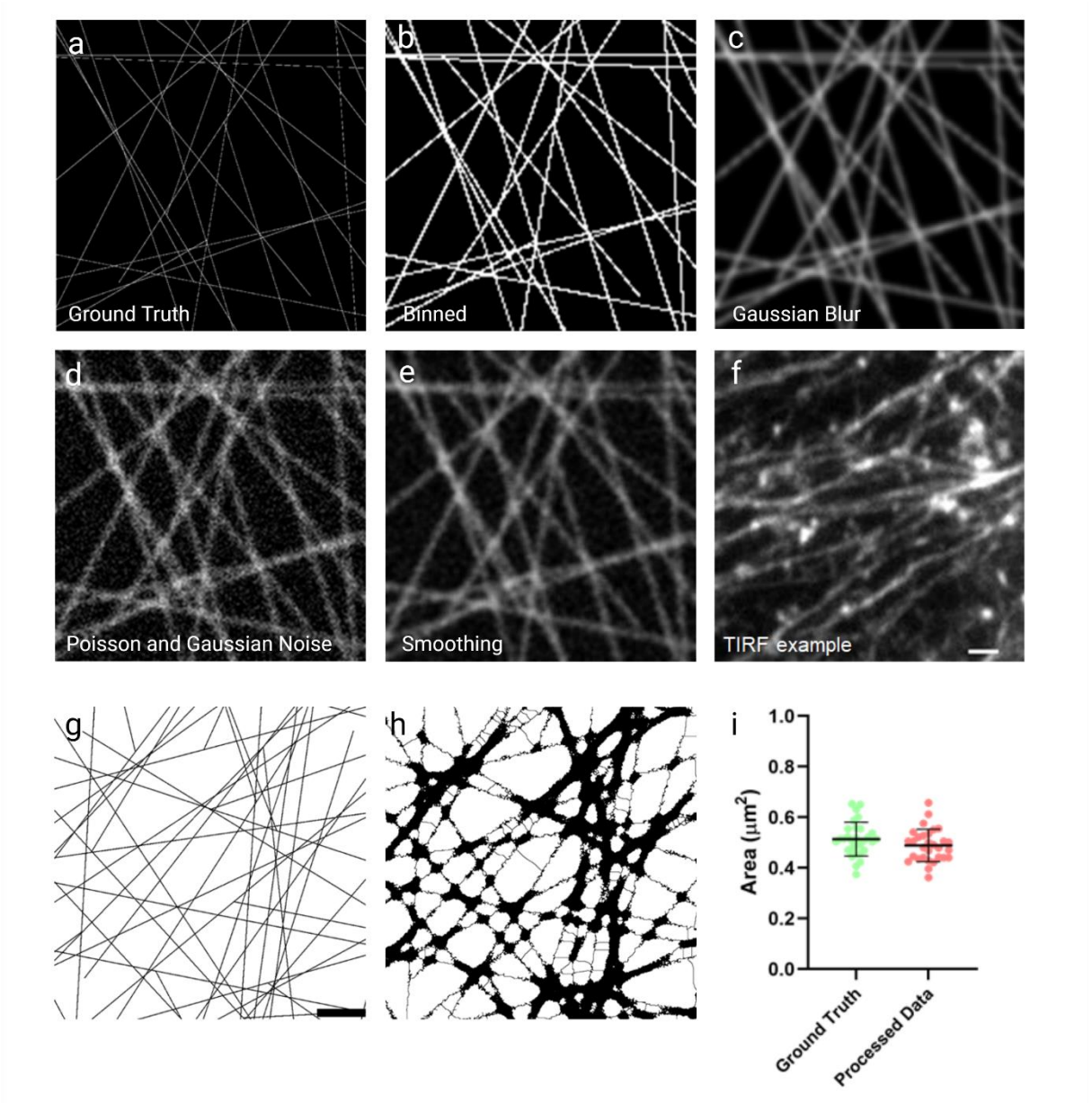

Figure 4.8 - Simulation of meshworks for analysis testing. *a) Initial output of 1px wide lines forming a simulated mesh. b) Image a) after dilation of lines to 7px and binning of the image, to match the pixel size of the cameras on our SIM system. c) Convolution with Gaussian blur, as calculated from an estimated PSF based on our optics. d) Application of Poisson and Gaussian noise to mimic noise from the camera. e) Smoothing of d). f) A TIRF image for comparison of the same scale as the simulated data (scale bar = 1 μm). g) Ground truth simulated meshwork (scale bar 1.5 μm), shown in h) after convolution and application of our meshwork analysis. i) Comparison of mean area ± standard deviation of identified corrals from over 30 repeats of network simulation against the ground truth.*

Analysis of these simulated networks using our analysis workflow showed good correlation in the identification of the same corrals in both the ground truth and simulated data (Figure 4.8g-i). Analysis of the area of individual corrals gave similar mean ± SD values in the processed data as for the corrals in the ground truth image (ground truth - 0.51 μm^2 ± 0.067, processed data 0.49 μm^2 ± 0.064). The small, but not statistically significant reduction in area in processed images is likely to be a result of the convolution increasing the relative filament thickness, subsequently reducing the corral area. In a similar vein, most incongruities occur with small corrals that become obscured when the PSF is applied. These small corrals can be considered to be below the resolution limit of the images and can be accounted for by filtering out corrals under such a size.

As a final validation, the examples of 3D SIM, TIRF SIM, and SRRF meshworks shown in Figure 4.4 were analysed with the technique. In the 3D SIM images, regions of dense signal tend to show reduced signal to noise, making it harder to resolve individual filaments (Figure 4.9a, d, g). Suppression of out of focus light is performed as part of the reconstruction algorithm, and can struggle in dense regions to accurately represent the true structure of the actin. This may partially be an issue with parameter setting within the reconstruction, but assessment of the reconstructed images using SIMCheck shows that Fourier transforms are as expected and suggests generally accurate high-resolution outcomes (Figure 4.3). TIRF SIM provides consistent signal to noise and filament resolution across the region, likely due to the limited plane of illumination generated in this mode. When processed for corral analysis it is evident that the workflow struggles with 3D SIM data, generating

clearly undersized corrals in denser regions while missing some finer filaments entirely, resulting in somewhat of an inflation in mean corral size (Figure 4.9g, k). Corral assignment appeared accurate to the data provided for both TIRF SIM and SRRF images, and resulted in similar mean corral areas (Figure 4.9k). When comparing measurements across the techniques, there is no statistically significant difference between mean corral area or perimeter, but significantly fewer corrals identified in 3D SIM data (Figure 4.9k, l). It is therefore concluded that TIRF/SRRF provides robust accurate measurements of actin corrals.

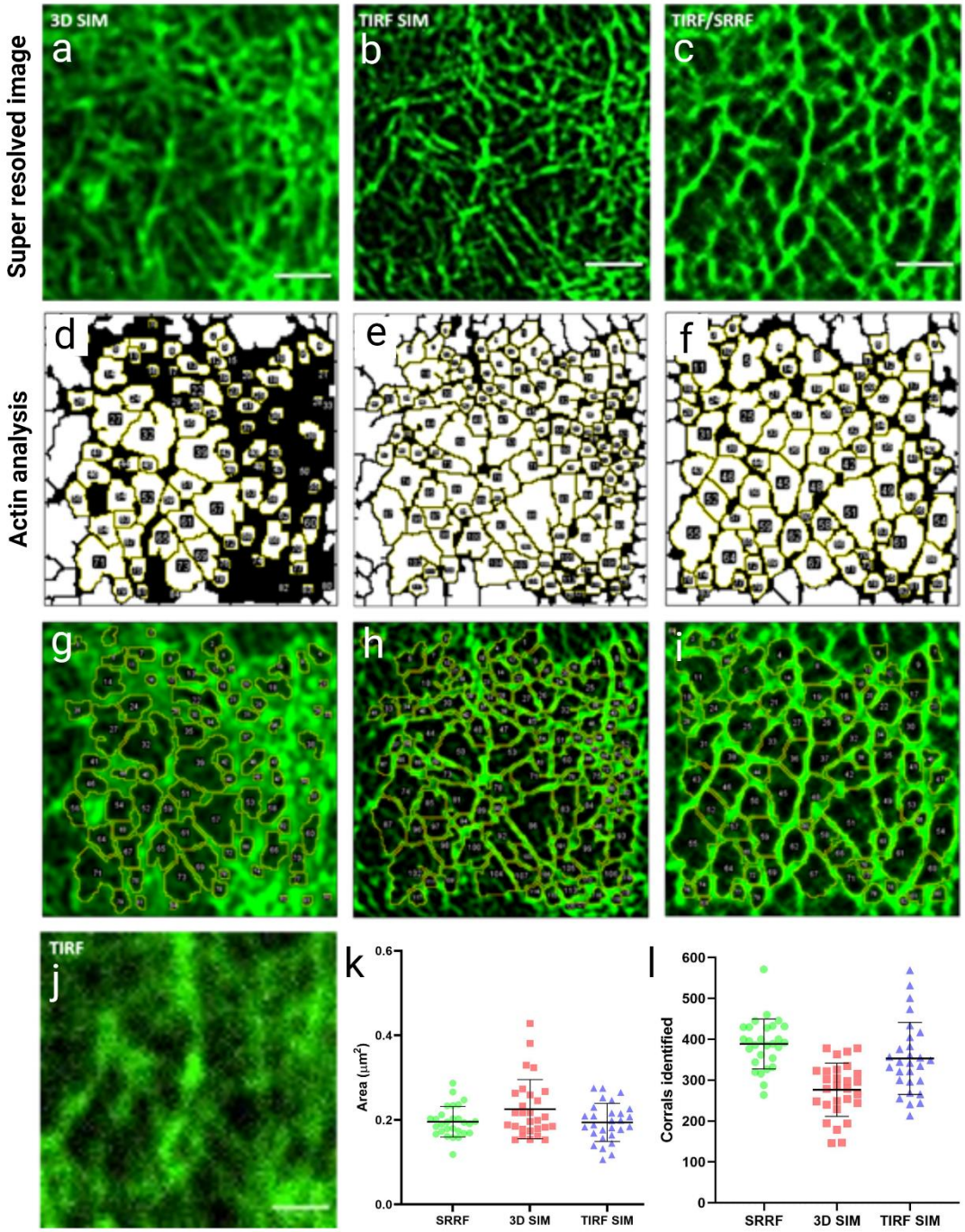

Figure 4.9 - Analysis is applicable to other super-resolution techniques with good SNR. *a) 3D SIM, b) TIRF SIM, and c) SRRF super resolved images of phalloidin-488 labelled actin, with accompanying corral analysis (d-f) overlaid on the ROI (g-i). j) Raw TIRF image corresponding to the ROI imaged in a-c. Mean area (k) and number of corrals identified (l) by automatic analysis of 30 ROIs per technique, indicating that 3D-SIM underestimates corrals while both TIRF based techniques perform robustly.*

4.3.3 Analysis can identify alterations in cortical actin structure after disruption

To assess the effect of disruption of actin polymerisation, or activation of the adenosine receptors, on actin corrals, untransfected A549 cells were treated with either cytochalasin D, which causes depolymerisation of actin filaments, or NECA, a non-selective adenosine receptor agonist. Representative images of treated cells can be found in Figures 4.10-12 & 4.14.

Treatment with 1 µM Cytochalasin D clearly showed the breakdown of normal cortical actin structure, but it is important to note that some regions of network do remain intact. In accordance with this, cytochalasin D treatment significantly increased the size of corrals identified by the analysis workflow. The mean area and perimeter calculated increased significantly, while the number of corrals identified in each ROI fell accordingly (Figure 4.10c-e). Representing the data as a histogram shows a drop in the smallest corrals and accompanying increase in the larger detected regions (Figure 4.10f).

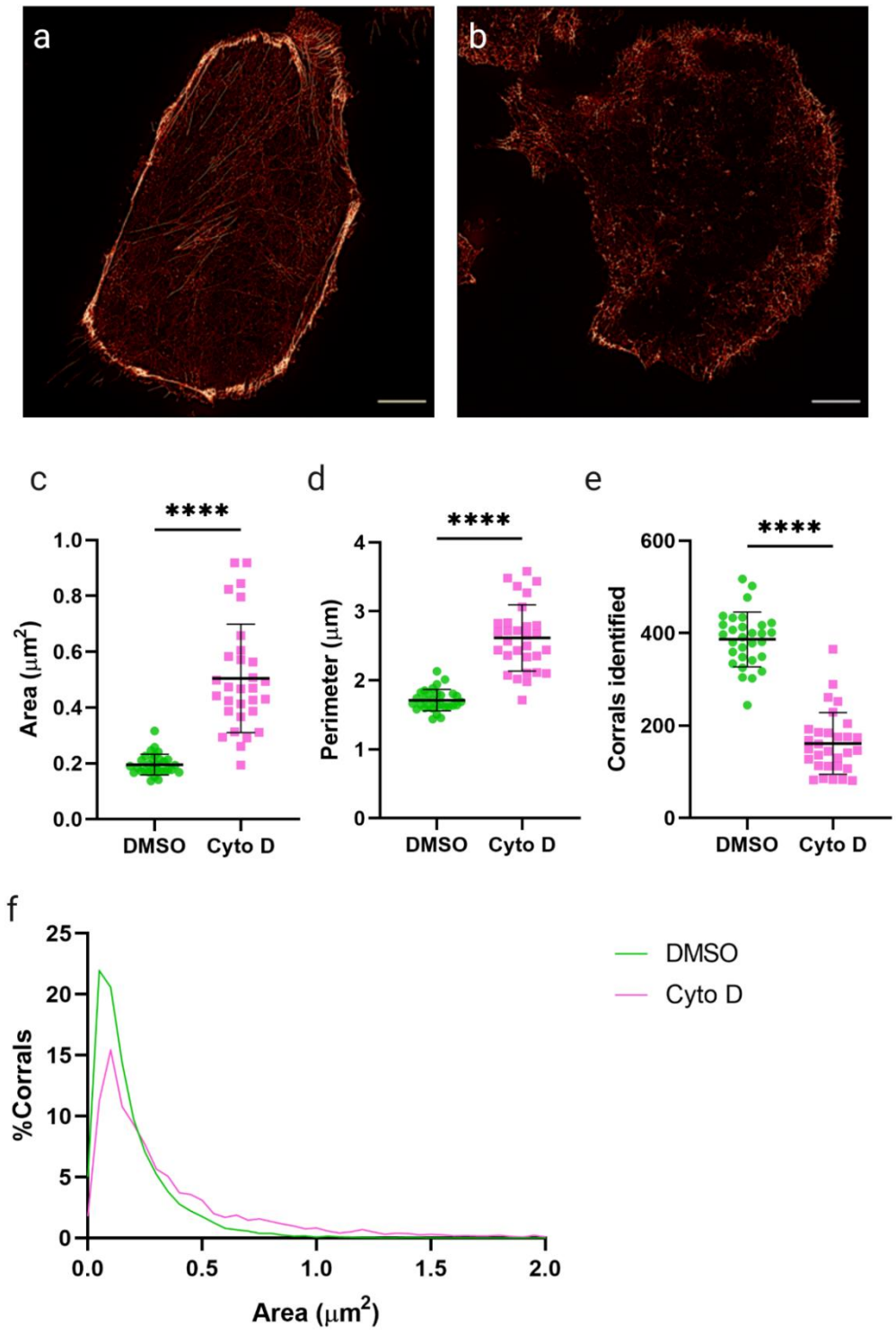

Figure 4.10 - Treatment with cytochalasin D induces significant increase in corral sizes. *a) Representative SRRF image of phalloidin labelled actin in DMSO treated untransfected A549 cells, and b) cytochalasin D treated cells. Scale bars = 10 μm. c) Mean area, d) Mean perimeter, and e) number of corrals identified in cytochalasin D treated cells vs. DMSO control. f) Histogram of all corral areas for cytochalasin D treated and control cells. n=3, 30 cells per treatment. **** = p<0.0001. All error bars show mean ± standard deviation.*

4.3.4 Alterations in cortical actin structure are apparent after adenosine receptor stimulation

Interestingly, when treating with 10 μM NECA there was a slight but statistically significant increase in corral area and perimeter when compared with the vehicle control, with an accompanying significant fall in the number of corrals (Figure 4.11c-e). When corral areas are plotted as a histogram, the shift is not as pronounced as in CD treated samples (Figure 4.10f, Figure 4.11f) but still shows a fall in prevalence of some of the smallest corrals.

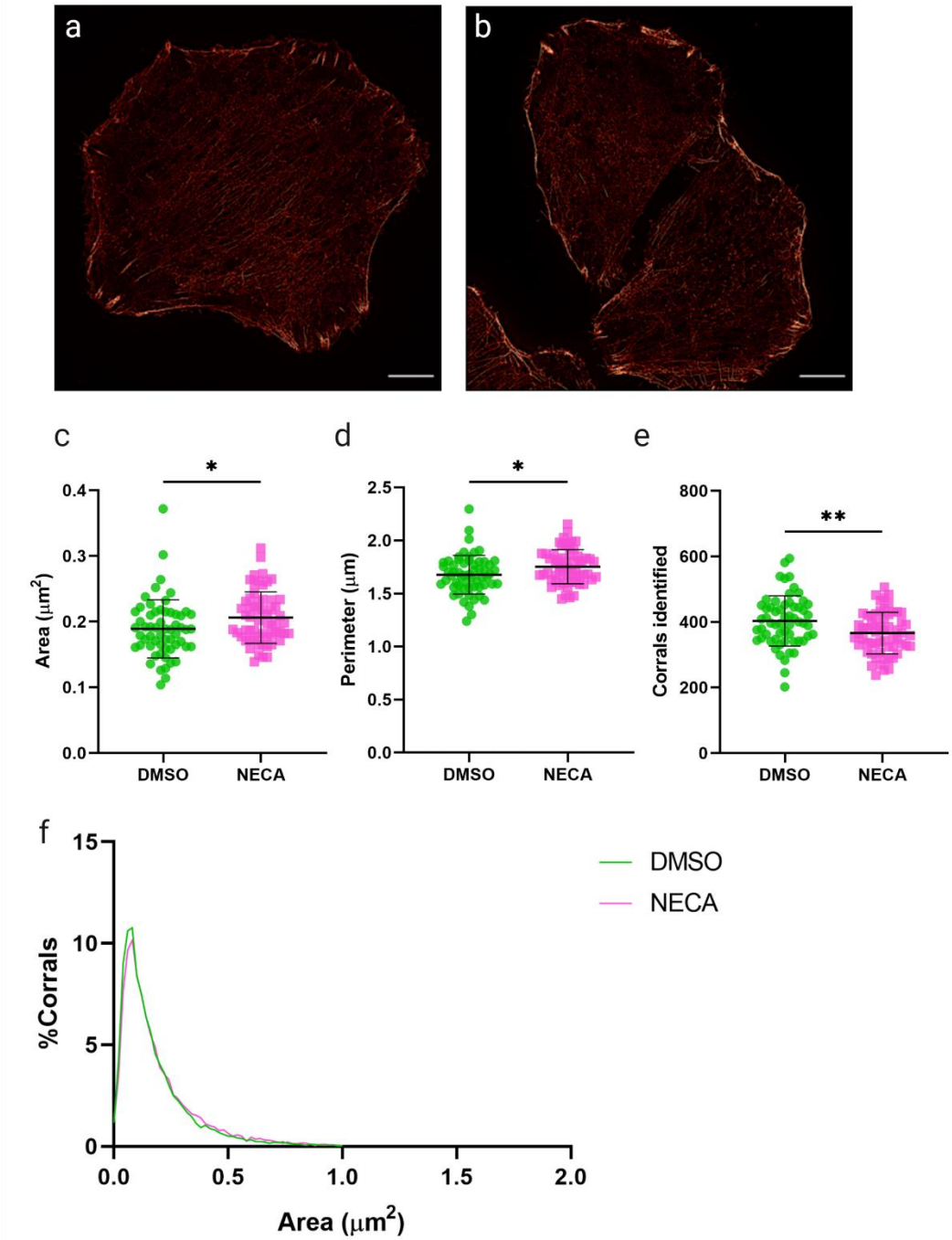

Figure 4.11 - Treatment with NECA induces significant increase in corral sizes*. a) Representative SRRF image of phalloidin labelled actin in DMSO treated untransfected A549 cells, and b) NECA treated cells. Scale bars = 10 µm. c) Mean area, d) Mean perimeter, and e) number of corrals identified in NECA treated cells vs. DMSO control. f) Histogram of all corral areas for NECA treated and control cells. n=3, min. 60 cells per treatment. All error bars show mean ± standard deviation.*

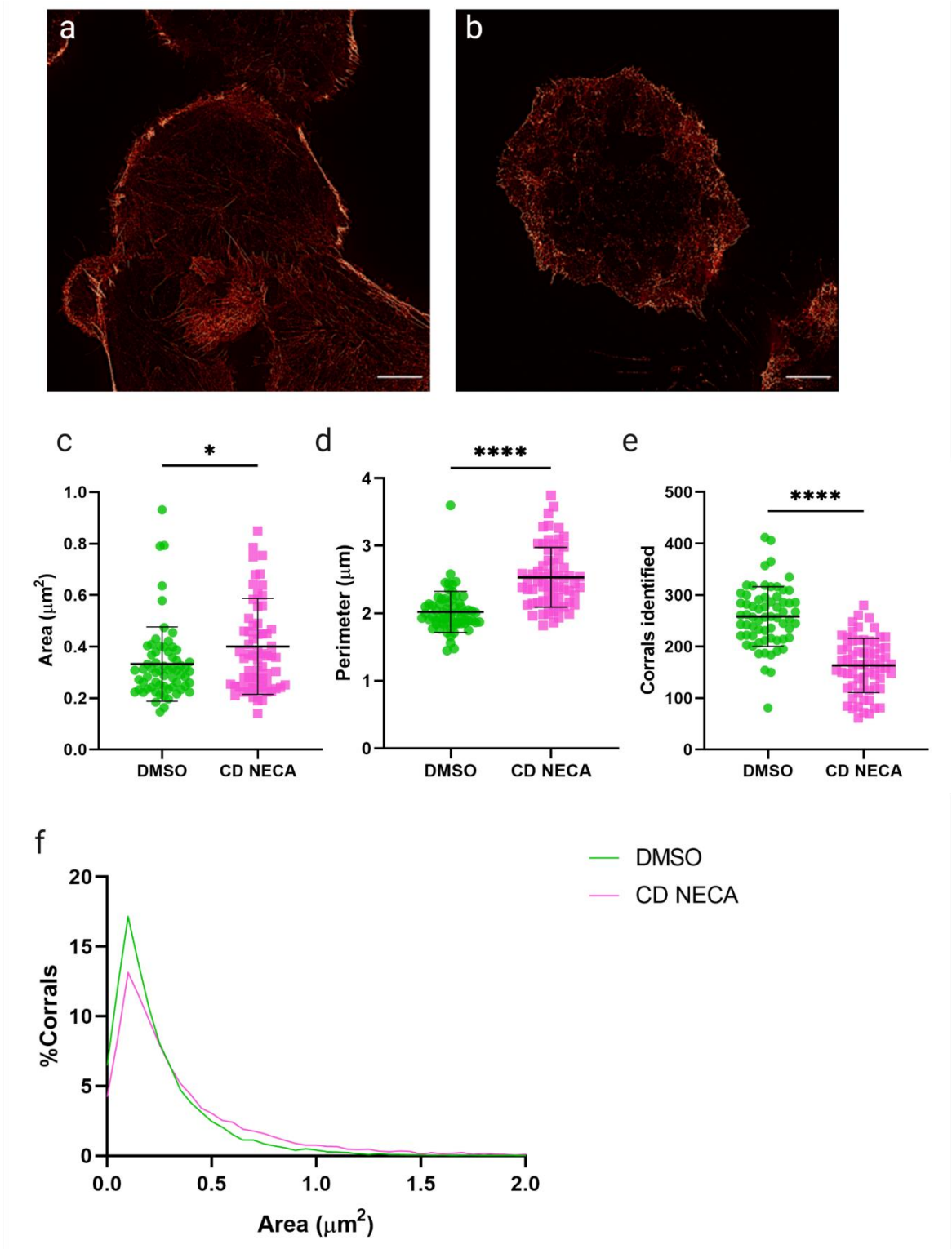

Figure 4.12 - Treatment with CD and NECA suggest abrogating effect of NECA treatment on CD actin disruption*. a) Representative SRRF image of phalloidin labelled actin in DMSO treated untransfected A549 cells, and b) CD + NECA treated cells. Scale bars = 10 µm. c) Mean area, d) Mean perimeter, and e) number of corrals identified in CD + NECA treated cells vs. DMSO control. f) Histogram of all corral areas for CD + NECA treated and control cells. n=3, min. 60 cells per treatment. All error bars show mean ± standard deviation.*

Concurrent actin disruption with CD and receptor activation with NECA showed a similar trend to treatment with CD alone, with the treated cells showing significantly larger and fewer corrals *(*Figure 4.12c-f). However, when normalising the results to the DMSO control as a baseline, it is evident that the size increase is less than in the samples treated with CD alone (Figure 4.14). This is also evident in that the mean area of corrals in CD + NECA treated samples is significantly smaller than in CD alone (Figure 4.13a). This suggests a potential partial rescue effect of adenosine receptor stimulation when combined with actin disruption.

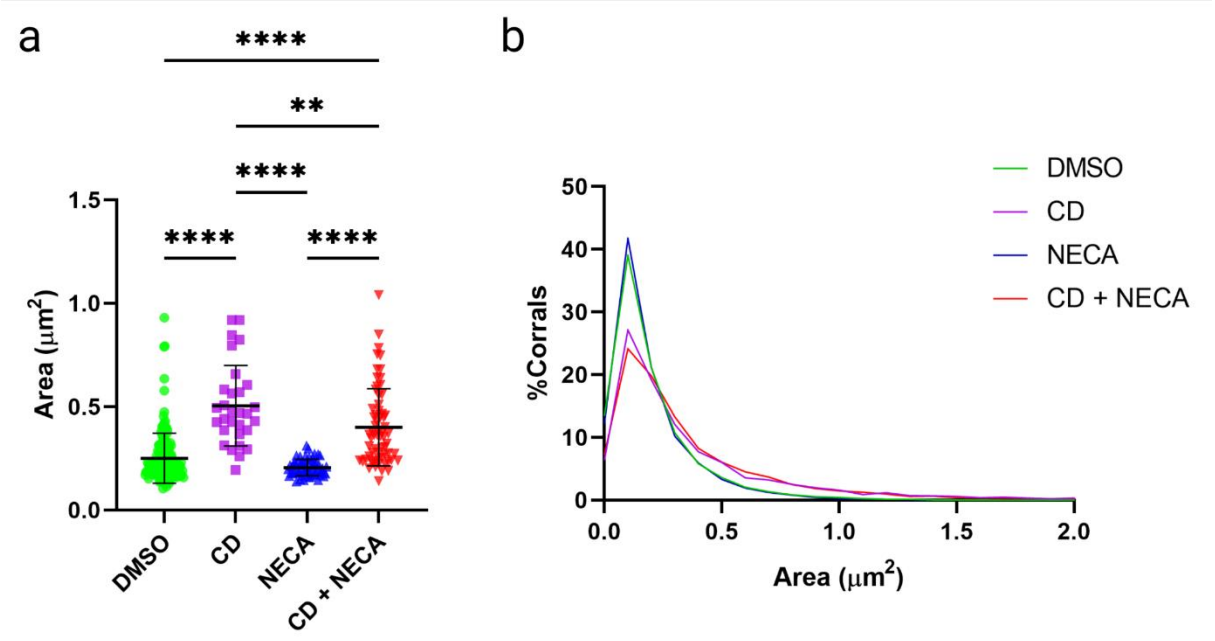

Figure 4.13 – Comparing corrals across drug treatments. *Direct comparison of corrals identified in untransfected A549 cells treated with either DMSO, 1 μM CD, 10 μM NECA, or 1 μM CD + 10 μM NECA. a) Mean area of corrals in each ROI assessed, plotted with error bars showing mean ± SD. ** = p ≤ 0.01, **** = p ≤ 0.0001. b) Histogram of area of all identified corrals across drug treatments.*

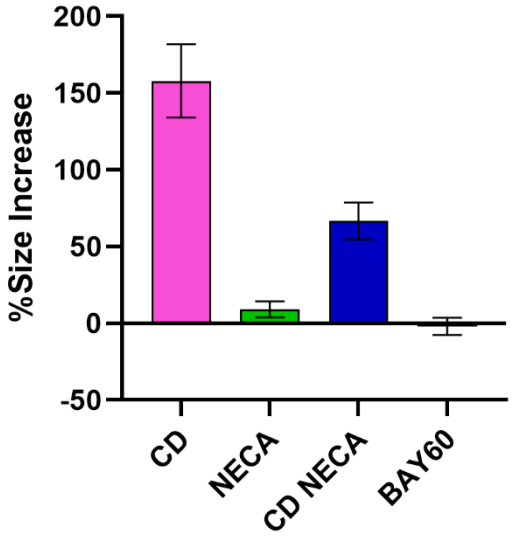

Figure 4.14 – Relative corral area changes across treatments. *% corral size increase for each treatment normalised to control corral area. Mean ± std. dev.*

With these findings in mind, investigation of the A_{2B}R specific agonist BAY60-6583 was undertaken to attempt to identify the specific receptor involved. This showed no significant difference in actin mesh detectable by the analysis method, with mean areas, perimeters and counts similar in both treated and control samples (Figure 4.15c-f). There was some relatively large variation in means between experiments, as can be seen especially clearly in the plots of average corral counts (Figure 4.15e), but the general pattern of no significant size changes was borne out within each independent repeat. The frequency distribution of all corral areas mirrors the averaged findings, showing very little deviation between BAY60-6583 and DMSO treated samples (Figure 4.15f).

So, while treatment with the general agonist NECA showed an effect, treatment with the A_{2B} receptor specific partial agonist BAY60-6583 showed no significant change from the vehicle treated cells.

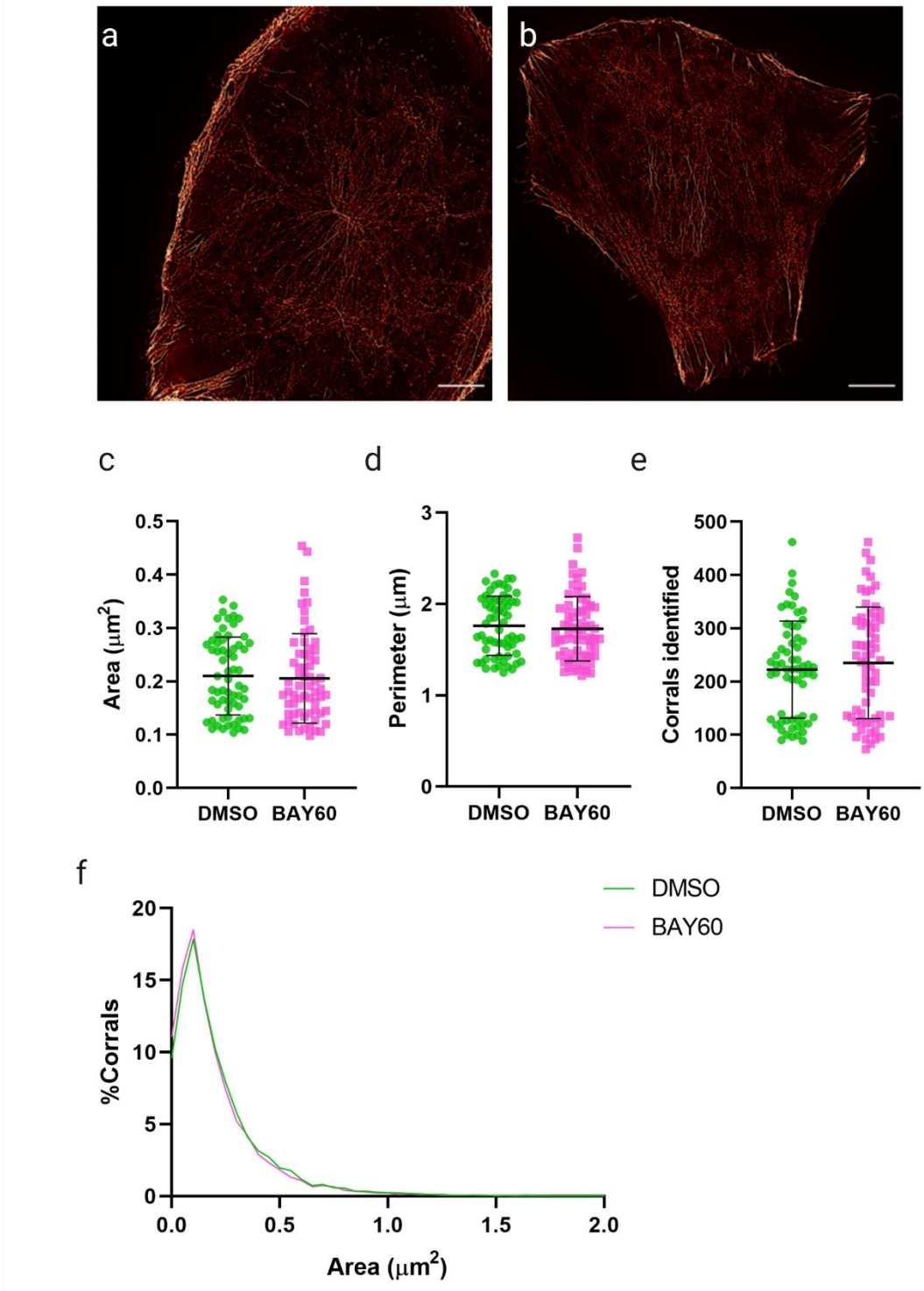

Figure 4.15 - Treatment with BAY60-6583 shows no significant effect*. a) Representative SRRF image of phalloidin labelled actin in DMSO treated untransfected A549 cells, and b) BAY60-6583 treated cells. Scale bars = 10 μm. c) Mean area, d) Mean perimeter, and e) number of corrals identified in BAY60-6583 treated cells vs. DMSO control. f) Histogram of all corral areas for BAY60-6583 treated and control cells. n=3, min. 60 cells per treatment. All error bars show mean ± standard deviation.*

4.3.5 Both LifeAct-mEGFP and SiR Actin permit live cell SRRF imaging

Using SRRF imaging of actin in live contexts necessitated a new actin label, as phalloidin is cell impermeable and toxic to live cells due to its actin stabilising capacity. There are a range of options for live actin labelling, as discussed in many reviews [232]. For the planned experiments in this work, two were tested.

LifeAct-mEGFP

Transient transfection with the LifeAct-mEGFP peptide gave good SNR and performed well when used for SRRF imaging. The labelling was bright and consistent and gave sufficient fluorescence intensity to reduce framerate of capture to 100 fps – 9.2 ms exposure – on the Nikon Ti TIRF system with EMCCD camera, with good SRRF reconstruction (Figure 4.16). Actin structure closely resembles that of the SRRF processed fixed samples, indicating no major effect of LifeAct-mEGFP on actin organisation – that is, at the resolution of this technique. However, this labelling strategy did require transfection, meaning multiplexing with the SNAP-receptors would create some technical and timing issues.

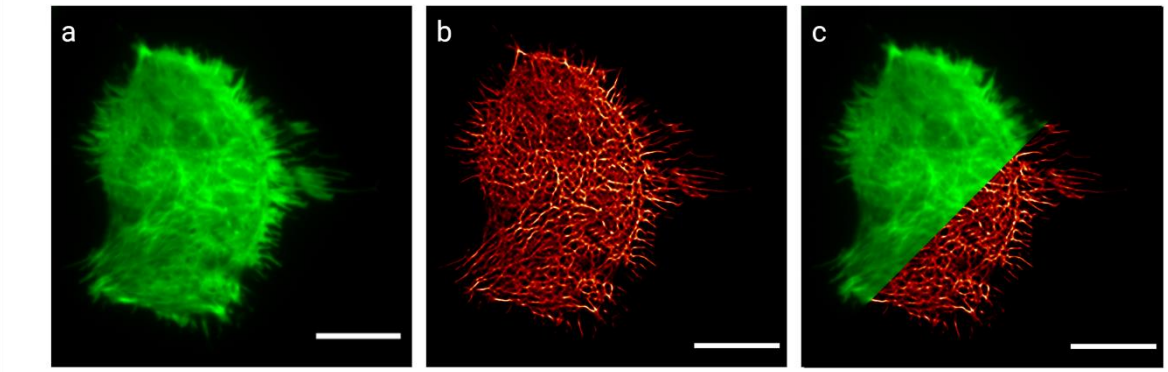

Figure 4.16 – LifeAct mEGFP performs well for SRRF imaging. *a) Raw TIRF image and b) SRRF output, compared in c). Scale bars = 10 µm.*

SiR Actin

The chemical probe SiR Actin is derived from the actin binding small molecule jasplakinolide and fluoresces in the far-red. A major benefit of chemical probes is avoidance of transfection steps and consistent staining of all cells within the sample. SiR Actin is also a fluorogenic probe, meaning wash steps are minimal if required at all. Verapamil, a broad-spectrum efflux pump inhibitor, is supplied with the reagent to reduce rapid expulsion of the probe, if necessary. Fluorescence intensity from varying concentrations of SiR Actin with and without 10 µM verapamil addition was assessed, indicating improved performance with the addition of verapamil (Figure 4.17a, b, f). Free barbed ends are labelled with greater intensity than seen in previous phalloidin labelled samples. Correlative comparison would be beneficial. FRC calculations across all SiR/Ver combinations show limited variation (Figure 4.17c, d*).*

The recommended starting point of 100 frames was used for the investigation of SRRF as a technique, as well as in the fixed cell experiments. However, in live cell contexts this would limit the live imaging framerate to 1 fps, assuming sufficient SNR for SRRF reconstruction at a capture rate of 100 fps, and far slower for less optimal signal. Considering this adaptation to live imaging, varying frame numbers were tested in reconstruction. Comparison of reduced number of frames to the standard 100 frames suggested that for samples with sufficient signal to noise it was possible to drop the frame requirement to half with limited detriment to the reconstruction quality (Figure 4.17e). Frame rate should then be largely dependent on SNR of the label chosen, as this would determine exposure times and therefore how long it would take to acquire a suitable number of TIRF frames per SRRF frame.

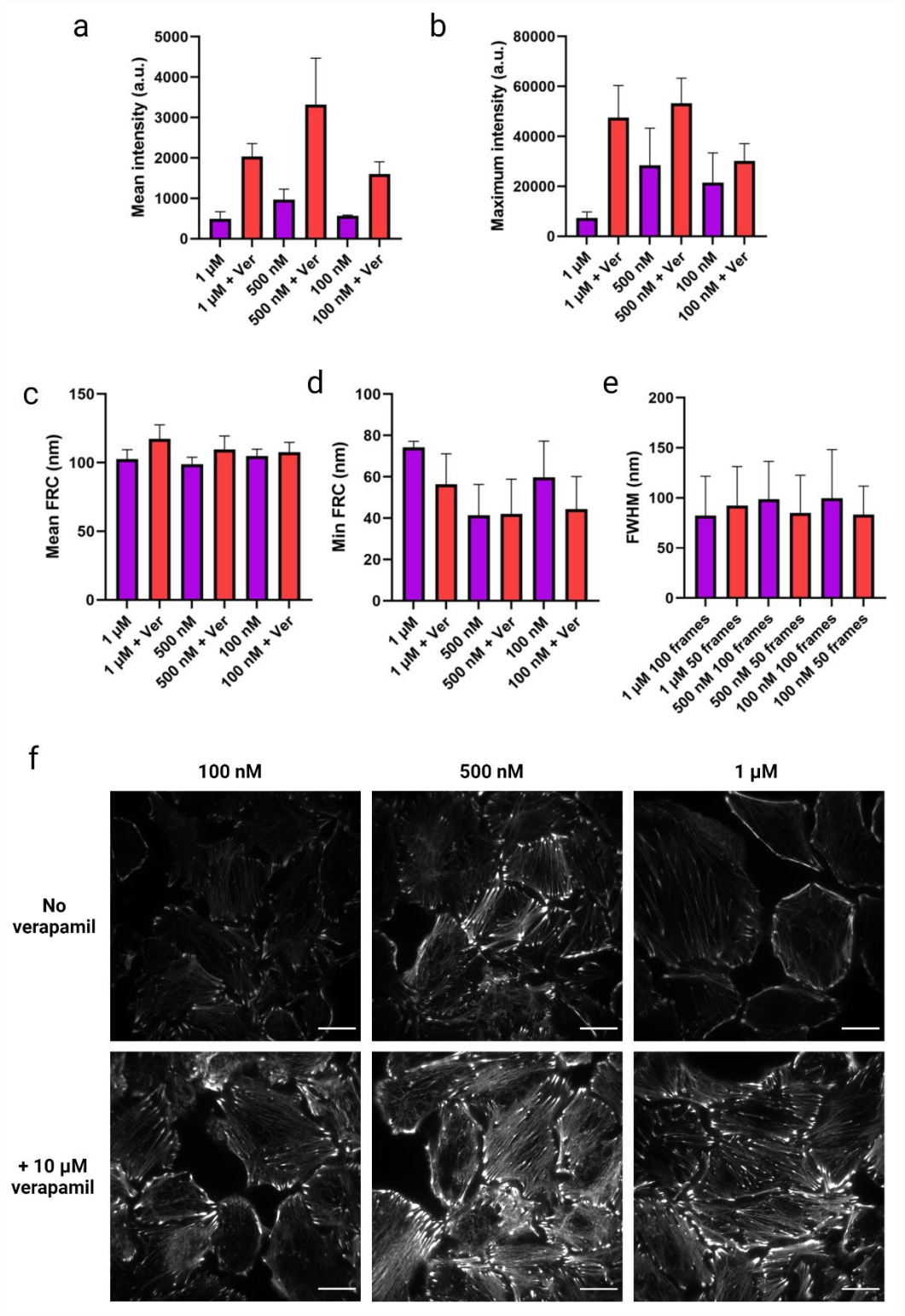

Figure 4.17 – SiR Actin labelling optimisation. *a) Mean and b) maximum fluorescence intensity obtained with and without verapamil treatment for increasing concentrations of SiR actin, with c) mean and d) minimum FRC values calculated for the same. e) Full width half maximum values for SRRF images of verapamil treated SiR labelled cells at standard frames per reconstruction (100 frames) and half frames (50 frames). f) Examples of SiR actin labelled cells described in the graphs above. Intensity range is consistent across the images. All scale bars = 20 µm.*

As an additional control, since SiR Actin is a derivative of jasplakinolide, an equivalent concentration of this actin polymerisation promoter was also tested. This, in accordance with jasplakinolide's actin stabilising capacity, showed significant effect, leaving cells dead and dislodged from the coverslips. Cells treated with a comparable concentration of SiR Actin were alive and well adhered (Figure 4.18*)*. Modifications to the SiR Actin probe have clearly divorced its effect significantly from the base molecule, but very high concentrations of SiR actin were still avoided as is indicated by the product literature and paper [233].

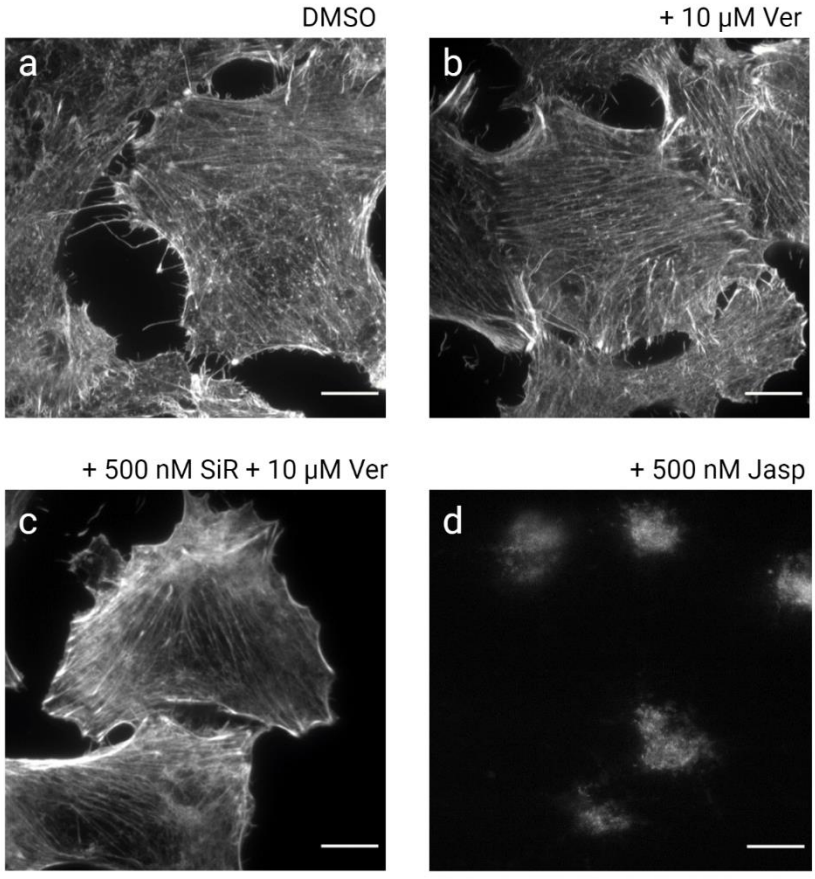

Figure 4.18 – SiR actin and verapamil have no major effect on actin structure*. Phalloidin Al 488 labelled cells imaged in TIRF and treated with either a) DMSO or b) verapamil. c) shows a TIRF image of a cell labelled with SiR actin and treated with verapamil. d) Phalloidin Al 488 labelled cells treated with jasplakinolide. All scale bars = 10 µm.*

4.3.6 Live SRRF analysis development

Using the analysis set out in section 3.3.2 as the starting point, live image analysis could be accomplished by simply calculating corral areas and parameters on a frame-by-frame basis and comparing over time. As a simple example, see Figure 4.19 & Figure 4.20, showing analysis over ten second acquisitions. Plotting all identified corrals from the time lapse overlaid shows the ability of the technique to identify the same regions over time, with a single corral followed as an example in Figure 4.19c, d showing minor fluctuations. Application to drug treated samples is demonstrated in Figure 4.20, showing a slight upwards trend in corral area over time for the CD treated samples (Figure 4.20c).

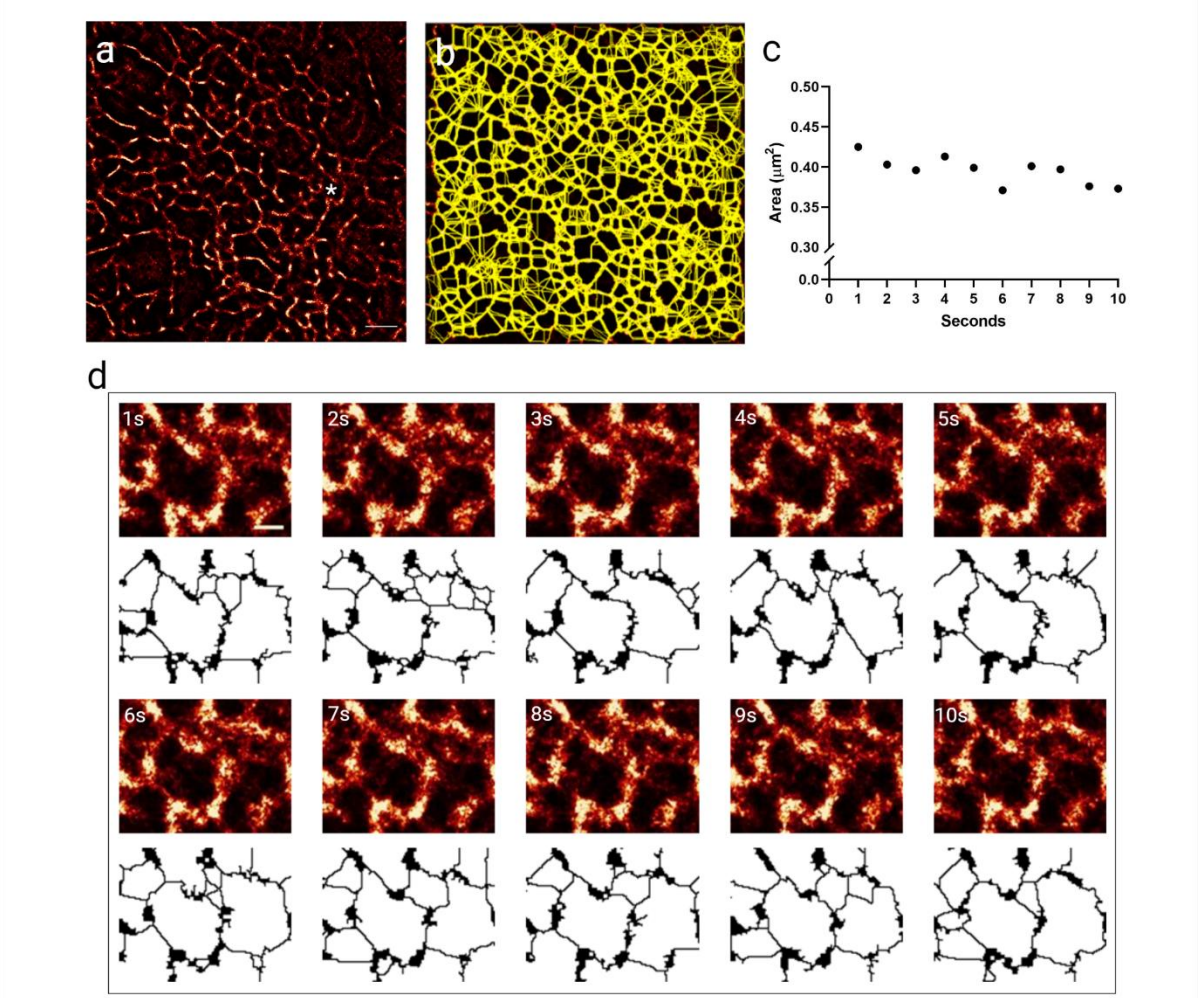

Figure 4.19 – Example of live corral imaging over a short period*. An A549 cell expressing LifeAct-mEGFP was imaged over time in TIRF and the movie used to produce a 1 fps SRRF movie. a) Example SRRF frame of a ten second acquisition, with b) all corrals identified in the ten frames plotted. c) Area of the corral labelled with * in a) over time. d) shows the corrals that are quantified in c). n=1 experiment.*

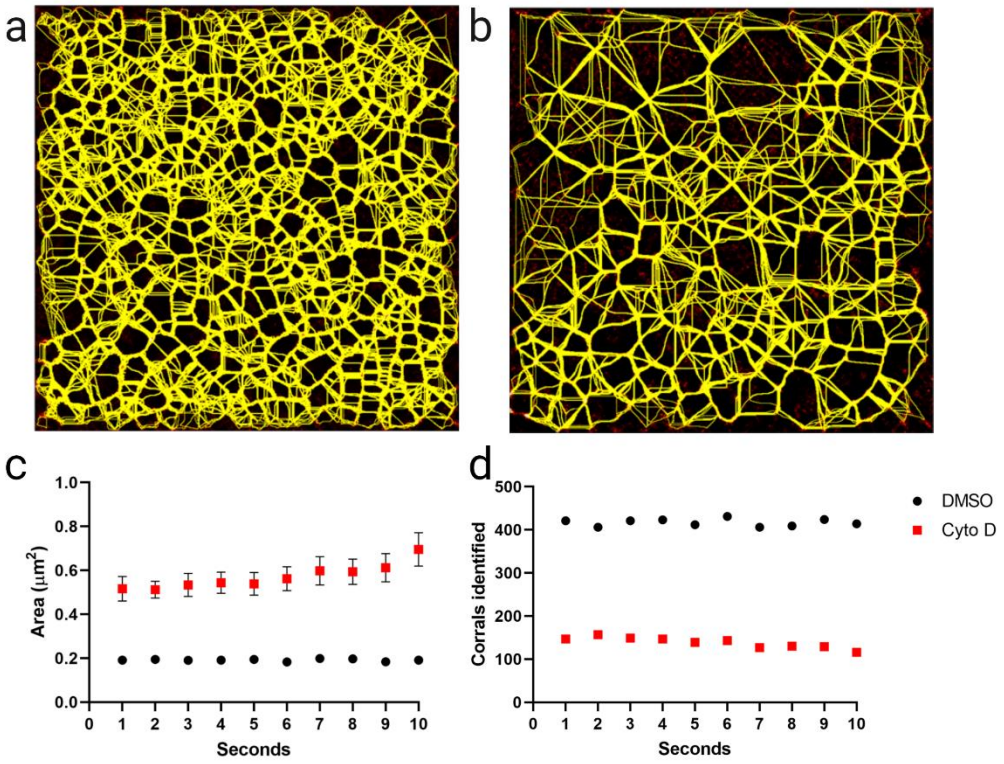

***Figure 4.20 - Analysis of live cell data**. Live SRRF movies underwent corral analysis as described above. Projections of all corrals identified over a 10 second movie are shown for a DMSO treated (a) and a 1 µM CD treated (b) A549 cell expressing LifeAct-mEGFP. Treatment was over 15 minutes prior to imaging. SRRF images were obtained at a rate of 1 frame per second. c) Mean area (± SEM) and d) corral count are plotted over time. n=1 experiment.*

4.4 Expansion Microscopy as a Method for Fine Cortical Actin Assessment

Expansion microscopy diverges from other super resolution techniques by manipulating the sample itself, rather than the photophysics of labels or illumination used. ExM techniques involve the formation of a swellable hydrogel throughout the sample, anchoring fluorophores and protein fragments into the mesh. The sample is then digested, leaving the anchored label in the polymer as a kind of ‘blueprint’ of the cell behind.

In this section, the term ExM is referring to the second iteration of Boyden’s technique, sometimes termed ‘pro-ExM’ in the literature [139], where AcX is used as an anchor to retain protein fragments in the gel post digestion. U-ExM, or ultrastructure ExM [141], was also tested and is covered in chapter 5, and involves protein retention in a modified gel (further described in introduction section 1.9.7).

4.4.1 ExM technique validation and 3D SIM ExM optimisation

Expansion is a robust and repeatable technique, but determination of isotropic expansion and accurate expansion factors is key for quantification of actin structures in this project. Validation and assessment of the performance of the technique in our hands was therefore carried out. For these experiments samples were immunolabeled for α tubulin, as the microtubule network is well characterised and a common imaging target in cells grown in vitro. The use of fluorescent secondary antibodies is also routine in expansion microscopy, thereby overcoming some of the

complexity introduced by non-standard labelling regimes, such as that necessary for actin imaging.

As described in methods section 2.7.6, cells were fixed and labelled pre-gelation. Initial tests showed poor microtubule retention and as such 0.1% glutaraldehyde (GA) was added to the 4% PFA in PEM fixative mixture. Inclusion of GA showed no detrimental effect on actin fixation, so GA was incorporated in all ExM fixes unless otherwise specified. Gel composition and anchor concentrations were as described by Tillberg et al. [139]. Expanded samples imaged with widefield fluorescence microscopy revealed well preserved microtubules, maintaining expected distribution and structure (Figure 4.21). Immobilisation of the gel segment with agarose was sufficient for this mode of imaging.

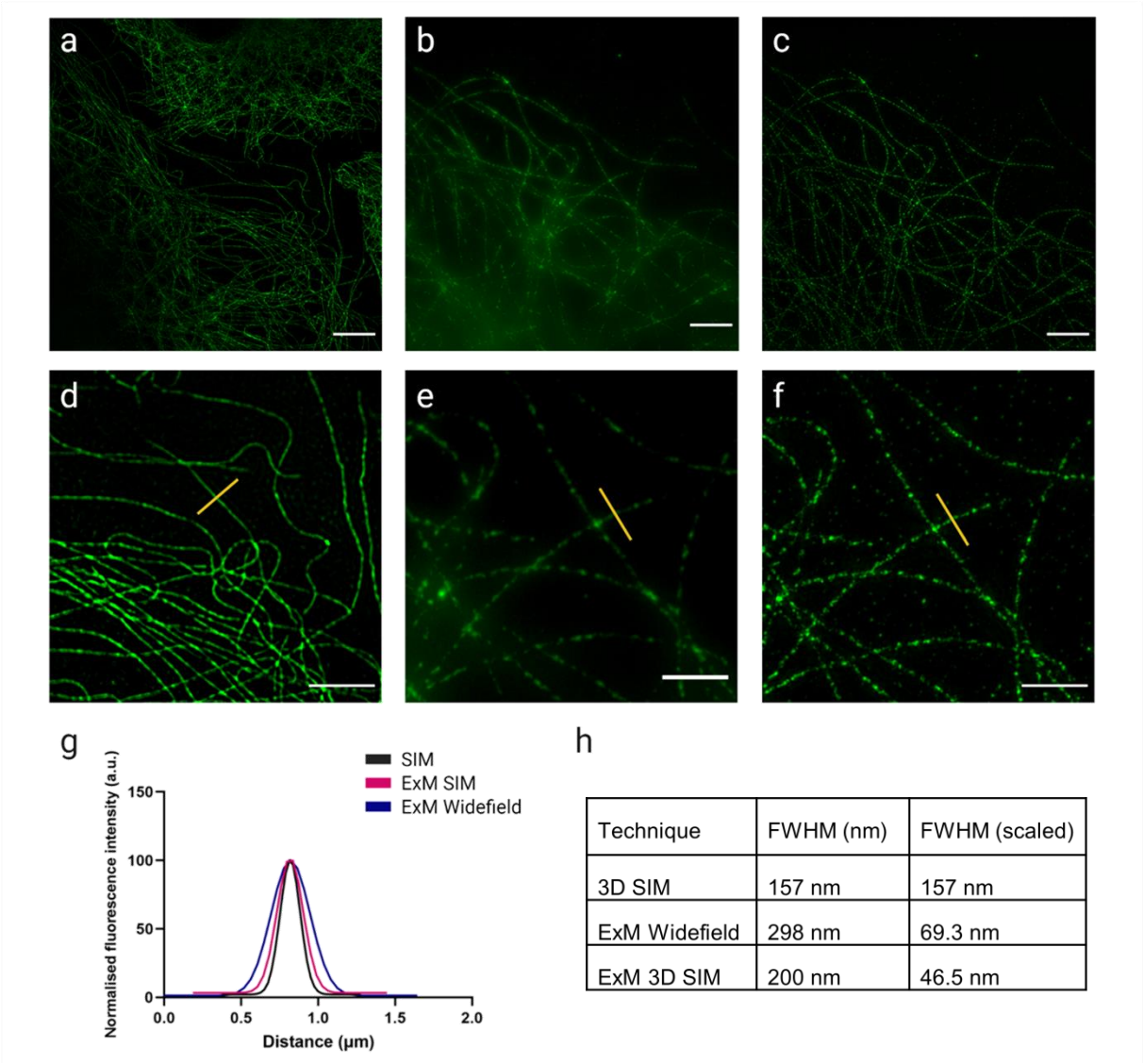

Technique	FWHM (nm)	FWHM (scaled)
3D SIM	157 nm	157 nm
ExM Widefield	298 nm	69.3 nm
ExM 3D SIM	200 nm	46.5 nm

Figure 4.21 – ExM SIM imaging offers a 3-fold increase in resolution over 3D SIM alone*. Examples of α tubulin labelled cells imaged in; a) unexpanded 3D SIM, b) expanded widefield, and c) expanded 3D SIM. d) Enlargement of a). e) Enlargement of b). f) Enlargement of c). Scale bars for a – c = 10 µm, for d – f = 5 µm. g) Gaussian fit of intensity profiles from the yellow lines marked in d-f. h) Full width half maximum values calculated from h), scaled by the calculated expansion factor for these experiments.*

While resolution in WF images was good (see Figure 4.21, Figure 4.24) 3D SIM ExM imaging was trialled in order to further improve resolution. Initial trials where gels were immobilised with agarose showed movement over the course of even a single slice of a 3D SIM image capture, meaning no super-resolved reconstruction was

possible (Figure 4.22c), as SIM is highly sensitive to sample movement. To improve this, poly-L-lysine coating of the imaging dish coupled with wicking of liquid on the cell-containing face of the gel was trialled. This resulted in a much better immobilisation of the sample and permitted SIM imaging throughout the depth of the expanded cells. As the hydrogel wept over the course of imaging, slight movement began to occur, but this seepage was in the order of hours rather than minutes, meaning the issue could be mitigated by limiting imaging time of each mounted section.

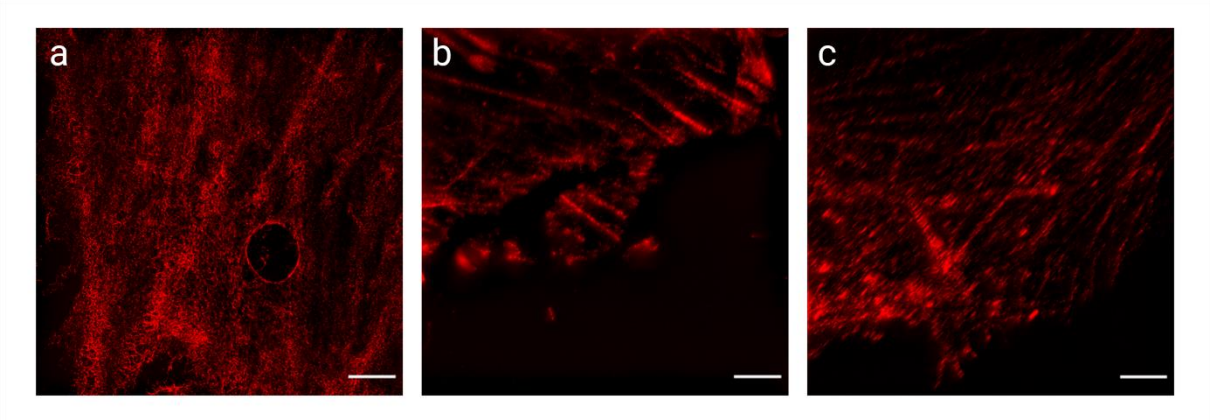

Figure 4.22 – Common issues with ExM Actin labelling. *a) Poor ExM Actin labelling caused by a lack of AcX anchoring step in preparation. b) Fracturing of the labelled cell caused by pre-digestion removal of the gel from the coverslip. c) Gel motion during capture, resulting in a blurred image. All scale bars = 10 µm (not adjusted for expansion).*

In order to confirm isotropic expansion, a correlative experiment was performed. Samples were labelled, anchored, and gelled – but not digested - prior to capture of 3D SIM images. Gels remained in situ on the high tolerance coverslips that cells were grown on, as removal prior to digestion caused fracturing in cellular ultrastructure once expanded (Figure 4.22b). After pre-expansion imaging, the sample was then digested and expanded as normal. The same regions were then imaged with 3D SIM

post expansion. Comparisons of these filaments pre and post expansion reveals clear structural retention (Figure 4.23a-c). Overlaying the two with a simple affine registration lends further weight. A non-rigid registration (elastic registration based on B-splines, using FIJI plugin BUnwarpJ) reveals minimal distortion, as illustrated by the deformation field (Figure 4.23d). This is in good agreement with the findings of the major ExM methods papers (e.g. [138]) and indicates isotropic and robust expansion.

Correlative measurements of features across multiple cells were collated to assess expansion factor, indicating an average expansion of 4.3 (Figure 4.23g). Resolution calculation by way of full width half maximum calculations was adjusted for this expansion factor, resulting in an average FWHM value of 42.38 nm ± 6.66 s.d. Comparisons of representative unexpanded 3D SIM, expanded widefield, and expanded 3D SIM FWHMs are shown in Figure 4.21, with averages calculated shown in Figure 4.23.

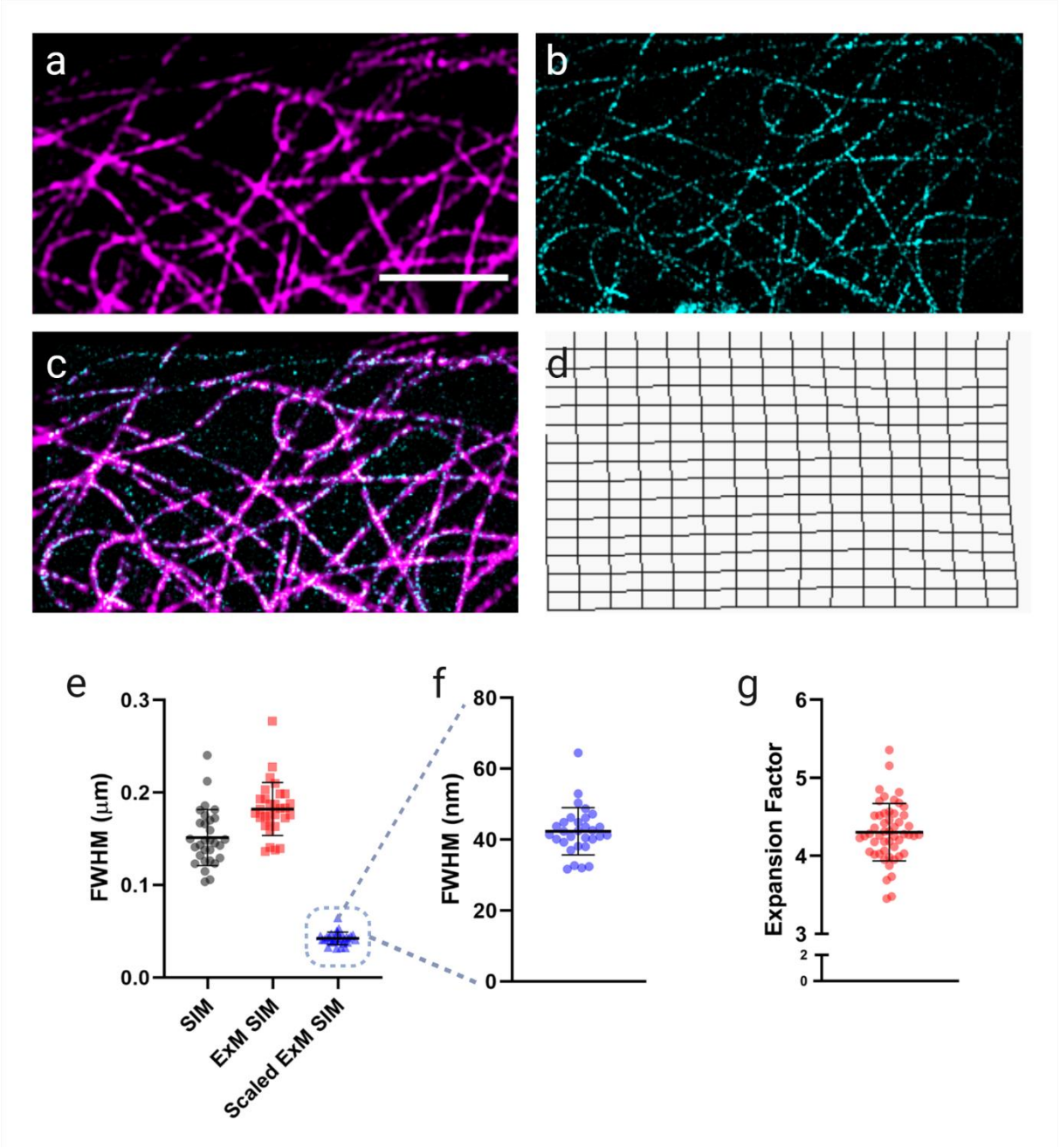

Figure 4.23 – Correlative imaging of microtubules pre- and post-expansion reveals minimal distortion. *a) Unexpanded 3D SIM image of anti-α tubulin labelled microtubules (scale bar = 3 µm), imaged again b) post expansion. c) Non-rigid registration of a & b, with the deformation field used shown in d). e) Full width half maximum calculations from unexpanded and expanded 3D SIM images. An elarged copy of the expansion-factor scaled ExM SIM FWHM is shown in f). g) Mean expansion factor calculated from 30 paired measurements from the correlative experiment.*

4.4.2 Optimising labelling of actin for ExM

Having optimised application of the technique with secondary antibody labelling, further labelling strategies were applied. Given the generally poor performance of actin antibodies, a phalloidin derivative suitable for gelation and retention is preferable. Standard phalloidin conjugates anchor very poorly [156], but currently two alternate approaches are readily available: a specially synthesised reagent functionalized with anchoring groups called Actin ExM (commercially available from Chrometra, based on chemistries published in [157]), or use of an anti-fluorophore antibody, allowing secondary antibody labelling as standard [156].

Labelling with the Actin ExM reagent in unexpanded cells shows similar actin structures to those labelled by standard fluorescent phalloidins (Figure 4.24a-d). For expansion, anchoring with AcX prior to Actin ExM labelling was found to be essential for undistorted retention post expansion (Figure 4.22a). A diffuse stain is characteristic of poor anchoring, and is also seen when anchoring reagents have hydrolysed and should be replaced.

Both widefield and 3D SIM images of expanded samples clearly show actin structure, with fine meshworks and thicker bundled fibres well labelled (Figure 4.24). 3D SIM imaging gives a clear improvement in resolution over widefield imaging, as illustrated in Figure 4.24e-h, and as such 3D SIM imaging was the primary modality used for all further ExM actin imaging.

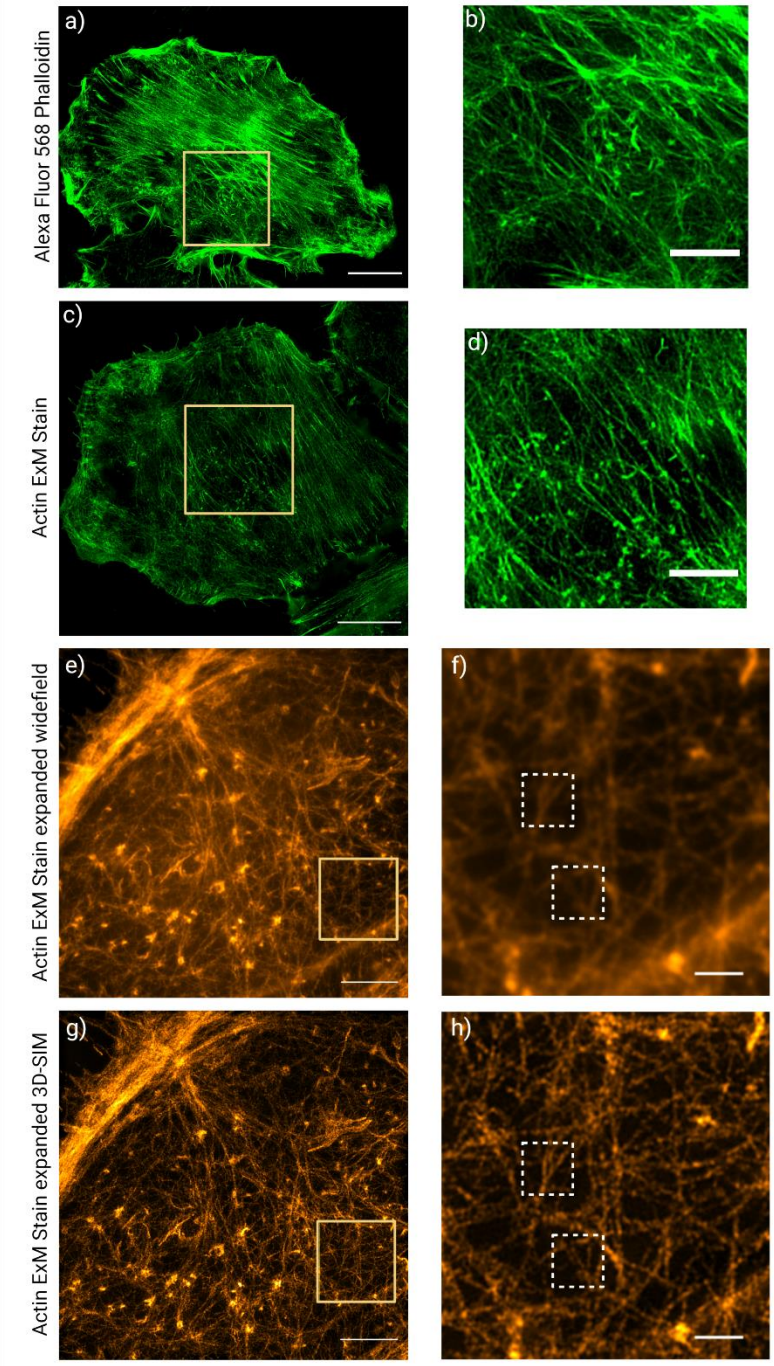

Figure 4.24 - Comparison of actin labelling and imaging modality for ExM samples.
a) Representative 3D SIM reconstruction of an A549 cell labelled with standard AF 568 phalloidin, with b) showing a zoom of the boxed region of the cell. c) Representative 3D SIM reconstruction of an unexpanded, un-gelled A549 cell labelled with Actin ExM, with d) showing a zoom of the boxed region of the celll. e) Representative widefield image of an Actin ExM labelled and expanded cell. f) Enlargement of the yellow boxed region in e). g) 3D SIM reconstruction of the same Actin ExM labelled expanded cell in e), with h) showing an enlargement of the yellow box. Boxed regions in f) and g) highlight regions of visibly improved resolution in the 3D SIM image. Scale bars: a, c, e & g = 10 µm, b & d = 4 µm, f & h = 2 µm. Scale bars are not adjusted for expansion factor for images e-h.

Improvement in Z resolution is also apparent, especially in 3D SIM images (Figure 4.25). The improvement in resolution is not isotropic given the nature of SIM as a modified widefield techniques. Image stacks were taken a few microns around the basal actin, permitting visualisation of, for example, stress fibres and apical cortex sitting higher than the underlying network (Figure 4.25, Video 1). This also made adjustment of reconstruction parameters involving out of focus light easier, as bright features like stress fibres can often present in other slices as artefacts. Having the raw data include these bright points allows more precise adjustment.

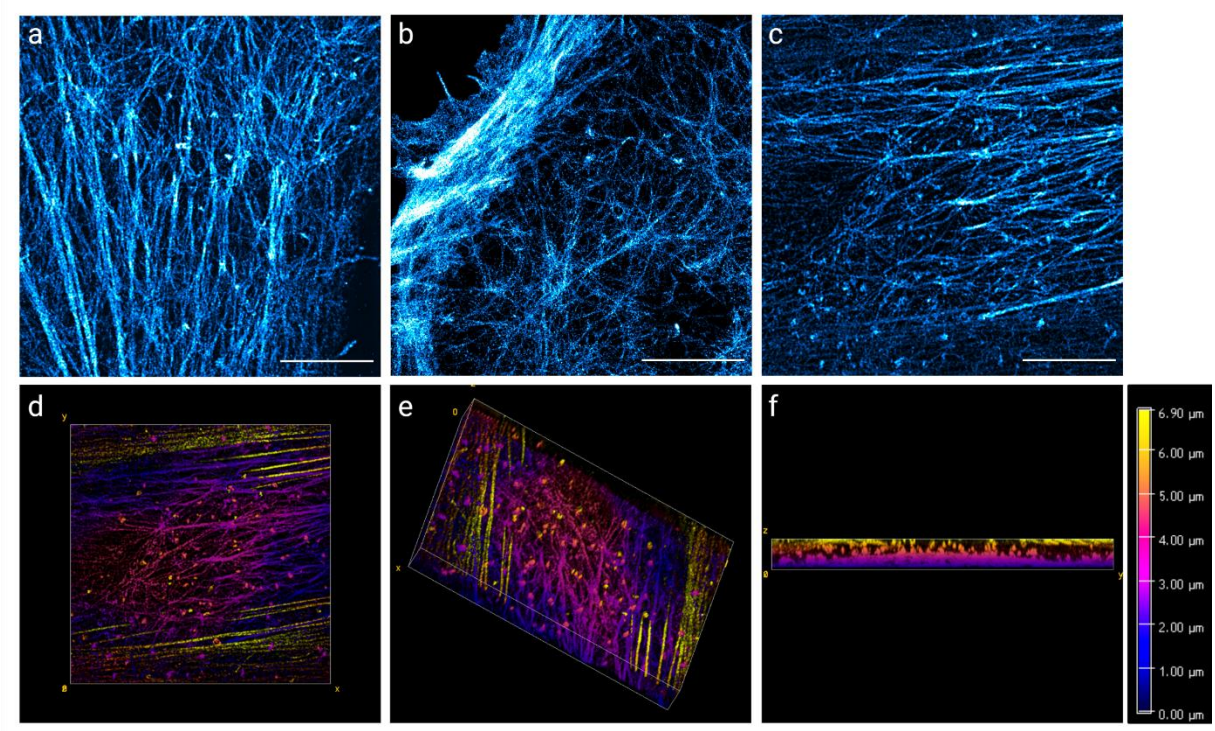

Figure 4.25 – ExM - 3D SIM imaging of actin reveals high resolution detail in all axes.
a – c) Examples of ExM Actin labelled expanded cells imaged using 3D SIM. All scale bars = 20 µm. d – f) Angles of the stack shown in c), demonstrating the improved Z resolution of the technique. The depth scale for images d-f) is shown. A video of this sample is shown in the appendix.

4.4.3 Developing ExM Actin analysis

Analysis of cortical actin from ExM images presented new challenges. Some discontinuity in filament labelling, significant intensity variations between thicker and finer filaments, as well as the contribution of out of focus light (although minimised by adjustment of SIM reconstruction parameters) made application of the analysis used for SRRF images (see section 4.3.2) unfavourable. At these scales, discontinuity is somewhat expected, given that the dilution of label 64-fold across all dimensions is inherent to expansion, coupled with anchor loss and occasional degradation of fluorophores during gelation.

It is also not possible to use TIRF-SIM for these samples as the expansion moves the sample too far from the coverslip for TIRF based techniques. As such cortical actin density was approximated by examining fluorescence intensity across ROIs of 3D SIM reconstructions. Randomly oriented lines across full ROIs were selected and fluorescence intensity graphs generated (Figure 4.26a-d). These values were normalised and local maxima identified, with a threshold to eliminate background but no threshold on peak prominence, allowing resolution of closely adjacent yet still separate filaments (Figure 4.26d-e). Where peaks were not clearly delineated, a straight line was drawn to separate each peak, and width at half prominence calculated from these (Figure 4.26e). Repeating this operation hundreds of times over a single image and comparing the numbers of peaks calculated for each ROI can serve as a way to compare filament density.

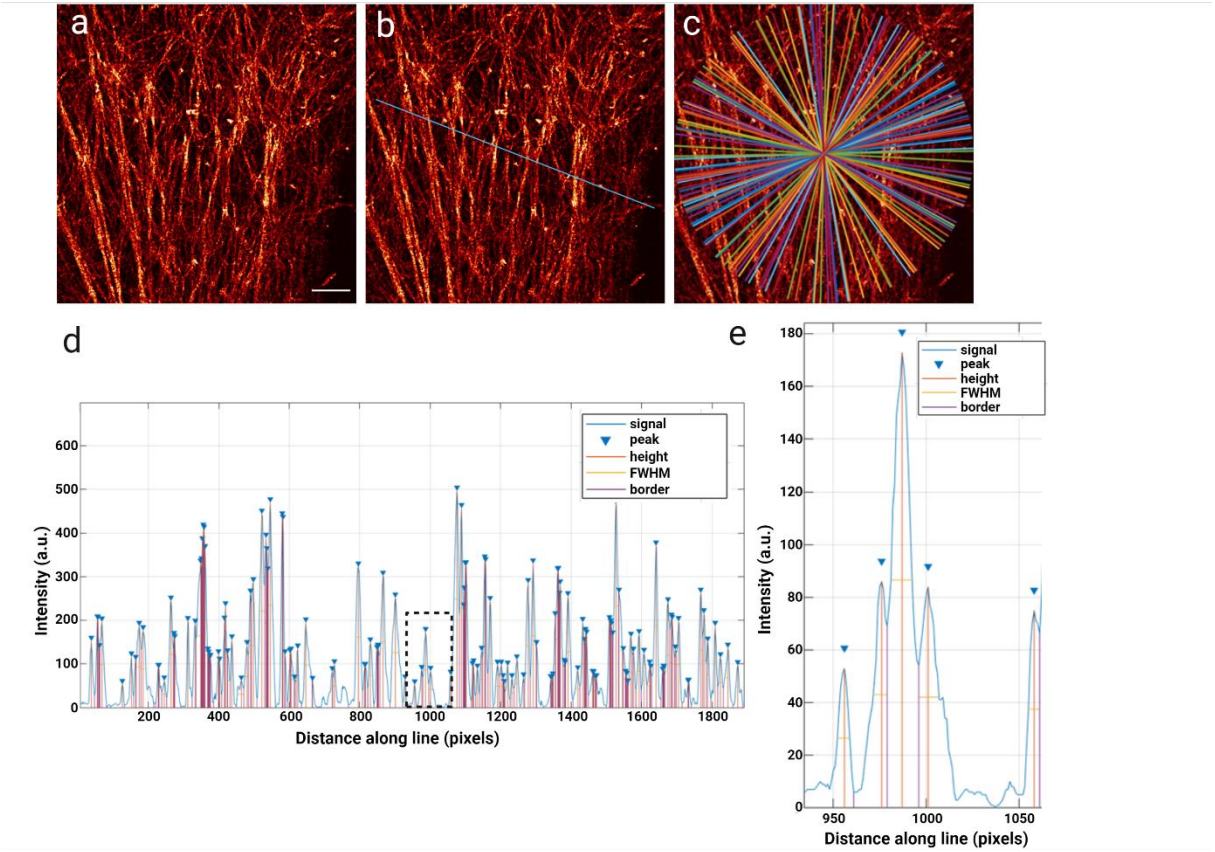

Figure 4.26 - Example of analysis of expanded actin. *a) Example of 3D SIM imaged expanded actin, with a scale bar of 10 µm (uncorrected for expansion factor). b) Randomly generated line across the image for analysis, where intensity along this line is plotted in d). c) Example of the distribution of randomly generated analysed lines when repeated 100 times. d) Normalised intensity line plot of fluorescence intensity (a.u.) vs pixels of line in b, with peaks identified and height and width denoted as in the key. e) Enlarged region of d), showing identification of all distinguishable peaks above a manually set threshold.*

As in the case of SRRF analysis, simulated data was generated as a way to test the behaviour of this density analysis. This time, filaments were convolved without additional noise, as this would not be representative of 3D SIM reconstructed images and would impede this particular analysis. Meshworks of varying densities, from 5 to 25 seed filaments, were generated and analysed (Figure 4.27a-e). Application of the analysis showed increase in mean peak numbers as density increased, and a concurrent drop in mean distance between identified peaks (Figure 4.27f-h) indicating that the method is robust and able to report on networks of varying density.

When comparing reported values from the convolved images to the actual number of filaments per image, consistent underestimation is evident (Figure 4.27i).

To demonstrate this on data from expansion experiments, images of expanded microtubules and actin were compared, showing clearly distinguishable differences in peak number and distance between peaks (Figure 4.28). Though peak to peak distance reported significant variability, especially for tubulin, when plotting this data as a histogram the two filament sets are still easily separable (Figure 4.28e, f).

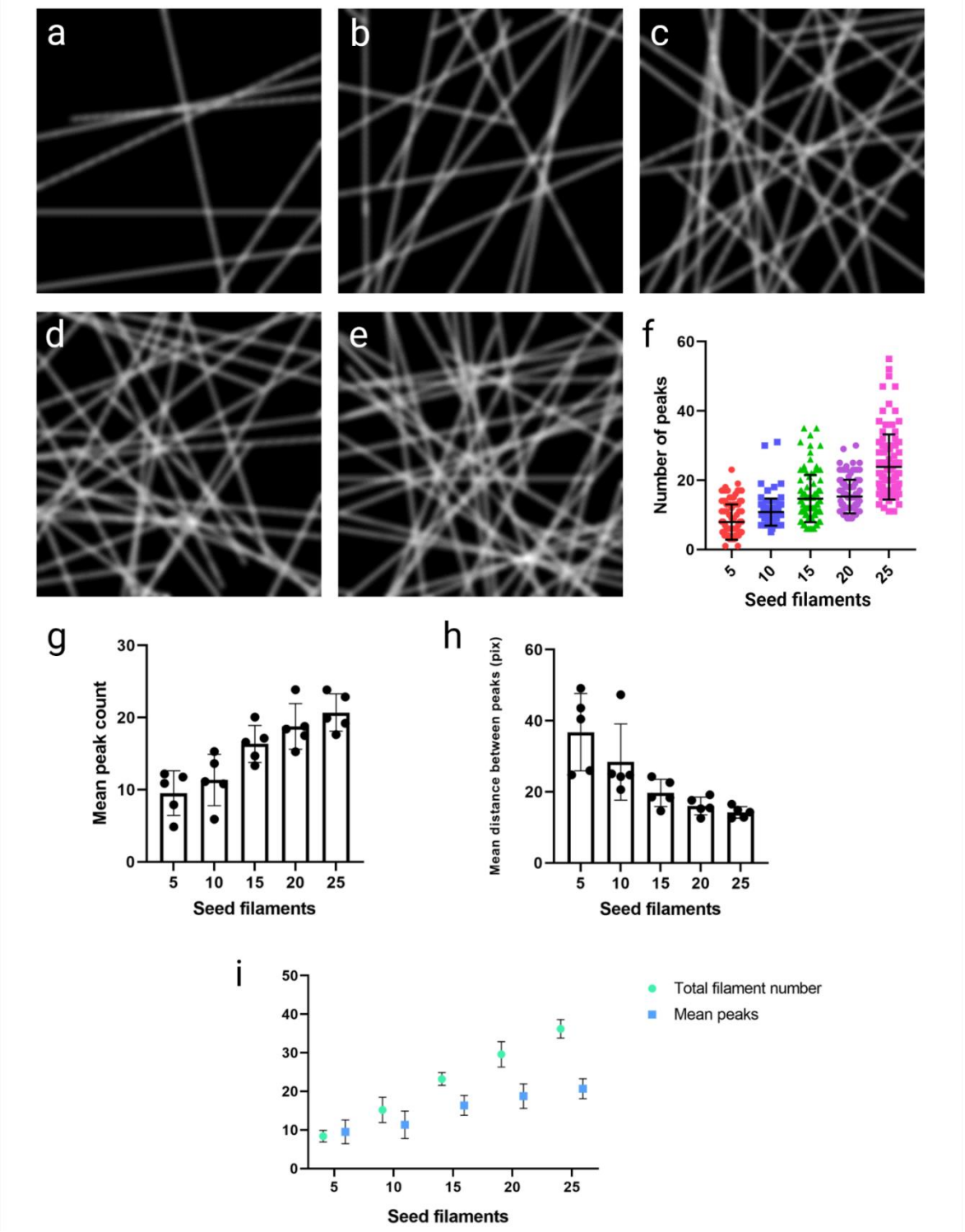

Figure 4.27 – Simulation of meshworks to test density analysis. *Simulated meshworks with a) 5, b) 10, c) 15, d) 20, and e) 25 seed filaments, with each filament having the potential to act as a seed to a daughter filament. f) Graph of peaks identified over 100 repeats of density analysis for the images shown in a–e). (g) Mean peak count and h) mean distance between peaks over 5 individual images for each seed filament condition. i) Density analysis underestimates total filament number. The graph shows the total number of filaments identified per ROI for 5 individual simulated images for each seed density, compared with the mean number of peaks identified in the same images using our density analysis.*

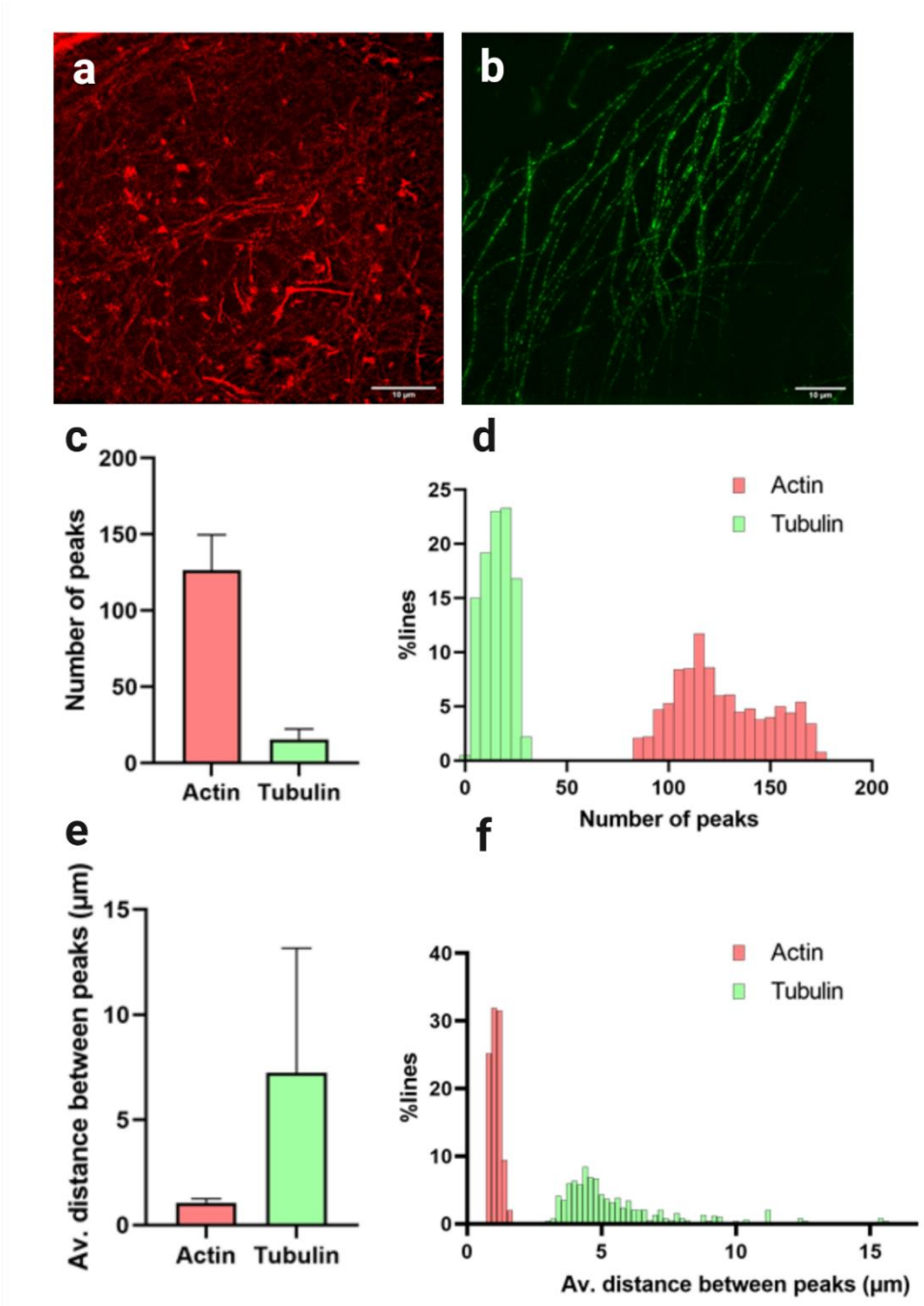

Figure 4.28 - ExM filament analysis distinguishes between small and large meshworks. *a) Example 3D SIM image of expanded actin and b) of expanded tubulin (both scale bars 10 µm). c) Mean number of peaks ± standard deviation. identified over 100 repeats of the analysis for each image, with d) showing a histogram of this dataset. e) Mean distance between identified peaks ± standard deviation over 100 repeats of the analysis for each image, with the histogram shown in f. Lengths in e and f are not corrected for expansion factor.*

4.4.4 Analysis of SIM ExM data requires additional optimisation for use with drug treatment

This method of analysis was subsequently applied to quantitatively compare actin organisation in NECA and cytochalasin D treated cells. For NECA treatment, repeats showed significant variability within the control, so data should be considered with this in mind. Two repeats showed the same pattern, with NECA treatment indicating an increase in the number of peaks identified. However, when including the third repeat which showed no significant change, there is no statistical significance between the two treatments (Figure 4.29a-c). Attempts to apply the technique to cytochalasin D treated samples were unfortunately less successful, as clumping of capped actin filaments resulted in very bright regions, increased background, and a more homogenous signal over filamentous samples (Figure 4.29d,e). This results in excessive high intensity peaks that are not easily filterable with a rigid threshold.

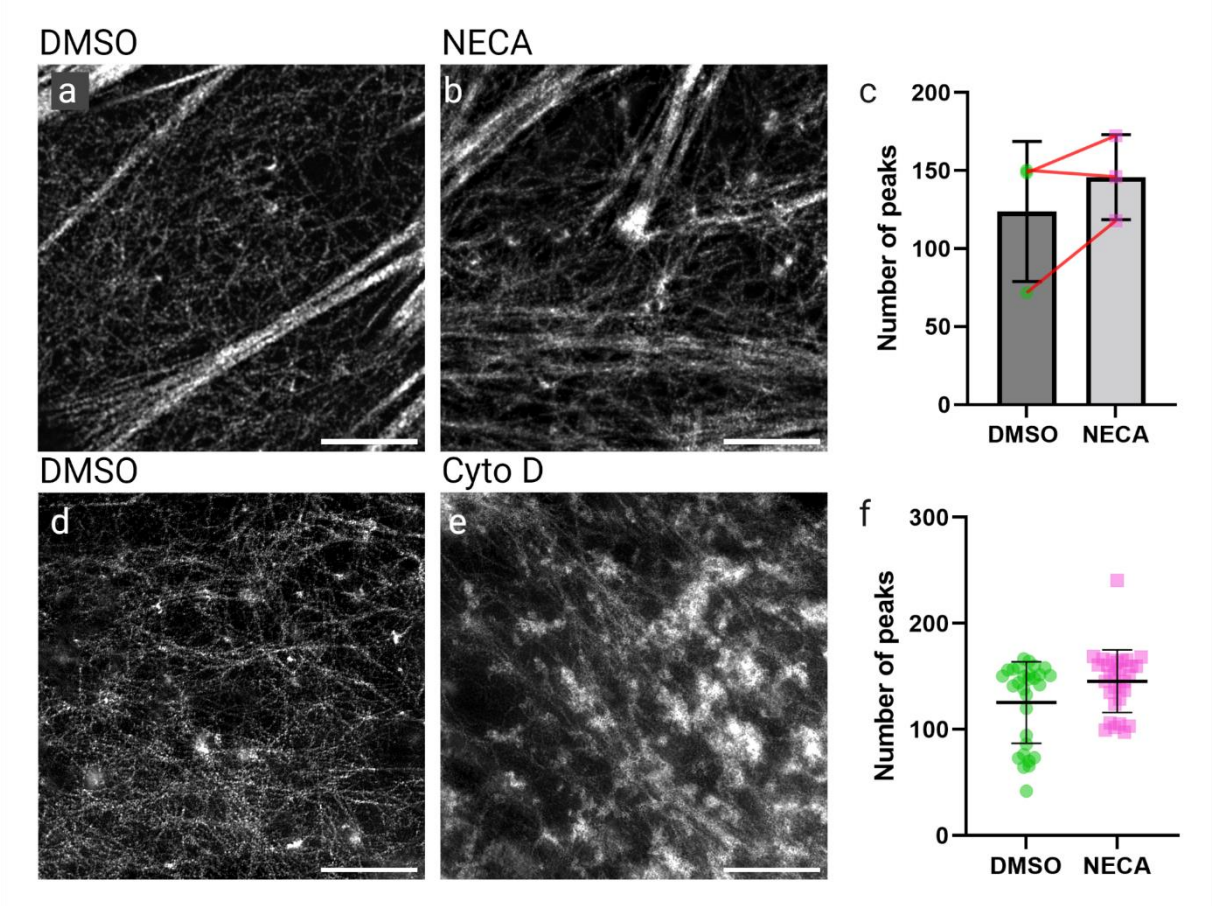

Figure 4.29 - Analysis of SIM ExM data requires additional optimisation for use with drug treatment. *3D SIM ExM images of representative examples of a) DMSO and b) NECA treated samples, with c) showing mean number of peaks over 3 independent repeats, >29 cells per treatment. f) Means of each cell ROI analysed for the data shown in c). d) DMSO and e) Cytochalasin D treated examples from actin disrupting experiments. All scale bars = 20 µm.*

4.5 Discussion

This chapter aimed to optimise workflows for analysis of both live and fixed actin with a view to the later dual imaging of both actin and receptors. Analysis was developed and applied to actin disrupting and receptor stimulating conditions for each method, providing measures of actin reorganisation.

4.5.1 SRRF actin analysis development and testing

The SRRF analysis presented here contrasts other actin filament analysis methods in that, rather than skeletonising the filaments and calculating filament length, filament branching, branching angle, etc., this method assesses the shapes and sizes of the meshwork.

Accurate quantitation of the actin meshwork depends on the generation of reliable, quality super-resolved images. SRRF imaging performs well on actin, giving clear and reproducible structures that correlate well with the TIRF raw data and as quantified by SQUIRREL analysis. However, false sharpening and the collapsing of adjacent objects is a common issue in SR reconstructions, including in common single molecule localisation microscopy reconstruction algorithms [166]. Care should be taken when reconstructing super-resolution images and appropriate quality control checking performed. The application of SQUIRREL [203] here helped to identify regions of possible error in reconstructions. These were mostly observed in brighter, sharper regions of the reconstruction. It is important to note, however, that the error

maps are only internally relative; RSP values give a more inter-experiment and inter-technique comparable value, and in our experiments RSP values were consistently high.

The meshwork analysis developed here performs well on SRRF data, and on data simulated to represent the binning and pixel size of SRRF data. The comparison of simulated versus ground truth data also highlighted that the analysis can underestimate some areas by over segmenting as well as missing smaller regions that sit below the resolution limit. This is, however, an issue inherent to any resolution limited image, and can be overcome by filtering out very small corrals (i.e., those below the resolution limit) from further analysis. With this caveat in mind, the analysis performed well, identifying similar regions, which were also similar in size, between our simulated and ground truth data.

Skeletonisation analysis methods work well for continuous, well separated filaments, such as microtubules, intermediate filaments, or even thicker actin stress fibres (see reference [230] for implementation of their technique SFEX to quantify actin stress fibres in TIRF images). When considering super resolved fine actin meshworks, however, discontinuity of labelling and reduced fluorescence intensity is an inherent issue. This can lead to artefacts like mismatching of filament segments and artificial removal of sparser filaments. Additionally, SRRF brings its own complexities – fluorescence intensity in the raw image does not directly correlate with intensity in the reconstructed image. Rather, this is defined by the goodness of fit for each pixel, and

therefore can have unexpected effects on methods designed for more traditional image types.

By focussing on the gaps the actin leaves rather than trying to extract information from the filaments themselves, artefacts introduced in the thresholding steps can be somewhat mitigated. A recent preprint describes an algorithm called FiNTA that performs more advanced and accurate filament tracing than typical skeletonisation [234], but this technique is reported to perform best on filaments of uniform thickness, an area where our analysis appears more robust.

The simple technique we describe should be easily applicable to other super resolution techniques, such as SIM and STED, but better options are available for SMLM. As a rule of thumb, where analysis can be applied directly to the point cloud data generated in single molecule techniques rather than images reconstructed from this data, it should be. This retains the maximum information and resolution gained by using these techniques. Peters et al. [114] developed an algorithm to perform filament tracing from the spatial point patterns generated in SMLM imaging of actin, allowing extraction of information directly from the point cloud rather than the reconstructed image. Identification and differentiation of fibrous and clustered structures in SMLM data is also possible using Williamson et al.'s machine learning based analysis approach [174].

4.5.2 Effects of actin disruption and receptor stimulation on actin

To further test the analysis, and to see if it could detect changes in the actin network, cells were treated with the actin disruptor cytochalasin D. From this analysis, the effect of cytochalasin D on the samples was as predicted – a visible disruption of normal cortical actin structure, with the persistence of some, especially thicker, filaments. Fritzche et al. used varying concentrations of cytochalasin D to distinguish between ‘typically long cytD-insensitive formin-mediated filaments’ and the shorter, more dynamic Arp2/3 nucleated filaments that were sensitive to the drug [26]. Cytochalasin D acts by binding the barbed end of actin filaments, inhibiting polymerisation and dissociation from this end. Typically, cytochalasin D induces the formation of denser focal accumulations of actin, likely by interrupting normal anchoring of filaments by capping proteins [235]. As such, normal membrane associations should be severely disrupted, as indicated by our data.

The accurate representation of cytochalasin D effects by our analysis workflow therefore strengthens justification for broader application and to assess subtle changes in cortical actin network organisation in response to receptor inhibitors and stimulation, among others. It should be considered, however, that all actin in the cell will be affected by cytochalasin D treatment, not just the cortical filaments.

With regards to NECA stimulation findings, there is evidence that stimulation of adenosine receptors can inhibit actin polymerisation in neutrophils via a cAMP

dependent mechanism [236]. Increased cAMP levels have been shown to reduce the volume of F-actin in treated CHO cells [191]. Other studies found that NECA treatment induced a transient increase in polymerization in RBL-2H3 cells, with values returning to baseline after 10 minutes [237]. In an endometrial adenocarcinoma cell line, more similar to the A549 line, it was shown through NECA and antagonist treatments that A_1R signalling was necessary for cortical F-actin maintenance, while treatment with an $A_{2B}R$ antagonist resulted in a moderate increase in cortical actin [238]. NECA treatment alone did not significantly alter overall F-actin levels by their measures. Given the differing affinities of the two receptors for adenosine, the two may act together to regulate nucleation of actin filaments, with $A_{2B}R$ being a natural limiter when high levels of extracellular adenosine are present. $A_{2B}R$ mRNA levels are significantly higher than A_1R mRNA in A549 cells, which may explain how NECA alone could have a significant effect. Measuring corrals is also a more sensitive technique than assessment of cortical fluorescence intensity, as performed in [238], and may therefore have picked up a more subtle shift.

Importantly, these experiments were performed in untransfected cells, indicating that endogenous expression of adenosine receptors in A549 cells is sufficient to induce remodelling of the cortical actin cytoskeleton. These experiments should be repeated with overexpressing cells and receptor-specific agonists to investigate possible specific responses. In a similar vein, it should be noted that NECA is a non-specific agonist and can stimulate any member of the adenosine receptor family. Cell Atlas (see [196]) indicates mRNA expression of all but ADORA3 in A549 cells, although

only A_1R and $A_{2B}R$ were detected at levels which the database defines as likely to result in protein expression, as supported by our findings that endogenous $A_{2A}R$ is not detectable with a fluorescent ligand in these cells. The response still cannot be definitively linked to one receptor when using NECA, so specific agonists and antagonists should be investigated.

BAY60-6583 treatment showed no significant effect on actin organisation, which may be in part due to the nature of this drug as only a partial agonist [215]. This could also suggest $A_{2B}R$ has limited effect on actin reorganisation, but solid conclusions cannot be drawn from this data alone. Experiments including selective antagonists and agonist combinations would be necessary to fully unpick these links.

When disrupting actin and treating with NECA simultaneously, the increase in corral size is similar to when treating with only cytochalasin D. Normalisation of results to the DMSO control as a baseline shows that the relative increase in size in NECA + CD samples is less than with CD treatment only. This suggests a potential partial rescue effect of adenosine receptor stimulation on actin disruption. Taken with receptor findings in chapter 3, and when linking this to the previously discussed effects of adenosine receptor stimulation on actin, we see a clear connection between the findings.

4.5.3 Live SRRF investigations are the next step to assess actin dynamics

SRRF imaging has been shown to be applicable to live imaging of membrane proximal actin structures in this chapter, building on existing applications of the technique [128]. A key consideration for this application, however, is live actin labelling.

The two options explored in this thesis were LifeAct-mEGFP and SiR Actin. While as shown above both performed well for imaging, neither are without issue. LifeAct-GFP2 has been reported to affect F-actin structure as well as cell morphology and migration in a dose dependent manner [239]. Transient transfection may therefore be best avoided to limit this source of experimental variability. These investigations were diffraction limited, so assessment of finer actin filaments would also be pertinent, as LifeAct tags are very commonly used in this research space. It should also be noted that constitutively expressing LifeAct mice are viable and have no major phenotype [240].

SiR Actin equally has concerns worth consideration, as it is a derivative of the actin stabilising drug jasplakinolide. Concentrations above 100 nm were reported to reduce cellular proliferation [233], but did not affect mitotic duration or cleavage furrow appearance. 23 hours of SiR Actin treatment resulted in only a 1.7% increase in multinucleated cells, indicative of aberrant division [233]. As such, the concentrations and incubation times used in the above work, major disruptions were not seen.

These potential limitations of live labelling are another argument for performing both fixed and live experiments – any major artefactual behaviours or structures should be identifiable when comparing between results.

When considering live SRRF analysis, two options are possible. As demonstrated above, the simplest application is calculating corral areas and parameters on a frame-by-frame basis and comparing over time. A more complex but equally more informative approach would be to assess corral persistence and the formation of new corrals between frames. This would involve identification of the same corral consistently across images, and a metric to assess if the corral had grown or split. This could be performed by calculating the centroid of each ROI and using this as in a spot tracking method – setting allowed distances between frames before the centroid would no longer be considered to refer to the same corral. An illustration of the concept is shown in Figure 4.30.

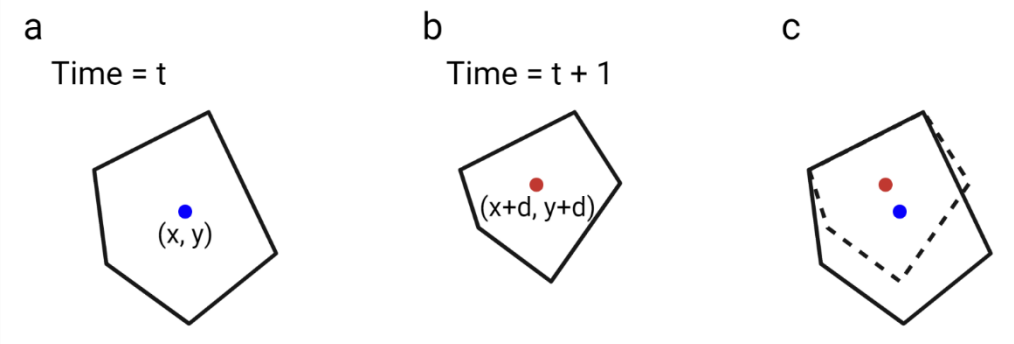

Figure 4.30 – Centroid based live SRRF tracking concept. *a) An example corral at time t, which has shrunk by time t + 1 as shown in b). The centroid has been displaced, as illustrated in the overlay in c).*

4.5.4 Application of expansion microscopy to actin imaging

Expansion microscopy offers a far superior resolution to SRRF, albeit only in fixed cell contexts. Underutilised in the study of actin, expansion microscopy is shown here to faithfully preserve both bundles and fine actin structure, with resolution almost comparable to SMLM when used in conjunction with SIM [152]. Expansion microscopy allows for simple and rapid multiplexing of labels. The nature of ExM as, essentially, a modified standard immunofluorescence technique, means that imaging four spectrally distinct labels in one sample is relatively easily achievable. While techniques like DNA-PAINT [241] are more applicable than dSTORM or PALM for multi-colour imaging, this comes at a significant time cost - a single image can take hours to acquire. In addition, as expansion microscopy sample preparation optically clears the sample, making samples amenable to super-resolution 3D imaging, expansion is a strong candidate for investigating complex actin structures in 3D in cells.

4.5.5 Labelling actin in expansion microscopy

Standard fluorescent phalloidin conjugates, often regarded as the ‘gold standard’ for labelling of fixed actin networks, are not well retained in expanded samples. Phalloidin is a small molecule with no free primary amine groups for functionalisation by anchors, meaning very little anchors in during the gelation step. Park et al. [156] show this loss of fluorescence in fig. 1 of their manuscript. In this thesis, I used a

phalloidin conjugate functionalised with an anchoring moiety of its own [157]. Theoretically, this should bypass the need for additional anchoring steps. However, as shown above, in my hands it was apparent that performance was significantly enhanced by continuing to incorporate the AcX incubation.

It has been noted that other custom-made probes with anchoring groups can also sometimes struggle to graft into the gel when no additional anchoring step is taken. It is suggested that the relatively low density of anchor on the probe surface in such cases limits the likelihood of polymerising monomers attaching to the target (Ewers, personal communication). In an anchored sample, the density of anchoring moieties is far higher, making the chance of a polymerising filament interacting with the target much higher (Figure 4.31). This fits well with the data shown here and would suggest anchoring steps should be at least trialled in all protocols using trifunctional probes.

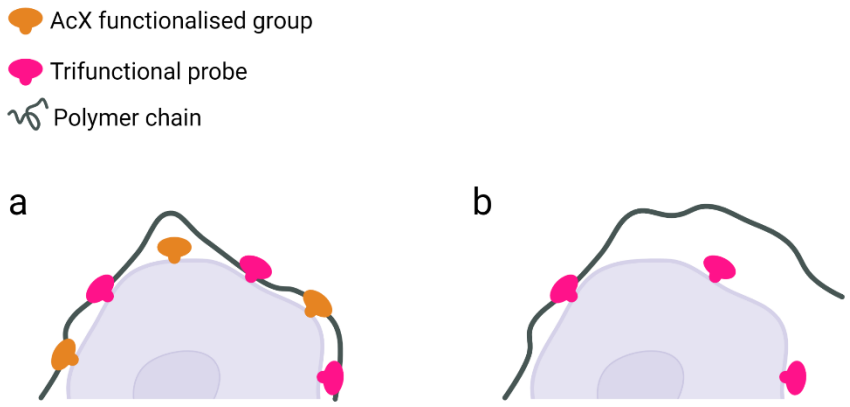

Figure 4.31 – Anchor grafting is likely to be density dependent. *The likelihood of a group grafting into the gel is increased by general anchoring (a) as opposed to no additional anchoring step (b).*

At higher resolutions, linkage error becomes more of a concern in ExM techniques [154]. Addition of a primary and secondary antibody to the existing label pre-expansion can add at least another ~ 20 nm of distance from the original fluorophore, multiplying to a lateral error of ~ 80 nm post 4 x expansion. It would be preferable, especially in combined applications like ExM SIM, ExM STED, or ExM STORM, to avoid this. Directly anchorable labels, like the trifunctional phalloidin used in this thesis, are one way of overcoming this issue, with post expansion labelling (like UExM, protein retention, or CLICK chemistries) being another. Labelling post gelation results in a minimisation of error to the size of the primary/secondary antibody displacement, as opposed to compounding this with the expansion factor [154].

Discontinuities in label may be due to destruction of a proportion of fluorophores during gelation [139], or incomplete immunofluorescence labelling that was indistinguishable before samples were expanded. Degree of labelling – and the degree to which labels survive – should also be considered in ExM experiment design. Post labelling can eliminate gelation-based fluorophore destruction, but epitope destruction or alteration during the digestion step instead must be taken into account.

4.5.6 Analysis of expanded actin images

Whilst filament tracing routines have been applied to microtubules post expansion [234], the relative density and continuity of fine actin filaments continues to restrict

application. The method described here uses fluorescence intensity fluctuations as a proxy for filament density and allows these complex filament networks to be quickly quantified. As is highlighted in results section 4.4.3, when comparing reported values from convolved simulated images to the actual number of filaments per image, consistent underestimation is evident (Figure 4.27). This is unsurprising, as many filaments do not extend across the full width of the ROI, and therefore each analysis repeat will only identify a subset of the filaments. The method averages over these repeats, providing a value that gives a comparable approximation of density, rather than a direct fibre count. In the same vein, the peaks plotted as results are not useable for calculation of fibre FWHM measurements, as the angle at which the filament is crossed is not necessarily across its shortest diameter (see Figure 4.32). When treating with NECA, relative increases in density were calculated, but results were variable between repeats and should not be overinterpreted. The technique is also not applicable to more pan – or non-filamentous stains, as this lack of sharp intensity variation instead leads to high intensity peaks across the full sample.

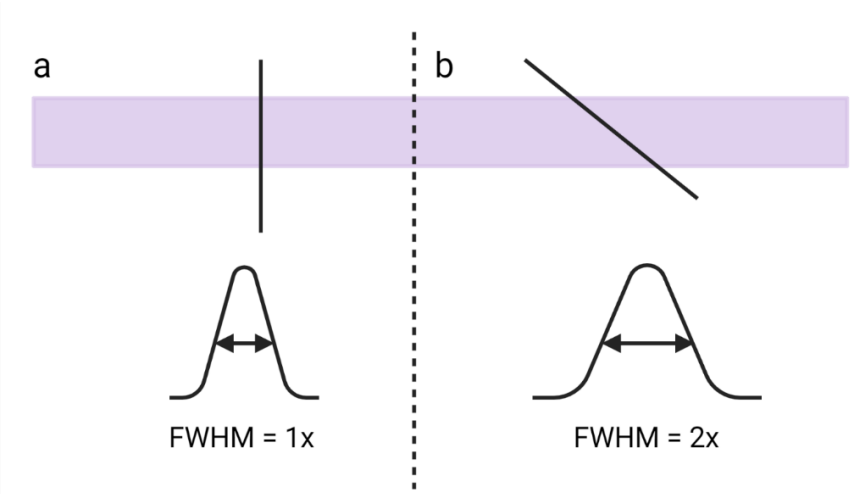

Figure 4.32 – Angle of dissection affects width of fit. *Given the random nature of the angles generated in the ExM analysis, a filament of a single thickness could result in calculation of multiple widths.*

4.6 Chapter Conclusions

Work in this chapter demonstrated two simple analysis methods for quantifying cortical actin networks in super-resolved microscopy images. These methods allow for quick, reproducible quantitation of actin corral number and size in SRRF images, and for quantitation of filament density in ExM images. These methods are also amenable to batch processing of large data sets, and to adaptation for live cell analysis of actin dynamics.

In terms of actin behaviour under receptor stimulating and actin disrupting conditions, NECA treatment was shown to induce a small but significant increase in corral size. When incorporating actin disruption and receptor stimulation simultaneously, disruption is less marked than when treating with cytochalasin D alone.

CHAPTER 5 – IMAGING ACTIN AND RECEPTORS

5.1 Chapter Overview

Having visualised both receptors and cortical actin independently, the next step in building a cohesive model of actin/receptor interactions is imaging both simultaneously. This allows a more holistic overview of behaviour to be garnered. As with the individual imaging experiments, this chapter will cover both fixed- and live-cell approaches.

Fixed cell imaging adds flexibility for dual super-resolution approaches by eliminating temporal concerns. In this chapter, 3D SIM imaging was used to investigate actin and receptor under actin disrupting and receptor stimulating conditions, allowing a direct investigation of potential interactions. To improve resolution significantly, ExM techniques were also trialled for SNAP incorporation.

One approach for the imaging of live receptor dynamics with super-resolved actin involves imaging receptors, fixing the sample, and then imaging the actin. For example, Sungkaworn et al. [163] captured SPT data for the adrenergic receptor α_{2A} and overlaid this on a subsequently captured PALM image of mEOS-LifeAct labelled actin, using this to assess the organisational ability of the actin mesh. Alternatively, simultaneous live investigation has been performed using SRRF for actin and Imaging FCS to assess receptor behaviour, allowing both sets of raw data to be recorded on a dual camera TIRF system [242]. The SPT work in this chapter will

describe a workflow and potential analysis methods for an alternative way to image live actin/receptor dynamics.

This chapter also addresses the imaging and localisation of the potential interacting protein, α-actinin-1 – introduced more thoroughly in section 1.6.2. Found in vivo as an anti-parallel dimer, this protein has been proposed as a mechanism for $A_{2A}R/A_{2B}R$ heterodimerisation [83]. Given its activity in binding both actin and the two receptors, it may also play a role in mediating direct actin association. At all points in this work, the phrases α-actinin or actinin will be referring to the α-actinin-1 isoform.

This chapter aims to investigate the behaviour of actin and adenosine receptors simultaneously, providing further insight into how receptor behaviour may be directed by actin structure. Fixed drug treated receptor expressing cells will be assessed by SIM microscopy to explore interactions with actin under conditions similar to investigations in chapters 3 and 4. α actinin-1 localisation will also be assessed in these contexts. Adaptations to ExM techniques discussed in chapter 4 to allow for incorporation of the SNAP tag will be tested. Dual SPT and SRRF imaging will also be discussed.

Core chapter aims:

- Assess relationship of actin and A_2 receptors in fixed cells using 3D SIM imaging.
- Test SNAP-label incorporation for high resolution 3D SIM ExM imaging.
- Demonstrate and establish workflow for dual SRRF/SPT imaging.
- Investigate α-actinin behaviour with and without receptor expression, relative to actin structure.

5.2 SIM Imaging of A_2 Receptors and Actin Further Supports Differential Regulation

5.2.1 Receptor/actin distribution

Having already demonstrated in chapter 4 that SIM imaging provided robust results for actin imaging, with a clear improvement in detail afforded over TIRF or widefield imaging, the technique was applied to simultaneous imaging of fixed receptors and actin. When applied to cells transfected with SNAP-A_2 receptors, it is evident that receptor distribution can be well visualised with this technique. As seen in Figure 5.1, variations in receptor density are clearly distinguishable, with higher expressing cells displaying a more pan rather than punctate labelling. This is by no means a homogenous stain, however, and variation can still be seen across the basal membrane. Cells expressing moderate to sparse levels of SNAP-A_2 receptor resulted in the capacity to identify individual spots (Figure 5.2), be those clusters of receptors or individual fluorophores. This formed the basis of the following analysis.

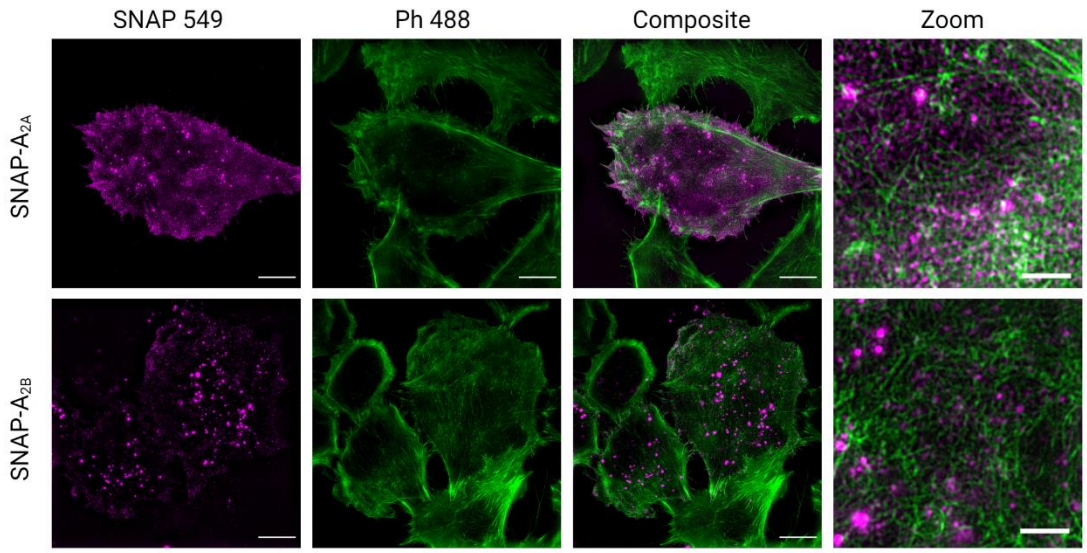

Figure 5.1 – Examples of 3D SIM images of SNAP-A_{2A}R and SNAP-A_{2B}R expressing cells. *Scale bars (excluding zoom) = 10 µm. Zoom scale bar = 2 µm.*

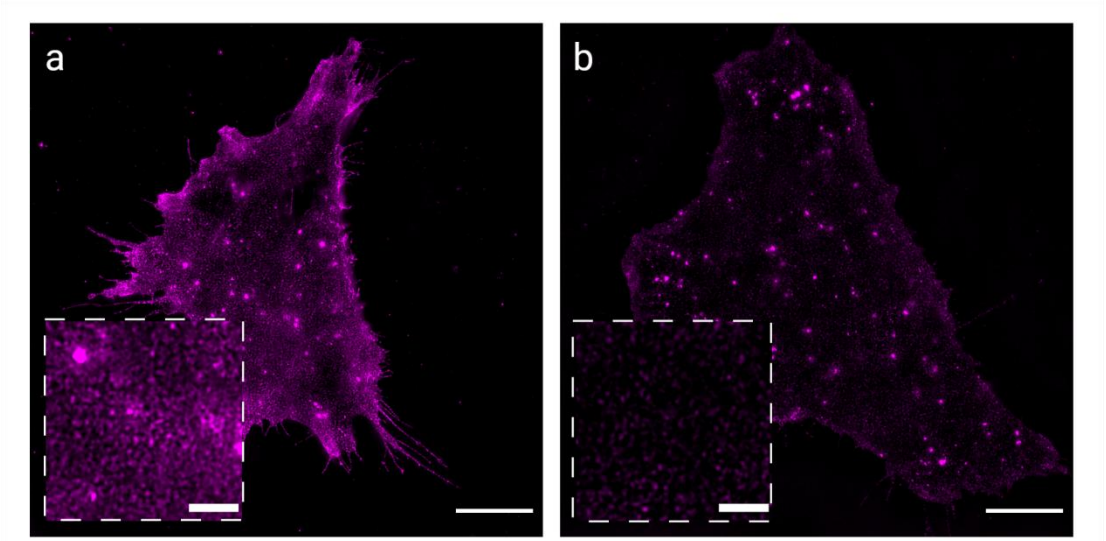

Figure 5.2 – Variations in expression level are evident between cells. *Two A_{2A}R expressing cells labelled with SNAP 549 and imaged with 3D SIM. Scale bars – full ROI = 10 µm, inset = 2 µm.*

5.2.2 Analysis development

In order to assess organisation of actin and receptors relative to one another, an object-based analysis was performed on two channel images. Actin filaments were thresholded and a mask generated in order to create a binary description of the presence and absence of actin. Receptor points were then identified with a Laplacian of Gaussian spot detection, followed by calculation of the spot centroid. These coordinates were then compared to the masked actin, with overlap of pixels being termed ‘on’ the actin, a proximity of less than 3 pixels (97 nm accounting for the pixel size of the reconstructions) being termed ‘adjacent’, and a greater than 3 pixels distance being termed ‘off’ of the network. These were plotted out to give a visual representation of the categorisations, as shown in Figure 5.3.

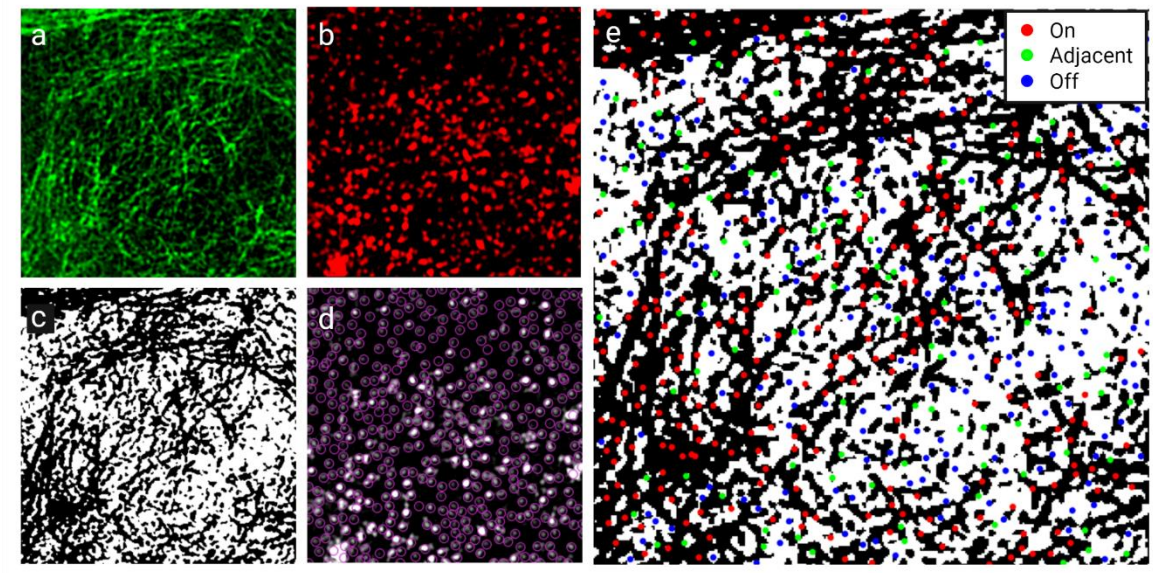

Figure 5.3 – 3D SIM actin and receptor analysis process. *After cropping of a 10 µm x 10 µm region of interest, a) 3D SIM actin is first c) thresholded, then b) SNAP-A_2 receptors undergo d) point detection. After comparison of the centroid coordinates with the actin channel, receptors are categorised as in e).*

5.2.3 Receptor/actin drug treatment

The effect of agonists or cytoskeletal disruption on the localisation of SNAP-A_2 receptors relative to the actin cytoskeleton was investigated with the same CD and NECA treatments previously described. All data here should be interpreted with the caveat that some internalised receptors – rather than membranous - may also be identified, as the imaging was performed using 3D SIM and therefore has a still-limited Z-resolution. Further restriction of imaging to the basal membrane using TIRF SIM would have been ideal.

Treatments again altered the outcomes differentially between the two receptor types. Examples of drug treated cells are shown in Figure 5.5 (A_{2A}R) and Figure 5.7 (A_{2B}R). For A_{2A}R expressing cells, the average receptor counts per ROI analysed are consistent (Figure 5.4d), indicating cells of similar expression level were selected. No significant differences were seen between DMSO control cells and cells that underwent no treatment (Figure 5.4a-c). Treatment with NECA showed no significant change in receptor localisation – on, off, or adjacent - when compared with DMSO treated controls (Figure 5.4a-c). CD treatment, however, showed a greater proportion of receptors existing ‘off’ the actin meshwork, and fewer ‘on’ (Figure 5.4a, b). This shift was also seen when treating with both CD and NECA together, with significantly more receptors being ‘off’ than ‘on’. Across treatments, the number of adjacent receptors remained largely consistent, but CD + NECA treatment showed significantly fewer in this category than in samples treated with CD alone. If this shift

is compared to the number of pixels occupied by actin for each condition, it is clear that CD treatment, alone and in combination with NECA, reduces the area covered in the assessed ROI. This inherently would lead to reduced ‘on’ receptors. However, the actin area does not drop additionally when treating with NECA and CD together (Figure 5.4e).

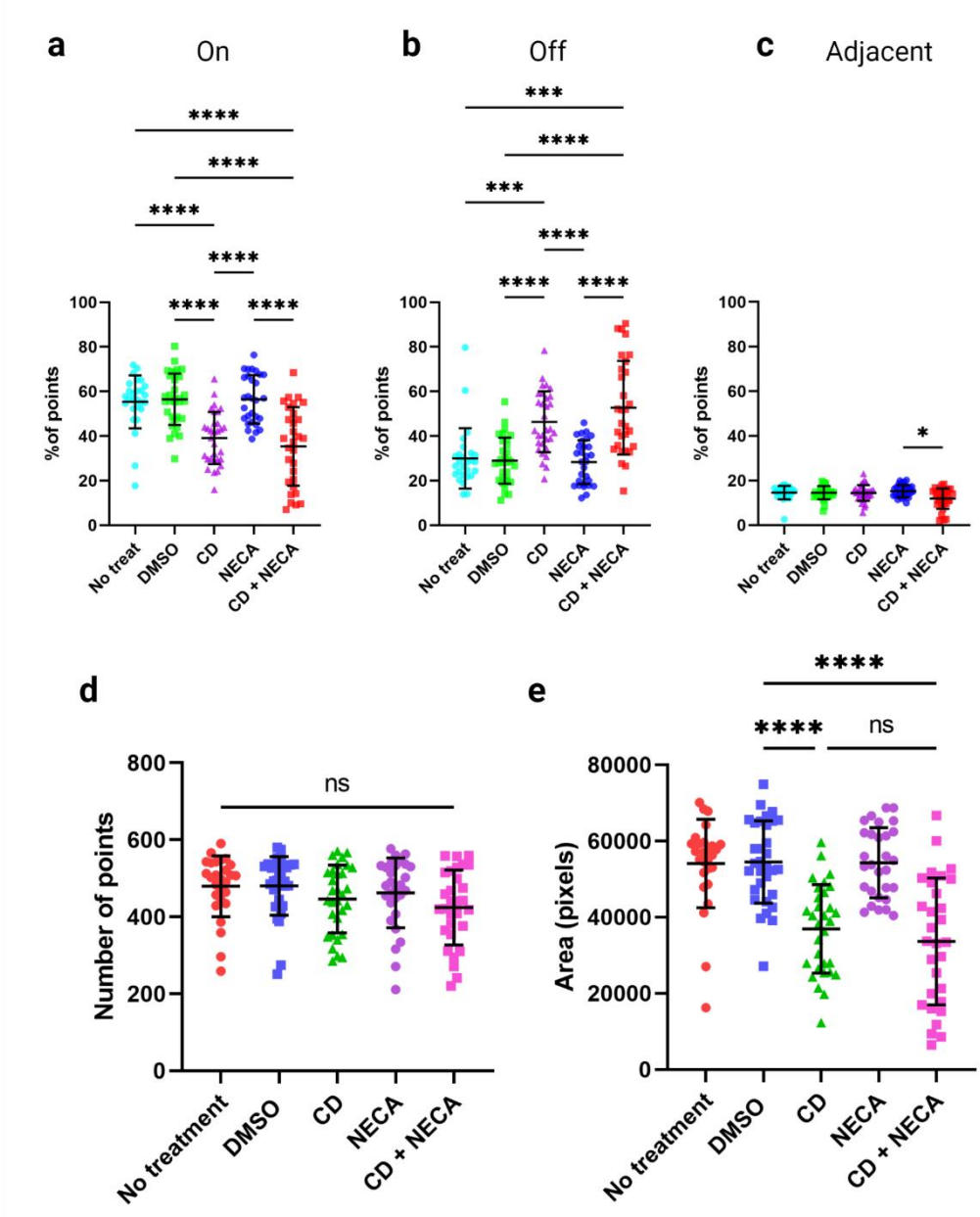

Figure 5.4 – CD and dual CD and NECA treatment has an effect on A_{2A} receptor localisation. *For transiently transfected A_{2A}R expressing cells, no treatment and vehicle only controls are compared with 1 µM CD, 10 µM NECA, and 1 µM CD + 10 µM NECA treatments when receptor points are categorised as a) on, b) off, or c) adjacent to the actin mask. d) The number of identified points and e) area covered by the actin mask in pixels across the full ROI analysed are also compared across treatments. n = 3 independent repeats, ≥27 cells per treatment. * = p ≤ 0.05, *** = p ≤ 0.001, **** = p ≤ 0.0001.*

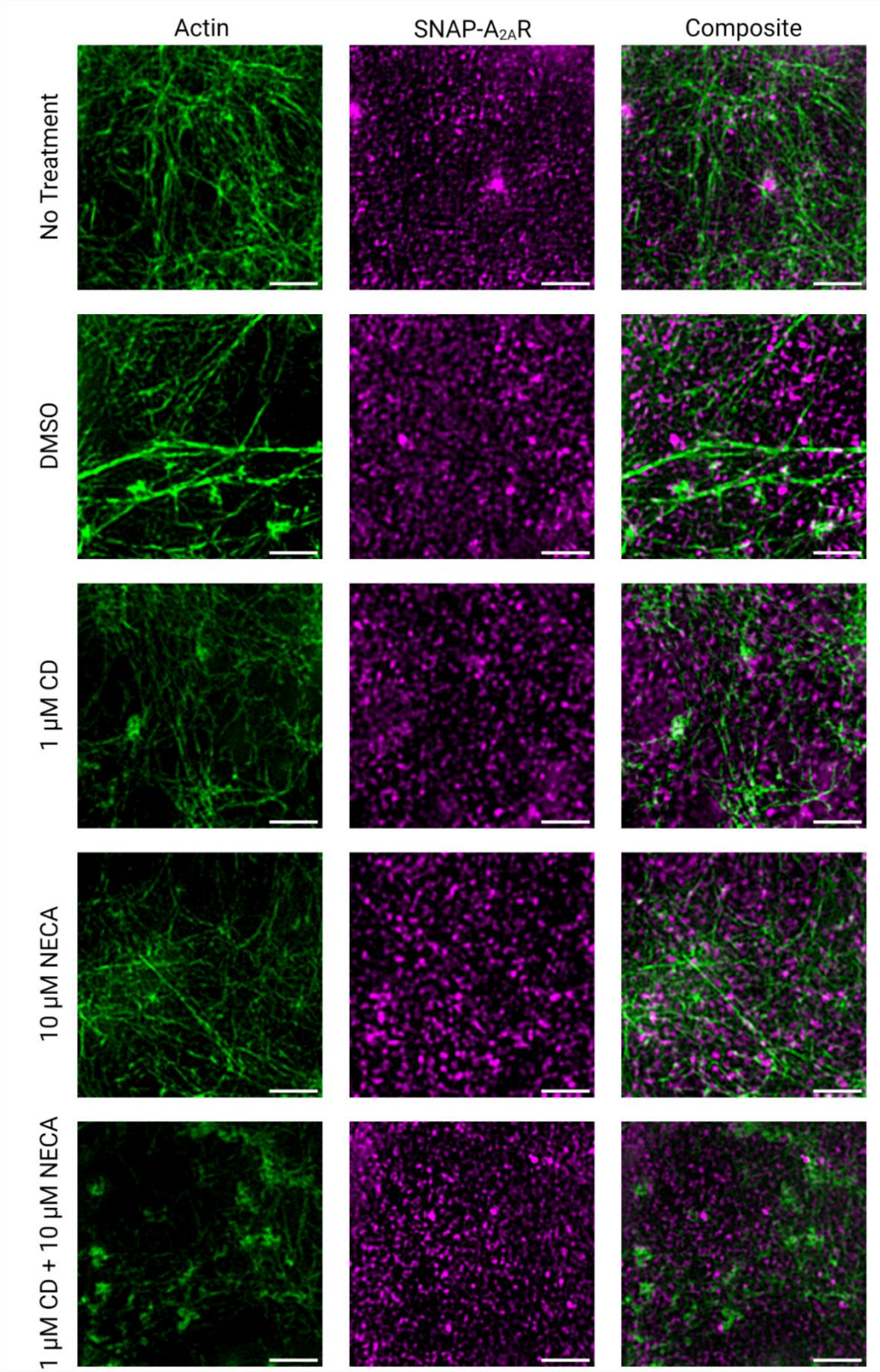

Figure 5.5 – Examples of SNAP-A_{2A}R and Actin 3D SIM images in drug treated cells. *Phalloidin 488 was used to label actin, and SNAP-Surface 549 was used to label SNAP-A_{2A}R. All scale bars = 2 µm.*

When looking at $A_{2B}R$ expressing cells, average counts for receptor points per ROI are more variable than for $A_{2A}R$ expressing cells (Figure 5.6d). This is despite the same efforts being taken as for $A_{2A}R$ cells to select similarly expressing cells, suggesting more variable receptor expression within the population overall. A different arrangement to $A_{2A}R$ expressing cells is also seen with each drug treatment, with CD but not CD + NECA treatment resulting in a significant increase to the number of points situated 'off' actin compared to DMSO treated cells (Figure 5.6b). This is not matched by a significant decrease in the number of points classified as 'on', however (Figure 5.6a), with the shift likely account for by significantly fewer points being classified as 'adjacent' under CD treatment (Figure 5.6c). There is a significant difference between no treatment and DMSO treatment cells for both 'on' and 'off' receptor points (Figure 5.6a, b), which should be considered in context of the significantly different areas of actin imaged in these two sets (Figure 5.6e). CD and CD + NECA treatments do not show major changes in behavioural pattern between the two. Together, these data again support the argument for differential basal regulation between the two receptors, as well as differing links between receptor stimulation and behaviour with regards to actin.

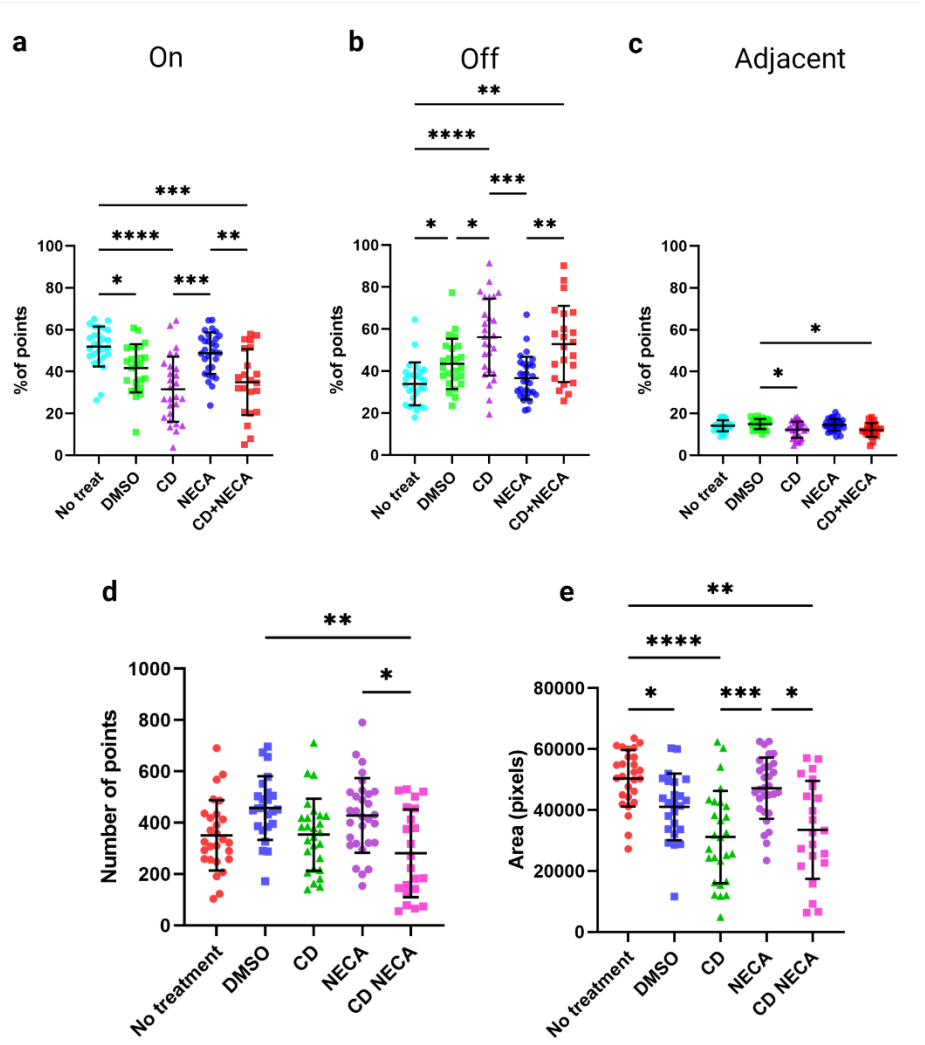

Figure 5.6 - A_{2B} receptor localisation relative to actin is variable. *For transiently transfected A_{2B}R expressing cells, no treatment and vehicle only controls are compared with 1 μM CD, 10 μM NECA, and 1 μM CD + 10 μM NECA treatments when receptor points are categorised as a) on, b) off, or c) adjacent to the actin mask. d) The number of identified points and e) area covered by the actin mask in pixels across the full ROI analysed are also compared across treatments. n = 3 independent repeats for all treatments except CD + NECA, where n = 2, with ≥ 24 cells per treatment, bar CD + NECA with 22 cells analysed.*
** = p ≤ 0.05, ** = p ≤0.01, *** = p ≤ 0.001, **** = p ≤ 0.0001.*

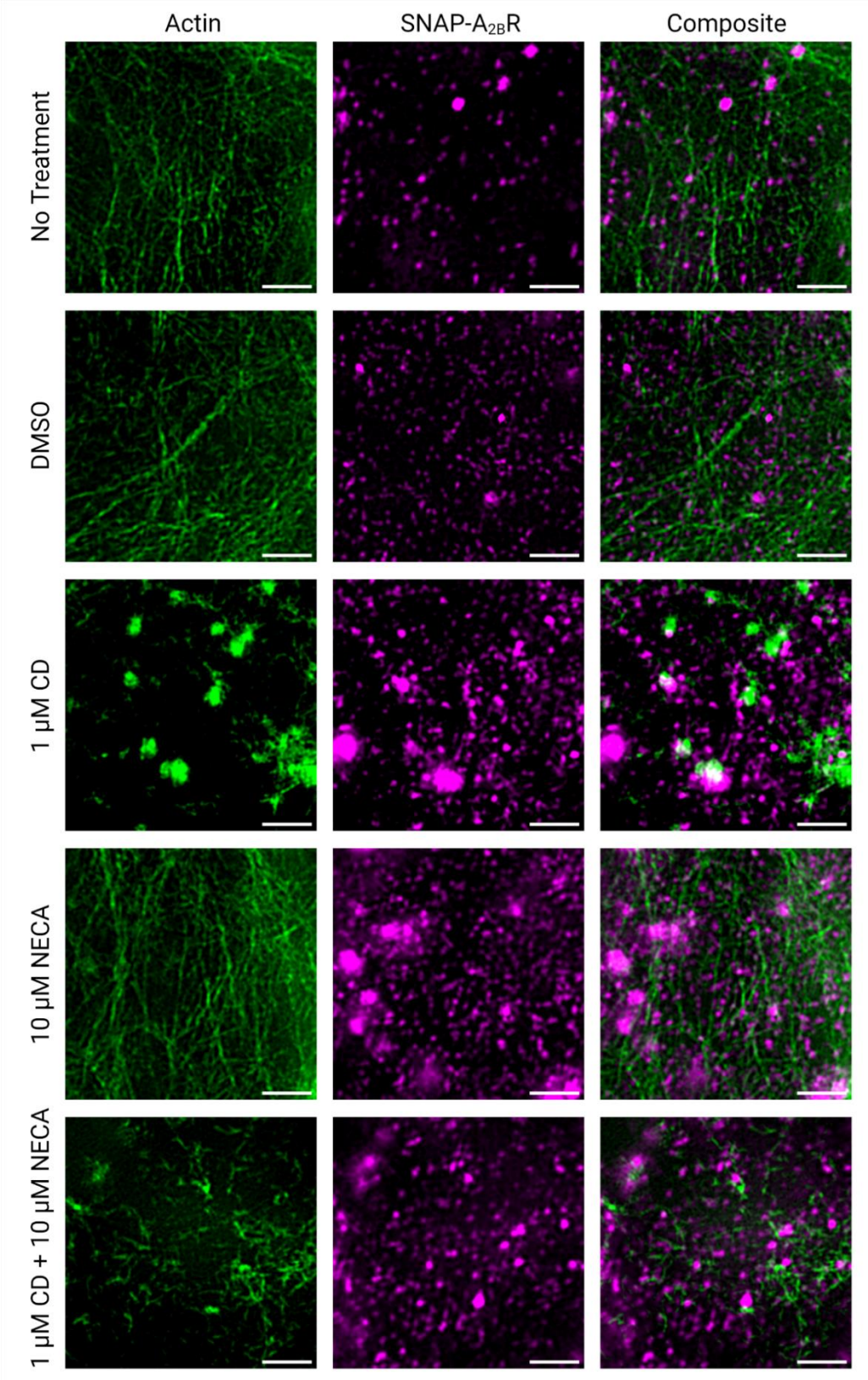

Figure 5.7 – Examples of SNAP-A_{2B}R and Actin 3D SIM images in drug treated cells. *Phalloidin 488 was used to label actin, and SNAP-Surface 549 was used to label SNAP-A_{2B}R. All scale bars = 2 µm.*

5.2.4 Three colour SIM imaging with α-actinin-1

Given that α-actinin-1 has been reported to interact with both $A_{2A}R$ and $A_{2B}R$, which indicates a potential role in heterodimerisation, as well as its inherent actin binding ability, it is a logical candidate for mediation of some receptor/actin interaction. As such, its localisation was assessed in combination with either SNAP-$A_{2A}R$ or SNAP-$A_{2B}R$ and actin.

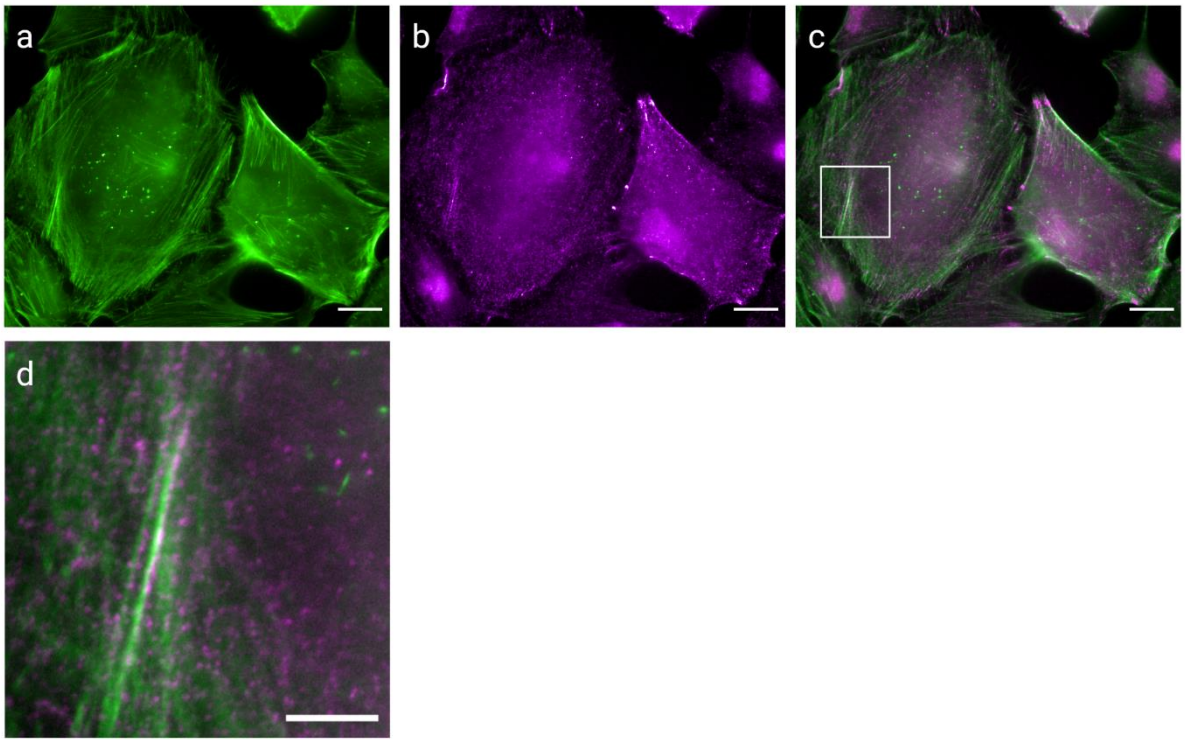

Figure 5.8 – Epifluorescence examples of α-actinin-1 labelling. *a) Actin, b) α-actinin 1, and c) overlay of the two, with a zoom in on the boxed area shown in d). Scale bars a-c = 20 µm, d = 7.5 µm.*

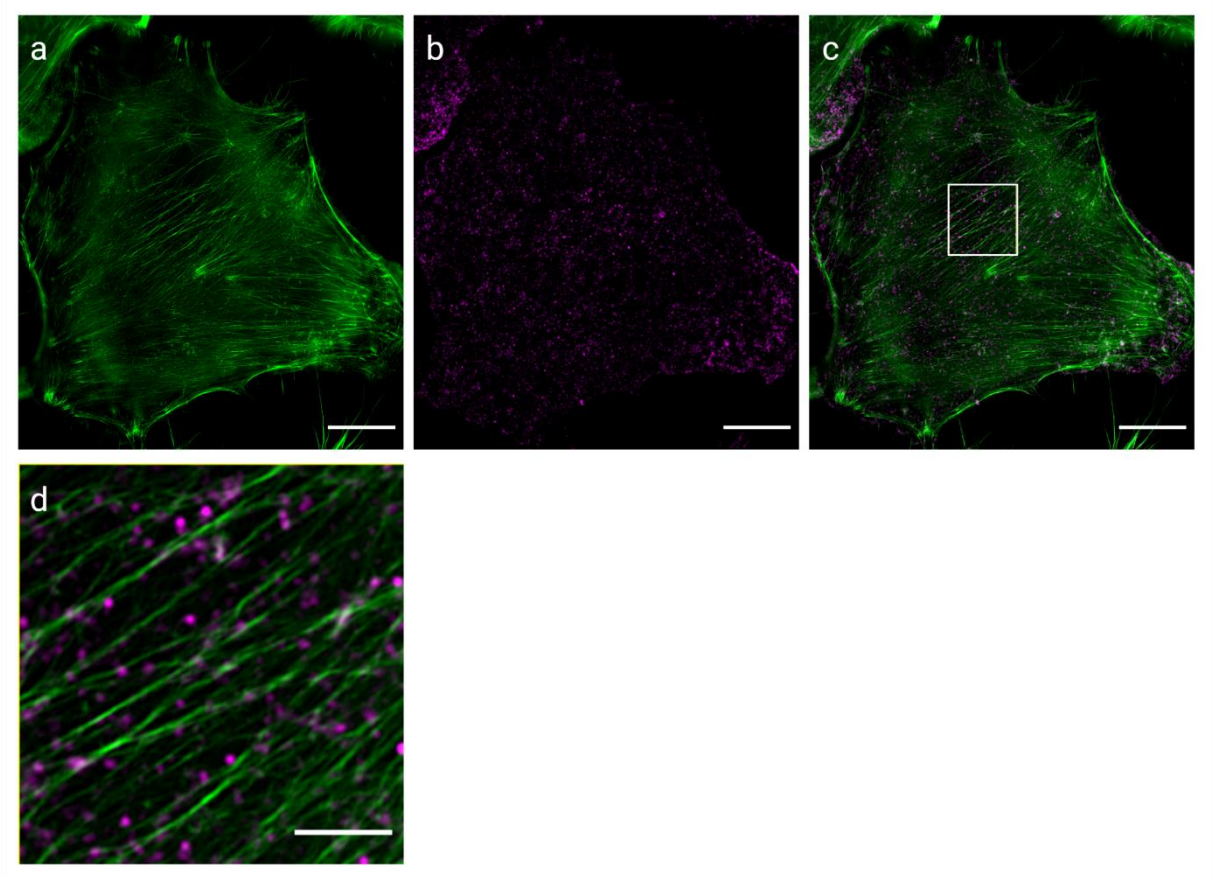

Figure 5.9 – 3D SIM examples of α-actinin-1 labelling. *a) Actin, b) α-actinin 1, and c) overlay of the two, with a zoom in on the boxed area shown in d). Scale bars a-c = 10 µm, d = 2.5 µm.*

The α-actinin-1 antibody was tested first with epifluorescence microscopy. The α-actinin-1 stain was not consistent with the expected distribution. While it did show some labelling along defined actin filaments, it also showed a more general distribution throughout the cell – a more faithful mirroring of the F-actin stained by phalloidin would have been expected given the known localisation of the protein on actin filaments (Figure 5.8). At the higher resolutions provided by SIM, α-actinin-1 can be seen localised on thicker actin bundles and branch points (Figure 5.9), but again points can also be seen apparently detached from actin filaments.

In order to quantify α-actinin-1 localisation, the analysis detailed in section 5.2.2 was also applied to α-actinin-1/actin 3D SIM images in cells expressing $A_{2A}R$ under the drug treatments used previously. Results are shown in Figure 5.10, but should be considered in context of the above concerns.

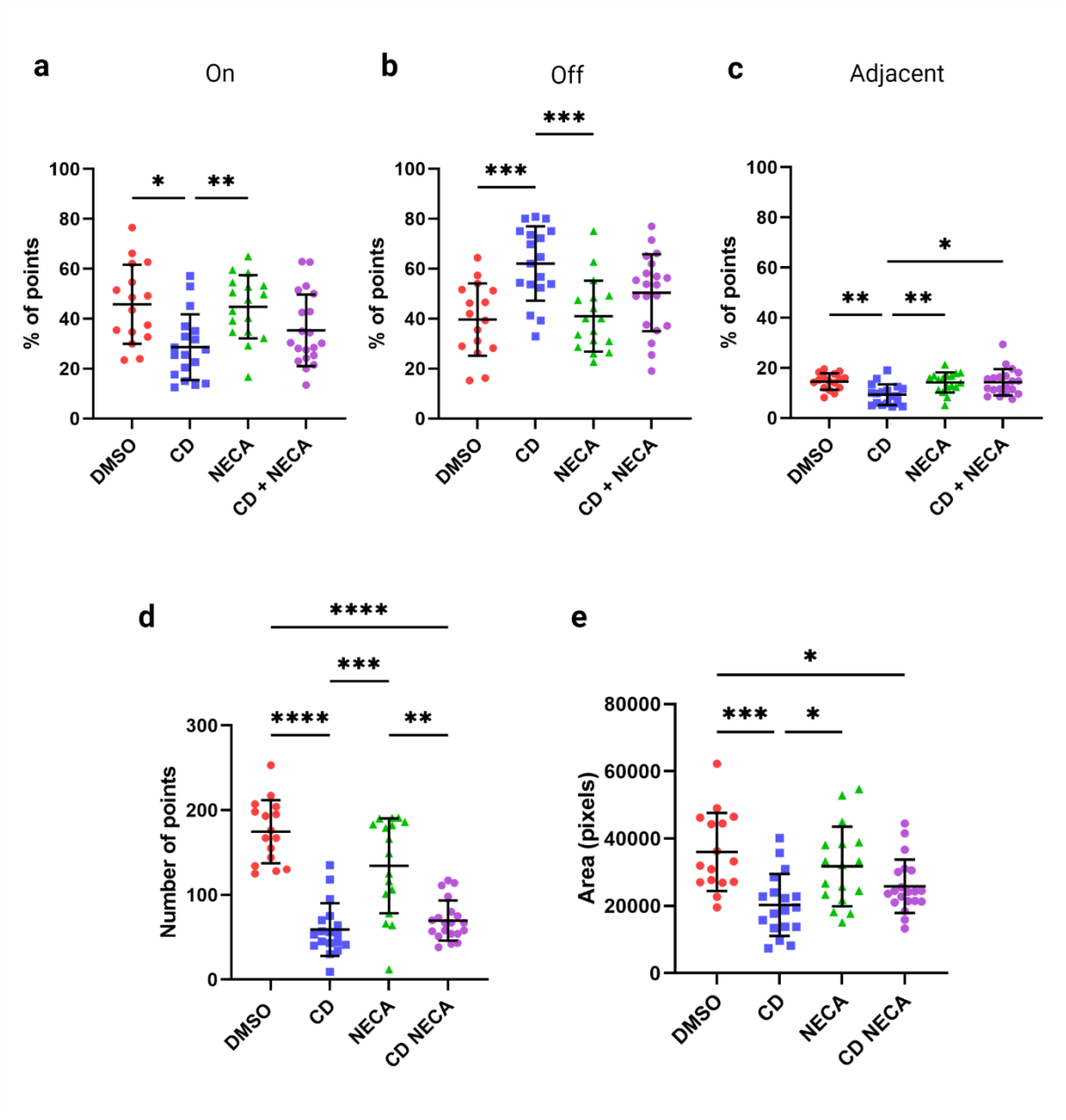

Figure 5.10 – Localisation of α-actinin-1 relative to actin*. For α-actinin-1 and actin labelled $A_{2A}R$ expressing cells, vehicle only controls were compared with 1 μM CD, 10 μM NECA, and 1 μM CD + 10 μM NECA treatments when α-actinin-1 points are categorised as a) on, b) off, or c) adjacent to the actin mask. d) The number of identified points and e) area covered by the actin mask in pixels across the full ROI analysed are also compared across treatments. n = 2 individual repeats, ≥ 16 cells per treatment. * = p ≤ 0.05, ** = p ≤0.01, *** = p ≤ 0.001, **** = p ≤ 0.0001.*

α-actinin localisation showed a significant reduction of points being colocalised with actin relative to DMSO control treatments under CD treatment, but not CD + NECA treatment (Figure 5.10a, b). Overall actin area is significantly reduced compared to control with CD both alone and in addition to NECA treatment (Figure 5.10e), but there is no change in area between these two actin disrupting treatments themselves. Unlike with the relatively consistent point counts in receptor assessments, the number of identified α-actinin-1 points varies significantly between treatments (Figure 5.10d). Control counts are significantly reduced again by CD and CD + NECA treatments, though as with actin there is no significant change between the treatments themselves.

α-actinin-1 labelling was next assessed alongside $A_{2A}R$ or $A_{2B}R$ expression in a three-colour imaging experiment. The previously discussed SIM analysis was adapted to assess the behaviour of α-actinin-1 in relation to actin with and without association with an A_2 receptor (Figure 5.11). Examples of image outcomes are shown in Figure 5.12. Distances between each α-actinin point and the closest SNAP-A_2R point were calculated with a custom MATLAB script (see appendix 1), with distances below a threshold classed as associating.

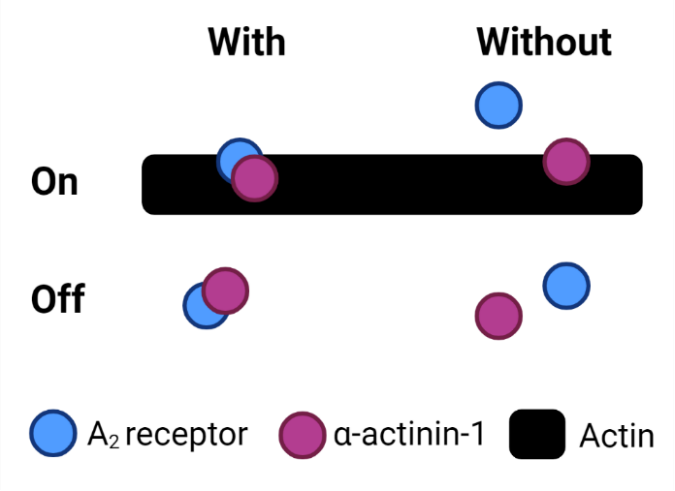

Figure 5.11 – Categories for α-actinin-1/receptor analysis*. Each point is determined to be either on or off the actin mask, and with or without a receptor in close proximity.*

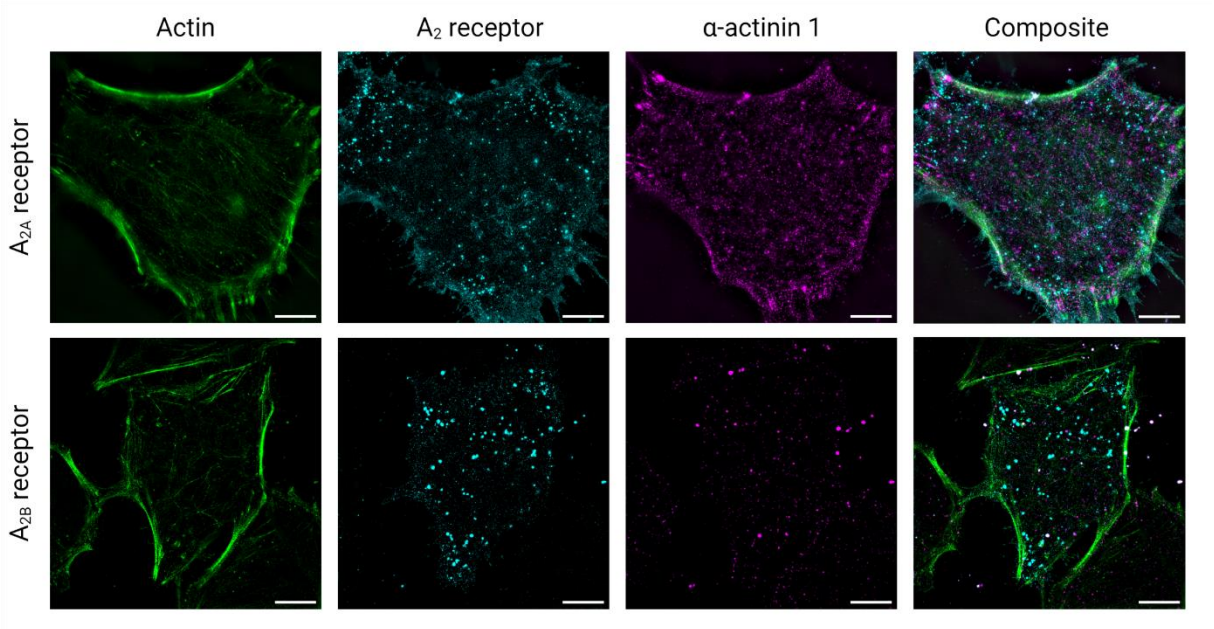

Figure 5.12 – Example 3D SIM images from 3-colour actin/α-actinin-1/A2 receptor imaging. *Transiently transfected SNAP-A2 receptor expressing A549 cells co-labelled with phalloidin Al.488 and anti- α-actinin-1 antibody. Scale bars = 10 µm.*

Examples of cells for each treatment are given in Figure 5.13. Association of $A_{2A}R$ with α-actinin-1 does not appear to affect the trends of association and dissociation evident in Figure 5.10. This is represented through statistical comparison of percentage of points associated with (Figure 5.14 a, b) or without (Figure 5.14 c, d) the receptor. The category of adjacent has been omitted here for simplicity of data presentation.

For α-actinin-1 points associated with an $A_{2A}R$ receptor, significantly fewer points are found ‘on’ actin and more are found ‘off’ in CD treated samples than in DMSO or NECA treated samples (Figure 5.14 a, b). There may be an abrogating effect on CD treatment upon the addition of NECA, as there is no significant change between DMSO and CD + NECA treatment for proportions of points either ‘on’ or ‘off’ (Figure 5.14 a, b).

Looking at α-actinin-1 not associated with the receptor (Figure 5.14 c, d), CD treatment again shows significantly fewer points colocalising with actin compared to DMSO treatment. CD + NECA treatment together was not significantly different from either CD or DMSO treatment alone (Figure 5.14 c, d).

For $A_{2B}R$, only untreated samples were assessed, with very few α-actinin-1 points identified for each region of interest (Figure 5.15b) – especially when considered in the context of the $A_{2A}R$ expressing cells analysed (Figure 5.10d). Here again the

association pattern shown for α-actinin-1 with actin (Figure 5.15a) is mimicked regardless of receptor association status (Figure 5.15c, d).

Actin-actinin localisations are examined further with the additional resolution provided by SIM ExM in section 5.3.2 below.

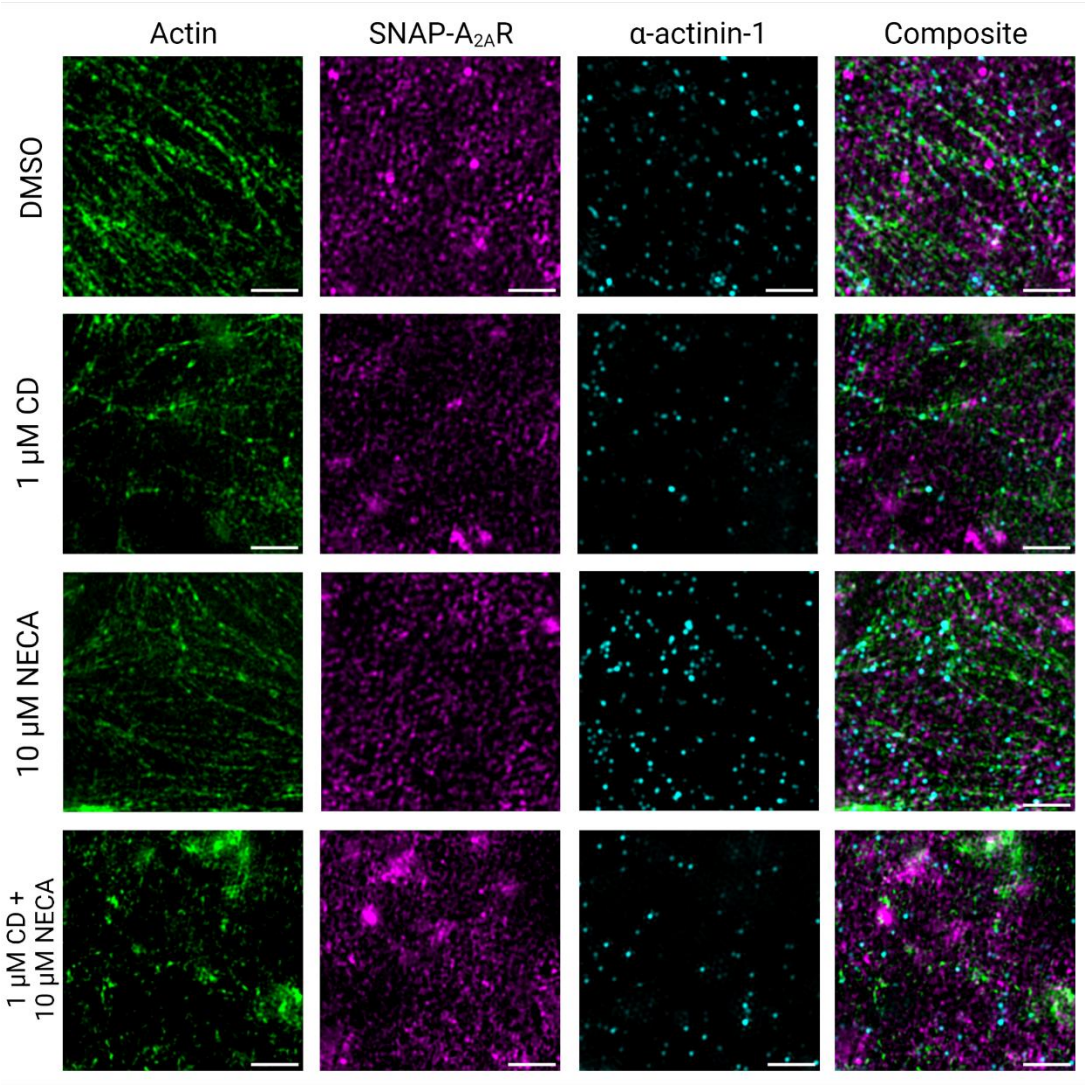

Figure 5.13 - Examples of SNAP-A_{2A}R, actin, and α-actinin-1 three colour 3D SIM images in drug treated cells. *Phalloidin 488 was used to label actin, SNAP-Surface 549 was used to label SNAP-A_{2B}R, and the α-actinin-1 antibody was labelled with Alexa-Fluor 647. All scale bars = 2 µm.*

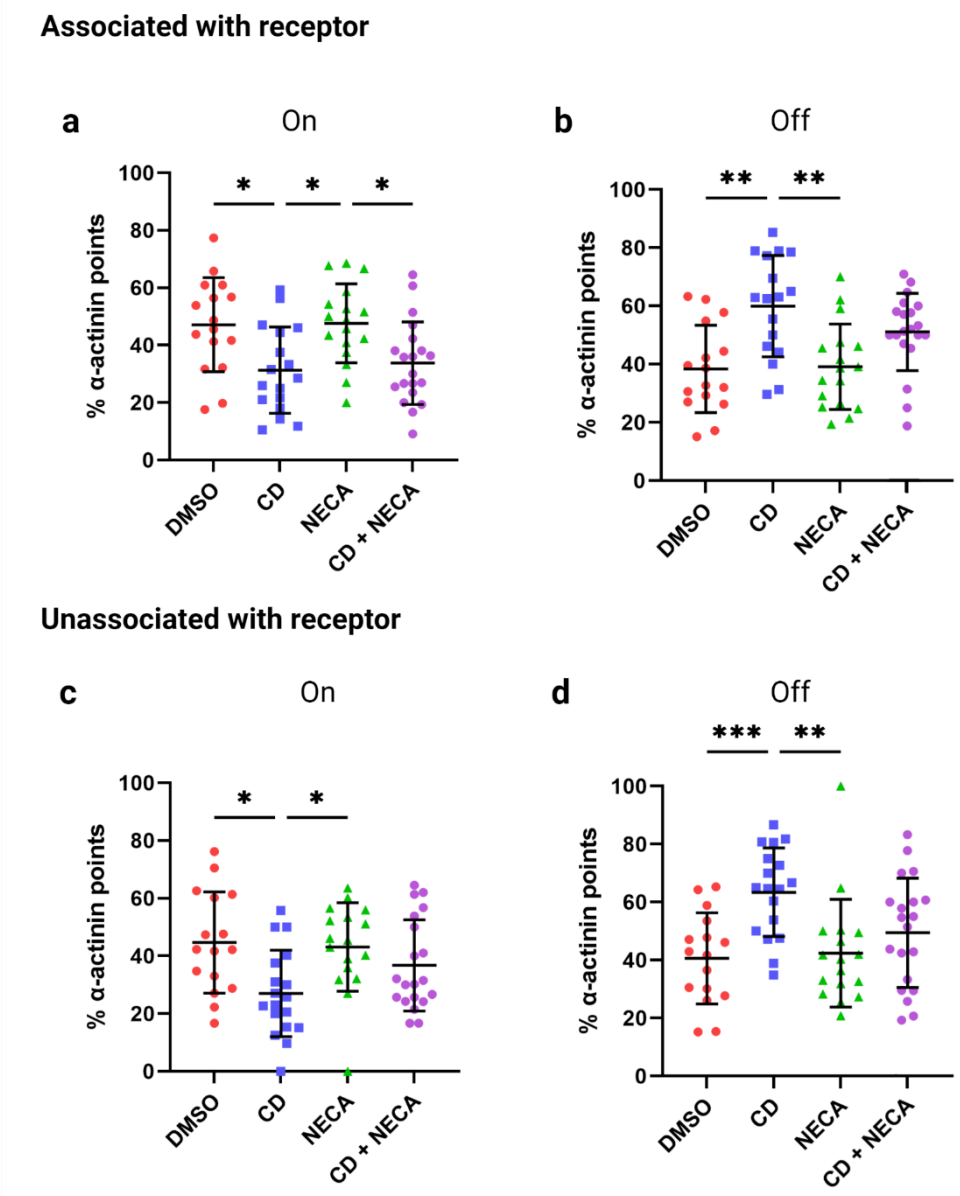

Figure 5.14 – Outcomes of drug treatment on A_{2A} receptor associated and unassociated α-actinin-1 points. *A_{2A}R expressing cells were treated with DMSO, 1 μM CD, 10 μM NECA, or 1 μM CD + 10 μM NECA and each identified α-actinin-1 point interrogated for receptor association and relation to the actin mask. Statistical comparisons for α-actinin-1 points associated with A_{2A}R points for a) the proportion of points located on actin and b) proportion of points located off actin for all four treatments are shown. α-actinin-1 points unassociated with A2AR points are compared for each treatment comparing proportions of points c) on actin and d) off actin. All data is presented as mean ± SD. n = 2 individual repeats, ≥ 16 cells per treatment. * = p<0.05, ** = p<0.01, *** = p<0.001.*

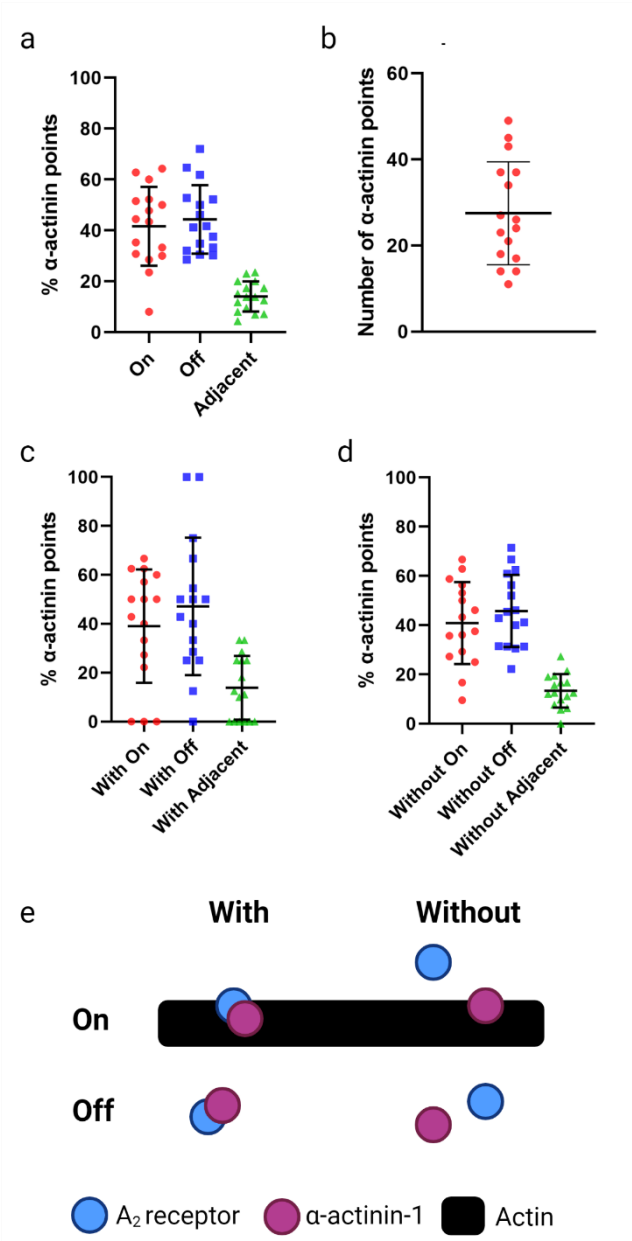

Figure 5.15 – α-actinin-1 behaviour relative to A_{2B} receptor association. *Transiently transfected A_{2B}R expressing cells were co-labelled for actin and α-actinin-1. a) α-actinin-1 localisation relative to actin and b) the number of α-actinin-1 points identified in each ROI assessed. c) and d) show relative percentages of A_{2B} receptor associated α-actinin-1 (c) and unassociated α-actinin-1 (d). A visual representation of the categorisation previously set out is given again in e). n = 2, 16 individual cells. All data is presented as mean ± SD.*

5.3 Expansion SIM Could Provide High Resolution Insight into Protein-Actin Interactions

As discussed in chapter 4, expansion SIM imaging affords significant resolution improvements over SIM alone. An important point to note is that this is possible while retaining the ability to simply perform multicolour imaging, smoothing some of the roadblocks that can be present during acquisition with techniques like multicolour STORM. To this end, it was evident that ExM SIM could be a useful technique for looking at actin and receptors simultaneously and at high resolution.

5.3.1 Standard ExM preparations fail to incorporate SNAP ligands

Incorporation of the SNAP label into the gel was the first challenge to be broached. While there are several papers describing specialised methods of incorporating SNAP probes [155, 158], at the time of experimentation none were commercially available. An alternative approach was to adapt the method of Park et al. [156], who used anti-488 antibodies on phalloidin 488 labelled actin to allow for a more traditional - and importantly, non-specialised - approach to label anchoring. SNAP-Surface Alexa-488 should also be recognised by this antibody, so this technique was trialled in our set up.

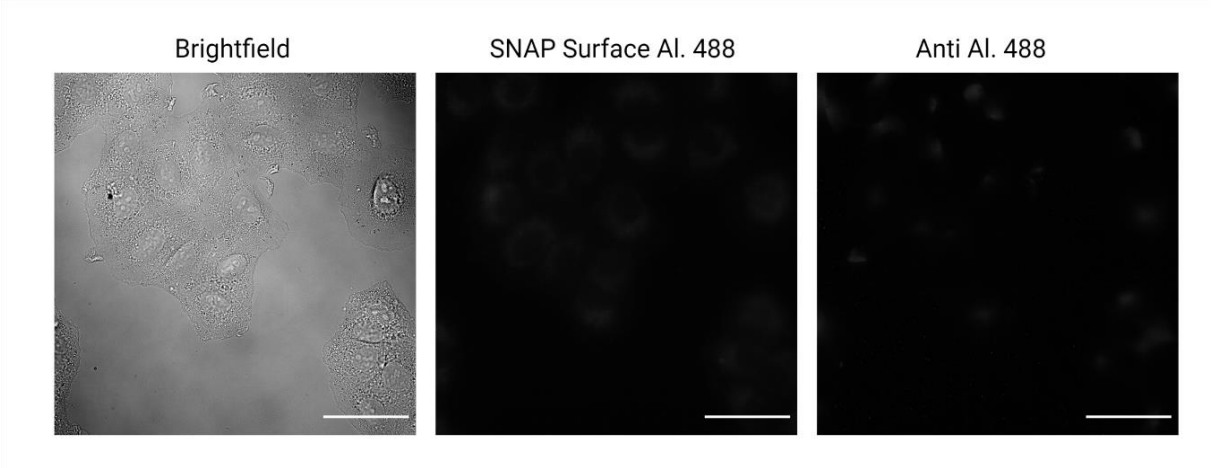

Figure 5.16 – Untransfected controls do not show non-specific labelling*. Untransfected A549 cells labelled with SNAP-Surface Alexa Fluor 488 and anti-Alexa Fluor 488, showing no significant non-specific labelling. Scale bars = 50 µm.*

Non-specific labelling was not seen to be an issue in control experiments (Figure 5.16). While initial tests for SNAP-488 labelled cells were carried out in unextracted cells, as the only label of interest was cell surface, it became clear that this was impeding access of the antibody to the basal membrane and extraction was reincorporated into the labelling routine (Figure 5.17). This improved widefield outcomes somewhat, but correlative images pre- and post- anti-488 labelling showed that this approach was not suitable. There is limited quenching of the 488 signal by the anti-488 antibody, which would typically be expected with a saturating stain.

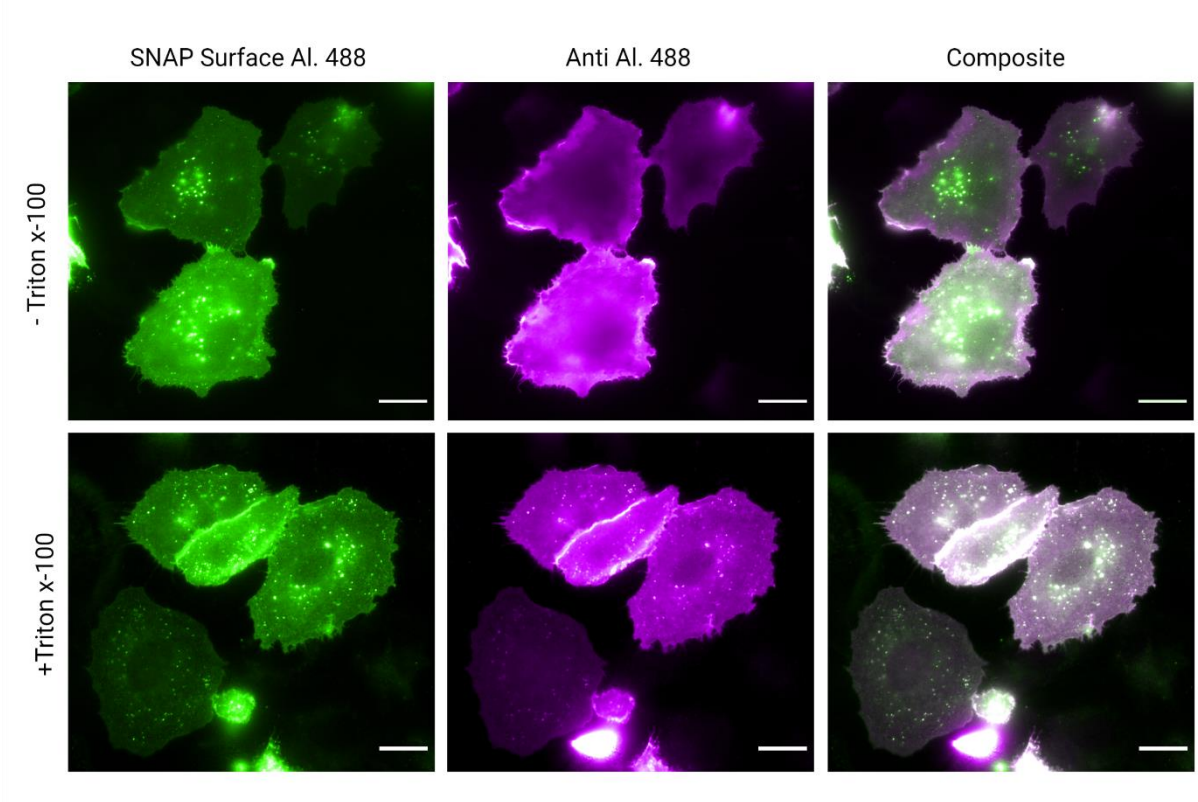

Figure 5.17 – Anti-488 labelling performs best when cells are extracted. *Epifluorescence examples of anti-488 labelling behaviour on $A_{2A}R$ expressing A549 cells with and without detergent extraction. All scale bars = 20 µm.*

Unfortunately, in all further trials the anti-488 stain was variable and incomplete, even when matching the antibody concentration cited in the original work [156] (1:100 dilution to a concentration of 10 µg mL^{-1}) (Figure 5.18). This was the case for samples when labelling actin (Figure 5.18, Figure 5.19), SNAP-488 (Figure 5.17) and microtubules (data not shown), ruling out a protein specific issue. In our hands, counter-labelling Phalloidin Alexa Fluor 488 stained cells with anti-Alexa Fluor 488 showed incomplete labelling, with areas - especially stress fibres - clearly lacking label (Figure 5.18, Figure 5.19). While the labelling clearly did follow some filaments, it was still insufficient to image fine detail. An example of a large multinucleated cell,

similar to one shown by Park in their work, is given in Figure 5.19. Labelling of Alexa 488 with the anti – Alexa 488 was therefore poor and not suitable for quantitative analysis.

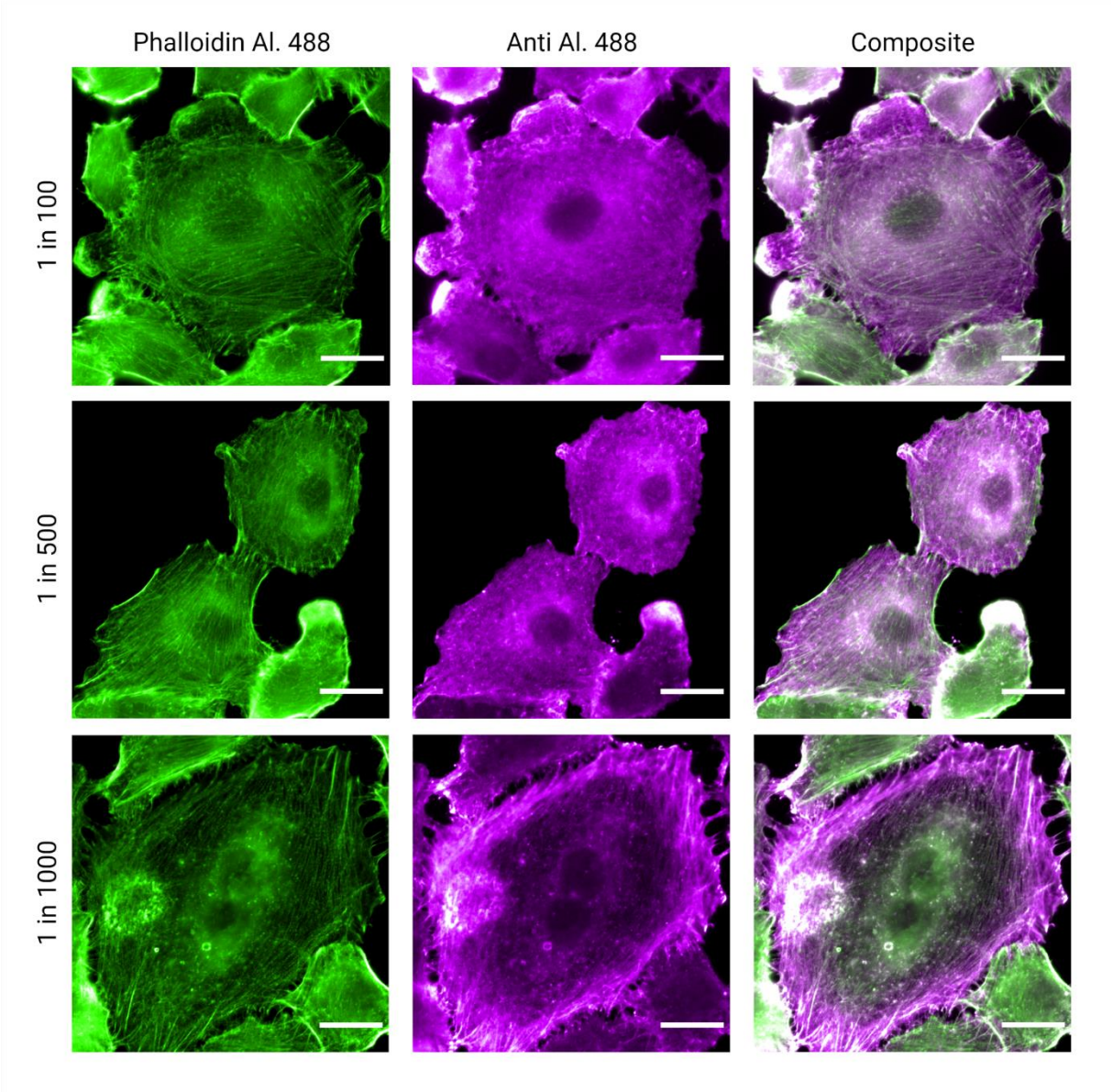

Figure 5.18 – Fidelity of actin labelling is not greatly improved by anti-488 antibody titration. *Epifluorescence representative images of phalloidin labelled with increasing concentrations of anti-488 antibody. All scale bars = 20 µm.*

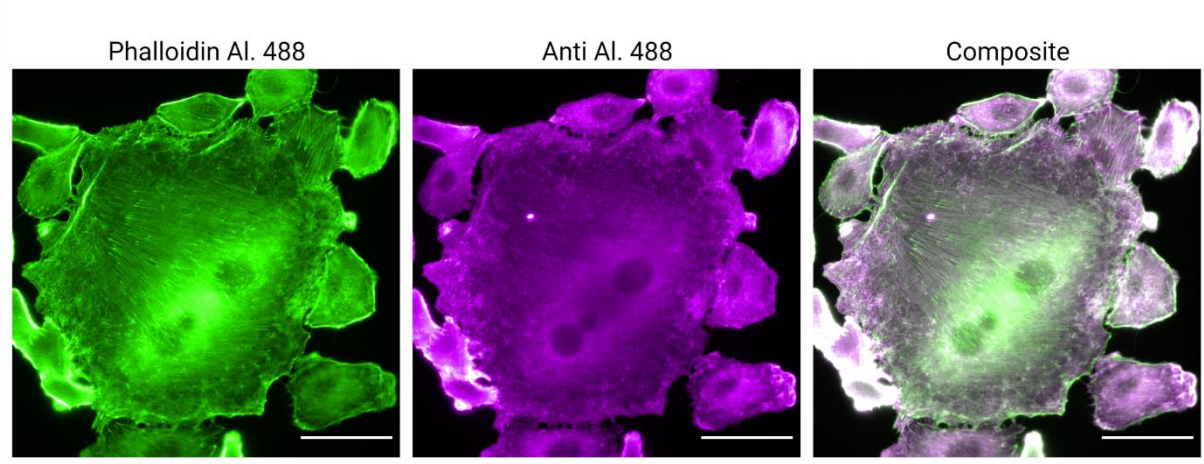

Figure 5.19 – Multi-nucleated cell example. *Epifluorescence example of a large multinucleated cell labelled with phalloidin and anti-488 antibody. Scale bars = 50 µm.*

In a similar approach, an anti-SNAP antibody was also assessed, again with limited success. Labelling was broadly membranous, but did not show direct correlation with SNAP ligand labelled receptor (Figure 5.20). No further tests were performed with this antibody.

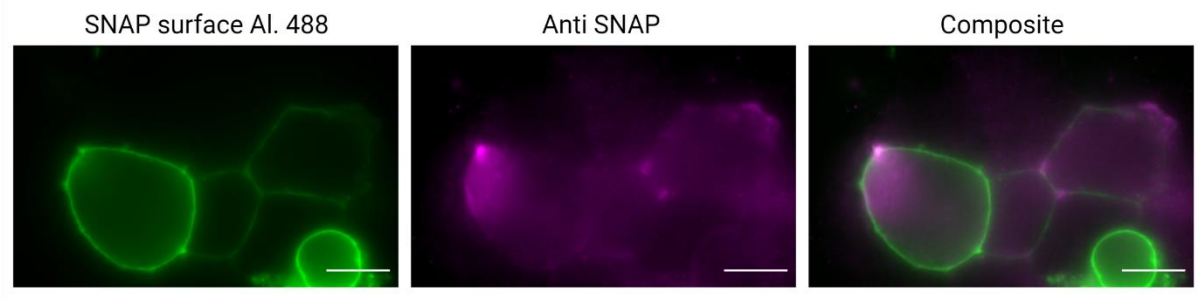

Figure 5.20 – Anti-SNAP antibody performs poorly compared to standard SNAP label. *Equatorial slice of an epifluorescence stack showing SNAP-488 labelled A_{2B} receptor, also labelled with anti-SNAP antibody. Scale bars = 10 µm.*

Direct incorporation of the SNAP-labelled receptor into a standard ExM gel was another potential approach. The reaction between the SNAP ligand and SNAP tag should be irreversible, meaning that if the SNAP tagged portion of the protein is suitably incorporated into the gel, fluorescence should also be retained. ProExM was carried out as described previously (section 4.4). Despite some promising initial indications, consistent retention of well labelled, verifiably non-background level label proved impossible with this approach. Control untransfected samples also showed the same kind of signal as transfected and labelled cells (Figure 5.21).

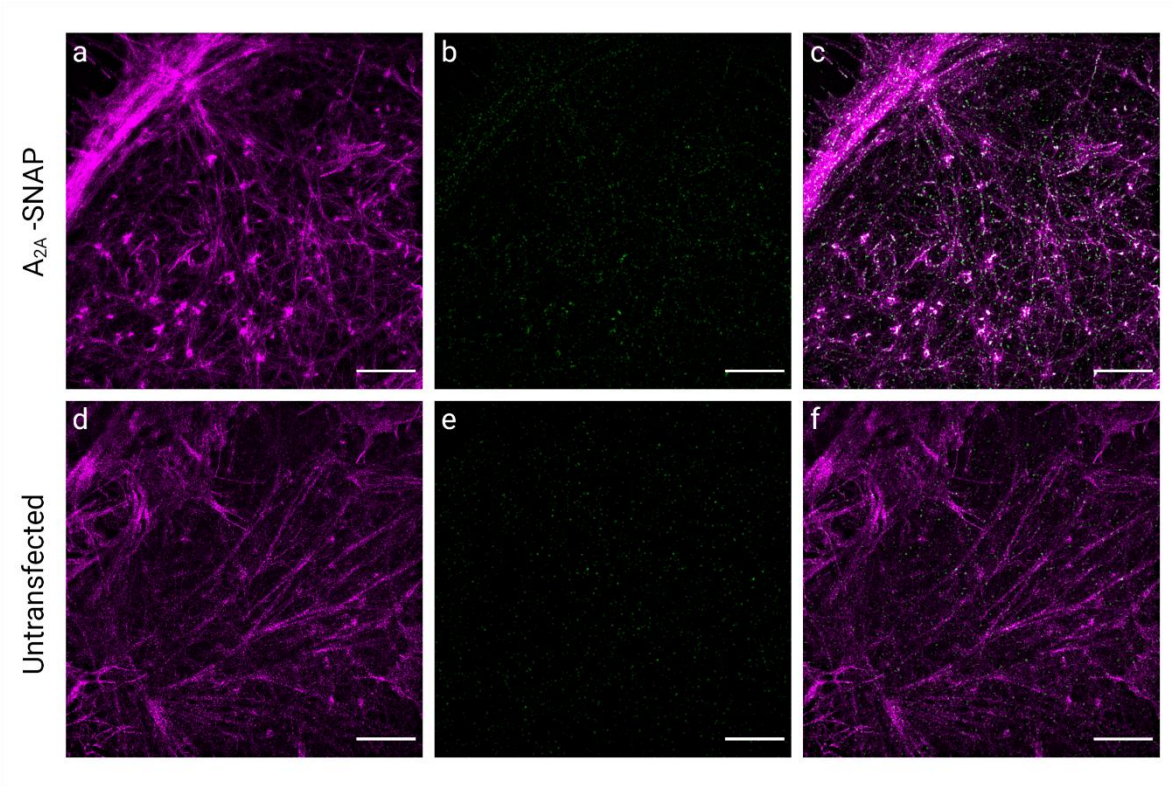

Figure 5.21 – Background is a significant issue in ExM SNAP retention. *3D SIM ExM examples of transfected and untransfected cells labelled with a,d) Actin ExM and b,e) SNAP-488 label. c,f) show merged images. All scale bars = 10 µm, not corrected for expansion factor.*

Signal does appear to be largely restricted to the cellular area, as evidenced in Figure 5.22, as well as following denser regions of actin signal. Bleed through is unlikely given the spectral separation of the two labels and it is likely that non-specific binding of the SNAP ligand is responsible.

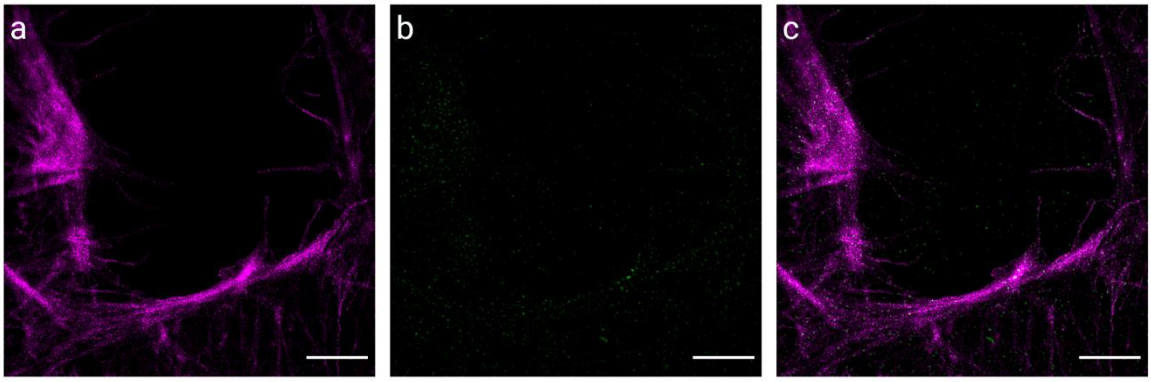

Figure 5.22 – Background appears constrained to the cell*. 3D SIM ExM examples of untransfected cells labelled with SNAP-488 and the Actin ExM label. Scale bars = 10 µm, not corrected for expansion factor.*

Another option was the use of U-ExM, or Ultrastructure Expansion Microscopy. Through a modified gel composition and homogenisation routine, U-ExM retains the organisation of molecular assemblies and results in improved fidelity of ultrastructure. The background of this technique is further discussed in introduction section 1.9.7. As the sample is homogenised through heat and SDS detergent treatment as opposed to a proteinase, I hypothesised that the SNAP-receptor and SNAP ligand complex - which are bound by a theoretically irreversible reaction as described in chapter 3 - was more likely to be retained in U-ExM than in a Proteinase K based digestion. This would theoretically result in additional fluorophores surviving the gelation, homogenisation, and expansion process when compared to typical proExM.

It was important to check that the Actin ExM probe would also work in conjunction with the U-ExM protocol. Experiments adding the probe just prior to gelation, as for the standard ExM prep, showed good retention (Figure 5.23, Figure 5.24). Post labelling of tubulin was also performed to help optimise the protocol. Given that the Actin ExM probe is based on phalloidin, a filamentous actin binder, and coupled with previous poor performance in the absence of anchor (as shown in chapter 4), it is unlikely that Actin ExM can work as a post label, and must be used to label cells prior to gelling steps.

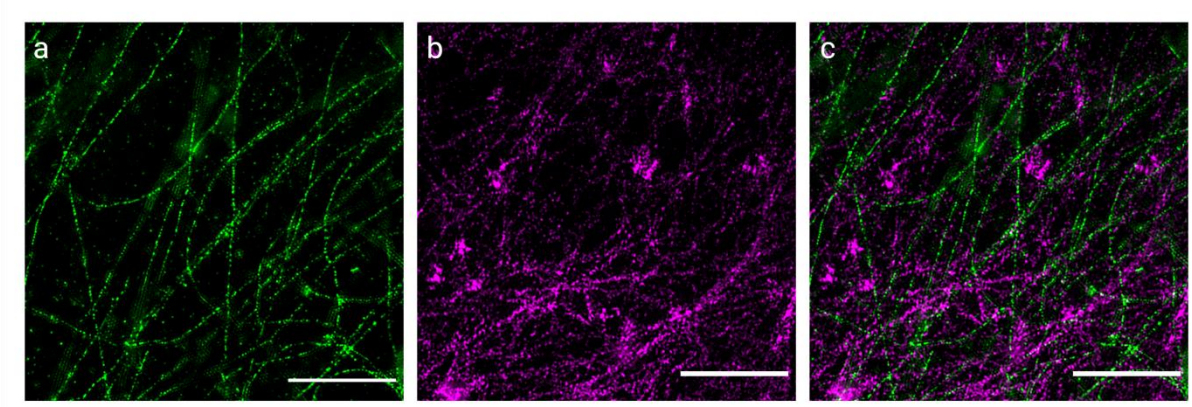

Figure 5.23 – U-ExM preparation allows Actin ExM retention*. a) Post-gelation labelled tubulin and b) pre-gelation Actin ExM labelled actin, merged in c). Scale bars = 10 µm, not corrected for expansion factor.*

In practice, SNAP retention in U-ExM gels was minimal. Similar to results seen in ExM trials, consistent and reliable SNAP retention was not seen (Figure 5.24). Therefore, alternative methods are required which are beyond the scope of this study. Options for this in future work are discussed in section 5.5.2 below.

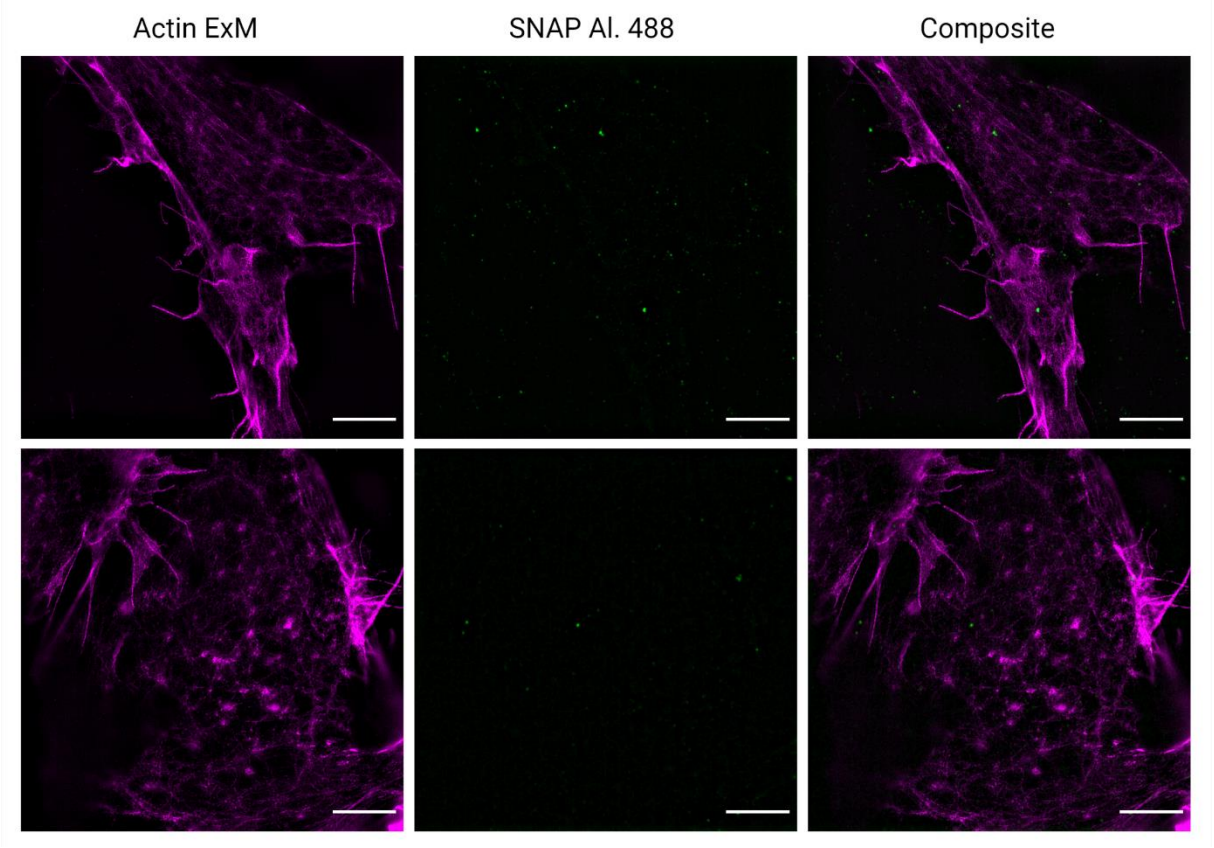

Figure 5.24 – U-ExM preparation does not show reliable SNAP label retention. *Examples of A549 cells transiently transfected with $A_{2A}R$ and labelled with SNAP-Surface Alexa 488 and Actin ExM before U-ExM preparation and expansion. Scale bars = 10 µm, not corrected for expansion factor.*

5.3.2 Localisation of α-actinin-1 illustrates power of the technique

In the absence of being able to label SNAP-tagged receptors in ExM, imaging of antibody labelled α-actinin-1 alongside the Actin ExM labelled actin network was carried out as a pilot experiment for future studies. As previously shown in section 5.2.3, α-actinin-1 labelling with our antibody does not show expected distribution, but does allow for standard primary/secondary labelling and fluorophore retention in the expansion process.

As shown in Figure 5.25, α-actinin-1 is visualised as points at the resolutions achievable with ExM SIM. Label and fluorophore loss, as well as the existing antibody issue, should be considered. Initial appearances may suggest some labelling not associated with the underlying actin, as is also indicated in unexpanded 3D SIM imaging (Figure 5.9). However, it becomes apparent that very fine filaments of actin are underlying many of these detections (Figure 5.25d, e). This illustrates the importance of improved resolution for actin imaging, especially when looking at interactions of receptors or adapter proteins with cortical actin.

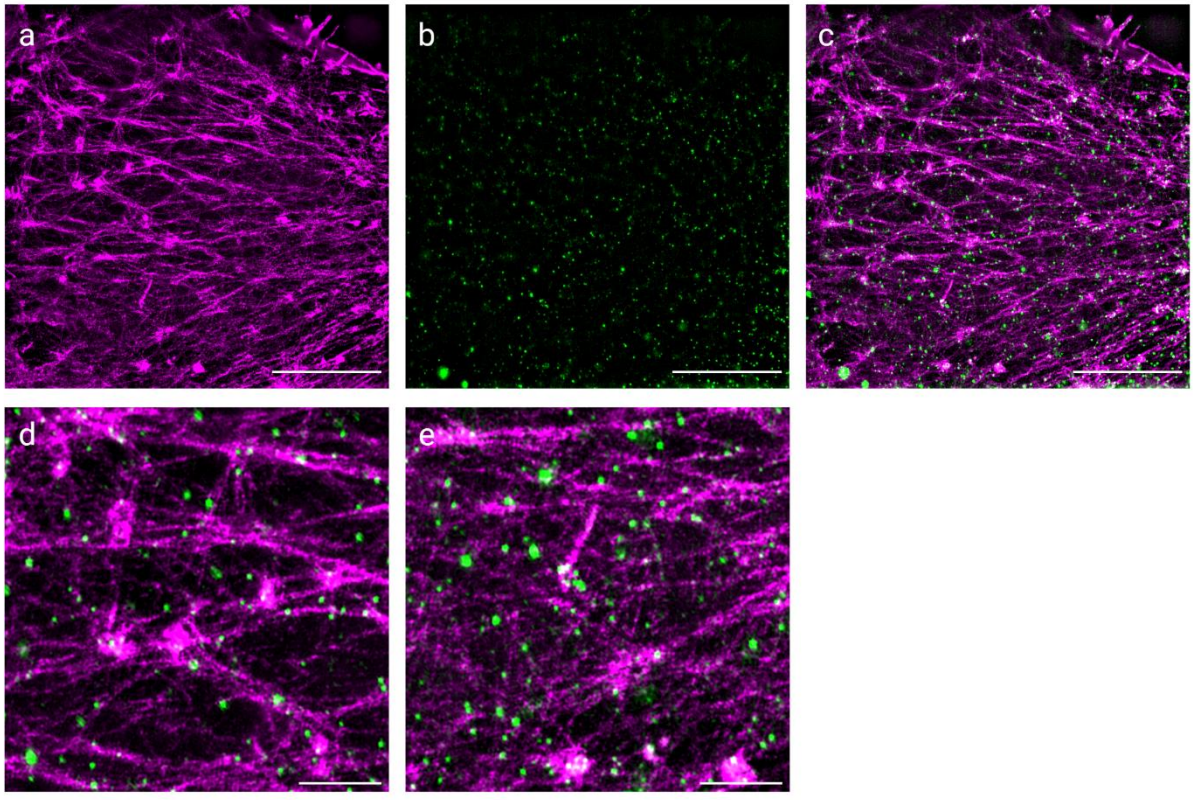

Figure 5.25 – 3D SIM ExM imaging of α-actinin 1 and fine actin. *a) Actin ExM labelled and b) α-actinin 1 labelled sample, shown together in c). d and e) show enlarged regions of c, with fine actin evidently underlying many α-actinin signals. Scale bars (adjusted for expansion) – a-c = 4 µm, d & e = 1 µm.*

5.4 Dual Imaging – Single Particle Tracking and Actin Dynamics

5.4.1 Dual imaging with LifeAct-mEGFP

As described earlier (section 4.3.5), Lifeact-mEGFP is a robust probe for live imaging of actin dynamics, and performs well with potential adaptions of the SRRF corral analysis described to live analysis.

While LifeAct mEGFP transfection into A549 cells did provide excellent signal to noise for SRRF actin imaging, it unfortunately introduced other issues. The intensity of the LifeAct signal resulted in some bleed through in the 560 nm channel – the channel in which the SNAP-549 ligand (used for above for SPT experiments) would be imaged in. Initial trials showed that dense actin regions could significantly impede point detection in the receptor channel, making accurate track generation difficult (Figure 5.26).

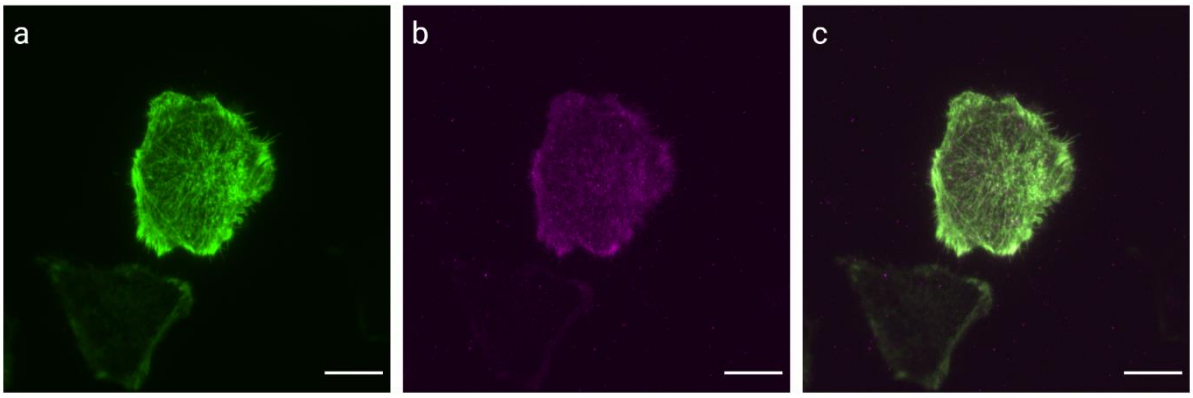

Figure 5.26 – LifeAct mEGFP brightness impedes single particle imaging. *Stills from a TIRF stack of a cell expressing a) LifeAct mEGFP and b) SNAP-A_{2B}R, labelled with SNAP-549. As shown in the overlaid image in c), fluorescence bleedthrough causes significant challenges. Scale bars = 10 µm.*

5.4.2 SiR actin labelling

The fluorogenic probe SiR actin, as tested in chapter 4, had useability benefits and theoretically provided further spectral separation from the 549 SPT probe. However, during imaging it became apparent that concurrent 560 nm and 640 nm illumination was causing significant bleaching of the SiR probe, more than 50% decrease in fluorescence intensity, and well above that seen with 647 illumination alone (Figure 5.27). This decrease was not seen when imaging in conjunction with 488 illumination.

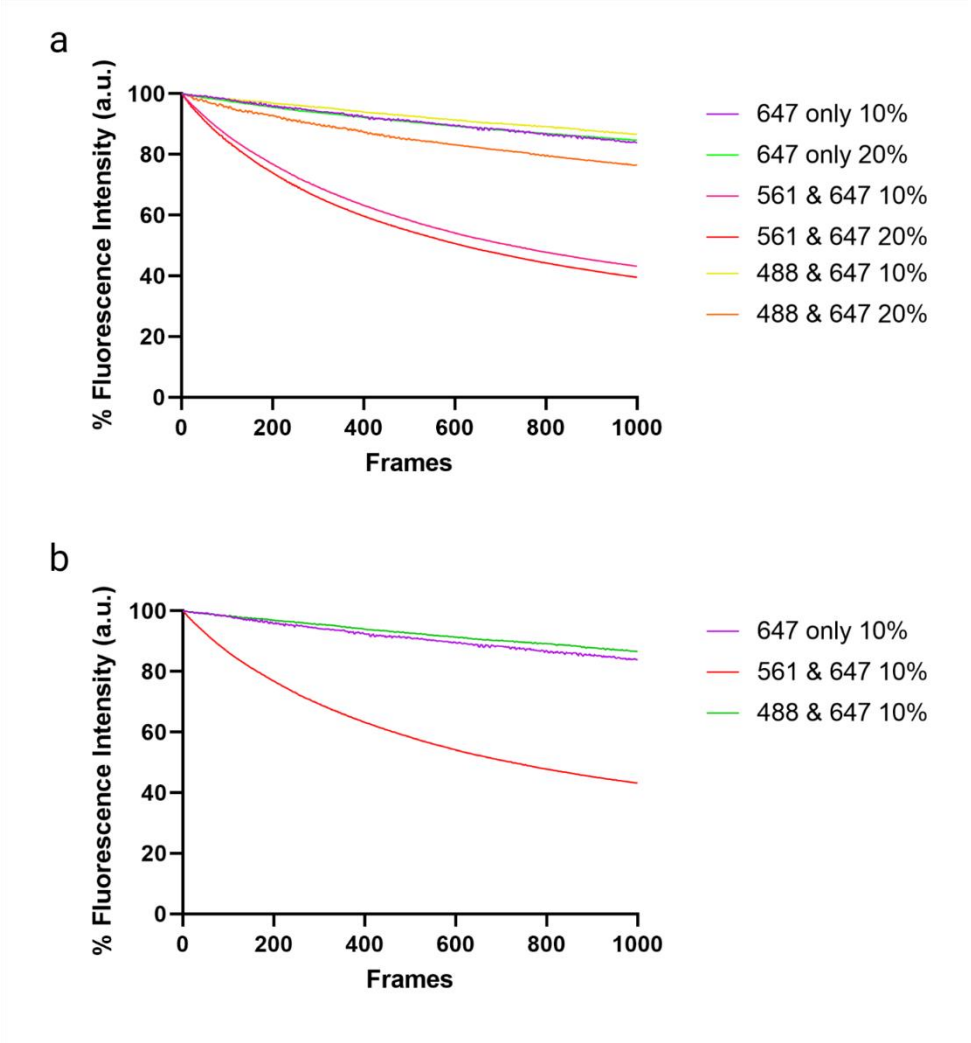

Figure 5.27 – Simultaneous 561 and 647 illumination results in significant bleaching of SiR Actin. *Over 1000 frames at 10 ms per frame, the combination of illumination in the 560 nm range and 640 nm range results in significant reduction in fluorescence intensity of SiR Actin. b) shows only 10% illumination intensity data from a) on a separate graph for ease of comparison. n = 1.*

For this reason, SNAP 488 was considered as an option for receptor labelling, but it did show less photostability and reduced fluorescence intensity compared to SNAP 549, meaning a longer exposure rate was required to obtain images with sufficient SNR for tracking. This longer exposure time limited the ability of the actin channel images to be used for good quality SRRF data.

Despite the optimisation issues some preliminary imaging was possible. When capturing dual channel data, exposure time must be the same for each channel. This presented an issue – optimal exposure time for live SRRF data was 10 ms (100 fps), while SPT data was best collected with exposures of 30 ms (33 fps). Matching the two at 30 ms exposure limited the SRRF actin framerate to 0.33 – 0.66 fps, given that 100 to 50 frames, dependent on SNR, are required for each reconstruction. Capture at 20 ms also permitted good tracking (50 fps) with a SRRF framerate of 0.5 – 1 fps, demonstrated in Figure 5.28 and Video 2. Capture at 10 ms – for a SRRF actin framerate of 1 to 2 fps – introduced SNR problems for single particle tracking.

Taken together, these experiments show that with careful optimisation and awareness of technique limitations it is possible to image both receptors and actin live and simultaneously. This could provide important insight into interactions between the actin cortex and receptor behaviour as both dynamically change.

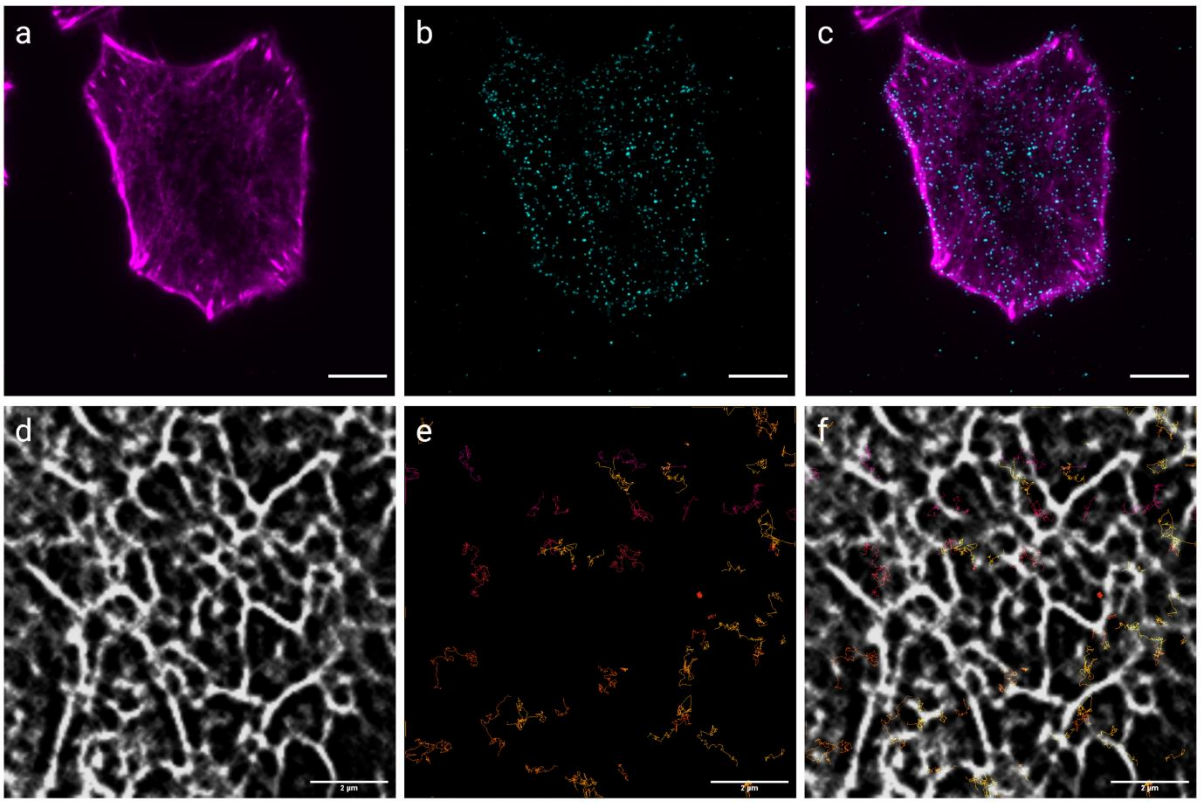

Figure 5.28 – SiR actin and SNAP-549 labelled $A_{2B}R$ permit dual colour SPT captures. *a) Raw TIRF frame of SiR actin. b) Single TIRF frame of SNAP-$A_{2B}R$ labelled with SNAP-549. c) Overlay of a) and b). d) SRRF frame from TIRF images of SiR Actin. e) Tracking of single fluorophores over time. f) Overlay of d) and e). Scale bars a-c = 10 µm, d-f = 2 µm. d-f were captured over 100 frames, at 20 ms exposure per frame.*

5.5 Discussion

This chapter explores multiple methods for investigating actin and receptor interactions in both live and fixed cell contexts. Having gathered 3D SIM data looking at actin and receptor interaction, optimisations for ExM receptor/actin imaging was started. Initial dual imaging experiments combining SPT and SRRF were also conducted.

5.5.1 3D SIM imaging of actin and receptors

Assessment of actin and receptor organisations using 3D SIM provides a sub-diffraction limit assessment of actin/receptor colocalization. For $A_{2A}R$, NECA treatment did not significantly change receptor distribution, with the majority of identified receptors classified as ‘on’ – or, essentially, colocalising with – actin in untreated, vehicle control, and NECA treated samples. Dissociation of the receptor appears to be promoted by both CD and CD + NECA treatment, with proportions of on- filament receptors decreased and off-filament receptors increased relative to DMSO. This is somewhat mirrored in previous findings – suggestive of more ‘free’ receptors, as described by SPT data, the confirmation of which would certainly benefit from the use of dual SPT and SRRF imaging as discussed below.

The A_{2B} receptor responded differently, and in general showed significantly more variability. While for the analysed $A_{2A}R$ expressing cells expression levels were not

significantly different across the treatment groups, $A_{2B}R$ expressing cells did show significant variability. This should be considered when drawing conclusions from the data, and also sits in accordance with the previous suggestion that $A_{2B}R$ clustering changes were not seen due to the heterogenous nature of transient over-expression. As discussed earlier, $A_{2B}R$ has been shown in some circumstances to rely on $A_{2A}R$ [86] to achieve membrane localisation – it may be that endogenous translocation partners, $A_{2A}R$ or otherwise, are saturated at relatively low levels in A549 cells.

For α-actinin-1 localisation, the relatively low association with actin (~ 50%) could be explained by the inability of 3D SIM and the relatively coarse thresholding approach used here to accurately capture very fine actin filaments, as shown in 3D SIM ExM experiments to be underlying a proportion of α-actinin-1 points. The issues with the antibody should also be taken into account in explaining this likely overly low association. As with $A_{2B}R$ above, the number of α-actinin-1 points identified in each drug treatment set was significantly variable, which should inform interpretation of results. This may be due to a reduction in cortical actin proximal to the membrane rather than a loss of α-actinin-1 protein, and therefore a reduction in associated α-actinin identifiable in the basal slices of the cell, as actin area also varies more than in previous experiments (Figure 5.10e). The issue may also stem from the labelling inconsistencies. Future experiments could include western blotting to assess cellular α-actinin-1 levels. The enhanced variability may also be due to fewer repeats being analysed in this experiment. It would be interesting to see if this continued to hold true if more repeats were performed.

When combining $A_{2A}R$ or $A_{2B}R$ with α-actinin-1 imaging and investigating potential behavioural differences with or without receptor association, α-actinin-1 appears to be largely unaffected by receptor association. The same trend of proportions of those on, off, and adjacent is observable regardless of status. This analysis could be further developed by assessing the inverse – that is, behaviour of the receptor with regards to actin association with and without α-actinin-1 proximity. Ways to account for the significant difference in point counts between receptors and α-actinin-1 would have to be carefully considered.

In terms of the analysis applied to SIM images in this chapter, an object based colocalization approach was chosen as opposed to intensity-based techniques like Pearson's correlation coefficient and overlap techniques such as Mander's overlap coefficient, which can be very sensitive to background and provide an overall value for the ROI, rather than the more granular assessment that would better answer the research question here. Using the co-ordinates of each identified points centroid and a search radius to define receptor position is a simplified take on the concepts used in SODA, or Statistical Object Distance Analysis [243], among other object and co-ordinate based approaches [244, 245].

5.5.2 Multicolour Expansion microscopy optimisation

One major benefit of expansion microscopy is the relative ease of multi-label imaging. Theoretically, expansion has the same spectral range as widefield

investigations. Blinking behaviour, as relevant for SMLM, or a suitable Stokes shift as for STED, are not a concern with this technique. Incorporation of the label into the gel can instead be a limiting factor. In standard proExM preparations, there is still a significant amount of label loss due to failure to anchor (and subsequent loss of either the label or the label-bound epitope), fluorophore destruction, or epitope destruction. U-ExM [141] and other post-labelling approaches aim to limit this, but still rely on epitope retention post homogenisation. For this reason, quantitation of ExM data should be approached with caution.

Beyond label loss, incorporation of non-antibody labels into the gel can also prove problematic. For AcX, the anchoring chemical used in this thesis, to functionalise a protein or small molecule, it must have a free amine group. This is unfortunately not true for phalloidin or for SNAP ligands, meaning alternatives had to be sought.

For SNAP labelled receptors, incorporation attempts in this chapter were made through standard ExM preparations – both pro- and U-ExM. Theoretically, SNAP labelling is an irreversible reaction, meaning that the fluorophore should be directly conjugated to the receptor after incubation with the ligand. As such, anchoring of the receptor itself into the gel could have allowed label retention. Unfortunately, this was not seen with pro-ExM preparations. It was then hypothesised that the proteinase K digestion could be impeding retention, leading to the testing of U-ExM gelation. The homogenisation step in the U-ExM protocol relies on heat and detergent rather than

proteinase, with the additional formaldehyde incubation step also serving to better preserve ultrastructure. Initial trials of this approach were also unsuccessful.

Our label of choice for actin was ActinExM, a commercially available phalloidin derivative with a trifunctional linker in addition to the fluorophore [157]. Publications imaging actin with ExM have also reported the use of LifeAct-SNAP [158]. Recently, Park et al. [156] used anti-fluorophore antibodies to image actin labelled with standard Alexa 488 conjugated phalloidin, a potentially simple workaround for non-antibody label incorporation. However, in our hands the anti-488 antibody approach was inconsistent and led to incomplete labelling. Using the same polyclonal anti-Alexa 488 antibody listed by Park et al., this technique was tested with phalloidin Alexa 488, α tubulin labelled with a mouse primary and anti-mouse Alexa 488 secondary (data not shown), and with SNAP-Surface Alexa 488. In each case, the anti-fluorophore antibody failed to fully quench the Alexa 488, which would be expected from complete labelling based on personal communications with Invitrogen. Concentration of the anti-fluorophore primary was matched to the value published by Park et al. (10 μg mL^{-1}), which did not significantly affect the degree of labelling. Therefore, whilst the anti-488 antibody approach offers a potential solution to the labelling challenge, in our hands this was not a robust and reliable approach.

For SNAP incorporation in future works, other options would include custom made trifunctional SNAP probes – such as those employed by Shi et al. [155] – or revisiting

the concepts established by Park et al. and attempting the use of an anti-biotin antibody, for example.

Despite not being able to gather receptor/actin data, investigation of the potential receptor-actin bridging protein α-actinin-1 can provide some insight into the power of multicolour ExM as an investigative technique. The very fine actin filaments evident in these images underlie some α-actinin-1 points, which in combination with receptor labelling could give a better assessment of actin-receptor and actin-receptor- α-actinin-1 interactions. Again, issues with the α-actinin-1 antibody should temper conclusions from data in this work.

5.5.3 Dual actin and receptor live imaging optimisation

Work in this chapter laid the groundwork for future dual SPT and SRRF investigations, as well as potential analysis methods. From a technical perspective there are still some key issues to be addressed. The bleaching of SiR actin when imaging concurrently with 560 nm laser does limit the SNAP ligands useable. A potential explanation comes from the excitation/emission graph for SiR actin from Spirochrome, which suggests potential for excitation with 560 nm laser given the hump on the left side of the curve (Figure 5.29a). Use of SiR 700 – a modified version of SiR actin with a further right emission spectra – may give more useful spectral separation, though the leftward shift in the excitation curve could still pose issues (Figure 5.29b).

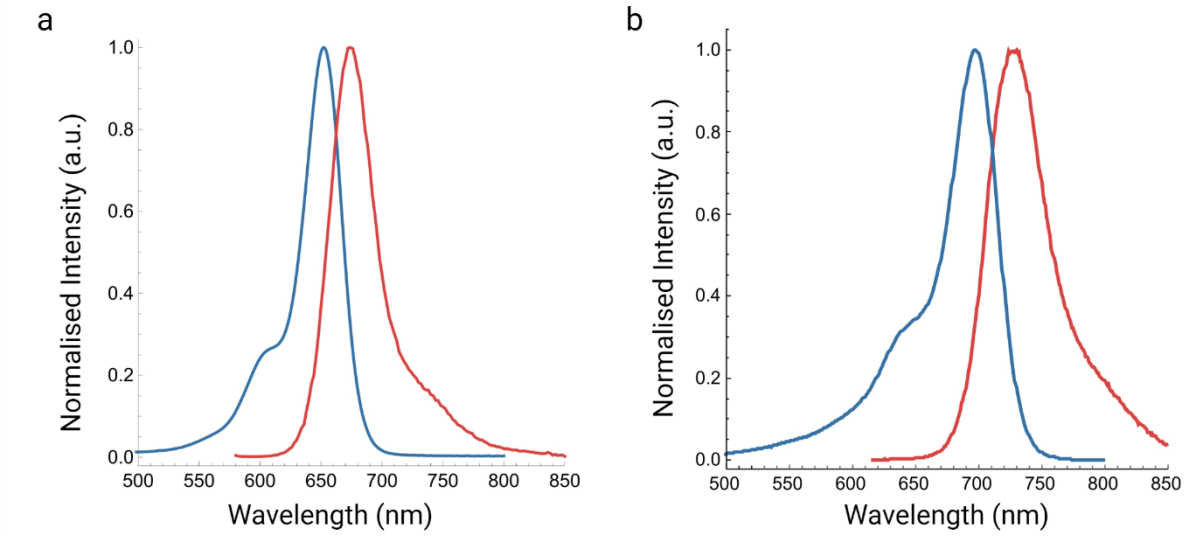

Figure 5.29 – Excitation and emission spectra for SiR Actin options. *Excitation (blue) and emission (red) spectra from Spirochrome.com/products for a) SiR Actin and b) SiR 700 Actin.*

In the work described in this chapter, two sCMOS cameras were used to capture TIRF data for SPT and SRRF analysis. While EMCCD cameras typically perform best in low light conditions, their large pixels and relatively slow read times can affect both temporal and spatial resolution outcomes.The sCMOS detectors used here have a relative pixel size of ~ 65 nm with the 100x objectives, but higher laser powers to obtain good SNR were necessary. Both camera options have pros and cons that should be considered.

In terms of analysis, a paper employing a similar dual SRRF/receptor imaging concept [242] argues that ‘off fibre’ actin pixels should be masked out of the SRRF image before later analysis.They use a combination of an unprocessed time-summed TIRF image and the dynamics of LifeAct binding and unbinding to generate the

mask. However, given data from chapter 4 (especially as demonstrated in Figure 4.6) and the level of detail visible when applying 3D SIM ExM – shown especially well by the α-actinin-1 and actin dual imaging (Figure 5.25) – this could be discarding genuine actin signal in favour of only thicker filaments. The authors do acknowledge that a SNR of at least 3x greater for actin than background is necessary for accurate masking, which may not be achievable for very fine or very dynamic actin filaments. Beyond these concerns, this paper argues that the EGF receptor is only indirectly modulated by actin, as there is no direct effect on oligomerisation or diffusion in the presense of actin. Actin disruption with LatA, however, does affect receptor diffusion – which the authors use to argue that actin affects EGFR only insofar as it organises the membrane in a more general sense, as opposed to a direct link. This is an important distinction to consider when interpreting results in this thesis, and another key reason to identify potential adaptor or interactor proteins like α-actinin-1.

5.6 Chapter Conclusions

Work in this chapter provides further insight into the differential behaviour of $A_{2A}R$ and $A_{2B}R$ with respect to actin association through 3D SIM two colour imaging, and begins to demonstrate further investigative options in the form of dual SRRF/SPT imaging and high-resolution actin/actin associating protein imaging. Technical limitations were identified, and optimisations trialled or suggested.

So, relative to the initial aims given in the chapter overview, this work has further assessed the relationship of actin, A_2 receptors, and α-actinin-1 using 3D SIM imaging. Steps were taken to assess options for receptor incorporation into ExM techniques, and α-actinin-1 labelling showed promising results. Dual imaging was also demonstrated in dynamic contexts using SRRF and SPT.

CHAPTER 6 – DISCUSSION AND FUTURE WORK

6.1 Conclusions from This Work

This work provides a range of evidence to indicate a role for actin in modulating adenosine receptor behaviour. In addition, a combination of imaging approaches and supporting pharmacological data show both that $A_{2A}R$ and $A_{2B}R$ are regulated differently with regards to actin.

When looking at the receptor alone using dSTORM to assess clustering, it was shown that $A_{2B}R$ clusters are unaffected by actin disruption or receptor stimulation. $A_{2A}R$ clusters, however, shrink significantly with CD treatment. When the receptor is activated at the same time as the actin is disrupted, this disruption is no longer seen. Similar cumulative effects from CD + NECA treatments are apparent in actin/receptor SIM investigations for $A_{2A}R$, but – again – not for $A_{2B}R$.

Considering dynamics, no major changes in diffusion coefficients were observed for the receptors, but time spent in different motion states was affected by drug treatments. This suggests a more local rather than global effect of actin on receptor behaviour. While this is somewhat counter intuitive to the idea of hop diffusion and its slowing effect on micrometre scale dynamics as proposed in the literature, other published findings argue for ‘complex counteractions’ of actin disruption within cells and show rapid recovery of fine corral structures post CD treatment [15], potentially explaining this apparent mismatch.

Linking some of this data with findings in chapter 4, the mean size of corrals identified in control SRRF data is ~0.2-0.3 μm^2. Relative to average size of resting SNAP-A_{2A}R clusters (~0.006 μm^2), and resting SNAP-A_{2B}R clusters (~0.005 μm^2), these corrals are significantly larger. Given the resolution limitations of SRRF data, finer scale organisation may not be identifiable in these experiments – and hence the optimisation of the 3D SIM ExM technique. It could also be that clustering is not directly maintained by actin corrals. SPT confinement radii are 0.146 µm for A_{2A}R and 0.143 µm for A_{2B}R respectively, which could indicate a more direct role for the actin corrals visualised here in constraint of dynamics rather than in direct cluster organisation.

Actin changes detectable with SRRF analysis could support an interesting link between actin organisation and receptor stimulation, which could be further assessed with dual imaging techniques. Proposed analysis methods for both live (SRRF/SPT) and high resolution fixed (3D SIM ExM) dual imaging could allow calculation of metrics otherwise obscured by non-simultaneous imaging. These techniques build off of existing published actin/receptor investigations, adapted for our purposes. All approaches and analysis within this thesis should be more generally applicable to other membrane receptors as well as GPCRs.

This thesis also demonstrated the importance of using a variety of techniques to answer a research question. Imaging approaches can give insight into dynamics as well as structural changes, which, when combined with pharmacological

investigations, form a more complete picture of receptor response to actin disruption with and without receptor stimulation.

6.2 Issues and Future Directions

6.2.1 Receptor expression and CRISPR-Cas9

Some general issues with receptor expression must be acknowledged. For example, A549 cells endogenously express both the A_{2B} and A_1 receptors according to Protein Atlas [196], meaning that there will inevitably be further effects from general NECA stimulation. In addition, any endogenous adenosine receptor would remain unlabelled in these experiments, potentially hiding reorganisation or dynamic changes.

Expression level is also inherently variable in an overexpression system. As shown by Khan et al. [205], this can extend to hiding significant changes in cluster behaviour. The authors engineered a CRISPR-Cas9 CXCR4-HALO knock-in HEK293T cell line and compared behaviour to cells transiently transfected with the CXCR4-HALO construct. They showed that CXCR4-HALO clustering was affected significantly by CXCL12 treatment only in the CRISPR line, with the overexpressed receptors showing no significant change.

As a result, initial plans were made here to endogenously N-terminally SNAP tag the A_{2B} receptor in the A549 cell line using CRISPR-Cas9. Initial attempts to produce the stable cell line were unsuccessful and further development was halted by Covid restrictions. For future works, this line would be essential to investigate endogenous response, and could provide important insight into any differences in behaviour induced by overexpression.

6.2.2 Expanding labelling and imaging options

Given the two receptors appear to be differentially regulated with regards to actin, imaging of both $A_{2A}R$ and $A_{2B}R$ together with the actin cortex could provide important insight. To permit simultaneous imaging of both receptors, an N-terminally HALO-tagged $A_{2A}R$ construct was generated (see section 2.3) for future testing and optimisation. This would allow dual imaging in all techniques applied in this thesis, adding an extra dimension to the findings.

As discussed in chapter 5, incorporation of SNAP – or, indeed, HALO - labelling into ExM techniques would require further optimisation over the methods attempted in this thesis. Custom made ligands with additional anchoring moieties have been previously demonstrated to be efficient in terms of label retention and would be a logical next step.

For dual SPT, use of less bright SNAP ligands could be permitted by summing frames prior to spot detection. This was tested briefly with SNAP Alexa 488 imaged at 10 ms exposure and summed to 30 ms, in order to better diversify both label wavelengths and exposure times in dual imaging experiments.

While the techniques already employed in this thesis could be further adapted to answer new questions, 3D information may be best garnered from expansion samples imaged with a lightsheet microscope. Initial tests were conducted on an iSPIM system with standard ExM samples, and permitted imaging of both apical and basal actin at comparable resolutions (Video 3). With inclusion of the receptor label, this could allow interesting comparison between arrangements across the cell membrane.

6.2.3 Analysis options

Application of machine or deep learning assisted analysis would be an interesting avenue for future work. A recent paper discusses the use of machine learning for cluster analysis of SMLM outputs, and explores the potential for use to identify fibrous structures [174]. Single particle tracking analysis is also another topic of significant machine learning interest. A range of works demonstrating model training and application have been published (for example, [246-248], among others). Generalisability of these models would need careful assessment for our purposes.

6.2.4 Further membrane investigations

It is also worth considering that the receptor is only one part of the signalling pathway. Actin could be affecting likelihood of encountering G proteins (as evidenced by Sungkaworn et al.'s signalling hotspots [163]), or modulating local membrane components and then, through this, A_2 receptor behaviour. $A_{2A}R$ has been reported to be particularly strongly associated with cholesterol, with cholesterol sequestration having major effect on lateral diffusion [195]. The existence of cholesterol mediated membrane organisation by no means precludes potential actin related effects – in fact, several papers report links between the two. For example, chronic depletion of cholesterol from the membrane significantly increases gross F-actin content in the cell [249], and there is evidence that cholesterol's organisation of phosphatidylinositol 4,5-bisphosphate, a known actin cytoskeletal regulator, is the root of this interdependence [250]. Imaging of receptors and actin during cholesterol sequestration through the workflows established in this thesis could provide more context to this interplay.

6.2.5 Actin interacting proteins and the C-terminal tail

While initial work in this thesis demonstrated imaging of α-actinin-1 together with the A_2 receptors and actin, this potential mechanism for receptor/actin interaction warrants further investigation. As $A_{2A}R$ association with α-actinin-1 has been shown to be displaced by calmodulin binding in a Ca^{2+} dependent fashion [67], modification

to this C-terminal binding site may help to clarify whether this association has organisational consequences. Assessing A_{2B}R/α-actinin-1 association could also help explain the differential behaviours between the A_2 receptors. Generation of A_{2A}R and A_{2B}R constructs with a C-terminal tail truncation, or swapping the tail between the two receptors, could also confirm if this major structural difference is the cause of the receptors differing organisations.

6.3 Final Conclusions

Key outcomes, both in terms of biological findings and technique development and optimisation, are listed in Figure 6.1. In short, this thesis demonstrates a differential regulation of the A_2 receptors A_{2A}R and A_{2B}R by actin, through a range of fixed and live cell super resolution imaging approaches. In addition to these biological findings, methods for dual colour and higher resolution investigations were established and analysis pipelines developed. These approaches would also be amenable to use with other membrane receptors, with many potential applications of biological interest. This work provides a hypothesis on the nature of the behavioural differences of the receptors, and further development of these imaging approaches would allow a more detailed investigation of receptor and actin behaviours to be explored.

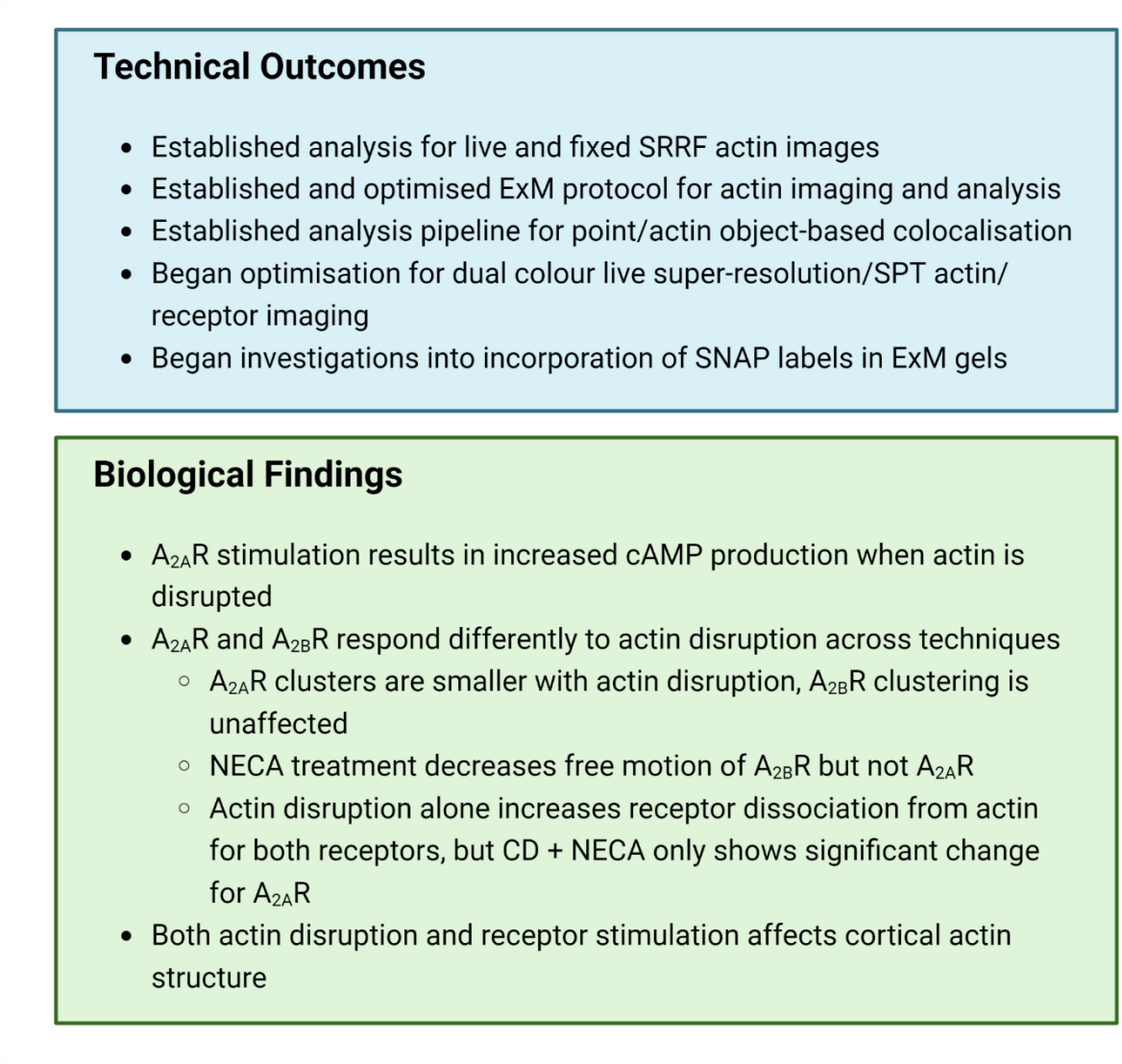

Figure 6.1 – Summary of outcomes of this thesis.

REFERENCES

1. Hauser, A.S., et al., *Trends in GPCR drug discovery: new agents, targets and indications.* Nature Reviews Drug Discovery, 2017. **16**: p. 829.
2. Bernardino de la Serna, J., et al., *There Is No Simple Model of the Plasma Membrane Organization.* Frontiers in cell and developmental biology, 2016. **4**: p. 106-106.
3. Robertson, J.D., *Membrane structure.* Journal of Cell Biology, 1981. **91**(3): p. 189s-204s.
4. Singer, S.J. and G.L. Nicolson, *The Fluid Mosaic Model of the Structure of Cell Membranes.* Science, 1972. **175**(4023): p. 720.
5. Nicolson, G.L., *The Fluid—Mosaic Model of Membrane Structure: Still relevant to understanding the structure, function and dynamics of biological membranes after more than 40years.* Biochimica et Biophysica Acta (BBA) - Biomembranes, 2014. **1838**(6): p. 1451-1466.
6. Sezgin, E., et al., *The mystery of membrane organization: composition, regulation and roles of lipid rafts.* Nature Reviews Molecular Cell Biology, 2017. **18**(6): p. 361-374.
7. Eggeling, C., et al., *Direct observation of the nanoscale dynamics of membrane lipids in a living cell.* Nature, 2009. **457**(7233): p. 1159-1162.
8. Mostowy, S. and P. Cossart, *Septins: the fourth component of the cytoskeleton.* Nature Reviews Molecular Cell Biology, 2012. **13**(3): p. 183-194.
9. Möckl, L., *The Emerging Role of the Mammalian Glycocalyx in Functional Membrane Organization and Immune System Regulation.* Frontiers in Cell and Developmental Biology, 2020. **8**.
10. Yáñez-Mó, M., et al., *Tetraspanin-enriched microdomains: a functional unit in cell plasma membranes.* Trends in Cell Biology, 2009. **19**(9): p. 434-446.
11. Bailey, R.L., et al., *The emerging role of tetraspanin microdomains on endothelial cells.* Biochemical Society Transactions, 2011. **39**(6): p. 1667-1673.
12. Freeman, S.A., et al., *Transmembrane Pickets Connect Cyto- and Pericellular Skeletons Forming Barriers to Receptor Engagement.* Cell, 2018. **172**(1-2): p. 305-317.e10.
13. Fujiwara, T., et al., *Phospholipids undergo hop diffusion in compartmentalized cell membrane.* Journal of Cell Biology, 2002. **157**(6): p. 1071-1082.
14. Morone, N., et al., *Three-dimensional reconstruction of the membrane skeleton at the plasma membrane interface by electron tomography.* Journal of Cell Biology, 2006. **174**(6): p. 851-862.
15. Fujiwara, T.K., et al., *Confined diffusion of transmembrane proteins and lipids induced by the same actin meshwork lining the plasma membrane.* Molecular biology of the cell, 2016. **27**(7): p. 1101-1119.
16. Andrade, D.M., et al., *Cortical actin networks induce spatio-temporal confinement of phospholipids in the plasma membrane – a minimally invasive investigation by STED-FCS.* Scientific Reports, 2015. **5**(1): p. 11454.
17. Lagerholm, B.C., et al., *Convergence of lateral dynamic measurements in the plasma membrane of live cells from single particle tracking and STED-FCS.* Journal of Physics D: Applied Physics, 2017. **50**(6): p. 063001.

18. Paller, M.S., *Lateral mobility of Na,K-ATPase and membrane lipids in renal cells. Importance of cytoskeletal integrity.* The Journal of Membrane Biology, 1994. **142**(1): p. 127-135.
19. Edidin, M., M.C. Zúñiga, and M.P. Sheetz, *Truncation mutants define and locate cytoplasmic barriers to lateral mobility of membrane glycoproteins.* Proceedings of the National Academy of Sciences, 1994. **91**(8): p. 3378.
20. Stanly, T.A., et al., *The cortical actin network regulates avidity-dependent binding of hyaluronan by the lymphatic vessel endothelial receptor LYVE-1.* The Journal of biological chemistry, 2020. **295**(15): p. 5036-5050.
21. Sperotto, M.M. and O.G. Mouritsen, *Monte Carlo simulation studies of lipid order parameter profiles near integral membrane proteins.* Biophysical journal, 1991. **59**(2): p. 261-270.
22. Saxton, M.J., *Anomalous diffusion due to obstacles: a Monte Carlo study.* Biophysical journal, 1994. **66**(2 Pt 1): p. 394-401.
23. Bussell, S.J., D.L. Koch, and D.A. Hammer, *Effect of hydrodynamic interactions on the diffusion of integral membrane proteins: diffusion in plasma membranes.* Biophysical journal, 1995. **68**(5): p. 1836-1849.
24. Jacobson, K., P. Liu, and B.C. Lagerholm, *The Lateral Organization and Mobility of Plasma Membrane Components.* Cell, 2019. **177**(4): p. 806-819.
25. Ashdown, G.W., et al., *Live-Cell Super-resolution Reveals F-Actin and Plasma Membrane Dynamics at the T Cell Synapse.* Biophysical journal, 2017. **112**(8): p. 1703-1713.
26. Fritzsche, M., et al., *Cytoskeletal actin dynamics shape a ramifying actin network underpinning immunological synapse formation.* Science Advances, 2017. **3**(6): p. e1603032.
27. Bovellan, M., et al., *Cellular Control of Cortical Actin Nucleation.* Current Biology, 2014. **24**(14): p. 1628-1635.
28. Machesky, L.M. and K.L. Gould, *The Arp2/3 complex: a multifunctional actin organizer.* Current Opinion in Cell Biology, 1999. **11**(1): p. 117-121.
29. Levayer, R. and T. Lecuit, *Biomechanical regulation of contractility: spatial control and dynamics.* Trends in Cell Biology, 2012. **22**(2): p. 61-81.
30. Clausen, M.P., et al., *Dissecting the actin cortex density and membrane-cortex distance in living cells by super-resolution microscopy.* Journal of physics D: Applied physics, 2017. **50**(6): p. 064002-064002.
31. Fritzsche, M., et al., *Actin kinetics shapes cortical network structure and mechanics.* Science Advances, 2016. **2**(4): p. e1501337.
32. Chalut, Kevin J. and Ewa K. Paluch, *The Actin Cortex: A Bridge between Cell Shape and Function.* Developmental Cell, 2016. **38**(6): p. 571-573.
33. Escuin, S., et al., *Rho-kinase-dependent actin turnover and actomyosin disassembly are necessary for mouse spinal neural tube closure.* Journal of cell science, 2015. **128**(14): p. 2468-2481.
34. Fievet, B.T., et al., *Phosphoinositide binding and phosphorylation act sequentially in the activation mechanism of ezrin.* The Journal of cell biology, 2004. **164**(5): p. 653-659.
35. Pearson, M.A., et al., *Structure of the ERM Protein Moesin Reveals the FERM Domain Fold Masked by an Extended Actin Binding Tail Domain.* Cell, 2000. **101**(3): p. 259-270.

36. Köster, D.V. and S. Mayor, *Cortical actin and the plasma membrane: inextricably intertwined.* Current Opinion in Cell Biology, 2016. **38**: p. 81-89.
37. Nygaard, R., et al., *Ligand binding and micro-switches in 7TM receptor structures.* Trends in Pharmacological Sciences, 2009. **30**(5): p. 249-259.
38. Syrovatkina, V., et al., *Regulation, Signaling, and Physiological Functions of G-Proteins.* Journal of Molecular Biology, 2016. **428**(19): p. 3850-3868.
39. Corriden, R., et al., *Kinetic analysis of antagonist-occupied adenosine-A3 receptors within membrane microdomains of individual cells provides evidence of receptor dimerization and allosterism.* FASEB journal : official publication of the Federation of American Societies for Experimental Biology, 2014. **28**(10): p. 4211-4222.
40. Dorsch, S., et al., *Analysis of receptor oligomerization by FRAP microscopy.* Nature Methods, 2009. **6**(3): p. 225-230.
41. Hebert, T.E., et al., *A Peptide Derived from a β2-Adrenergic Receptor Transmembrane Domain Inhibits Both Receptor Dimerization and Activation.* Journal of Biological Chemistry, 1996. **271**(27): p. 16384-16392.
42. Ferré, S., et al., *G protein-coupled receptor oligomerization revisited: functional and pharmacological perspectives.* Pharmacological reviews, 2014. **66**(2): p. 413-434.
43. Hübner, H., et al., *Structure-guided development of heterodimer-selective GPCR ligands.* Nature Communications, 2016. **7**(1): p. 12298.
44. AbdAlla, S., et al., *Increased AT1 receptor heterodimers in preeclampsia mediate enhanced angiotensin II responsiveness.* Nature Medicine, 2001. **7**(9): p. 1003-1009.
45. Gomes, I., et al., *G Protein-Coupled Receptor Heteromers.* Annual review of pharmacology and toxicology, 2016. **56**: p. 403-425.
46. Kniazeff, J., et al., *Dimers and beyond: The functional puzzles of class C GPCRs.* Pharmacology & therapeutics, 2011. **130**(1): p. 9-25.
47. Getter, T., et al., *Identification of small-molecule allosteric modulators that act as enhancers/disrupters of rhodopsin oligomerization.* Journal of Biological Chemistry, 2021. **297**(6).
48. Fung, J.J., et al., *Ligand-regulated oligomerization of β2-adrenoceptors in a model lipid bilayer.* The EMBO Journal, 2009. **28**(21): p. 3315-3328.
49. Scarselli, M., P. Annibale, and A. Radenovic, *Cell Type-specific β2-Adrenergic Receptor Clusters Identified Using Photoactivated Localization Microscopy Are Not Lipid Raft Related, but Depend on Actin Cytoskeleton Integrity *.* Journal of Biological Chemistry, 2012. **287**(20): p. 16768-16780.
50. Martínez-Muñoz, L., et al., *Separating Actin-Dependent Chemokine Receptor Nanoclustering from Dimerization Indicates a Role for Clustering in CXCR4 Signaling and Function.* Molecular Cell, 2018. **70**(1): p. 106-119.e10.
51. Sheth, S., et al., *Adenosine receptors: expression, function and regulation.* International journal of molecular sciences, 2014. **15**(2): p. 2024-2052.
52. Fredholm, B.B., et al., *Comparison of the potency of adenosine as an agonist at human adenosine receptors expressed in Chinese hamster ovary cells11Abbreviations: cAMP, cyclic adenosine 3',5'-monophosphate; CHO, Chinese hamster ovary; NBMPR, nitrobenzylthioinosine; and NECA, 5'-N-ethyl carboxamido adenosine.* Biochemical Pharmacology, 2001. **61**(4): p. 443-448.

53. Fredholm, B.B., *Adenosine—a physiological or pathophysiological agent?* Journal of Molecular Medicine, 2014. **92**(3): p. 201-206.
54. Fredholm, B.B., *Adenosine, an endogenous distress signal, modulates tissue damage and repair.* Cell Death & Differentiation, 2007. **14**(7): p. 1315-1323.
55. Jaakola, V.-P., et al., *The 2.6 angstrom crystal structure of a human A2A adenosine receptor bound to an antagonist.* Science (New York, N.Y.), 2008. **322**(5905): p. 1211-1217.
56. Carpenter, B. and G. Lebon, *Human Adenosine A2A Receptor: Molecular Mechanism of Ligand Binding and Activation.* Frontiers in Pharmacology, 2017. **8**.
57. García-Nafría, J., et al., *Cryo-EM structure of the adenosine A2A receptor coupled to an engineered heterotrimeric G protein.* eLife, 2018. **7**: p. e35946.
58. Burnstock, G., *Purinergic Signalling: Therapeutic Developments.* Frontiers in Pharmacology, 2017. **8**.
59. Cooper, S.L., et al., *Regionally selective cardiovascular responses to adenosine A2A and A2B receptor activation.* The FASEB Journal, 2022. **36**(4): p. e22214.
60. Borea, P.A., et al., *Pharmacology of Adenosine Receptors: The State of the Art.* Physiological Reviews, 2018. **98**(3): p. 1591-1625.
61. Canals, M., et al., *Homodimerization of adenosine A2A receptors: qualitative and quantitative assessment by fluorescence and bioluminescence energy transfer.* Journal of Neurochemistry, 2004. **88**(3): p. 726-734.
62. Vidi, P.-A., et al., *Adenosine A2A receptors assemble into higher-order oligomers at the plasma membrane.* FEBS Letters, 2008. **582**(29): p. 3985-3990.
63. Nguyen, K.D.Q., et al., *Homo-oligomerization of the human adenosine A2A receptor is driven by the intrinsically disordered C-terminus.* eLife, 2021. **10**: p. e66662.
64. Canals, M., et al., *Adenosine A_{2A}-Dopamine D₂ Receptor-Receptor Heteromerization: QUALITATIVE AND QUANTITATIVE ASSESSMENT BY FLUORESCENCE AND BIOLUMINESCENCE ENERGY TRANSFER *.* Journal of Biological Chemistry, 2003. **278**(47): p. 46741-46749.
65. Woods, A.S., et al., *How Calmodulin Interacts with the Adenosine A2A and the Dopamine D2 Receptors.* Journal of Proteome Research, 2008. **7**(8): p. 3428-3434.
66. Burgueño, J., et al., *The Adenosine A_{2A} Receptor Interacts with the Actin-binding Protein α-Actinin *.* Journal of Biological Chemistry, 2003. **278**(39): p. 37545-37552.
67. Piirainen, H., et al., *Calcium modulates calmodulin/α-actinin 1 interaction with and agonist-dependent internalization of the adenosine A2A receptor.* Biochimica et Biophysica Acta (BBA) - Molecular Cell Research, 2017. **1864**(4): p. 674-686.
68. Sjöblom, B., A. Salmazo, and K. Djinović-Carugo, *α-Actinin structure and regulation.* Cellular and Molecular Life Sciences, 2008. **65**(17): p. 2688.
69. Aherne, C.M., E.M. Kewley, and H.K. Eltzschig, *The resurgence of A2B adenosine receptor signaling.* Biochimica et Biophysica Acta (BBA) - Biomembranes, 2011. **1808**(5): p. 1329-1339.

70. Varadi, M., et al., *AlphaFold Protein Structure Database: massively expanding the structural coverage of protein-sequence space with high-accuracy models.* Nucleic Acids Research, 2022. **50**(D1): p. D439-D444.
71. Jumper, J., et al., *Highly accurate protein structure prediction with AlphaFold.* Nature, 2021. **596**(7873): p. 583-589.
72. De Filippo, E., et al., *A2A and A2B adenosine receptors: The extracellular loop 2 determines high (A2A) or low affinity (A2B) for adenosine.* Biochemical Pharmacology, 2020. **172**: p. 113718.
73. Gao, Z.-G., A. Inoue, and K.A. Jacobson, *On the G protein-coupling selectivity of the native A(2B) adenosine receptor.* Biochemical pharmacology, 2018. **151**: p. 201-213.
74. Cohen, M.V., X. Yang, and J.M. Downey, *A(2b) adenosine receptors can change their spots.* British journal of pharmacology, 2010. **159**(8): p. 1595-1597.
75. Sun, Y. and P. Huang, *Adenosine A2B Receptor: From Cell Biology to Human Diseases.* Frontiers in chemistry, 2016. **4**: p. 37-37.
76. Kong, T., et al., *HIF-dependent induction of adenosine A2B receptor in hypoxia.* The FASEB Journal, 2006. **20**(13): p. 2242-2250.
77. Xaus, J., et al., *IFN-γ Up-Regulates the A_{2B} Adenosine Receptor Expression in Macrophages: A Mechanism of Macrophage Deactivation.* The Journal of Immunology, 1999. **162**(6): p. 3607.
78. Xu, X., et al., *A2BAR activation attenuates acute lung injury by inhibiting alveolar epithelial cell apoptosis both in vivo and in vitro.* American Journal of Physiology-Cell Physiology, 2018. **315**(4): p. C558-C570.
79. Zhou, Y., et al., *Distinct Roles for the A_{2B} Adenosine Receptor in Acute and Chronic Stages of Bleomycin-Induced Lung Injury.* The Journal of Immunology, 2011. **186**(2): p. 1097.
80. Iannone, R., et al., *Blockade of A2b Adenosine Receptor Reduces Tumor Growth and Immune Suppression Mediated by Myeloid-Derived Suppressor Cells in a Mouse Model of Melanoma.* Neoplasia, 2013. **15**(12): p. 1400-IN10.
81. Sorrentino, C. and S. Morello, *Role of adenosine in tumor progression: focus on A_{2B} receptor as potential therapeutic target.* Journal of Cancer Metastasis and Treatment, 2017. **3**: p. 127-138.
82. Eisenstein, A., S. Patterson, and K. Ravid, *The Many Faces of the A2b Adenosine Receptor in Cardiovascular and Metabolic Diseases.* Journal of cellular physiology, 2015. **230**(12): p. 2891-2897.
83. Sun, Y., et al., *Actinin-1 binds to the C-terminus of A2B adenosine receptor (A2BAR) and enhances A2BAR cell-surface expression.* Biochemical Journal, 2016. **473**(14): p. 2179-2186.
84. Herrera, C., et al., *Adenosine A_{2B} Receptors Behave as an Alternative Anchoring Protein for Cell Surface Adenosine Deaminase in Lymphocytes and Cultured Cells.* Molecular Pharmacology, 2001. **59**(1): p. 127.
85. Hinz, S., et al., *Adenosine A(2A) receptor ligand recognition and signaling is blocked by A(2B) receptors.* Oncotarget, 2018. **9**(17): p. 13593-13611.
86. Moriyama, K. and M.V. Sitkovsky, *Adenosine A2A Receptor Is Involved in Cell Surface Expression of A2B Receptor.* Journal of Biological Chemistry, 2010. **285**(50): p. 39271-39288.

87. Chalfie, M., et al., *Green Fluorescent Protein as a Marker for Gene Expression.* Science, 1994. **263**(5148): p. 802-805.
88. Rodriguez, E.A., et al., *The Growing and Glowing Toolbox of Fluorescent and Photoactive Proteins.* Trends in biochemical sciences, 2017. **42**(2): p. 111-129.
89. Zacharias David, A., et al., *Partitioning of Lipid-Modified Monomeric GFPs into Membrane Microdomains of Live Cells.* Science, 2002. **296**(5569): p. 913-916.
90. Campbell, R.E., et al., *A monomeric red fluorescent protein.* Proceedings of the National Academy of Sciences of the United States of America, 2002. **99**(12): p. 7877-7882.
91. Cormack, B.P., R.H. Valdivia, and S. Falkow, *FACS-optimized mutants of the green fluorescent protein (GFP).* Gene, 1996. **173**(1): p. 33-38.
92. Nelson, A.L., *Antibody fragments: hope and hype.* mAbs, 2010. **2**(1): p. 77-83.
93. Muyldermans, S., *Nanobodies: Natural Single-Domain Antibodies.* Annual Review of Biochemistry, 2013. **82**(1): p. 775-797.
94. de Beer, M.A. and B.N.G. Giepmans, *Nanobody-Based Probes for Subcellular Protein Identification and Visualization.* Frontiers in Cellular Neuroscience, 2020. **14**.
95. Keppler, A., et al., *A general method for the covalent labeling of fusion proteins with small molecules in vivo.* Nature Biotechnology, 2003. **21**(1): p. 86-89.
96. Los, G.V., et al., *HaloTag: A Novel Protein Labeling Technology for Cell Imaging and Protein Analysis.* ACS Chemical Biology, 2008. **3**(6): p. 373-382.
97. Gautier, A., et al., *An Engineered Protein Tag for Multiprotein Labeling in Living Cells.* Chemistry & Biology, 2008. **15**(2): p. 128-136.
98. Wulf, E., et al., *Fluorescent phallotoxin, a tool for the visualization of cellular actin.* Proceedings of the National Academy of Sciences of the United States of America, 1979. **76**(9): p. 4498-4502.
99. Kozma, E., et al., *Fluorescent ligands for adenosine receptors.* Bioorg Med Chem Lett. , 2013. **23**(1464-3405 (Electronic)): p. 26-36.
100. Yang, X., et al., *Molecular probes for the human adenosine receptors.* Purinergic Signalling, 2021. **17**(1): p. 85-108.
101. Abbe, E., *Beiträge zur Theorie des Mikroskops und der mikroskopischen Wahrnehmung.* Archiv für Mikroskopische Anatomie, 1873. **9**(1): p. 413-468.
102. Chen, B.-C., et al., *Lattice light-sheet microscopy: Imaging molecules to embryos at high spatiotemporal resolution.* Science, 2014. **346**(6208): p. 1257998.
103. Stone, M.B., S.A. Shelby, and S.L. Veatch, *Super-Resolution Microscopy: Shedding Light on the Cellular Plasma Membrane.* Chemical Reviews, 2017. **117**(11): p. 7457-7477.
104. Lelek, M., et al., *Single-molecule localization microscopy.* Nature Reviews Methods Primers, 2021. **1**(1): p. 39.
105. Sharonov, A. and R.M. Hochstrasser, *Wide-field subdiffraction imaging by accumulated binding of diffusing probes.* Proceedings of the National Academy of Sciences, 2006. **103**(50): p. 18911.
106. Rust, M.J., M. Bates, and X. Zhuang, *Sub-diffraction-limit imaging by stochastic optical reconstruction microscopy (STORM).* Nature methods, 2006. **3**(10): p. 793-795.

107. Dempsey, G.T., et al., *Evaluation of fluorophores for optimal performance in localization-based super-resolution imaging.* Nature methods, 2011. **8**(12): p. 1027-1036.
108. Betzig, E., et al., *Imaging Intracellular Fluorescent Proteins at Nanometer Resolution.* Science, 2006. **313**(5793): p. 1642.
109. Hess, S.T., T.P.K. Girirajan, and M.D. Mason, *Ultra-high resolution imaging by fluorescence photoactivation localization microscopy.* Biophysical journal, 2006. **91**(11): p. 4258-4272.
110. Wiedenmann, J., et al., *EosFP, a fluorescent marker protein with UV-inducible green-to-red fluorescence conversion.* Proceedings of the National Academy of Sciences, 2004. **101**(45): p. 15905-15910.
111. McKinney, S.A., et al., *A bright and photostable photoconvertible fluorescent protein.* Nature Methods, 2009. **6**(2): p. 131-133.
112. Schnitzbauer, J., et al., *Super-resolution microscopy with DNA-PAINT.* Nature Protocols, 2017. **12**(6): p. 1198-1228.
113. Kiuchi, T., et al., *Multitarget super-resolution microscopy with high-density labeling by exchangeable probes.* Nature Methods, 2015. **12**(8): p. 743-746.
114. Peters, R., et al., *Quantitative fibre analysis of single-molecule localization microscopy data.* Scientific Reports, 2018. **8**(1): p. 10418.
115. Klein, T., et al., *Live-cell dSTORM with SNAP-tag fusion proteins.* Nature Methods, 2010. **8**: p. 7.
116. Hu, Y.S., H. Cang, and B.F. Lillemeier, *Superresolution imaging reveals nanometer- and micrometer-scale spatial distributions of T-cell receptors in lymph nodes.* Proceedings of the National Academy of Sciences, 2016. **113**(26): p. 7201.
117. Fourier, J.B.J., *Théorie analytique de la chaleur (in French)*. 1822, Paris: Firmin Didot, père et fils.
118. Gustafsson, M.G.L., *Surpassing the lateral resolution limit by a factor of two using structured illumination microscopy.* Journal of Microscopy, 2000. **198**(2): p. 82-87.
119. Gustafsson, M.G.L., et al., *Three-dimensional resolution doubling in wide-field fluorescence microscopy by structured illumination.* Biophysical journal, 2008. **94**(12): p. 4957-4970.
120. Thomas, R. *Fourier transforms of images*. 2017; Available from: https://plus.maths.org/content/fourier-transforms-images.
121. Demmerle, J., et al., *Strategic and practical guidelines for successful structured illumination microscopy.* Nature Protocols, 2017. **12**(5): p. 988-1010.
122. Cox, S., *Super-resolution imaging in live cells.* Developmental biology, 2015. **401**(1): p. 175-181.
123. Lal, A., C. Shan, and P. Xi, *Structured Illumination Microscopy Image Reconstruction Algorithm.* IEEE Journal of Selected Topics in Quantum Electronics, 2016. **22**(4): p. 50-63.
124. Mönkemöller, V., et al., *Multimodal super-resolution optical microscopy visualizes the close connection between membrane and the cytoskeleton in liver sinusoidal endothelial cell fenestrations.* Scientific Reports, 2015. **5**(1): p. 16279.

125. Poulter, N.S., et al., *Platelet actin nodules are podosome-like structures dependent on Wiskott-Aldrich syndrome protein and ARP2/3 complex.* Nature communications, 2015. **6**: p. 7254-7254.
126. Klar, T.A., et al., *Fluorescence microscopy with diffraction resolution barrier broken by stimulated emission.* Proceedings of the National Academy of Sciences, 2000. **97**(15): p. 8206.
127. Balzarotti, F., et al., *Nanometer resolution imaging and tracking of fluorescent molecules with minimal photon fluxes.* Science, 2017. **355**(6325): p. 606-612.
128. Gustafsson, N., et al., *Fast live-cell conventional fluorophore nanoscopy with ImageJ through super-resolution radial fluctuations.* Nature Communications, 2016. **7**(1): p. 12471.
129. Dertinger, T., et al., *Fast, background-free, 3D super-resolution optical fluctuation imaging (SOFI).* Proceedings of the National Academy of Sciences, 2009. **106**(52): p. 22287.
130. Romarowski, A., et al., *Super-resolution imaging of live sperm reveals dynamic changes of the actin cytoskeleton during acrosomal exocytosis.* Journal of cell science, 2018. **131**(21): p. jcs218958.
131. Lukeš, T., et al., *Quantifying protein densities on cell membranes using super-resolution optical fluctuation imaging.* Nature Communications, 2017. **8**(1): p. 1731.
132. Yang, T., et al., *Advancing biological super-resolution microscopy through deep learning: a brief review.* ArXiv, 2021. **abs/2106.13064**.
133. Qiao, C., et al., *Evaluation and development of deep neural networks for image super-resolution in optical microscopy.* Nature Methods, 2021. **18**(2): p. 194-202.
134. Ouyang, W., et al., *Deep learning massively accelerates super-resolution localization microscopy.* Nature Biotechnology, 2018. **36**(5): p. 460-468.
135. Lam, F., et al., *Super-resolution for everybody: An image processing workflow to obtain high-resolution images with a standard confocal microscope.* Methods, 2017. **115**: p. 17-27.
136. Zhao, W., et al., *Sparse deconvolution improves the resolution of live-cell super-resolution fluorescence microscopy.* Nature Biotechnology, 2022. **40**(4): p. 606-617.
137. Masuho, I., N.A. Martemyanov Ka Fau - Lambert, and N.A. Lambert, *Monitoring G Protein Activation in Cells with BRET.* Methods Mol Biol., 2015. **1335**: p. 107-113.
138. Chen, F., W. Tillberg Paul, and S. Boyden Edward, *Expansion microscopy.* Science, 2015. **347**(6221): p. 543-548.
139. Tillberg, P.W., et al., *Protein-retention expansion microscopy of cells and tissues labeled using standard fluorescent proteins and antibodies.* Nature biotechnology, 2016. **34**(9): p. 987-992.
140. Chozinski, T.J., et al., *Expansion microscopy with conventional antibodies and fluorescent proteins.* Nature Methods, 2016. **13**(6): p. 485-488.
141. Gambarotto, D., et al., *Imaging cellular ultrastructures using expansion microscopy (U-ExM).* Nature methods, 2019. **16**(1): p. 71-74.
142. Faulkner, E.L., et al., *Imaging nanoscale nuclear structures with expansion microscopy.* Journal of Cell Science, 2022: p. jcs.259009.

143. Truckenbrodt, S., et al., *X10 expansion microscopy enables 25-nm resolution on conventional microscopes.* EMBO reports, 2018. **19**(9): p. e45836.
144. Chang, J.-B., et al., *Iterative expansion microscopy.* Nature Methods, 2017. **14**(6): p. 593-599.
145. Ku, T., et al., *Multiplexed and scalable super-resolution imaging of three-dimensional protein localization in size-adjustable tissues.* Nature Biotechnology, 2016. **34**(9): p. 973-981.
146. Chozinski, T.J., et al., *Volumetric, Nanoscale Optical Imaging of Mouse and Human Kidney via Expansion Microscopy.* Scientific Reports, 2018. **8**(1): p. 10396.
147. Wassie, A.T., Y. Zhao, and E.S. Boyden, *Expansion microscopy: principles and uses in biological research.* Nature Methods, 2019. **16**(1): p. 33-41.
148. Vanheusden, M., et al., *Fluorescence Photobleaching as an Intrinsic Tool to Quantify the 3D Expansion Factor of Biological Samples in Expansion Microscopy.* ACS Omega, 2020. **5**(12): p. 6792-6799.
149. Scheible, M.B. and P. Tinnefeld, *Quantifying Expansion Microscopy with DNA Origami Expansion Nanorulers.* bioRxiv, 2018: p. 265405.
150. Düring, D.N., et al., *Expansion Light Sheet Microscopy Resolves Subcellular Structures in Large Portions of the Songbird Brain.* Frontiers in Neuroanatomy, 2019. **13**.
151. Halpern, A.R., et al., *Hybrid Structured Illumination Expansion Microscopy Reveals Microbial Cytoskeleton Organization.* ACS nano, 2017. **11**(12): p. 12677-12686.
152. Wang, Y., et al., *Combined expansion microscopy with structured illumination microscopy for analyzing protein complexes.* Nature Protocols, 2018. **13**(8): p. 1869-1895.
153. Gao, M., et al., *Expansion Stimulated Emission Depletion Microscopy (ExSTED).* ACS Nano, 2018. **12**(5): p. 4178-4185.
154. Zwettler, F.U., et al., *Molecular resolution imaging by post-labeling expansion single-molecule localization microscopy (Ex-SMLM).* Nature Communications, 2020. **11**(1): p. 3388.
155. Shi, X., et al., *Label-retention expansion microscopy.* Journal of Cell Biology, 2021. **220**(9): p. e202105067.
156. Park, C.E., et al., *Super-Resolution Three-Dimensional Imaging of Actin Filaments in Cultured Cells and the Brain via Expansion Microscopy.* ACS Nano, 2020. **14**(11): p. 14999-15010.
157. Wen, G., et al., *Evaluation of Direct Grafting Strategies via Trivalent Anchoring for Enabling Lipid Membrane and Cytoskeleton Staining in Expansion Microscopy.* ACS Nano, 2020. **14**(7): p. 7860-7867.
158. Yao, L., et al., *Application of SNAP-Tag in Expansion Super-Resolution Microscopy Using DNA Oligostrands.* Frontiers in Chemistry, 2021. **9**.
159. Heil, H.S., et al., *Mapping densely packed αIIbβ3 receptors in murine blood platelets with expansion microscopy.* Platelets, 2022: p. 1-10.
160. Shen, H., et al., *Single Particle Tracking: From Theory to Biophysical Applications.* Chemical Reviews, 2017. **117**(11): p. 7331-7376.
161. Chang, Y.-P., et al., *Tracking bio-molecules in live cells using quantum dots.* Journal of biophotonics, 2008. **1**(4): p. 287-298.

162. Nenasheva, T.A., et al., *Abundance, distribution, mobility and oligomeric state of M_2 muscarinic acetylcholine receptors in live cardiac muscle.* Journal of molecular and cellular cardiology, 2013. **57**: p. 129-136.
163. Sungkaworn, T., et al., *Single-molecule imaging reveals receptor–G protein interactions at cell surface hot spots.* Nature, 2017. **550**(7677): p. 543-547.
164. Ovesný, M., et al., *ThunderSTORM: a comprehensive ImageJ plug-in for PALM and STORM data analysis and super-resolution imaging.* Bioinformatics (Oxford, England), 2014. **30**(16): p. 2389-2390.
165. Sage, D., et al., *Super-resolution fight club: assessment of 2D and 3D single-molecule localization microscopy software.* Nature Methods, 2019. **16**(5): p. 387-395.
166. Marsh, R.J., et al., *Artifact-free high-density localization microscopy analysis.* Nature Methods, 2018. **15**(9): p. 689-692.
167. Jensen, L.G., et al., *Correction of multiple-blinking artifacts in photoactivated localization microscopy.* Nature Methods, 2022.
168. Bohrer, C.H., et al., *A pairwise distance distribution correction (DDC) algorithm to eliminate blinking-caused artifacts in SMLM.* Nature methods, 2021. **18**(6): p. 669-677.
169. Jungmann, R., et al., *Quantitative super-resolution imaging with qPAINT.* Nature Methods, 2016. **13**(5): p. 439-442.
170. Khater, I.M., I.R. Nabi, and G. Hamarneh, *A Review of Super-Resolution Single-Molecule Localization Microscopy Cluster Analysis and Quantification Methods.* Patterns, 2020. **1**(3): p. 100038.
171. Ester, M., et al., *A density-based algorithm for discovering clusters in large spatial databases with noise*, in *Proceedings of the Second International Conference on Knowledge Discovery and Data Mining*. 1996, AAAI Press: Portland, Oregon. p. 226–231.
172. Pike, J.A., et al., *Topological data analysis quantifies biological nano-structure from single molecule localization microscopy.* bioRxiv, 2018: p. 400275.
173. Levet, F., et al., *SR-Tesseler: a method to segment and quantify localization-based super-resolution microscopy data.* Nature Methods, 2015. **12**(11): p. 1065-1071.
174. Williamson, D.J., et al., *Machine learning for cluster analysis of localization microscopy data.* Nature Communications, 2020. **11**(1): p. 1493.
175. Nieves, D.J., et al., *A framework for evaluating the performance of SMLM cluster analysis algorithms.* bioRxiv, 2021: p. 2021.06.19.449098.
176. Tinevez, J.-Y., et al., *TrackMate: An open and extensible platform for single-particle tracking.* Methods, 2017. **115**: p. 80-90.
177. Oviedo-Bocanegra, L.M., et al., *Single molecule/particle tracking analysis program SMTracker 2.0 reveals different dynamics of proteins within the RNA degradosome complex in Bacillus subtilis.* Nucleic Acids Research, 2021. **49**(19): p. e112-e112.
178. Endesfelder, M., Schießl, C., Turkowyd, B., Lechner, T., Endesfelder, U., *SWIFT: Manuscript in Prep*.
179. Kuhn, T., et al., *Single molecule tracking and analysis framework including theory-predicted parameter settings.* Scientific Reports, 2021. **11**(1): p. 9465.
180. Jaqaman, K., et al., *Robust single-particle tracking in live-cell time-lapse sequences.* Nature Methods, 2008. **5**(8): p. 695-702.

181. Hansen, A.S., et al., *Robust model-based analysis of single-particle tracking experiments with Spot-On.* eLife, 2018. **7**: p. e33125.
182. Karslake, J.D., et al., *SMAUG: Analyzing single-molecule tracks with nonparametric Bayesian statistics.* Methods, 2021. **193**: p. 16-26.
183. Das, R., C.W. Cairo, and D. Coombs, *A Hidden Markov Model for Single Particle Tracks Quantifies Dynamic Interactions between LFA-1 and the Actin Cytoskeleton.* PLOS Computational Biology, 2009. **5**(11): p. e1000556.
184. Vega, A.R., et al., *Multistep Track Segmentation and Motion Classification for Transient Mobility Analysis.* Biophysical journal, 2018. **114**(5): p. 1018-1025.
185. Briddon, S.J., L.E. Kilpatrick, and S.J. Hill, *Studying GPCR Pharmacology in Membrane Microdomains: Fluorescence Correlation Spectroscopy Comes of Age.* Trends in Pharmacological Sciences, 2018. **39**(2): p. 158-174.
186. Comeo, E., et al., *Subtype-Selective Fluorescent Ligands as Pharmacological Research Tools for the Human Adenosine A2A Receptor.* Journal of Medicinal Chemistry, 2020. **63**(5): p. 2656-2672.
187. Otsu, N., *A Threshold Selection Method from Gray-Level Histograms.* IEEE Transactions on Systems, Man, and Cybernetics, 1979. **9**(1): p. 62-66.
188. Ball, G., et al., *SIMcheck: a Toolbox for Successful Super-resolution Structured Illumination Microscopy.* Scientific Reports, 2015. **5**(1): p. 15915.
189. Baker, J.G., I.P. Hall, and S.J. Hill, *Pharmacological characterization of CGP 12177 at the human beta(2)-adrenoceptor.* British journal of pharmacology, 2002. **137**(3): p. 400-408.
190. Ganguly, S., T.J. Pucadyil, and A. Chattopadhyay, *Actin Cytoskeleton-Dependent Dynamics of the Human Serotonin1A Receptor Correlates with Receptor Signaling.* Biophysical Journal, 2008. **95**(1): p. 451-463.
191. Ganguly, S., R. Saxena, and A. Chattopadhyay, *Reorganization of the actin cytoskeleton upon G-protein coupled receptor signaling.* Biochimica et Biophysica Acta (BBA) - Biomembranes, 2011. **1808**(7): p. 1921-1929.
192. Jaqaman, K., et al., *Cytoskeletal Control of CD36 Diffusion Promotes Its Receptor and Signaling Function.* Cell, 2011. **146**(4): p. 593-606.
193. Navarro, G., et al., *Quaternary structure of a G-protein-coupled receptor heterotetramer in complex with Gi and Gs.* BMC biology, 2016. **14**: p. 26-26.
194. Lillo, A., et al., *Adenosine A(2A) and A(3) Receptors Are Able to Interact with Each Other. A Further Piece in the Puzzle of Adenosine Receptor-Mediated Signaling.* International journal of molecular sciences, 2020. **21**(14): p. 5070.
195. Charalambous, C., et al., *Restricted Collision Coupling of the A_{2A} Receptor Revisited: EVIDENCE FOR PHYSICAL SEPARATION OF TWO SIGNALING CASCADES *.* Journal of Biological Chemistry, 2008. **283**(14): p. 9276-9288.
196. Thul, P.J., et al., *A subcellular map of the human proteome.* Science, 2017. **356**(6340): p. eaal3321.
197. Hill, S.J., J.G. Baker, and S. Rees, *Reporter-gene systems for the study of G-protein-coupled receptors.* Current Opinion in Pharmacology, 2001. **1**(5): p. 526-532.
198. Baker, J.G., et al., *Influence of fluorophore and linker composition on the pharmacology of fluorescent adenosine A1 receptor ligands.* British journal of pharmacology, 2010. **159**(4): p. 772-786.

199. Cooper, S.L., et al., *The effect of two selective A(1) -receptor agonists and the bitopic ligand VCP746 on heart rate and regional vascular conductance in conscious rats.* British journal of pharmacology, 2020. **177**(2): p. 346-359.
200. Stoddart, Leigh A., et al., *Fragment Screening at Adenosine-A3 Receptors in Living Cells Using a Fluorescence-Based Binding Assay.* Chemistry & Biology, 2012. **19**(9): p. 1105-1115.
201. Jimenez, A., K. Friedl, and C. Leterrier, *About samples, giving examples: Optimized Single Molecule Localization Microscopy.* Methods, 2020. **174**: p. 100-114.
202. Palayret, M., et al., *Virtual-'Light-Sheet' Single-Molecule Localisation Microscopy Enables Quantitative Optical Sectioning for Super-Resolution Imaging.* PLOS ONE, 2015. **10**(4): p. e0125438.
203. Culley, S., et al., *Quantitative mapping and minimization of super-resolution optical imaging artifacts.* Nature Methods, 2018. **15**(4): p. 263-266.
204. Khan, A.O., et al., *CRISPR-Cas9 Mediated Labelling Allows for Single Molecule Imaging and Resolution.* Scientific Reports, 2017. **7**(1): p. 8450.
205. Khan, A.O., et al., *Optimised insert design for improved single-molecule imaging and quantification through CRISPR-Cas9 mediated knock-in.* Scientific Reports, 2019. **9**(1): p. 14219.
206. Mylvaganam, S., et al., *Stabilization of Endothelial Receptor Arrays by a Polarized Spectrin Cytoskeleton Facilitates Rolling and Adhesion of Leukocytes.* Cell Reports, 2020. **31**(12).
207. Kirui, J., et al., *The Phosphatidylserine Receptor TIM-1 Enhances Authentic Chikungunya Virus Cell Entry.* Cells, 2021. **10**(7).
208. Ditlev, J.A., et al., *A composition-dependent molecular clutch between T cell signaling condensates and actin.* eLife, 2019. **8**: p. e42695.
209. White, C.W., et al., *NanoBRET ligand binding at a GPCR under endogenous promotion facilitated by CRISPR/Cas9 genome editing.* Cellular Signalling, 2019. **54**: p. 27-34.
210. Erdmann, R.S., et al., *Labeling Strategies Matter for Super-Resolution Microscopy: A Comparison between HaloTags and SNAP-tags.* Cell Chemical Biology, 2019. **26**(4): p. 584-592.e6.
211. Köse, M., et al., *Fluorescent-Labeled Selective Adenosine A2B Receptor Antagonist Enables Competition Binding Assay by Flow Cytometry.* Journal of Medicinal Chemistry, 2018. **61**(10): p. 4301-4316.
212. Klotz, K.N., et al., *Comparative pharmacology of human adenosine receptor subtypes – characterization of stably transfected receptors in CHO cells.* Naunyn-Schmiedeberg's Archives of Pharmacology, 1997. **357**(1): p. 1-9.
213. Insel, P.A., et al., *Compartmentation of G-protein-coupled receptors and their signalling components in lipid rafts and caveolae.* Biochemical Society Transactions, 2005. **33**(5): p. 1131-1134.
214. Khan, A.O., et al., *Optimised CRISPR-Cas9 mediated single molecule imaging for accurate quantification through endogenous expression.* bioRxiv, 2018: p. 482596.
215. Hinz, S., et al., *BAY60-6583 Acts as a Partial Agonist at Adenosine A_{2B} Receptors.* Journal of Pharmacology and Experimental Therapeutics, 2014. **349**(3): p. 427.

216. Murase, K., et al., *Ultrafine Membrane Compartments for Molecular Diffusion as Revealed by Single Molecule Techniques.* Biophysical Journal, 2004. **86**(6): p. 4075-4093.
217. Peters, D.M., et al., *Agonist-Induced Desensitization of A2B Adenosine Receptors.* Biochemical Pharmacology, 1998. **55**(6): p. 873-882.
218. Matharu, A.-L., et al., *Rapid Agonist-induced Desensitization and Internalization of the A2B Adenosine Receptor Is Mediated by a Serine Residue Close to the COOH Terminus*.* Journal of Biological Chemistry, 2001. **276**(32): p. 30199-30207.
219. Chugh, P. and E.K. Paluch, *The actin cortex at a glance.* Journal of Cell Science, 2018. **131**(14).
220. Gowrishankar, K., et al., *Active Remodeling of Cortical Actin Regulates Spatiotemporal Organization of Cell Surface Molecules.* Cell, 2012. **149**(6): p. 1353-1367.
221. Pollard, T.D. and J.A. Cooper, *Actin, a central player in cell shape and movement.* Science (New York, N.Y.), 2009. **326**(5957): p. 1208-1212.
222. Xu, K., G. Zhong, and X. Zhuang, *Actin, Spectrin, and Associated Proteins Form a Periodic Cytoskeletal Structure in Axons.* Science, 2013. **339**(6118): p. 452-456.
223. Aizawa, H., M. Sameshima, and I. Yahara, *A Green Fluorescent Protein-actin Fusion Protein Dominantly Inhibits Cytokinesis, Cell Spreading, and Locomotion in Dictyostelium.* Cell Structure and Function, 1997. **22**(3): p. 335-345.
224. Deibler, M., J.P. Spatz, and R. Kemkemer, *Actin Fusion Proteins Alter the Dynamics of Mechanically Induced Cytoskeleton Rearrangement.* PLOS ONE, 2011. **6**(8): p. e22941.
225. Nagasaki, A., et al., *The Position of the GFP Tag on Actin Affects the Filament Formation in Mammalian Cells.* Cell Struct Funct, 2017. **42**(2): p. 131-140.
226. DesMarais, V., et al., *Optimizing leading edge F-actin labeling using multiple actin probes, fixation methods and imaging modalities.* BioTechniques, 2019. **66**(3): p. 113-119.
227. Xu, K., H.P. Babcock, and X. Zhuang, *Dual-objective STORM reveals three-dimensional filament organization in the actin cytoskeleton.* Nature Methods, 2012. **9**(2): p. 185-188.
228. Xia, S., et al., *Nanoscale Architecture of the Cortical Actin Cytoskeleton in Embryonic Stem Cells.* Cell Reports, 2019. **28**(5): p. 1251-1267.e7.
229. Kronlage, C., et al., *Feeling for Filaments: Quantification of the Cortical Actin Web in Live Vascular Endothelium.* Biophysical Journal, 2015. **109**(4): p. 687-698.
230. Zhang, Z., S. Xia, and P. Kanchanawong, *An integrated enhancement and reconstruction strategy for the quantitative extraction of actin stress fibers from fluorescence micrographs.* BMC Bioinformatics, 2017. **18**(1): p. 268.
231. Mullins, R.D., J.A. Heuser, and T.D. Pollard, *The interaction of Arp2/3 complex with actin: Nucleation, high affinity pointed end capping, and formation of branching networks of filaments.* Proceedings of the National Academy of Sciences, 1998. **95**(11): p. 6181.
232. Melak, M., M. Plessner, and R. Grosse, *Actin visualization at a glance.* Journal of Cell Science, 2017. **130**(3): p. 525-530.

233. Lukinavičius, G., et al., *Fluorogenic probes for live-cell imaging of the cytoskeleton.* Nature Methods, 2014. **11**(7): p. 731-733.
234. Flormann, D.A.D., et al., *A novel universal algorithm for filament network tracing and cytoskeleton analysis.* bioRxiv, 2021: p. 2021.01.04.425230.
235. Cooper, J.A., *Effects of cytochalasin and phalloidin on actin.* The Journal of cell biology, 1987. **105**(4): p. 1473-1478.
236. Zalavary, S. and T. Bengtsson, *Adenosine inhibits actin dynamics in human neutrophils: Evidence for the involvement of cAMP.* European Journal of Cell Biology, 1998. **75**(2): p. 128-139.
237. Apgar, J.R., *Polymerization of actin in RBL-2H3 cells can be triggered through either the IgE receptor or the adenosine receptor but different signaling pathways are used.* Molecular biology of the cell, 1994. **5**(3): p. 313-322.
238. Bowser, J.L., et al., *Loss of CD73-mediated actin polymerization promotes endometrial tumor progression.* The Journal of Clinical Investigation, 2016. **126**(1): p. 220-238.
239. Flores, L.R., et al., *Lifeact-TagGFP2 alters F-actin organization, cellular morphology and biophysical behaviour.* Scientific Reports, 2019. **9**(1): p. 3241.
240. Riedl, J., et al., *Lifeact mice for studying F-actin dynamics.* Nature Methods, 2010. **7**(3): p. 168-169.
241. Jungmann, R., et al., *Single-Molecule Kinetics and Super-Resolution Microscopy by Fluorescence Imaging of Transient Binding on DNA Origami.* Nano Letters, 2010. **10**(11): p. 4756-4761.
242. Sankaran, J., et al., *Simultaneous spatiotemporal super-resolution and multi-parametric fluorescence microscopy.* Nature Communications, 2021. **12**(1): p. 1748.
243. Lagache, T., et al., *Mapping molecular assemblies with fluorescence microscopy and object-based spatial statistics.* Nature Communications, 2018. **9**(1): p. 698.
244. Helmuth, J.A., G. Paul, and I.F. Sbalzarini, *Beyond co-localization: inferring spatial interactions between sub-cellular structures from microscopy images.* BMC Bioinformatics, 2010. **11**(1): p. 372.
245. Malkusch, S., et al., *Coordinate-based colocalization analysis of single-molecule localization microscopy data.* Histochemistry and Cell Biology, 2012. **137**(1): p. 1-10.
246. Arts, M., et al., *Particle Mobility Analysis Using Deep Learning and the Moment Scaling Spectrum.* Scientific Reports, 2019. **9**(1): p. 17160.
247. Pinholt Henrik, D., et al., *Single-particle diffusional fingerprinting: A machine-learning framework for quantitative analysis of heterogeneous diffusion.* Proceedings of the National Academy of Sciences, 2021. **118**(31): p. e2104624118.
248. Wang, Q., et al., *Deep-Learning-Assisted Single-Molecule Tracking on a Live Cell Membrane.* Analytical Chemistry, 2021. **93**(25): p. 8810-8816.
249. Sarkar, P., et al., *Chronic cholesterol depletion increases F-actin levels and induces cytoskeletal reorganization via a dual mechanism.* Journal of Lipid Research, 2022. **63**(5).
250. Kwik, J., et al., *Membrane cholesterol, lateral mobility, and the phosphatidylinositol 4,5-bisphosphate-dependent organization of cell actin.*

Proceedings of the National Academy of Sciences, 2003. **100**(24): p. 13964-13969.

APPENDICES

Appendix 1 – Analysis Scripts

Pseudo codes

1.1 Actin image simulation

```
Set imageMode: ‘SRRF’, ‘3D SIM’, ‘TIRF SIM’, ‘TIRF’
For imageMode:
    case 'SRRF'
        sizeI = 10010;
        bin = 776;
        psf = 8.02;
    case '3D SIM'
        sizeI = 10020;
        bin = 310;
        psf = 3.2
    case 'TIRF SIM'
        sizeI = 10020;
        bin = 310;
        psf = 3.2;
    case 'TIRF'
        sizeI = 10020;
        bin = 155;
        psf = 1.6;
end
Set number of filaments
Set filament length (L)
Create blank image array of size sizeI

For set number of filaments;
Set variable alpha (line angle) to random integer between 0 and 360
Set random seed (xS, yS) between 0 and sizeI
```

```
Calculate line start (x1, y1) and line end (x2, y2) using alpha and L
Draw line (x1 y1, x2 y2) on blank image array
Set daughter filament length (LD)
Select randomised point on mother filament (xD, yD)
Set angleAlpha as positive or negative at random
Calculate end of daughter filament xD2, yD2 using angleAlpha and LD
Draw line (xD yD, xD2 yD2) on image array
end

Dilate lines
Bin dilated mesh pixels to imageMode bin size
Apply Gaussian filter using imageMode PSF
Apply 'poisson' noise
Apply 'localvar' noise
Apply smoothing (optional)
Save output
```

1.2 ExM actin analysis

```
Load image
Set peak height threshold

For 100 repeats;
Calculate image centre (xS, yS)
Set line length (L) as half image height
Set line angle to integer between 0 and 360 at random
Set line start (x1, y1) and set line end (x2, y2)
Calculate image intensity profile for line x1 y1, x2 y2
Normalise intensity profile
Find peak location, width, and distance between peaks
End

Save output
```

1.3 SIM actin/receptor analysis

```
load binary actin image
load receptor point coordinates
set adjacency threshold

function loc = disttoact(actcord, actin, coord, thresh)
for all points
if
point sits on actin mark point 'ON'
else if
point sits within adjacency threshold mark point 'ADJACENT'
else
point sits off actin mark point 'OFF'
end
end
```

1.4 SIM actin/α-actinin-1/receptor analysis

```
load point results for point/actin analysis
load receptor point coordinates
set adjacency threshold for receptor/alpha actinin

find distances between all points in two coordinate sets
find distances below and above threshold

   for all alpha actinin points above threshold
       report actin association
   for all alpha actinin points below threshold
       report actin association

Output data
```

1.5 Code availability

Full scripts are accessible at https://github.com/biologevie/thesis-scripts and https://github.com/biologevie/actin-analysis.

Appendix 2 – Videos

Videos are currently accessible at https://drive.google.com/drive/folders/17ptZ15hbju8HFhflAvzoa13Yq4gK8h7w?usp=sharing.

Video 1 – 3D SIM ExM actin example. A ~7 µm deep 3D SIM stack of expanded Actin ExM labelled actin, showing resolution achievable in 3D with this technique. Measurements given are not adjusted for expansion factor.

Video 2 – Dual SRRF and SPT imaging over time. SRRF reconstructions of 100 frames of SiR actin with SNAP-549 labelled SNAP-A_{2B}R tracks, imaged at an exposure of 20 ms. Frame rates for actin are therefore 0.5 fps, and 50 fps for the receptor.

Video 3 – SPIM ExM actin imaging. Actin ExM labelled actin imaged across a full expanded A549 cell, imaged with an iSPIM lightsheet system.

Appendix 3 – Published Works

Published articles which arose from work in this thesis or contributions were made by adjacent experiments:

Faulkner, E. L., Pike, J. A., Densham, R. M., **Garlick, E.**, Thomas, S. G., Neely, R. K. and Morris, J. R. *Imaging nanoscale nuclear structures with expansion microscopy*. Journal of Cell Science. 2022;135(14). DOI: 10.1242/jcs.259009

Garlick, E., Faulkner, E. L., Briddon, S. J. and Thomas, S. G. *Simple methods for quantifying super-resolved cortical actin*. Scientific Reports. 2022;12(1). DOI: 10.1038/s41598-022-06702-w

Garlick, E., Thomas, S. G., Owen, D. M. *Super-Resolution Imaging Approaches for Quantifying F-Actin in Immune Cells*. Frontiers in Cell and Developmental Biology. 2021;9. DOI: 10.3389/fcell.2021.676066

Bourne, J. H., Beristain-Covarrubias, N., Zuidscherwoude, M., Campos, J., Di, Y., **Garlick, E.**, Colicchia, M., Terry, L. V., Thomas, S. G., Brill, A., Bayry, J., Watson, S. P. and Rayes, J. *CLEC-2 Prevents Accumulation and Retention of Inflammatory Macrophages During Murine Peritonitis*. Frontiers in Immunology. 2021;12. DOI: 10.1101/2020.12.21.423770